THE UNIVERSITY *of* EDINBURGH

Formation, Structure and Mechanical Properties of Hydrogel-Emulsions.

Fernando Carbonell-Aviñó

Doctor of Philosophy
The University of Edinburgh
March 2021

Abstract

Oil-in-water emulsions are ubiquitous in fields such as food, cosmetic and pharmaceutical industries due to their ability to impart texture, or transport or solubilise hydrophobic constituents in a water continuous phase. However, emulsions are thermodynamically unstable and a third constituent or more needs to be added to the mixture to prevent phase separation, at least during the product shelf-life. The use of networks with crosslinked hydrophilic polymer chains (hydrogels) to stabilise emulsions, have been exploited by scientists for long periods of time. Their ability to easily be modified with different functional groups, makes low molecular weight peptides an advantageous choice to form hydrogels. The aim of this thesis is to study the behaviour of dipeptide fibres at interfaces and in the bulk, using a combination of rheological, imaging and *in vivo* research techniques. Dipeptides are small proteins consisting of only two amino acids linked together by one peptide bond. At high pH, the dipeptide molecules form micelles which transform into a hydrogel of fibres in response to the addition of salt. Under high shear the hydrogel is disrupted and will reform around bubbles or droplets.

Following previous studies, we study the behaviour of the dipeptide at low concentration and use salt to trigger gelation. We first present a route to achieving repeatable hydrogel formation. We characterise the properties of the hydrogel for two different salt ($MgSO_4$) concentrations. Using the hydrogel, we proof that at such a low dipeptide concentration, the hydrogel is too weak to prevent ripening of the bubbles, which reduces the long-term stability of the foam. However, under the same conditions, emulsions prepared from some oils are highly stable. Finally, we examine the wetting properties of the oil droplets at a hydrogel surface as a guide to the resulting emulsions.

The behaviour of hydrogels were further characterised using extensional rheology. Hydrogels were prepared with different salts ($MgSO_4$, $CaCl_2$ and NaCl)

concentrations and stretched at different velocities. We show that the collapse scenario of the hydrogel films is salt type dependent. Hydrogels turn into elastic solid films that collapse at short distances when prepared with calcium chloride. By contrast, hydrogels prepared with sodium chloride develop into extremely viscous films that do not burst; they instead, form a thread that breaks under capillarity. In between, hydrogel films prepared with magnesium sulfate exhibit a viscoelastic response that allows the film to stretch and form a bridge that burst on itself. In addition to this, we observe a non-monotonic trend dependence of the film strength on salt ($MgSO_4$) concentration. Lastly, we observe a disagreement between image and equation based surface areas at intermediate and long distances; while equation based surface areas keep increasing linearly after overtaking the surface area of the rings holding the film, image based surface areas drop to zero when they are near or equal the surface area of the rings.

The behaviour of fibre-coated interfaces prepared at different salt ($MgSO_4$) concentrations were studied by conducting strain and frequency sweep tensiometer based dilatational experiments. We have shown that stable liquid-liquid interfaces stabilised by dipeptide fibres, can have a highly nonlinear response to dilatational strain amplitudes. Interfaces prepared at high salt concentrations show an increase in the elastic response, as opposed to films prepared at low salt concentrations, which collapse at small deformations. In between, films prepared at intermediate salt concentrations, show a more viscoelastic response, with lower resistance to deformation. Furthermore, films prepared at high salt concentrations show a strain softening/hardening response when deformed at intermediate and high amplitudes not reported before in large amplitude oscillatory dilatational (LAOD) experiments. Finally, we observe that the method to quantify the degree of nonlinearities in Lissajous curves fails in some cases and hence propose a different approach to quantify nonlinearities that span over the whole range of strains.

Last, the effect of salt triggered hydrogel-emulsions with different mechanical properties on the lipid digestion was investigated using a static *in vitro* model. The rate and extent of lipid digestibility was observed to be higher for emulsions prepared with calcium chloride than with magnesium sulfate. Emulsions prepared with magnesium sulfate show a non-monotonic dependence of digestion on salt concentration, probably caused by the increase in film strength observed in chapter 3 when using extensional rheometry.

Declaration

I declare that this thesis was composed by myself, that the work contained herein is my own except where explicitly stated otherwise in the text, and that this work has not been submitted for any other degree or professional qualification except as specified.

Parts of this work have been published in jointly authored articles and the contribution of the candidate to these articles is explicitly stated here. The work presented in Chapter 3 has already been published in [1]. For this article the candidate performed all the experiments and wrote some of the sections in the draft paper.

(*Fernando Carbonell-Aviñó, March 2021*)

Acknowledgements

I wish to express my sincere appreciation to the person who, without him, I would not have been able to complete this thesis, my supervisor, Paul Clegg. Thanks Paul for guiding and encouraging me over the past few years and for all the meetings and conversations we had, these were vital to make the most of me.

Many thanks to Tao Li who for explaining me how to prepare dipeptide-based hydrogels that I have been using through all my thesis. I would like to thank Cecile Monteux for showing us how to use the extensional tensiometer used in Chapter 4 and for being always so kind. I am very grateful to Martin Lellep for the creation of an image processing script to characterise the catenoid-shaped films from Chapter 4 and for introducing me to python. Thanks to Rudy Mears for teaching me how to use the tedious drop profile tensiometer to measure the rheological properties of interfacial films studied in Chapter 5. Thanks to Pete Wilde and Ana-Isabel Mulet-Cabero for allowing me to work at the Quadram Institute in Norwich and teaching me the pH stat method used in Chapter 6 to study the effect of salt in hydrogel-emulsions subjected to *in vitro* intestinal digestions.

Thanks to all my colleagues that I have worked with over the years for all the useful advice and stimulating discussions.

Lastly, I would like to thank my friends and family for their support and for being always there, specially my siblings Edu and Mary.

Contents

List of Figures

List of Tables

List of Symbols

γ	interfacial tension [N/m^{-1}]
γ_{ow}	oil-water interfacial tension [N/m^{-1}]
γ_{po}	particle-oil interfacial tension [N/m^{-1}]
γ_{pw}	particle-water interfacial tension [N/m^{-1}]
Δp	density difference between phases
ΔP	Laplace pressure [N/m^2]
ΔP_0	pressure difference at a reference plane [N/m^2]
ϵ	strain [s^{-1}]
ϵ_0	strain of a non-deformed interface [s^{-1}]
η_d	dilattaional viscosity [N·s/m^2]
η'_L	large-rate dynamic viscosity [N·s/m^2]
η'_M	minimum-rate dynamic viscosity [N·s/m^2]
μ	micro
Π	surface pressure [N/m^{-1}]
ρ_d	density of the droplet phase
υ	bulk viscosity [N·s/m^2]
υ_D	interfacial dilatational viscosity [N·s/m^2]
ϕ	tangent angle
ω	frequency [Hz]
Ω	ohm [Kg·m^2· s^{-3}· A^{-2}]
a	radius of the mid-plane
A	area [m^2]
a_c	critical radius of the mid-plane
A_0	area of a non-deformaed interface [m^2]

B	coefficient describing the shape of the curve
Bo	Bond number
Bq	Boussinesq number
C	critical point at which a film cannot exist
$\circ C$	degree Celsius
E	elastic modulus [N/m^{-1}]
$E'_{L,C}$	large strain modulus in compression [N/m^{-1}]
$E'_{L,E}$	large strain modulus in extension [N/m^{-1}]
$E'_{M,C}$	minimum strain modulus in compression [N/m^{-1}]
$E'_{M,E}$	minimum strain modulus in extension [N/m^{-1}]
E_0	elastic modulus of a non-deformaed interface [N/m^{-1}]
F	Helmholtz energy [J/K]
FFA	precentage of free fatty acids released
g	acceleration due to gravity [m/s^2]
G	Gibbs energy [J/K]
G'	storage modulus [N/m^2]
G''	elastic modulus [N/m^2]
G'_L	large strain modulus [N/m^2]
G'_M	minimum strain modulus [N/m^2]
h	distance between the rings
h_c	critical distance between rings
h_o	distance at which the area of the film equals the area of the rings
L	length-scale of the system
M	mole
n	number of moles
p	pressure [N/m^{-1}]
r	radius
R	radius of the rings
R_0	radius of curvature at the drop apex
R_z	axial radius of the profile curve
S	surface area [m^2]

$S - factor$	strain siftenig ratio
S_{com}	strain siftenig ratio in compression
S_{ext}	strain siftenig ratio in extension
t	time [s]
T	temperature [K]
V	volume [m^3]
wt	weight percentage
X_i	horizontal coodinate or distance
X_L	horizontal of the lowest point of the curve
Y_i	vertical coodinate or height
Y_L	height of the lowest point of the curve
z	vertical coordinate of the drop

Chapter 1

Introduction and Background

1.0.1 Surfaces and Interfaces

Atoms or molecules at surfaces have different properties from those in the bulk phase. In the case of an air-water interface, water molecules in the bulk phase, experience a uniform force field caused by the interaction with the surrounding neighbour molecules (see Figure 1.1). However, if the water molecules are at the surface, it can be seen that the force exerted by the neighbouring molecules, is not uniform any more and molecules at the surface experience a net force instead, that pulls them inward and perpendicular to the surface. This force creates a lateral tension along the surface that gives rise to what is known as the surface tension [7]. The difference between forces, gives rise to a different energetic environment between molecules in the bulk and at the surface, and hence changing the total free energy of the system [7]. This extra of energy is known as the surface free energy or excess surface free energy [7]. While surface tension is restricted to phase boundaries, in which one of the phases is a gas, interfacial tension is commonly used to describe the boundary between two immiscible liquids. In thermodynamics, the interfacial tension γ is described as the increase in energy (Helmholtz or Gibbs) of the system when the area of the interface under consideration is increased by an infinitesimal amount δA [7]. Interfacial tension obtained from Gibbs energy and Helmholtz energy:

$$\gamma = \left(\frac{\delta G}{\delta A}\right)_{p,T,n} \quad \text{and} \quad \gamma = \left(\frac{\delta F}{\delta A}\right)_{V,T,n} \tag{1.1}$$

where V is the volume, T is the temperature, A is the surface area, p is the pressure and n is the number of moles of the component conforming the system. The units of γ are energy/area (mJ m^{-2}), although it is more common to see the units of γ expressed as the dimensional equivalent units of force/length (mN m^{-1}).

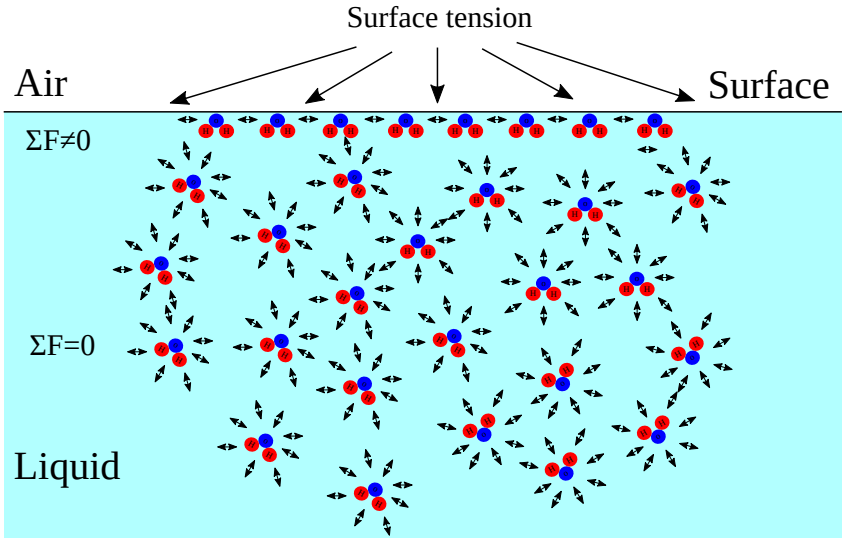

Figure 1.1 *Diagram of an air/water interface, showing the unbalance forces between water molecules at the surface and in the bulk. Water molecules in the liquid have forces acting on them in all directions, which when added, cancel each other. In contrast, at the surface, there are not molecules above the surface water molecules, only below and at each side. The net force is therefore inwards. This creates longitudinal forces along the surface which, gives rise to the surface tension.*

1.0.2 Interfacial Rheology

Interfacial rheology is the study of the behaviour of interfaces in response to deformations. Bare interfaces are scarcely elastic - because of the mobility of molecules at the interface - and without the presence of an adsorbed monolayer film, they cannot support foams or emulsions for long periods [7]. However, the presence of an adsorbed monolayer film can change drastically the rheological properties of interfaces, thus making possible the formation of stable foams and emulsions. The molecules conforming the adsorbed monolayer will replace some

of the water molecules in the interface and the forces of attraction between surfactant and water molecules are less than those between two water molecules, hence the contraction force is reduced. The main type of deformations used in interfacial rheology are, dilatational (change in area at constant shape) and shear (change in shape at constant area) (see Figure 1.2) - in this thesis we focus in dilatational deformations. Dilatational deformations, are based on variations of the interfacial tension as a response to changes in interfacial area by compressing and expanding the interface of a droplet or bubble via increasing and decreasing its volume. The rheological properties of interfacial films are determined by oscillating droplets and bubbles at different frequencies and measuring the dynamic interfacial tension [8]. When dealing with viscoelastic films, the elastic modulus E_0 and dilatational viscosity η_d introduced by [9] are represented as

$$E_0 = \frac{d\gamma}{dlnA} \tag{1.2}$$

and

$$\eta_d = \frac{\Delta\gamma}{dlnA/dt} \tag{1.3}$$

where γ is the surface tension and t is the time. For small strains, the interfacial tension is observed to have some phase lag with respect to the interfacial area due to the viscoelastic properties of the interfacial film - we will discussed this in more detail in Chapter 5.

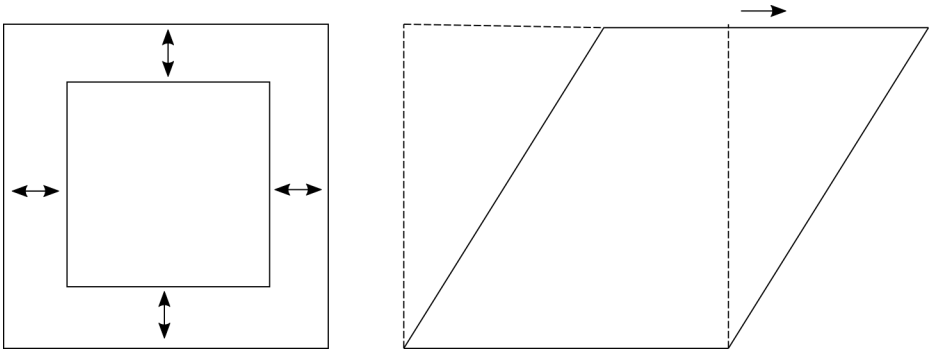

Figure 1.2 *Interfacial deformations, dilatational (left) and shear (right).*

1.0.3 Emulsions

Emulsions are the result of two immiscible liquids mixed together, with one of them dispersed as tiny droplets into the other [10]. The two immiscible liquids are usually oil and water, although it does not necessarily have to be the case. For example, "water-in-water" and "oil-in-oil" are other type of emulsions, often used in the food and the pharmaceutical industry [11, 12]. Separation of two immiscible aqueous solutions (a polymer-rich phase and a salt-rich phase) can be caused by the addition of salting-out electrolytes to hydrophilic polymer solutions [11]. The term "emulsion" usually makes reference to emulsions with oil droplets in the microscale, whereas microemulsions refer to emulsions with oil droplets in the nanoscale (see Figure 1.3) [13]. A foam is usually defined as a dispersion of a large volume of gas in the form of bubbles in a liquid, solid or gel [14, 15]. Emulsions and foams are thermodynamically unstable because of the interfacial tension resulting from mixing two unfavourable substances, like water and oil or gas and water [16, 17]. If we leave them to stand long enough, they will phase separate. To achieve kinetically stable emulsions and foams, a third or more constituents need to be added to the system. An example of these, are surfactants, with polar and nonpolar regions at each end, that make the molecules to have a greater preference for the interface than for the bulk.

When dissolved in emulsions, Surfactants reorient themselves in a way such that the hydrophilic part interacts with the water phase and the lipophilic with the gas or the oil phase. This arrangement results in a net decrease of the interfacial free energy. Proteins are another example of natural macromolecules used as constituent to achieve stable emulsions. Similarly their amphiphilic structure drive them to adsorb to interfaces. However, their polar and nonpolar groups are randomly spread all over the first and tertiary structure and not necessary placed at the ends as found in surfactants. This makes the adsorption process to interfaces slower and more complex than that of surfactants. Upon adsorption, proteins self-assemble via noncovalent interactions into viscoelastic two-dimensional nanolayers that decrease the interfacial tension [18, 19] and protect the colloidal system from several destabilisation mechanisms [20, 21]. While the interface activity of proteins is certainly important, the stability of emulsions is not just due to the decrease in interfacial tension. The essential stabilising function of proteins is their ability to make interfaces withstand the tangential stresses of adjacent fluids. [22]. Because of polar and nonpolar groups randomly distributed over the whole structure of the protein, only a small amount

Macroemulsions	**Microemulsions**
Unstable, eventually will separate	Thermodynamically stable
Large droplets (1 - 10 µm)	Small droplets (~ 10 nm)
Static system	Highly dynamic system
Moderately large interfacial area	Significantly large interfacial area
Moderate amount of surfactant needed	High amount of surfactant needed
Small interface curvature	Highly curved interface

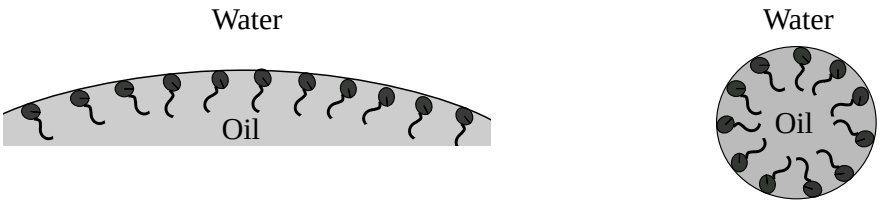

Figure 1.3 *Differences between emulsions and microemulsions.*

of the hydrophobic residues are located at the interface facing the hydrophobic phase, being most of the protein molecule hanging in the water phase [21]. The segments of the protein suspended in the aqueous phase form loops that provide steric stability against flocculation and coalescence of oil droplets [21]. Additionally, colloidal particles may also assemble to interfaces and stabilise emulsions. They differ from surfactants and proteins in that they remain basically irreversibly adsorbed in systems at rest [23]. Particles may be surface active however, they are not amphiphilic like surfactants [24]. For particles to assemble at an interface, they will have to be wetted by both phases [25]. Wettability can be quantified by the contact angle the particle adopts at the interface [26]. Contact angles lower than 90°C are related to hydrophilic particles, forming oil-in-water emulsions, while contact angles higher than 90°C correspond to hydrophobic particles forming water-in-oil emulsions [27].

Surfactants, certain proteins, peptides, phospholipids, polysaccharides and particles are examples of emulsifiers [28]. Emulsifiers are sometimes used with other substances, namely stabilisers. Stabilisers can either form a protective coating around bubbles and droplets and/or modify the texture of the bulk phase, both aiding to the stability of the emulsion or the foam [29]. Stabilisers can either increase the viscosity of the continuous phase (thickening agent) or turn this into a self-supporting three-dimensional continuous network (gelling agent) [29].

1.0.4 Hydrogels

Hydro- / organo-gels are a class of an elastic cross-linked polymer network that, due to the nature of its regions, can retain large amounts of water [30]. In the swollen state, they exhibit mechanical properties characteristic of both solid and liquid systems [31–33]. Hydro-/ organo-gels can be classified as natural or synthetic, according to the source and chemical or physical, depending on whether the atoms conforming the molecules share or not electrons. In this thesis, we deal with physical hydrogels made of synthetic low molecular weight peptides. The network of the self-assembled low molecular weight peptide hydrogel, is made of nanoscale anisotropic structures [34–36]. Nanoscale structures in peptide hydrogels, are formed by non-covalent bonds including, π-π stacking, van der Waals interactions, chiral dipole-dipole interactions, hydrophobic interactions, electrostatic interactions, hydrogen bonding and repulsive steric forces [36–38]. The fibre-like structures, range from a few nanometers in diameter to hundreds of micrometers in length, interacting via multiple mechanisms (see Figure 1.4) [33, 39–41]. The internal structure of peptide hydrogels at the microscale, is able to adsorb and hold large amounts of water with just a tiny concentration of this molecules ≈ 0.1 wt% [1, 42]. This effect is caused by the presence of hydrophilic groups in peptide molecules, that makes possible the transition from a soluble to an insoluble phase. The mechanical properties of the hydrogel are determined by factors such as, the number of fibres, their diameter and individual mechanical properties, the number of crosslinks, the distance at which these are from each other and the number of entanglements [33, 43].

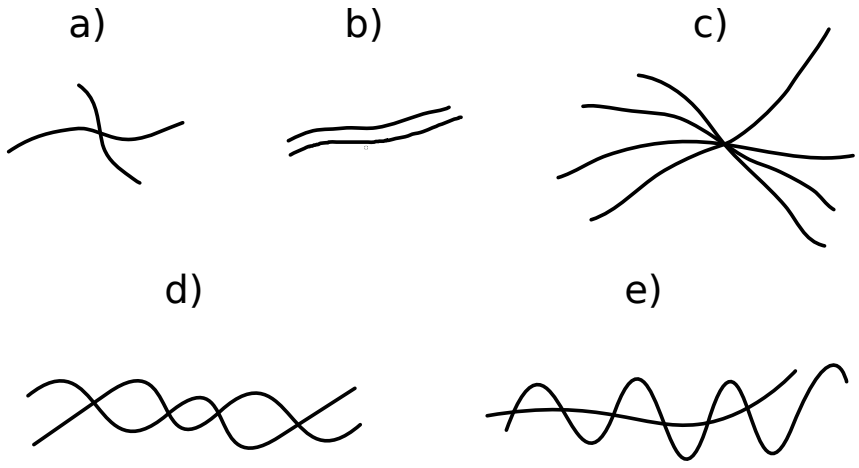

Figure 1.4 *Schematic diagram of different peptide hydrogel stabilisation mechanisms* ***a:*** *cross-links,* ***b:*** *lateral association,* ***c:*** *dense nucleation region,* ***d:*** *intertwined junctions and* ***e:*** *entanglements.*

1.0.5 Hydrogel Emulsions

Emulsions with a continuous phase exhibiting semi-solid like behaviour, have often been described as "emulsion filled gels" [44], "composite gels" [45], "emulsion gels" [46] "emulgels" [47] or "emulsion hydrogel" [48]. Despite the discrepancies between names, what they have in common is the structure, in which oil droplets, acting as a filler particles, are entrapped within the gel matrix [49]. The most common way of trigger gelation, is by a change in temperature or pH, salt addition and enzymatic activation. A hydrogel emulsion can be formed by either gelling the continuous phase and/or flocculation of the oil droplets [46]. In the former, the droplets can be either active or inactive fillers. Active oil droplets are chemically bounded to the gel network, whereas inactive oil droplets hardly interact with the gel matrix [46, 50–52]. The interactions between the droplet and the gel network, are governed by the type of emulsifier adsorbed to the oil droplet interface [49]. In any case, the rheological properties of gel emulsions, depend on the physicochemical properties of the gel network and the oil droplets, the volume fraction of the oil droplets, their size and spacial distribution, as well as the strength of the interaction between the emulsion droplets and the gel network [53]. However, the modulus of emulsions with active oil droplets, may be influenced by the ratio droplet/gel network modulus. For example, emulsions containing oil droplets with higher modulus than the gel network, will be stronger than emulsions with oil droplets with lower modulus than the matrix [51, 52, 54]. Inactive oil droplets in hydrogel emulsions will always tend to weaken the network of the gel [50]. Figure 1.5 shows a schematic diagram of the way in which oil-in-water emulsions are prepared in this thesis.

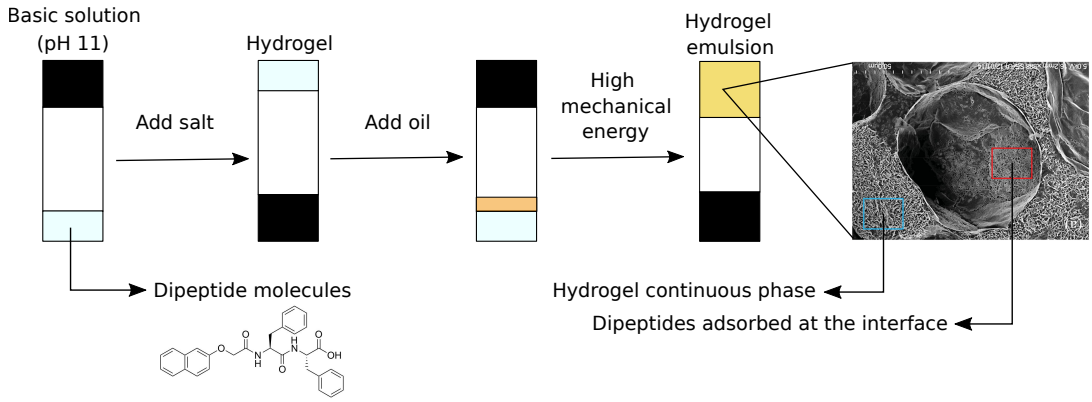

Figure 1.5 *Hydrogel emulsion preparation.*

1.1 The aim of the thesis

The main goal of this thesis is to expand the work initiated by Li et al., where dipeptide molecules (2NapFF) succeeded in forming interfacial films at an air−water interface [55] and in stabilising foams with long-term stability [56]. The foams, are stabilised by hydrogel fibres made of dipeptide molecules adsorbed to interfaces of bubbles and entangled in the bulk. Foams were stabilised by first dispersing the dipeptide molecules in a basic solution and then adding salt to the solution to induce gelation. Once the gel is formed, this is disrupted with the help of a rotor stator homogeniser to make the foam. While the authors succeeded stabilising foams for more than two weeks, they observed that the hydrogels were prone to phase separate. Interestingly, the presence of the bubbles when foams were formed reduced the amount of phase separation between the hydrogel and the water phase. This thesis deals with the study of the foaming and emulsification properties of short peptide molecules, mainly 2NapFF. The first goal in Chapter 3 was to get rid of phase separation and achieve repeatable hydrogels. To achieve this, we carefully studied each of the steps involved in the process of making the gel used in [56] and tuned these to achieve our goal. Then, the foaming and emulsification properties of 2NapFF were investigated at a lower concentration (0.1 wt%) than the one used in [56] (1 wt%). In Chapter 4 we were interested in studying the response of hydrogel films made of 2NapFF and ThNapFF (a new dipeptide) subjected to uniaxial deformations using a new custom made interfacial extensional tensiometer to mimic the deformation occurring in emulsion formation, where films are stretched under shear flow. The aim of Chapter 5 was to gain information on the properties of dipeptide fibres adsorbed to interfaces and check whether interfaces prepared with magnesium sulfate showed the non-monotonic response observed in Chapter 4 with hydrogels. Last, in Chapter 6 we link our work to an application. Emulsions made of 2NapFF prepared with different salts and salt concentrations are used in lipid digestion to observed the effect og the mechanical properties on lipid bioaccessibility.

1.2 Logic behind experiments

Due to a surge in finding new routes to form hydrogels, a decade ago, Chen et al., [42] designed a collection of new low molecular weight gelling agents (LMWGs)

using naphthalene-based dipeptides. Most of these dipeptides, 2NapFF among them, proved to be very effective forming gels. A few years later, Li et al., [57] showed that 2NapFF could become trapped at an air-water interface and two years later, the authors were using the same dipeptide to stabilise foams for more than two weeks. In this thesis, we study the behaviour of salt-triggered dipeptide fibres formed at liquid-liquid interfaces in the first three experimental chapters and then close the thesis by linking the properties of emulsions stabilised by these fibres to an application in the last chapter. In Chapter 4 we decrease the dipeptide concentration from 10 mg/mL used in [42] to 1 mg/mL to explore whether at that concentration, 2NapFF was still able to stabilise foams. Besides lowering the dipeptide concentration, we also tried two different salt concentrations when preparing the hydrogels, to investigate whether this may have an effect on foam stability. Before we do this, we first draw a route to get rid of the phase separation observed in [56] and achieve more stable hydrogels. After achieving repeatable hydrogels, we demonstrate that foams are less stable at lower dipeptide concentration. However, at this dipeptide concentration, we stabilise emulsions made of four different oils. Next, we investigate the behaviour of hydrogel films by stretching hydrogels in Chapter 5. Experiments in Chapter 5 were performed to mimic the deformation that droplets and bubbles experience under shear flow in emulsion and foam formation. Based on results from Chapter 4, where foams prepared at lower salt concentration resulted in higher quality foams, in Chapter 5 we prepared hydrogels with different salts and concentrations to further investigate the effect of salt on the properties of the films. After Chapter 5, we decide to further investigate the properties of interfacial films at liquid-liquid interfaces in Chapter 6. To do this, we prepared interfacial films with our preferred salt and concentrations, and use a drop profile tensiometer to oscillate oil droplets at different strain amplitudes and frequencies. Finally, to link our work to an application, we used a static *in vitro* digestion model in Chapter 7 to study the effect of the mechanical properties of emulsions on lipid digestion.

1.3 Thesis Outline

In this thesis we investigate the behaviour of one dipeptide, 2NapFF, which imparts stabilisation to droplet emulsions. 2NapFF behaves as a emulsifier, as a stabiliser and as a gelling agent. Dipeptides, when dispersed in a basic solution, self-assemble to form nanofibres that adsorb to bubble and droplet

interfaces. At high enough concentration (> 0.02 wt%), the nanofibres start to entangle in response to the addition of metal ions, holding large amounts of water and subsequently solidifying the continuous phase. To accomplish our goal, we first present a route to achieve repeatable stable hydrogels in Chapter 3. Next, we characterise the rheological properties of hydrogels with different mechanical properties in response to shear deformations and use the hydrogels to stabilise foams and emulsions at a very low dipeptide concentration (0.1 wt%). Finally, we consider the role of dipeptide fibres to be similar to that of particles at interfaces and study the wetting behaviour of the oils at an interface between the hydrogel and the aqueous phase. In Chapter 4, we further analyse the mechanical properties of hydrogels by subjecting them to extensional deformations. The hydrogels were prepared using different salts and concentrations and stretched at different velocities. In Chapter 5, we investigate the rheological properties of fibre-coated interfaces in response to dilatational deformations. The dipeptide concentration is decreased by one fold to avoid bulk gelation and the interfaces are probed by imposing strain and frequency sweep compression/extension cycles. Lastly, the mechanical properties of salt-triggered hydrogel emulsions are linked to lipid release and bioaccessibility during digestion in Chapter 6. Hydrogel emulsions prepared with different salts and concentrations are left to digest for two hours to simulate normal intestinal conditions in a static *in vitro* digestion model.

1.4 List of Publications

The work done in Chapter 3 has been published in [1].

1.5 List of Oral Presentations

During this thesis I have contributed with oral presentations at:

- the Annual European Rheology Conference (AERC), Portoroz, Slovenia, April 2019 (Tittle: Dynamics of thin films studied by extensional rheology).
- the Institute for Condensed Matter and Complex Systems, Edinburgh, UK, October 2018 (Dynamics of thin films studied by extensional rheology).

- the School of Physics, The University of Edinburgh, Edinburgh, UK, October 2018 (Stabilising drops and bubbles by interfacial rheology design).
- the 92nd ACS Colloid & Surface Science, State College, Pennsylvania, USA, June 2018 (The static and dynamic properties of dipeptide hydrogels on interfaces).
- the School of Mathematics, The University of Bristol, Bristol, UK, May 2018 (The static and dynamic properties of dipeptide hydrogels on interfaces).
- the School of Physics, The University of Durham, Durham, UK, May 2017 (The effect of dipeptide concentration on foam stability).

Chapter 2

Peptide Background

A peptide is a molecule made of a short chain of amino acids (see Figure 2.1). The amino acids are connected together by bonds, namely amide or peptide bonds. They differ from proteins in that dipeptides are shorter in length, i.e., peptides have between two and fifty amino acids approximately, whereas proteins contain fifty or more.

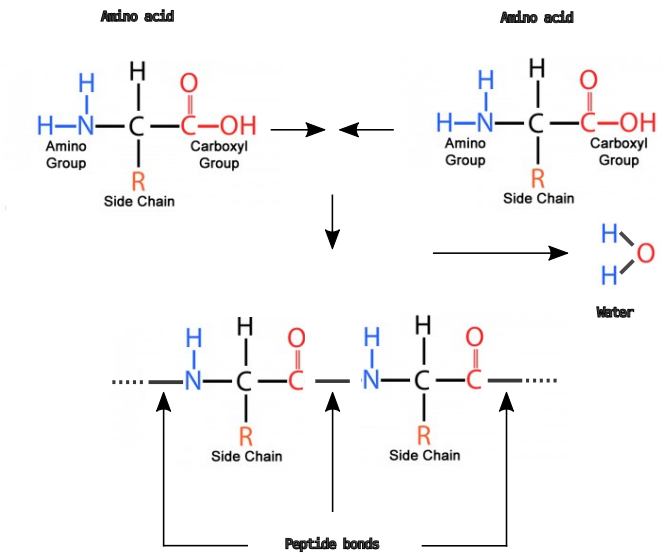

Figure 2.1 *General structure of a peptide molecule.*

Amino acids are organic compounds that contain an amine ($-NH_2$), a carboxylic acid (-COOH) and functional groups, along with a side chain (R group) [58, 59]. There are approximately 20 amino acids with 20 different side chains, giving

amino acids their unique characteristics and variability [58, 59]. Because of this, peptides can be organised into categories according to their chemical composition, e.g., hydrophobic or hydrophilic; aliphatic or aromatic; neutral, positively or negatively charged [58, 60]. Varying the amino acids in the side chain, allows peptides to form complex self-assembled nanostructures like, micelles, twisted ribbons and nanofibres [58, 59]. The interactions within these structures are governed by hydrogen bonds, electrostatic interactions, hydrophobic interactions, aromatic interactions (π-π stacking) and van der Waals forces [41, 58]. In this thesis, we focus on a naphthalene-protected dipeptide, 2NapFF (see Figure 2.2), which have been widely used to form hydrogels by a number of groups [3, 61, 62].

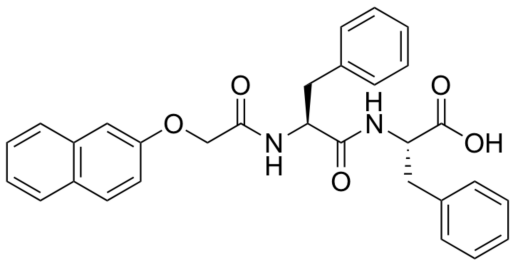

Figure 2.2 *Structure of 2NapFF.*

Peptides as gelling agents

Spontaneous aggregation and organisation of particles (atoms, molecules, colloids, micelles, etc.) into rational and well-defined structures is ubiquitous in nature at macro- and microscales [63]. The chemical and structural properties of molecules with reactive functional groups, known as building blocks, dictate the dynamic features, versatility, reversibility and tunability of biomaterials [64]. This extraordinary process can be observed in bones [65], polysaccharides and proteins [66] or eggshells [67] to name a few.

In the past few years, an increasing number of self-assembled noncovalent hydrogels have been reported in literature, especially for various biomedical applications including, tissue engineering [68–70], drug delivery [71, 72] and cell culture [73, 74], among others. At a sufficiently high concentration, peptide molecules in hydrogels, self-assemble into polymer-like fibres that entangle to form a cross-linked three-dimensional network with anisotropic properties [41, 68]. Noncovalent interactions between molecular building blocks on peptides include, π-π stacking, hydrogen bonding and hydrophobic, and electrostatic interactions

[36, 37, 64]. The internal structure of peptide hydrogels at the microscale, is able to adsorb and hold large amounts of water with just a tiny concentration of this molecules $\approx$ 0.1 wt% [1, 42]. This effect is caused by the presence of hydrophilic groups in the peptide, which makes possible the transition from a soluble to an insoluble phase. The mechanical properties of the hydrogel are determined by factors such as, the number of fibres, their diameter and individual mechanical properties, the number of crosslinks, the distance at which these are from each other and the number of entanglements [33, 43]. The gelation process, is usually triggered by an external stimulus including, pH and [75, 76] temperature modulation [77, 78], solvent exchange [79], presence of salts [1, 56], sonication [80], light irradiation [81] and peptide concentration [82] (see Figure 2.3 for an example of the gelation process with addition of salt).

Hydrogels may be classified in different ways. For example, depending on the characteristics of the building blocks, hydrogels can be either natural or synthetic or neutral or ionic. They can also be distinguished by their mechanical and structural properties, such as the degree of cross-linking and the structural integrity of the hydrogel or by the way in which the building blocks bond together, which can be chemical or physical [83]. As an alternative to more complex natural protein-based hydrogels, synthetic peptide based hydrogels are

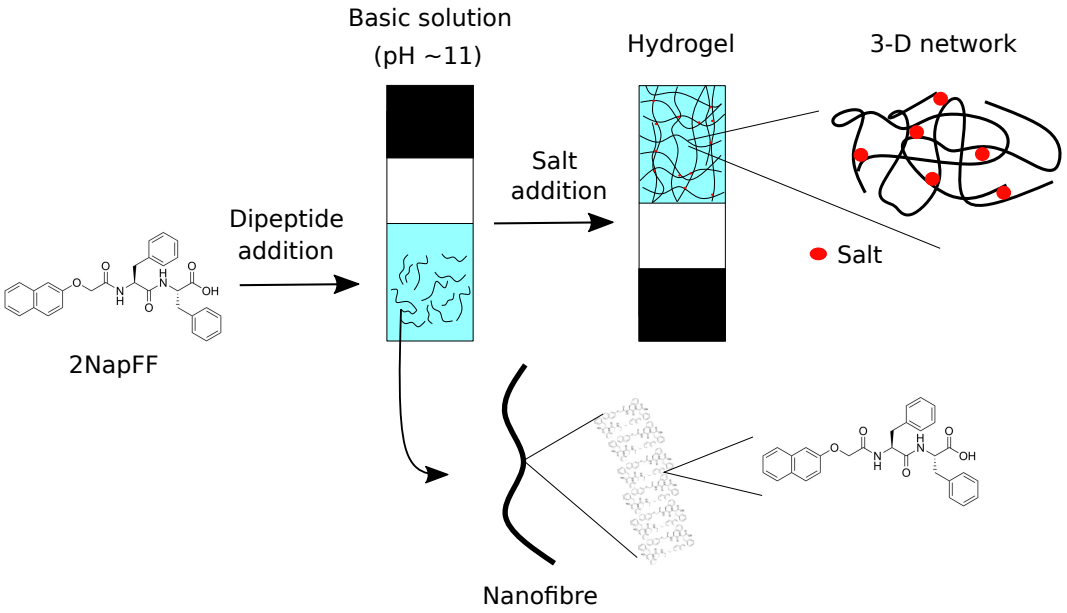

Figure 2.3 *Schematic diagram of a sol-to-hydrogel transition by addition of salt. Peptides in a basic solution self-assemble into nanofibres, which in turn entangle to form the matrix of the hydrogel with the addition of salt.*

more attractive because they are structurally less complicated than proteins, are easy to synthesise and technologically speaking, can be scaled up extremely easy [84].

Probably, the most studied short peptides in literature are Fmoc N-protected dipeptides such as, Fmoc-$_D$-Ala-$_D$-Ala, which were shown to form gels almost two decades ago [85]. Later, the same protecting group with different amino acids, was proved to form stable hydrogels at physiological pH [75]. Similarly, the mechanical properties of hydrogels made of a combination of these dipeptides were also studied in [86, 87]. The authors demonstrated that both, the final pH and the way Fmoc molecules are agitated during gelation, can dramatically influence the mechanical properties. Adams's group reported that, the change in pH using mineral acids, occur at a time scale lower than the gelation, hence making gels irreproducible [76, 86]. This problem was later fixed using glucono-δ-lactone (GdL), which hydrolyses in water to form gluconic acid. GdL adjusted the pH of the solutions in a much more uniform way, providing extremely reproducible gels and with better mechanical properties with respect to gels prepared with hydrochloric acid [76, 86, 88]. Another advantage of adjusting the pH with GdL, was that the time scale for hydrolysis is slow, making possible to monitor the process of self-assembly using different microscopy and spectroscopy techniques [88].

For improved performance and more precise control over the properties of hydrogels, new peptides with metal-binding moieties were synthesised. These, aim to overcome the limitations of peptides self-assembling only via hydrogen bonds and hydrophobic interactions [89, 90]. An example of this, is our dipeptide of choice, 2NapFF, which has been studied in great detail in bulk [91–94]. For example, different salts were used to trigger gelation of a number of 2NapFF solutions [2]. Apparently, the formation of the hydrogel with metal ions, occurs because of the carboxylic groups from different micelles, cross-linking via salt bridges. In this work, hydrogels triggered with divalent metal ions resulted in stronger hydrogels than those prepared with monovalent ions. What is more, hydrogels prepared with calcium, had the highest storage modulus of all hydrogels and showed a non-monotonic increase in storage modulus, with a maximum value at a calcium: carboxylic acids of 2:1 (see Figure 2.4). At a higher salt concentration, the storage modulus started to decrease, which implies that the hydrogel becomes weaker. In another work, the concentration of 2NapFF in the phase solution, was investigated [92].

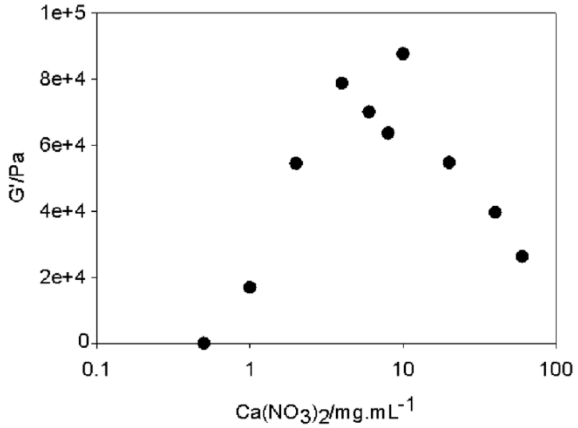

Figure 2.4 *Storage modulus (G') as a function of calcium concentration for a hydrogel made of 2NapFF at 0.05 wt%. Reproduced from [2] with permission.*

The authors found two critical micelle concentrations (cmc) for 2NapFF; one found at a concentration between 0.008 wt% and 0.02 wt%, and a second one between 0.05 wt% and 0.1 wt%. The first cmc was attributed to the dipeptides aggregating into spherical micelles, whereas the second cmc it was due to spherical micelles self-assembling into long worm-like structures. Likewise, in the same study, it was found that the minimum gelation concentration (mgc) for 2NapFF prepared with calcium chloride at a constant ratio is 0.02 wt%.

The process of gelation for 2NapFF, can be induced in different ways including, change in pH, addition of salt or dissolving the dipeptide in an organic solvent such as, dimethyl sulphoxide (DMSO) and subsequently diluting it with water (see Figure 2.5). While the hydrogel strength does not change significantly when prepared by these different routes, the microstructure and yielding behaviour do alter [93]. When gelation is triggered by the addition of salt, the system exhibits a significant sensitivity to the initial high pH chosen which, may be due to the differing degrees of lateral association between micelles. Early experiments had suggested that worm-like micelles always preceded salt-induced hydrogelation [91]. More recently, a subtler relationship has been revealed: at high pH, 2NapFF self-assembles into spherical micelles above a first cmc of 0.01 wt%, where worm-like micelles are found above a second cmc of 0.07 wt% [92]. At around 1 wt%, the worm-like micelles are found to aggregate. Typically addition of the calcium salt transforms worm-like micelles into hydrogels. However, above the first cmc, there appears to be structural transformations that occur on addition of the calcium salt, which allows gels to form in this intermediate regime.

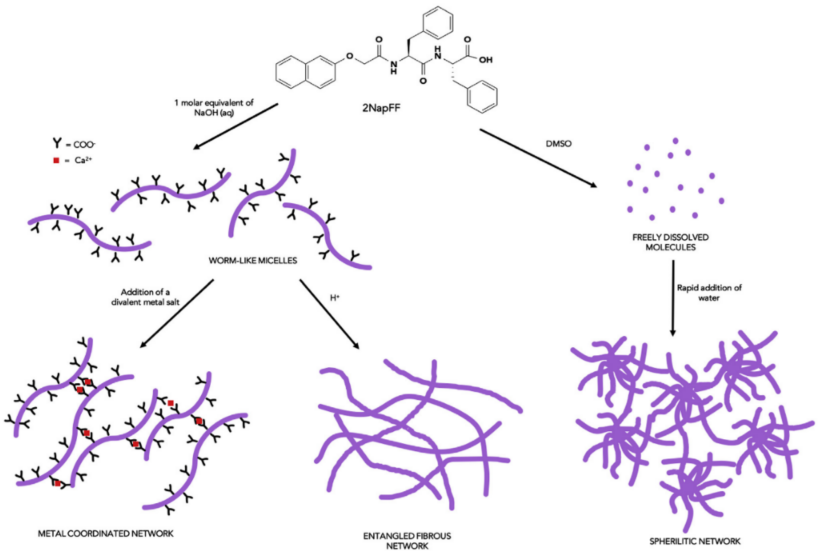

Figure 2.5 *The process of assembly using different triggers. 2NapFF dispersed in a basic solution, can form a hydrogel in different ways, hence leading to different types of networks. Reproduced from [3] with permission.*

Peptides at interfaces

Peptide adsorption to interfaces has become an important field of research since the last two decades or so, however, researchers have been studying the conformation of peptides in solution for a bit longer. For example, to determine the function of the amino acid sequence in peptides and proteins in regulating the formation of secondary structures at interfaces [95]. Similarly, protein molecular structures were investigated by synthesising peptide amphiphiles with different amino acids, that self-assembled into highly ordered triple-helical like structures in the bulk. These results were supported by surface rheology experiments, where the peptide molecules where spread on an air-water subphase to conduct compression cycles at constant speed. The peptides formed a stable monolayer, that increased the surface pressure to values above 70 mN/m [96]. In a different study, peptide amphiphiles derived from collagen were reported to form stable monolayers at the air/water interface with high collapse pressures [97]. More recently, the adsorption kinetics of two peptides at the octane/water interface have been investigated to understand the role of protein structure in controlling the dynamics of protein adsorption [98]. Amphiphilic peptides with hydrophilic and hydrophobic amino acids residues were designed to form secondary structures of self-assembled β-sheet monolayers at the air/water interface. The surface pressure versus area was, like in the studies above, measured by compressing

the area of the monolayer using a Langmuir minitrough. Variations in the amino acid sequence were used to tune the dimensions of the β-sheet domains and hence the properties of the monolayers [99]. Monolayer structures and salt-binding activities of peptide lipids with amino acid residues attached, were investigated by spreading the peptide lipid solution on a water subphase and compressing it to measure the surface pressure. The authors concluded, that peptide lipid monolayers prepared with Cu^{2+} and Zn^{2+}, behaved similar to proteins at interfaces, with different secondary structures and functions than in the bulk [100]. The concentration dependence of peptide self-assembly in aqueous solution, have also been investigated at an air/water interface [101]. In this work, the authors studied a wide range of peptide concentrations and determined the surface tension and self-assembled structures using axisymmetric drop shape analysis-profile (ADSA-P) and atomic force microscopy (AFM). The former revealed that the surface tension decreased with increasing peptide concentration. However, at a peptide concentration of 0.3 mg/mL, the surface tension plateaus, revealing a critical self-assembly peptide concentration. AFM images showed an agreement with rheological measurements, with two structural transitions occurring at a dipeptide concentration of 0.05 mg/mL and 0.3 mg/mL, with globular structures transitioning to fibrils and these to fibres respectively. Last, two peptide lipids linked to Alzheimer disease were investigated at an air/water interface to observe whether aggregation took place. The dipeptide solution was spread on a water subphase placed in a Langmuir trough. Prior to compression, the dipole moment was equal to zero, due to the peptide molecules being randomly oriented at the interface. With the subsequent compression, the dipole moment increased, implying that molecules began to orient to form a monolayer. The authors concluded that, the aggregation process took place for both peptides during compression of the monolayer [102]. All these studies, demonstrate that peptides were, at the beginning, used as a model to study the behaviour of larger and more complicated polymers, however, researchers soon realised that peptides, due to their structure and size, could also be used as emulsifiers and stabilisers themselves.

Peptides as surface active agents

To our knowledge, the use of peptides as stabilising agents, was first explored by Dexter et al. in [103], when studying a 21-residue peptide molecule, namely AM1, that switches molecular structure at liquid-liquid interfaces in response

to changes in the bulk solution composition. At neutral pH, peptides formed cohesive films in the presence of zinc, however, in the absence of these or at low pH, the peptides instead formed mobile layers, characteristic of low-molecular-weight surfactants. Most important, was the ability of AM1 to actively and reversibly switch between these states. This work was later extended by the addition of new metal ions to form cohesive interfacial films and by designing a new peptide molecule, AFD4, which formed stronger interfacial films and more stable foams than AM1, in the presence of the same metal ions [104]. AM1, with two histidine residues, under-went intermolecular cross-linking with metal ions at the air/water interface, however, AFD4, with four histidine residues, formed both, inter- and intra-molecular bonds with the same metal ions. Film formation and foam stabilisation could be reversed for both peptides by decreasing the pH or addition of a metal chelating agents.

Recently, the behaviour of very short peptide sequences at air/water interfaces has begun to be explored [55, 105]. Here, a naphthalene protected diphenylalanine (2NapFF) dipeptide have been investigated most. One approach was to investigate the self-assembly of the dipeptide at the air/water interface prepared via drop-casting. A thin interfacial film formed from a dispersion of 2NapFF at high pH on contact with a low pH subphase. FTIR and pH variation tests showed that, this self-assembly behaviour, is associated with the carboxylic acid group of the dipeptide becoming rapidly protronated at the interface. The film, was made up of self-assembled nanofibres and behaved like an elastic sheet [105]. The same dipeptide, also formed a hydrogel via the addition of metal ions. This hydrogel was used to stabilise aqueous foams for weeks. The dipeptides at 1 wt% concentration, self-assemble into fibre-like networks at both, the air/water interface and in the bulk. Raman spectroscopy hinted at a possible change in the balance between, π-stacking and hydrogen bonding, with the latter appearing to drive self-assembly close to the interface. The dipeptide concentration as well as the type and concentration of metal ions, as showed to affect the foam stability [55]. When the bulk hydrogel had a yield stress larger than the Laplace pressure of the bubbles, ripening was suppressed.

Separately, the stabilization of emulsions using di-, tri- and hepta- peptides has also been investigated [106–109]. Initial experiments showed that, it was possible to stabilize chloroform droplets for months using an interfacial network of dipeptide fibres. Here, the dipeptide sequence was protected by Fmoc with self-assembly being driven by π-stacking and hydrogen bonding. The fibres

were self-assembled nanostructures and for a well-chosen dipeptide sequence, remained stable in the presence of added salt or when the temperature was raised. Curiously, using the tripeptide sequence Fmoc-FFF, it was possible to stabilize water droplets in chloroform, demonstrating the importance of the hydrophobicity of the fibres [107]. In a similar study, unprotected tripeptide emulsifiers divided into two classes, those that self-assembled into fibres prior to adsorption and those that adsorbed to droplets as a single molecule layer, were found to stabilise emulsion droplets, with the former being more effective than the latter [106]. As an alternative demonstration of the key role played by self-assembly, an Fmoc protected dipeptide sequence, Fmoc-tyrosine-leucine (FmocYL), was used as a switchable emulsifier. An enzyme was employed to cleave a phosphate group which, was initially attached to the tyrosine group. With the phosphate group attached, chloroform droplets are stable for less than an hour. However, when emulsification is carried out in the presence of the enzyme, the dipeptide self-assembles into nanofibres which, stabilises the emulsion for months [108]. These studies, strengthened the claim that, it is the fibres which are most effective at stabilizing the liquid interfaces and not the separate molecules. Very recently a heptapeptide molecule has been designed to self assemble into fibres with excellent surfactant properties [109]. At this length, the short peptide sequence has properties which are robust to changes in some parts of the sequence. Even more recently, a low molecular weight gelator has been synthesized at a liquid-liquid interface to create stable droplets combined with coalescence in response to a trigger [110].

Chapter 3

Stabilising bubble and droplet interfaces using dipeptide hydrogels

3.1 Abstract

Hydrophobic dipeptide molecules can be used to create interfacial films covering bubbles and droplets made from a range of oils. At high pH, the dipeptide molecules form micelles which transform into a hydrogel of fibres in response to the addition of salt. We first present a route to achieve repeatable hydrogels, then characterise their properties for two different salt ($MgSO_4$) concentrations and then we use these gels to stabilise interfaces. Under high shear, the hydrogel is disrupted and will reform around bubbles or droplets. Here, we reveal that at low dipeptide concentration, the gel is too weak to prevent ripening of the bubbles; this then reduces the long-term stability of the foam. Under the same conditions, emulsions prepared from some oils are highly stable. Last, we examine the wetting properties of the oil droplets at a hydrogel surface as a guide to the resulting emulsions.

3.2 Introduction

Proteins have been used by cooks to stabilize foams and emulsions for many centuries [111]. The proteins are typically trapped on the interface and can denature, especially at liquid/air interfaces. By comparison, small peptides can

potentially improve performance in two diametrically opposed ways. (1) Isolated small peptides will be adsorbed to the interface more quickly which can aid bubble or droplet formation [106]. This tends to be the more challenging route. (2) These small molecules may self-assemble into larger structures which retain their order at the interface [55, 105–109, 112, 113]; the trapping at the interface can be much stronger than for individual proteins. Proteins have also been used as subunits within robust composite particles which themselves are interfacially active [114–118]. Nonetheless, short peptide sequences offer the distinct advantages of ease of synthesis and design as well as the tendency to self-assemble at very low concentration.

The use of short peptides to form hydrogels has been studied in great detail by a number of groups [3, 39, 119, 120]. Because hydrogels can hold large amounts of water, while exhibiting solid-like mechanical properties, it is not surprising that the applications of hydrogels in industry has increased so much [120]. The use of such hydrogels to stabilise bubble and droplet interfaces however, is less common. The Ulijn group was the first to report the use of short peptides to stabilise emulsions for long periods [121]. Emulsions were made by shaking the solution by hand for a few seconds. The dipeptides, with polar and nonpolar sites, self-assembled into nanofibrous networks at the liquid-liquid interface, that kept the emulsion droplets stable for months. It was observed that, altering the dipeptide sequence changed drastically the mechanical properties of the emulsion, hence raising the possibility of using this as a tool to tune the performance. Lastly, by using enzymes, the networks disassembled, causing on-demand demulsification. Nevertheless, droplet stabilisation was achieved by the barrier formed at the interface by the nanofibrous structures, without need of altering the properties of the continuous phase, which remained always in the liquid form.

However, the stabilisation of bubble interfaces using short peptide-based hydrogels was first introduced, not long ago, by our group [56]. In this study, dipeptides were used to form a hydrogel that was then used to stabilise wet foams for long periods. The dipeptide molecules, self-assemble into nanofibres (in response to the addition of salt) that entangle to form the hydrogel. This, is then disrupted by high shear and reforms again at the air/water interface and in the bulk. The fibres at the interface stabilise the air bubbles, while the gel in the bulk delays growth by keeping the bubbles immobile. After this work and the publication of this chapter [1], the number of papers using short peptide-based hydrogels to stabilise emulsions keeps increasing. Very recently, a synthesised lipo-dipeptide, C_{13}-KR,

was found to form stable emulsions [122]. Dipeptides showed better emulsification properties with respect to Tween 80 and whey protein isolate (WPI). The authors hypothesised that this could be due to its relatively simple structure. While adsorption for Tween 80 and WPI occurs gradually, for C_{13}-KR this is instantaneous, thus achieving a lower and more stable interfacial tension more rapidly. Even more recently, a short peptide without self-assembly properties, was shown to self-assembled by making a minimal structural modification [123]. The authors replaced a flexible phenylalanine residue from the peptide backbone by a more rigid phenylglycine to favour π-stacking. By doing so, the peptide molecule self-assembled into β-sheet nanofibres (in response to a change in pH) which, at high enough concentration, entangled forming a hydrogel. Finally, the fibrils, with hydrophobic and hydrophilic regions, also showed preference for the interface as demonstrated by confocal microscopy.

The use of particles to stabilise oil and water droplets has become of great interest during the last two decades [124]. Solid particles form a steric barrier between immiscible liquids, which imparts kinetic stability to droplets, avoiding flocculation, coalescence and ultimately creaming [125]. Emulsions stabilised by solid particles are known as Pickering emulsions. The stability of Pickering emulsions, is determined by many factors including, particle concentration, size and shape, as well as particle wettability [126]. Particle wettability is defined as the three phase contact angle θ the particle forms between the interface and the water phase (see Figure 3.1.

If the particle is too hydrophobic (nonpolar), it will stay in the oil phase. In contrast, if it is too hydrophilic (polar), then it will prefer the water phase [126]. The three phase contact angle is related to the surface energy between the particle and the oil phase γ_{po}, the particle and the water phase γ_{pw} and γ_{ow} and can be

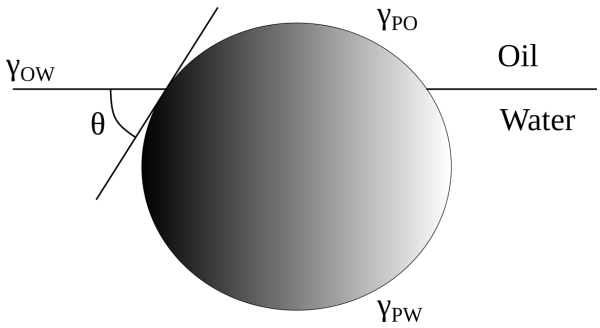

Figure 3.1 *Definition of the contact angle θ for a particle at the liquid-liquid interface.*

calculated using the Young's equation

$$cos(\theta) = \frac{\gamma_{po} - \gamma_{pw}}{\gamma_{ow}} \tag{3.1}$$

Recently, a new class of materials, microgels or microgel particles, have been demonstrated that can successfully stabilise droplet emulsions [127–131]. Each microgel is a submicrometer-sized hydrogel network, that is made of crosslinked polymers forming a three-dimensional network [132]. One advantage of microgel particles is that, they can be formed from a wide range of biopolymers. For example, proteins with limited solubility or complex aggregation properties can be converted into a supramolecular assembly called, microgels [132]. Since protein microgels are composed of polar and nonpolar groups, some of them seem to be very surface active, combining the high desorption energy of Pickering particles with the ability of proteins to adsorb to almost any interface. The adsorbed layer, forms a steric barrier much thicker than a protein layer, that can be beneficial to decrease the rate and extent of enzymatic digestion [132, 133].

The aim of this chapter was to achieve repeatable hydrogels made of dipeptide molecules (2NapFF) and investigate the effect of salt concentration on their rheological properties. In addition to this and following previous studies, we wanted to investigate the foaming properties of the hydrogels when prepared at lower (from 1 to 0.1 wt%) dipeptide and salt (35 to 4.5 mg/mL) concentration, as well as to stabilise emulsions prepared in similar manner to foams. To achieve this, we first outlined the route to form hydrogels that remained stable for months and then use these to stabilise foams and emulsions. Our results show that using a low concentration of dipeptide and magnesium sulfate rather than calcium chloride, undermines the stability of the foam compared to previous observations [105]. By contrast, it is possible to create highly stable emulsions based on several different oils. We separately characterize the wetting behaviour of the oils and a bubble at a hydrogel interface. We consider the stability of our composites in the light of the wetting character of the hydrogel film at the fluid-fluid interface.

3.3 Materials and methods

3.3.1 Materials

2NapFF was synthesised as described in [42]. All chemicals were purchased from Sigma-Aldrich and Fisher Chemicals and used as received. Isopropyl myristate (98%), 1-Octanol (= 99%), Dodecane (= 99%) and Silicone oil, were filtered through alumina (Honeywell, Aluminium Oxide, activated, basic, Brockmann I) placed in Whatman paper filters and filtered three times to trace impurities in the oil phase. Magnesium sulfate was dissolved in water and used as aliquots. Millipore water (resistivity = 18.2 MΩ. cm) was used throughout.

3.3.2 Methods

Hydrogel preparation

Vials and instruments were cleaned with hexane, followed by methanol and rinsed with ultra pure water before use. An equimolar quantity of NaOH (1 M, aq) was added to Millipore water (resistivity = 18.2 MΩ. cm) to give a basic solution (pH 11 ± 0.5). Then 0.1 wt% 2NapFF was added and the mixture was dispersed by placing the vial in an ultrasonic bath or using a magnetic stirrer. The time and temperature used to disperse the dipeptide molecules varied as one of the goals of this chapter, was to define a route to achieve repeatable hydrogels. The pH was 11 ± 0.5 measured with a Seven Easy pH probe (Mettler Toledo AG). Gelation was triggered by adding magnesium sulfate or calcium chloride aliquots on top of the translucent dispersion. The form of addition matters. By adding the salt already dissolved, hydrogels are more homogeneous compared to those prepared by adding the salt as a powder. It is possible that the latter favours the formation of two phase samples. In practice, all samples were prepared using 0.1 wt% dipeptide and were gelled using pre-dissolved salt to give a 1 mL sample. This was then left to stand for 12 h at room temperature before use in subsequent experiments.

Foam and emulsion preparation

Foams were prepared from the gels by using a rotor stator homogeniser (Polytron, PT-MR 3100) with a 12 mm diameter head (Kinematica, Standard Dispersing Aggregate), operating at 15,000 rpm (shear rate 25,700 s^{-1}) for 50 seconds. Immediately following foam formation, the samples were sealed with parafilm to prevent liquid evaporation; the height of the foam was recorded as a function of time. Emulsions with four different oils (isopropyl myristate, silicone oil, dodecane, octanol) were prepared in a similar manner to the foams described above. In each case 200 μL of oil was placed on top of the hydrogel to give a volume oil fraction of 0.2 prior to high shear mixing.

Rheology

Initial tests for gelation were performed by vial inversion. Oscillatory shear measurements, were conducted on a TA Instruments AR 2000 rheometer with cross-hatched parallel plates with 40 mm diameter and 1.0 mm gap distance. A 4 mL (0.1 wt%) dispersion solution of the dipeptide was previously prepared in a 7 mL glass vial, as described above. Gels were triggered on the bottom plate of the rheometer by loading the 4 mL dispersion and adding 4.5 mg/mL magnesium sulfate for hydrogels with low salt concentrations and 35 mg/mL magnesium sulfate for hydrogels with high salt concentration. The sides of the plates were covered with low viscosity mineral oil to avoid water evaporating from the hydrogel. Gelation process was observed by measuring the shear modulus (storage modulus G' and loss modulus G") as a function of time at a frequency of 1 Hz and at a constant strain of 0.5% for a period of $\approx$ 18 hours. Experiments were carried out at 22 °C.

Confocal microscopy

The measurements were carried out by using a Zeiss Axio Observer Z1 inverted microscope and a Zeiss LSM 700 scanning system 9 with a 20× (0.40 NA) objective. Nile Blue at a concentration of 0.55 mM was used to label the dipeptides; this was excited using a 633 nm semiconductor laser.

FTIR

IR spectra were measured using a Smiths Illuminat IR module coupled to a Renishaw inVia Raman microscope. Each spectrum was scanned between 4000 and 650 cm^{-1} at a resolution of 2 cm^{-1} and corrected for the influence of the optics and the substrate.

Contact angle

The hydrogel (blue) was created, using our standard protocol, in the base of a sample vial in the presence of Nile blue dye. Following gelation, additional salt solution was added above the hydrogel. This two phase cell was then inverted with the use of a petri dish. A droplet of oil or a bubble of air was added using a syringe with a U-shaped needle (see Figure 3.7a).

3.4 Results and Discussion

In order to investigate foams and emulsions, the underlying hydrogels need to be repeatable. For this reason, we carefully studied the process of dispersing and gelling the dipeptide (see Experimental section 3.3). Whether and how long it takes for a gel to form and its ultimate properties are affected by factors such as pH, temperature, ionic strength and mechanical shear rate [91, 92, 94, 134]. A thorough study of the effect of temperature on dispersions of 2NapFF has been published a decade ago [135]. Here, we compared the use of an ultrasound bath with a magnetic stirrer and found that the former resulted in more transparent dispersions. Dipeptide dispersion and gelation times initially differed between ostensibly identical hydrogels prepared using the ultrasonic bath presumably due to the ±8 °C variation in the bath temperature. For this reason, we established two temperatures (< 35 °C and 50 °C) for dispersing the dipeptide. The rate of dipeptide dispersion (unsurprisingly) and the subsequent gelation time (unexpectedly) were found to be faster for the hydrogels prepared at 50 °C compared to those prepared at < 35 °C. Our final protocol was to place the sample in an ultrasonic bath (at a controlled temperature) for 0.5 h until a translucent slightly viscous solution was formed, (see Figure 3.2a).

By leaving dispersions (prepared using either ultrasound or a magnetic stirrer) to

stand for 24 hours at a room temperature (22 °C), we found that self-supported gels, able to pass the inversion vial test, sometimes formed (see Figure 3.2b,c). Structural transitions, linked to increases in viscosity, have been observed before in 2NapFF dispersions which have been warmed in the temperature range of our bath (albeit at higher concentration). These changes in organization can then become trapped [41]. We suggest that we might be seeing similar behaviour here. To avoid this, all of our hydrogels were prepared by the addition of salt within 5 minutes of removal from the ultrasound bath. Figure 3.2d,e demonstrates how the temperature of the ultrasound bath influences the speed of subsequent behaviour. Dipeptide dispersed at 50 °C has begun to gel within two minutes of the addition of salt. Typical hydrogels for two difference concentrations of magnesium sulfate are shown in Figure 3.2f,g.

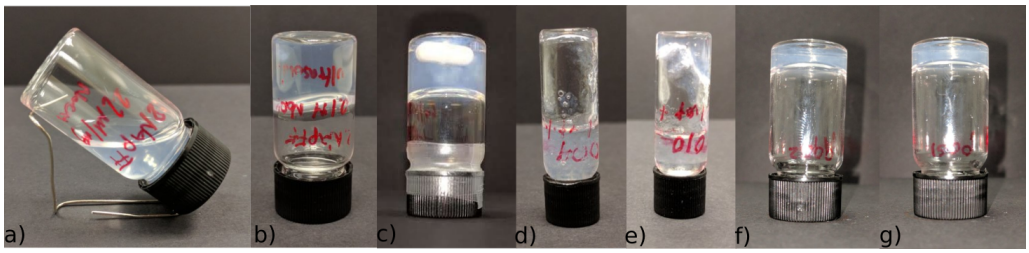

Figure 3.2 ***a:*** *dispersion of 0.1 wt% 2NapFF at pH 11 a few minutes after the ultrasonic bath;* ***b:*** *dispersion 24 hours after the ultrasonic bath;* ***c:*** *dispersion 24 hours after the magnetic bar;* ***d:*** *hydrogel prepared at 4.5 mg/mL magnesium sulfate dispersed at 25°C, 2 minutes after addition of salt;* ***e:*** *hydrogel prepared at 4.5 mg/mL magnesium sulfate dispersed at 50°C, 2 minutes after addition of salt;* ***f,g:*** *our preferred protocol for producing a hydrogel from 0.1 wt% 2NapFF at <35°C;* ***f:*** *4.5 mg/mL magnesium sulfate and;* ***g:*** *35 mg/mL magnesium sulfate.*

The evolution of shear modulus was measured as a function of time to study the strength of hydrogels prepared at 4.5 mg/mL and 35 mg/mL magnesium sulfate (see Figure 3.3). G' and G" of hydrogels with high salt concentration rise faster than hydrogels with low salt concentration within the first 10,000 seconds. At this point, G' and G" of hydrogels with high salt concentration hardly increase, reaching their maximum at 6 kPa for G' after a few thousand seconds, while G' and G" of low salt concentration hydrogels continue to increase even after 63,000 seconds. Salt induced gelators which become weaker at higher salt concentration have been seen previously. The strength of a hydrogel prepared at 0.1 wt% of 2NapFF and calcium chloride salt was found to reach its maximum value at a concentration of 2:1 calcium chloride to dipeptide. Increasing further the concentration of calcium chloride resulted in weaker gels [91].

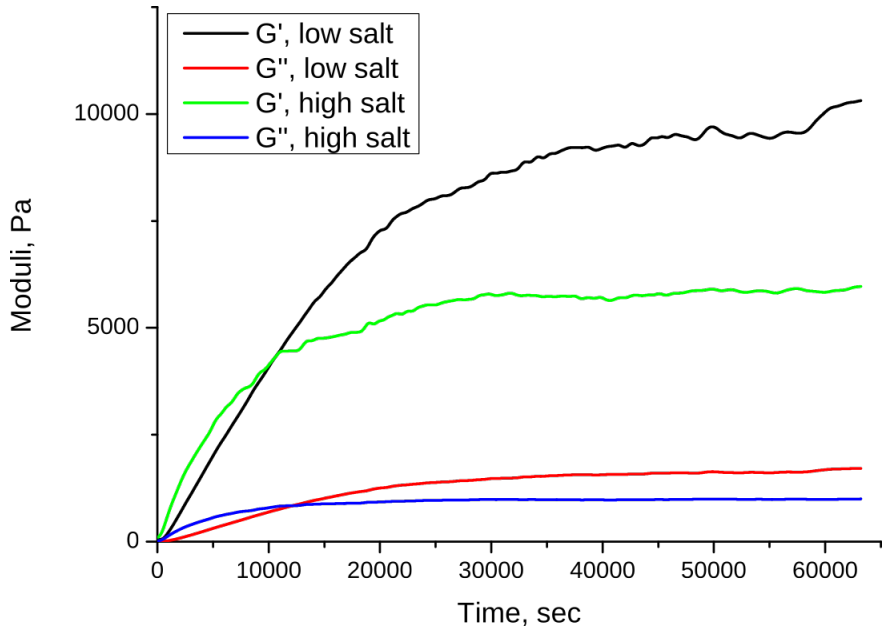

Figure 3.3 *Storage, G', and loss, G", moduli measured using oscillating rheometry for hydrogels prepared at low and high salt concentrations.*

Figure 3.4a,c shows foams formed from dispersions prepared at < 35°C which were gelled with 4.5 mg/mL and 35 mg/mL magnesium sulfate respectively. The formation method is described in the Experimental section 3.3. Foams with low salt concentration (see Figure 3.4a) resulted in higher quality foams with small average bubble size and a higher volume of liquid entrained in the foam compared to those prepared at a high salt concentration (see Figure 3.4c). The bubble size is often related to foam stability due to the enhanced buoyancy of large bubbles; however, in this case we find that after 0.5 h it is the foam with smaller bubbles that has collapsed more (see Figure 3.4b,d). Evidently, while these hydrogels provides a good environment for creating bubbles the interfacial layer and sparse bulk gel are unable to prevent rapid coalescence. This is especially true with small bubbles which consume a greater proportion of fibres as the interfacial layer.

Fluorescence confocal microscopy was carried out to try to understand the foam performance. Figure 3.4e shows the organization of a fresh foam prepared at 35 mg/mL magnesium sulfate and 50°C. The nanofibres prefer to adsorb at the air/aqueous interface (similar to ref. [136]) rather than being dispersed in the continuous phase (see Figure 3.4e). However, over the next hour hydrogel begins to emerge between bubbles. This is very much reminiscent of the foams reported in ref. [105] which were created at significantly higher dipeptide concentration and gelled using calcium chloride . In that work, the hydrogel initially formed on the bubble interfaces but then steadily appeared between the bubbles but

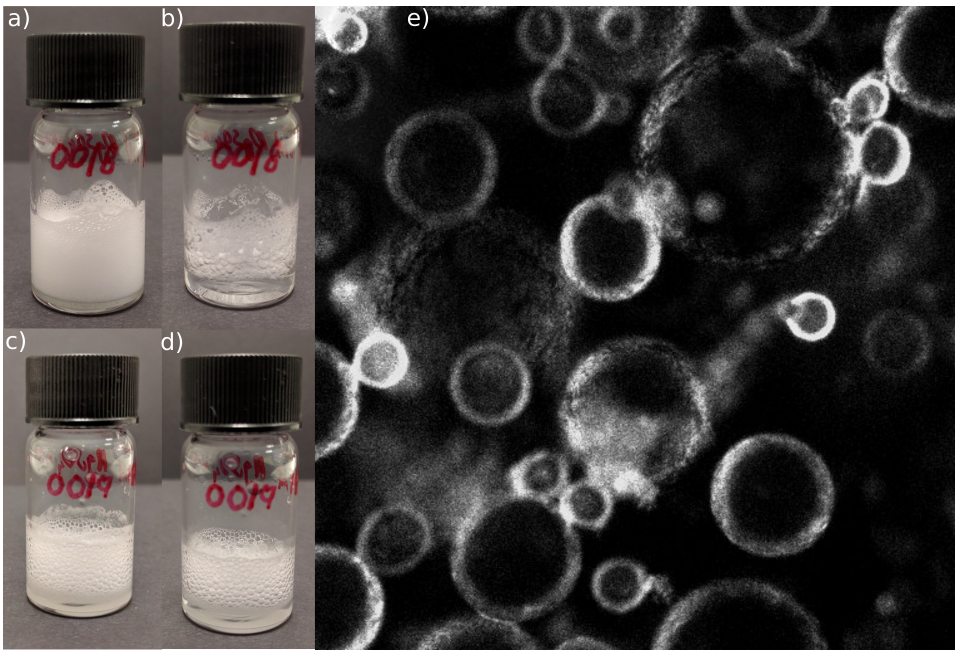

Figure 3.4 *Illustrates fresh foams* ***a,c:*** *and foams after 0.5 hours* ***b,d:*** *prepared from 0.1 wt% 2NapFF and dispersed at < 35°C;* ***a,b:*** *4.5 mg/mL magnesium sulfate and* ***c,d:*** *35 mg/mL magnesium sulfate.* ***e:*** *confocal micrograph of a fresh foam prepared at 0.1 wt% 2NapFF, 35 mg/mL, magnesium sulfate and dispersed at 50°C. Dipeptides are dyed using Nile Blue; scale bar 100µm.*

now over a time-scale of days rather than tens of minutes. At our very low concentrations of the dipeptide the foam lifetime is only two hours, indicating that the remnant hydrogel between the bubbles is now too weak to prevent coalescence and ripening.

As we have found changes in hydrogel properties depending on the ultrasound bath temperature, we repeated the same series of measurements starting from a dispersion made at both temperatures. No changes were observed. By contrast, using calcium chloride rather than magnesium sulfate to create the foam did lead to enhanced stability. With the calcium salt neither varying the salt concentration (4.5 mg/mL and 35 mg/mL) nor varying the initial ultrasound bath temperature, altered the foam properties noticeably. We conclude that any residual influence of the ultrasound bath temperature is negated once the rotor stator has been used to destroy the initial hydrogel. When the fibres reform on the surface of the bubbles, the detailed properties of gelator system can remain influential.

In order to examine the organization of the molecules we have used FTIR, for a dispersion of 2NapFF (black), a foam prepared at low salt concentration (red) and a foam prepared at high salt concentration (blue) (see Figure 3.5). The

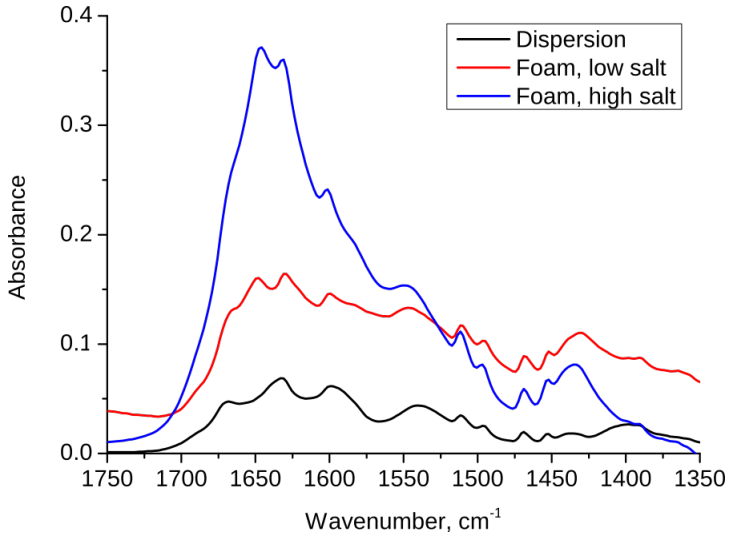

Figure 3.5 *Fourier Transform Infra Red absorbance data for a dispersion of 2NapFF and foams made at the two salt concentrations. There is a very significant growth in the peak around 1650 cm^{-1}*

samples were allowed to dry prior to characterization. The original dispersion has a peak at 1630 cm^{1} , which may reflect the initial micellar ordering. No peak was observed at 1720 cm^{1} , indicating that the carboxylic acid group is deprotonated. A peak appears at 1650 cm^{1} once salt has been added and grows with increasing salt concentration. This may well be related to the formation of a random coil structure, although we highlight that it is difficult to assign these dipeptides on the basis of conventional IR data.

Emulsions with four different oils (isopropyl myristate, silicone oil, dodecane, octanol), were prepared in a similar manner to the foams described above. Three out of four emulsions remained stable, with the droplet size unchanged and no signs of creaming for months (see Figure 3.6a,c,e).

Isopropyl myristate emulsions (see Figure 3.6a) appeared the most ideal in that there was no creaming. At the other end of the range, octanol emulsions (see Figure 3.6g) could not be stabilised, phase separating immediately after preparation. Indeed, it appears that the dipeptide material occupies the small volume of oil phase at the top of the sample (see Figure 3.6g). Less surprisingly, a small amount of creaming occurred within the first hour for silicone oil (see Figure 3.6c) and dodecane (see Figure 3.6e) emulsions. The volume of the clear aqueous phase in these emulsions barely increased after months. The same set of measurements were repeated at 50°C and 35 mg/mL magnesium sulfate and at $<$ 35°C, 4.5 mg/mL and 35 mg/mL magnesium sulfate for each of the oils. The

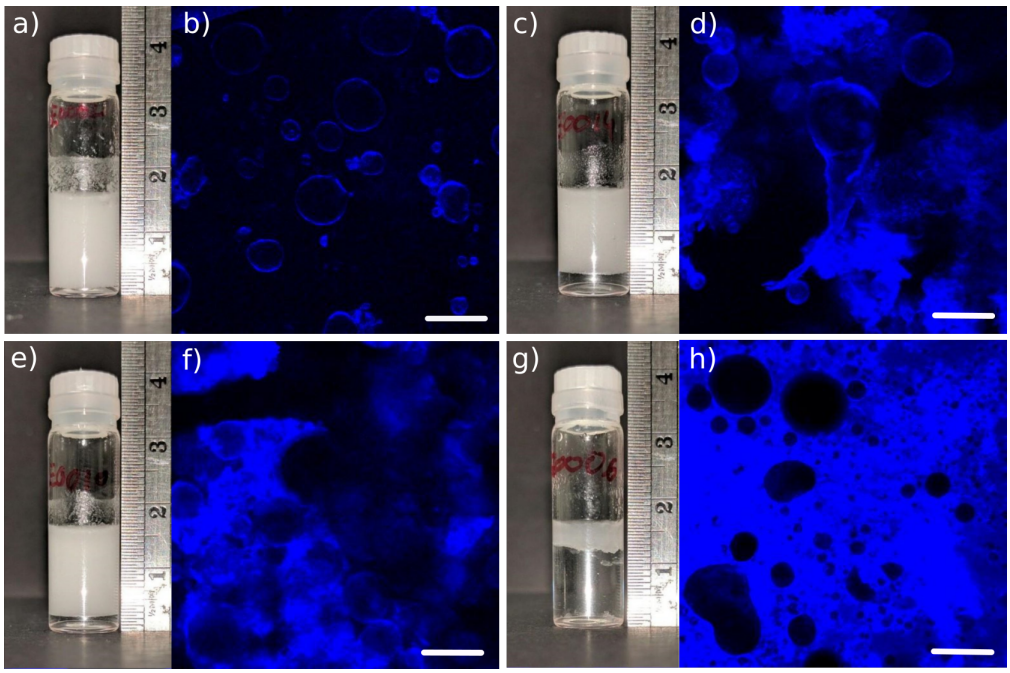

Figure 3.6 *Shows the macroscopic and microscopic characteristics of four emulsions prepared at 0.1 wt% 2NapFF, 4.5 mg/mL magnesium sulfate at 50°C; in the confocal micrographs the dipeptide has been dyed using Nile blue and the scale bar is 100 μm. The oil is* ***a, b:*** *isopropyl myristate;* ***c, d:*** *silicone oil;* ***e, f:*** *dodecane;* ***g, h:*** *octanol.*

emulsification performance and stability are broadly similar.

Confocal images of the emulsions are presented in Figure 3.6b,d,f,h. Here, the dipeptides show a preference for the oil phase in the following sequence: octanol (3.4) > isopropyl myristate (3.3) > silicone oil (2.6) > dodecane (2). The numbers in brackets are the dielectric constants. Self-assembled dipeptides in isopropyl myristate emulsions (see Figure 3.6b) show a clear preference for the interfaces. The concentration of dipeptide in the aqueous phase increases slightly for silicone oil emulsions (see Figure 3.6d) and further still for the dodecane emulsions (see Figure 3.6f).Octanol samples (Figure 3.6h) underwent phase inversion, with the dispersed phase being the water droplets and the continuous phase the oil with dipeptide molecules dispersed in it. This unexpected behaviour is consistent with our observations of the macroscopic emulsion (see Figure 3.6g).

It is tempting to consider the role of the interfacial dipeptide fibres to be similar to the interfacial particles in a Pickering emulsion [137]. Under this scenario, whether the dipeptide fibres become trapped at the interface depends on their wettability by the two fluid phases.

To explore this idea we have carried out an experiment to observe the wetting behaviour of the oils † at an interface between the hydrogel and an aqueous phase of the same salt concentration (see Figure 3.7a). If the hydrogel surface was precisely horizontal and reasonably flat we would be able to use the angle with which the droplet or bubble meets the hydrogel surface (measured through the aqueous phase) as a quantitative measurement of the wettability of the hydrogel. Unfortunately, since the surface is somewhat rough it is not possible to be quantitative. The air and the dodecane appear to make approximately similar (small) angles to the hydrogel surface (see Figure 3.7c,d). This suggests that in both cases the hydrogel greatly prefers contact with the aqueous phase over contact with the droplet/bubble. By contrast, isopropyl myristate makes a more gentle angle with the surface of the gel (see Figure 3.7b). The preference of the hydrogel for contact with the aqueous phase is significantly less marked, this is consistent with the formation of a stable emulsion. If the behaviour of octanol, described above, was because of the wetting characteristics of this oil at a hydrogel surface then we would expect to see the droplet spread out to maximize the contact area with the hydrogel. This would be reflected in a large three phase contact angle. What we see (see Figure 3.7e), is a quite standard contact angle as though the octanol only partially wets the hydrogel. Evidently, the behaviour of this system does not fit easily within the Pickering emulsion picture. We note that the droplet is becoming darker, which might point to more complex changes taking place.

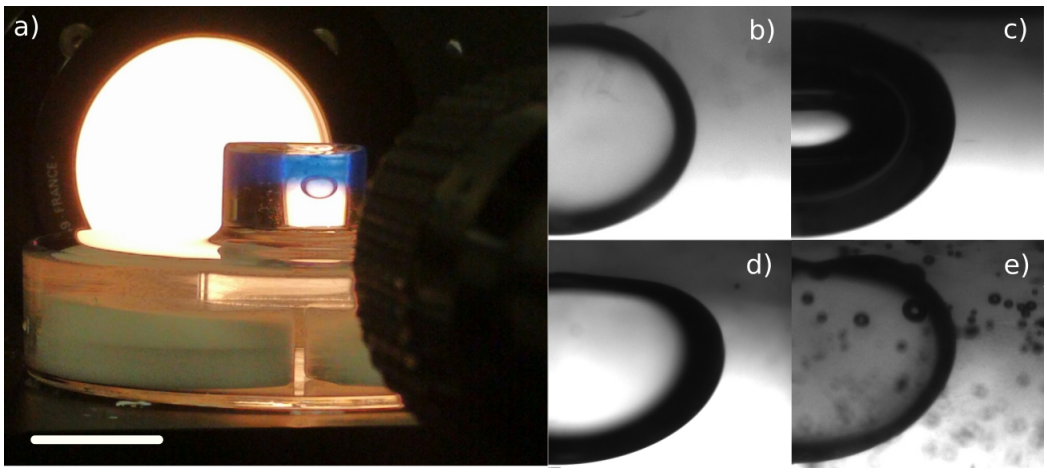

Figure 3.7 ***a:*** *experimental apparatus used to evaluate the wetting characteristics of droplets and bubbles. The hydrogel is visible via the Nile blue dye; scale bar 18 mm. Droplets / bubbles of* ***b:*** *isopropyl myristate* ***c:*** *air* ***d:*** *dodecane* ***e:*** *octanol*

3.5 Conclusions

Following previous studies stabilizing emulsions and foams using dipeptide hydrogels, we have investigated the behaviour of one dipeptide system at low concentration with the gelation induced by the addition of salt. We have presented a route to achieving repeatable gel formation based on the dipeptide 2NapFF and using the salt magnesium sulfate. Using this gel system we have demonstrated that foams become less stable at low dipeptide concentration. The fibre behaviour is found to be closely similar to that at higher concentrations but evidently the gel structure is now too weak. By contrast, we have been able to form long lived emulsions using three out of the four oil phases that we have tested. Here, the droplets could be stabilized by an interfacial film (isopropyl myristate) or by hydrogel both in the aqueous phase and on the interface (dodecane and silicone oil). The oil which could not be emulsified in this way (octanol), could not be described simply using the wetting characteristics of the hydrogel. This observation warns against a simple comparison between the behaviour of these self-assembled fibres and the particulate emulsifiers used in Pickering emulsions. The new process, not observed in Pickering emulsions, is that some components partition into the oil phase but apparently not the intact fibres which are preferentially wet by the aqueous phase.

Chapter 4

Hydrogel films deformation in response to extensional flow

4.1 Abstract

The rheological response of hydrogel films made of two different dipeptide molecules (2NapFF and NapFF) and salt ($MgSO_4$, $CaCl_2$, NaCl) concentrations (1–4 mg/mL), was investigated and compared between them using a custom made film collapse extensional rheometer. Hydrogels are placed between two parallel coaxial circular open rings of equal diameter and stretched at different velocities. The instantaneous radius, surface area and axial radius of the catenoid shaped films formed are calculated and plotted as a function of distance to analize and link their response in terms of interfacial microstructure. Hydrogel films collapse differently under high shear extensional flow. Films from hydrogels prepared with calcium chloride turned into elastic solid films that collapse at small distances. By contrast, films prepared with sodium chloride developed into extremely viscous networks that deform with increasing distance and formed a thread that flowed and collapsed due to capillarity. In between, films prepared with magnesium sulfate resulted in films with a viscoelastic response, with a non-monotonic effect dependence on the film strength on salt concentration. These findings show that films prepared with different salt and concentrations have a huge effect on the rheological properties of interfacial films. Last, the film collapse extensional rheometer could be a potential tool to investigate the dynamic response of viscoelastic films during emulsification or foaming.

4.2 Introduction

Hydrogels are useful materials, with a wide range of applications such as foods, cosmetics and medicine among others [138–141]. They are formed of hydrophilic polymers that are able to swell and contain a large amount of water, while maintaining a semi-solid structure by physical or chemical cross-linking of these polymers [142]. More recently, a new approach to prepare hydrogels *via* the self-assembly of small molecules, known as low molecular weight gelators (LMWG) in water, has been developed. An example of these effective LMWG are naphthalene protected dipeptides such as, 2NapFF and ThNapFF (see Figure 4.1). 2NapFF and ThNapFF are hydrophobic dipeptides that, when dispersed in a basic solution (pH $\approx$ 11), self-assemble to form long anisotropic structures that range from a few nanometers in diameter to a hundreds of micrometers in length [39, 40]. The self-assembly of 2NapFF and ThNapFF is governed by a combination of noncovalent forces, such as hydrogen bonds, π-π stacking, hydrophobic interactions, electrostatic interactions and repulsive steric forces [143]. For gelation to occur, a self-supporting water-swollen three-dimensional continuous network has to be formed [50]. This is formed by the anisotropic structures entangling and cross-linking between them [135]. The basic solutions, can then be gelled using different approaches such as, a change in temperature or pH, salt addition or solvent-switch.

We have previously shown that hydrogels made of 2NapFF are able to stabilise emulsions prepared with a range of oils for months (see Chapter 3).The emulsions are stabilized via two mechanisms; during emulsification, the hydrogels get disrupted and hydrophobic dipeptide fibres adsorb to the liquid-liquid interface. Cross-linked fibers form viscoelastic interfacial films at the interface of new born oil droplets and prevent them from coalescing. Meanwhile, the continuous phase hydrogel reforms again keeping the suspended oil droplets dispersed and stable,

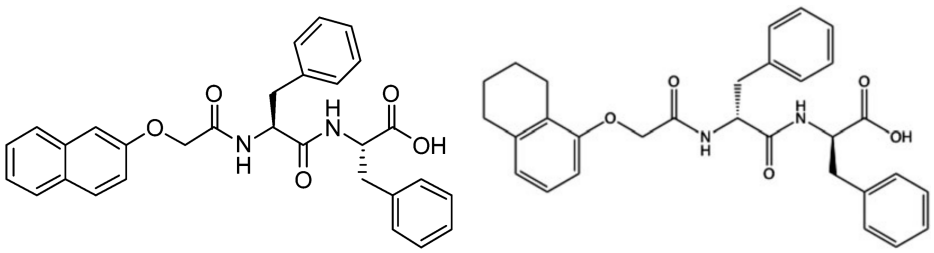

Figure 4.1 *Schematic of the molecular structure of 2NapFF (left) and ThNapFF (right).*

having little chance to collide, coalesce into larger droplets, and separate. In Chapter 5, we characterise the hydrogel films formed at the interfaces of oil droplets by subjecting them to oscillatory dilatational deformations. Nonetheless, for a full characterisation of hydrogel emulsions, it is also crucial to study the hydrogel formed between the oil droplets.

Rheological experimental techniques to characterise the viscoelastic properties of hydrogels have been employed for decades [144], with rotational rheometers being among the most popular instruments. However, it is well established, that the response of viscoelastic fluids to strong flows is considerably different than in simple shear [145]. For this reason, subjecting the hydrogel to strong extensional flow rates, offer us the possibility of expanding our investigations to instability mechanisms like necking. To mimic hydrogel thin films stretched under high shear during emulsification, we use a customise extensional device with modified end plates from which, stretched hydrogels, transform into catenoid-shaped films that we study as a function of plate separation.

Soap films formed between two open circular rings, having identical radii have been studied for decades [146]. When the distance between the two rings increases, the soap film forms a symmetric catenoid that has been used by mathematicians to study minimal surfaces. Figure 4.2 shows the evolution of the radius at the mid-plane of the film a as a function of distance h found by

$$r(z) = a \cosh \frac{z}{a}, \tag{4.1}$$

where a is the minimum value of r at z=0. The solid and dashed black lines are the radius at the mid-plane of the film of stable and unstable catenoid film respectively. Stable films become unstable at a distance $h/R = 1.05$, where the surface area of the film is equal to the surface area of the two end rings (see Figure 4.3). As the distance between the two rings increases, the radius decreases faster, until it reaches the critical distance ($h_c/R = 1.33$), where films cannot exist any more and they collapse into two planar-films suspended in the two rings.

The catenoid shaped film is described by the parameters h, R and a, where R is the radius of the end rings, a is the radius at the mid-plane of the film and h is the distance between the end rings (see Figure 4.3). Based on Equation 4.1,

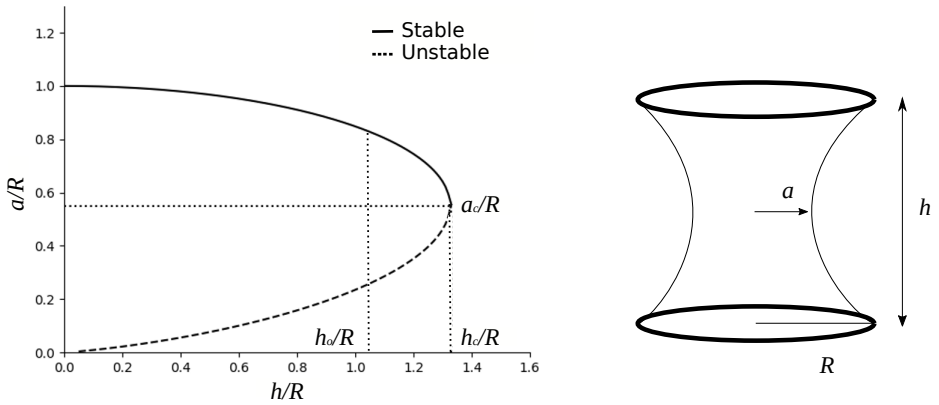

Figure 4.2 *Theoretical evolution of the radius at the mid-plane of the film a/R as a function of distance h/R of a minimal surface. The solid (stable catenoid) and dashed black (unstable catenoid) lines are the radius at the mid-plane of the film. Where R is taken to be 9.25 mm; h_o/R is the distance at which the surface area of the film is equal to the surface area of the end rings and the film becomes unstable; h_c/R and a_c/R are the critical distance and critical radius respectively, at which a minimal surface cannot exist any more.*

these three parameters are related by

$$h = 2a \cosh^{-1} \frac{R}{a}, \tag{4.2}$$

Similarly, the surface area of a catenoid film can be found to show why the film collapses at a distance equal to 1.33. Figure 4.3 shows the theoretical evolution of the area S as a function of ring separation (hereafter referred to as the distance) of a minimal surface found using Equation 4.3. Both, the area and the separation, have been non-dimensionalised. Here, two films (dashed and solid black lines) can be found at a distance lower than the critical distance h_c/R, albeit only the catenoid having the larger radius is observed experimentally. This is because the catenoid film, with the bigger radius, has the lower surface area for all distances. The horizontal dashed line, is the surface area of the two end rings. At a distance of 1.05 (h_o/R), the surface area of the film (with the bigger radius) and the area of the end rings, are equal and hence the film becomes unstable. Nonetheless, the surface area of the film keeps increasing, until a distance of 1.33, because of inertia. Notice, that the surface area of the film with the lowest radius, has a bigger surface area than the two rings for all distances; this is the reason why

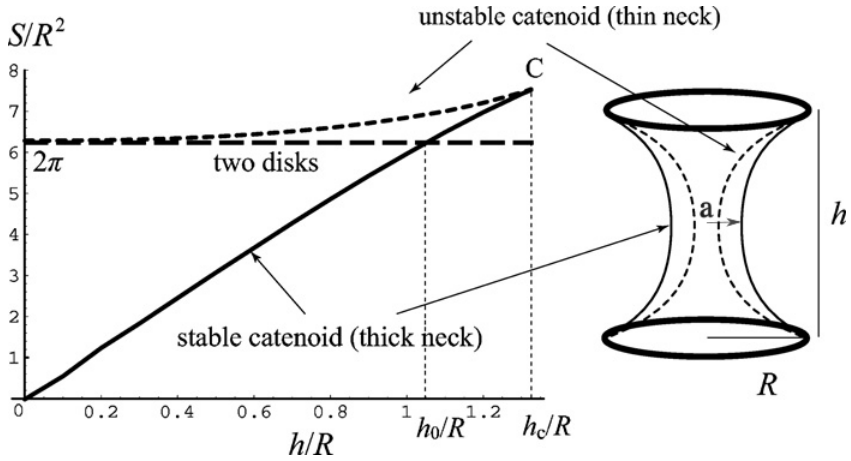

Figure 4.3 *The evolution of the surface area S/R^2 as a function of distance of two possible films predicted by Equation 4.3. Where C is the critical point at which a film cannot exist any more and $h_c/R = 1.33$ is the critical distance. The horizontal dashed line is the surface area of the two end rings; the intersection at which this line and the film intercept, $h_o/R = 1.05$, is the point at which the film is energetically unfavourable and becomes unstable because its area is equal to the area of the end rings.*

this film cannot be seen experimentally.

$$S = 2\pi a^2 \left(\cosh^{-1} \frac{R}{a} + \frac{1}{2} \sinh \left(2 \cosh^{-1} \frac{R}{a} \right) \right) \tag{4.3}$$

Salkin and coworkers, studied the deformation of soap films stretched by hand with the help of a calliper of different end ring diameters [147]. The authors demonstrated in this study that, soap films seeking to minimize their surface energy, had the same surface area as the minimal surface predicted by Equation 4.1.

Similar experiments were carried out with films made of a mixture of polymers [148]. Films made of PVA/borax, were stretched at high shear rates to investigate the dynamic response of thin films during foam formation. The authors found that, with increasing the concentration of cross-linker (borax), the radius of the films deviated more from the radius of the minimal surface. When this cross-linker was not present in the solution though, the radius of the films was identical to soap films and theory results. However, when the films reached the critical distance (1.33), they kept elongating until a distance of 1.8. The authors attributed this to the rate at which the films were stretched and to the relative high viscosity of the

polymer solution as opposed to a soap film. More importantly, stretching hydrogel films served to demonstrated that films with high concentration of borax, do not minimize their surface area like soap films and fracture under high stretching deformations. They hypothesized that PVA/borax networks, do not have time to rearrange at high shear flows and the films behave like an elastic solid.

Here, we probe hydrogel films with variable viscoelasticity at high rates. Furthermore, our results are unique and different to fluid filaments because of the dynamic response, as well as the motivation behind the experiments. For example, viscoelastic filaments are stretched to a specific distance and they are left to collapse under capillarity, whereas hydrogel films, are stretched such that the catenoid film shrinks until it self-intersects at the mid-plane and hence bursts. The exception are films prepared with sodium chloride, where the films do not burst and similarly to fluid filaments undergo capillary-driven break-up. However, in this chapter, we are not interested in this action and hence the results presented here are from films which mainly preserve a catenoid shape.

In this chapter, the dynamic response of a series of hydrogel films prepared in different ways and stretched at different velocities is investigated. The collapse scenarios of the films are discussed first. Next, the radius at the mid-plane of the films a and their surface area S are compared and explained from a rheological point of view. The axial radius of the profile curve R_z of catenoid shaped films is then compared and linked to a partial-decohesion between the films and the end rings observed in some of the films. Finally, we find the radius of the rings R for each film by rearranging Equation 4.2 and provide a few suggested conclusions based on the results.

The main objective of this chapter was to investigate the behaviour of hydrogel films stretched during emulsion formation. For this, we use a custom made film collaspe extensional tensiometer that mimics the stretching deformation films go through in emulsification. The main results from this chapter are that hydrogel films with different viscoelastic properties neck and break differently under high rate extensional flows. The dynamic response of the films might not differ that much at first, while the films are still in the stable regime. However, the changes are significantly more marked when they enter into the unstable regime; most probably is in this regime where hydrogel films are found during emulsification. In addition to this, we observe a non-monotonic effect on the film's strength when these were prepared with magnesium sulfate, indicating an optimal salt concentration at intermediate salt concentration. Finally, we demonstrate that

contrary to theoretical results, the surface area of the film, do not grow higher than the area of the two rings; instead the area drops back to zero when it equals (or is near) the area of the two rings.

4.3 Materials and methods

4.3.1 Materials

2NapFF and ThNapFF were synthesised as described previously [42]. The solvents hexane and ethanol, were purchased from Fisher Scientific UK. All other chemicals used were of analytical grade and were obtained from Sigma-Aldrich unless specified.

4.3.2 Methods

Hydrogel preparation

Vials and instruments were cleaned with hexane, followed by methanol and rinsed with ultra pure water before use. An equimolar quantity of NaOH (1 M, aq) was added to millipore water (resistivity = 18.2 MΩ.cm) to give a basic solution with pH 10.5 ± 0.5, measured with a Seven Easy pH probe (Mettler Toledo AG). Then, 2NapFF or ThNapFF were added and the mixture was dispersed. Gelation was triggered by adding $MgSO_4 \cdot 7H_2O$, $CaCl_2 \cdot 2H_2O$ or NaCl. In practice, all samples were prepared using 0.1wt% dipeptide and were gelled using 1, 2, 3, or 4 mg/mL pre-dissolved salt to give a 1 mL sample. This was then left to stand for 12 hours at room temperature before use in subsequent experiments.

Operational characteristics of the film stretching device

A custom film stretching rheometer designed and constructed by a team at ESPCI [148], was used to perform uniaxial extensional measurements (see Figure 4.4). The instrument is made of two parallel coaxial circular open rings of an interior diameter of 18.5 mm and exterior diameter of 25 mm (see Figure 4.5b). Uniaxial strain is applied via the lower ring, which is connected to a piezoelectric motor

unit that moves downwards at different stretching velocities.

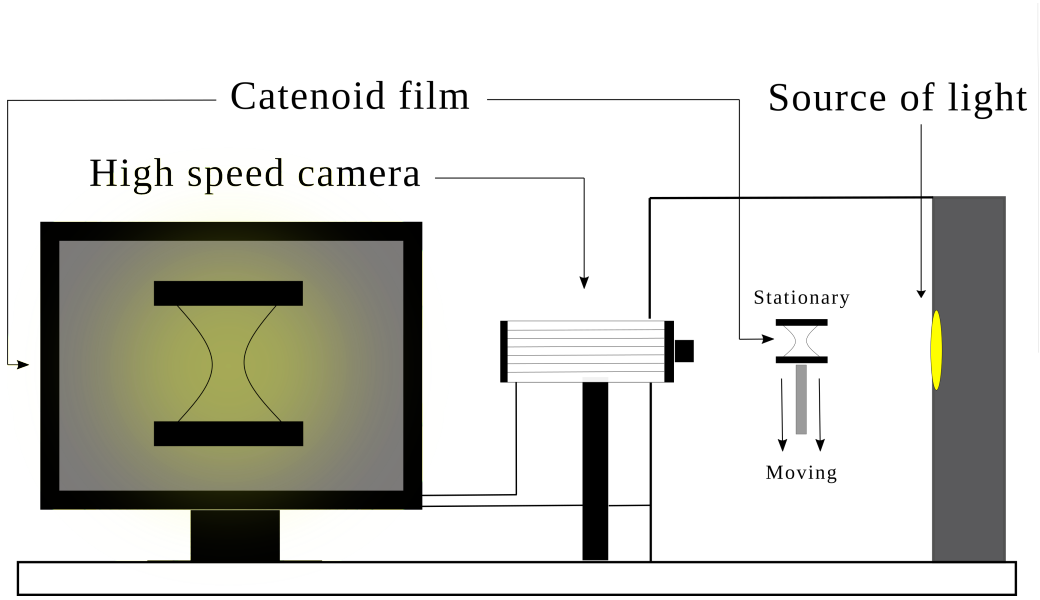

Figure 4.4 *Schematic diagram of the extensional tensiometer.*

The end stretching velocity profile is set up to increase to approximately 5, 50 and 500 mm/s. However, the final stretching velocity averaged over 10 samples is shown in Figure 4.6. Of those 10 samples, 2 were solutions and 8 hydrogels. The velocity increases linearly with an average velocity of 5 ± 0.5 mm/s for films stretched at the lowest velocity. Films set up to stretch at 50 mm/s, accelerate at first, but they become linear rapidly, with a final velocity of 45 ± 0.5 mm/s. Films set up to stretch at 500 mm/s with an exponential increase, acccelerate almost for all distances, with a final velocity of 100 ± 0.5 mm/s, when the lower ring reaches a distance of 12 mm. The stretching velocity increases linearly for the three velocities used in bare films, with an average velocity of 5, 45 and 85 ± 0.5 mm/s.

The experimental set up consists in placing a specific volume of the hydrogel (0.250 mL) on top of the lower ring with the help of a spatula. Next, the lower ring is brought up to the starting position, with an initial distance of 1.5 ± 0.2 mm between rings, ensuring that the hydrogel contacts entirely the surface of the upper ring as well. As the lower ring is set in motion, the hydrogel stretches until eventually becomes a film. The film, trying to minimise its surface area, shrinks from the mid-plane (weakest point) and forms a catenoid (see Figure 4.5a), from which the curvature of the air-fluid interface is monitored by using a high-speed camera at 2000 fps. The dynamic response of hydrogel films, is investigated

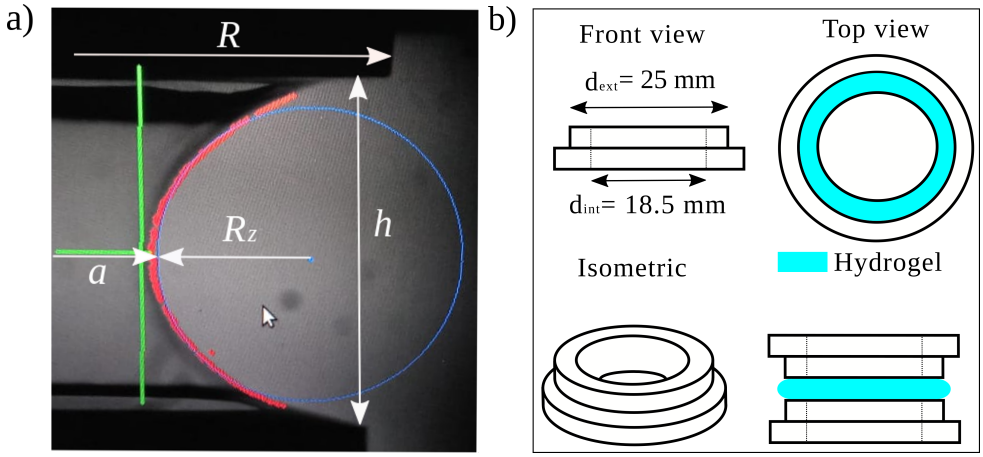

Figure 4.5 ***a:*** *film formed between two circular identical rings of radius R separated by a distance h. Where a is the radius at the mid-plane of the film and R_z the axial radius profile of the curvature of the air-fluid interface* ***b:*** *schematic diagram of the end rings dimensions. R is taken to be 9.25 mm.*

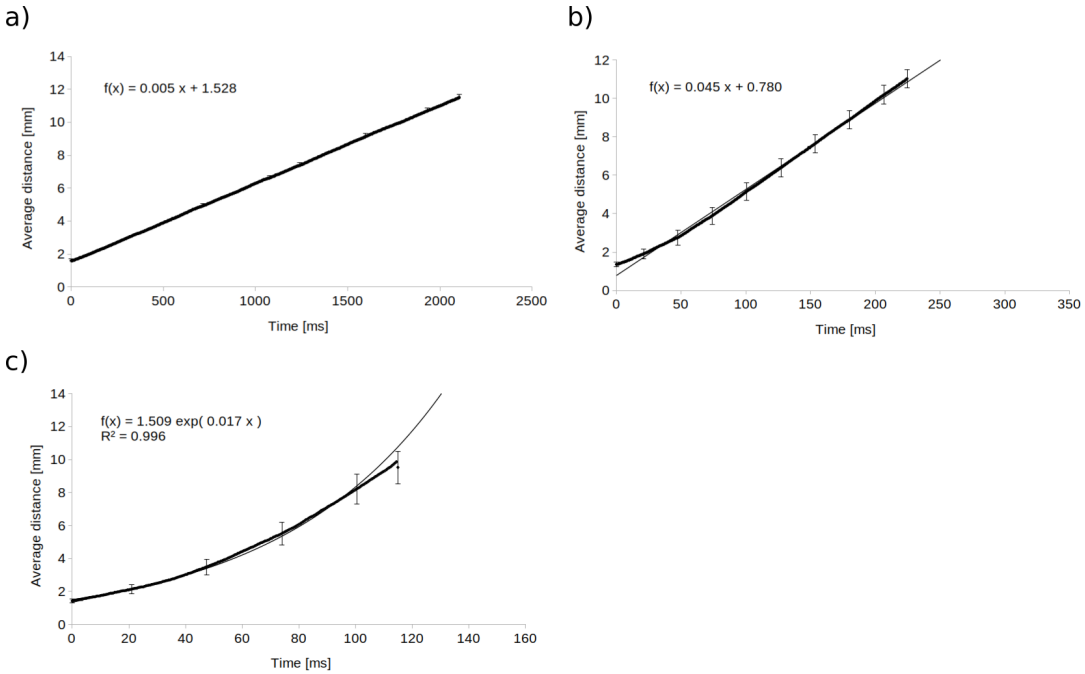

Figure 4.6 *Mean distance-time graphs of films stretched at* ***a:*** *low,* ***b:*** *medium and* ***c:*** *high stretching velocities.*

by extracting the x and y coordinates of the catenary curve from each frame, using a multi-dimensional image processing package (SciPy ndimage) available in Python. Finally, with the coordinates, we calculate the radius at the mid-plane of the film a and the surface area S, along with the axial radius profile of the curvature R_z of each catenoid and plot them as a function of the distance between the end rings h (see Figure 4.5a).

4.4 Results and Discussion

4.4.1 Visual evolution of the stretching and different collapse scenarios of hydrogelled films

An example of the experimental evolution of a hydrogel film under uniaxial stretching is shown in Figure 4.7. At the starting position, the sample is slightly squeezed by the end rings, causing the sides of the sample to protrude outside the diameter of the end rings (see Figures 4.5b and 4.7a). With this, we ensure that the hydrogel makes contact with both end rings equally. As the lower ring is set in motion, the sample tries to minimise its surface area by lowering its cross-section in the mid-plane (see Figures 4.5a and 4.7).

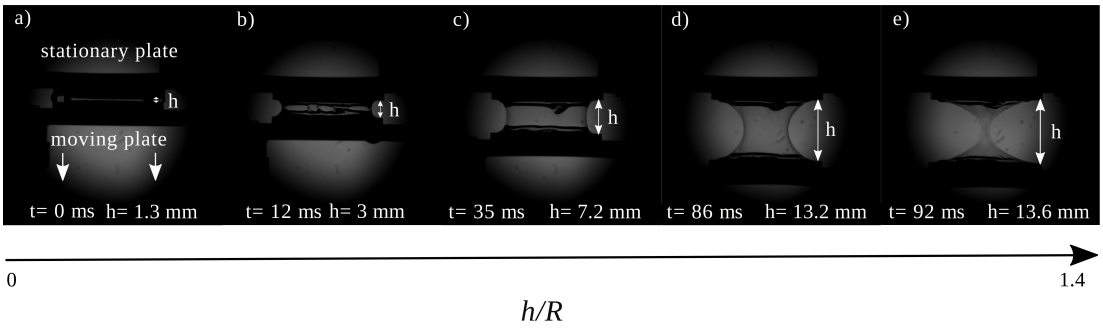

Figure 4.7 *Experimental evolution of a film made of 2NapFF. The upper ring is stationary, whereas the lower ring can be set to move at different stretching velocities.*

The hydrogel film continues to expand with distance until it eventually collapses in one of three possible ways; (i) the film shrinks and forms a bridge that bursts on itself (see Figure 4.8a), (ii) the film shrinks and forms a bridge that when both sides come into contact takes the shape of a thread that last hundreds of milliseconds before collapsing (see Figure 4.8b) and, (iii) the film does not deform and breaks by pinching-off or tearing up at an early stage (see Figure 4.8c). The way in which the hydrogel films collapse, has been observed to be salt dependent. Films prepared with magnesium sulfate showed a shrinkage collapse scenario, while the thread was the particular collapse scenario of films prepared with sodium chloride. Finally, films prepared with calcium chloride became more elastic and ripped or pinched-off prior to curving towards the mid-plane. While hydrogel films seem to increase in viscosity with sodium chloride (observed by

the flowing thread that forms between the end rings following cessation), films turn out to be brittle and less flexible with calcium chloride. In between, films prepared with magnesium sulfate appear to be viscoelastic instead. In the next section, we plot the measurements of the radius at the mid-plane of the film a/R as a function of distance h/R for bare (pure water), dispersion (basic solution with dipeptides dispersed) and hydrogel films.

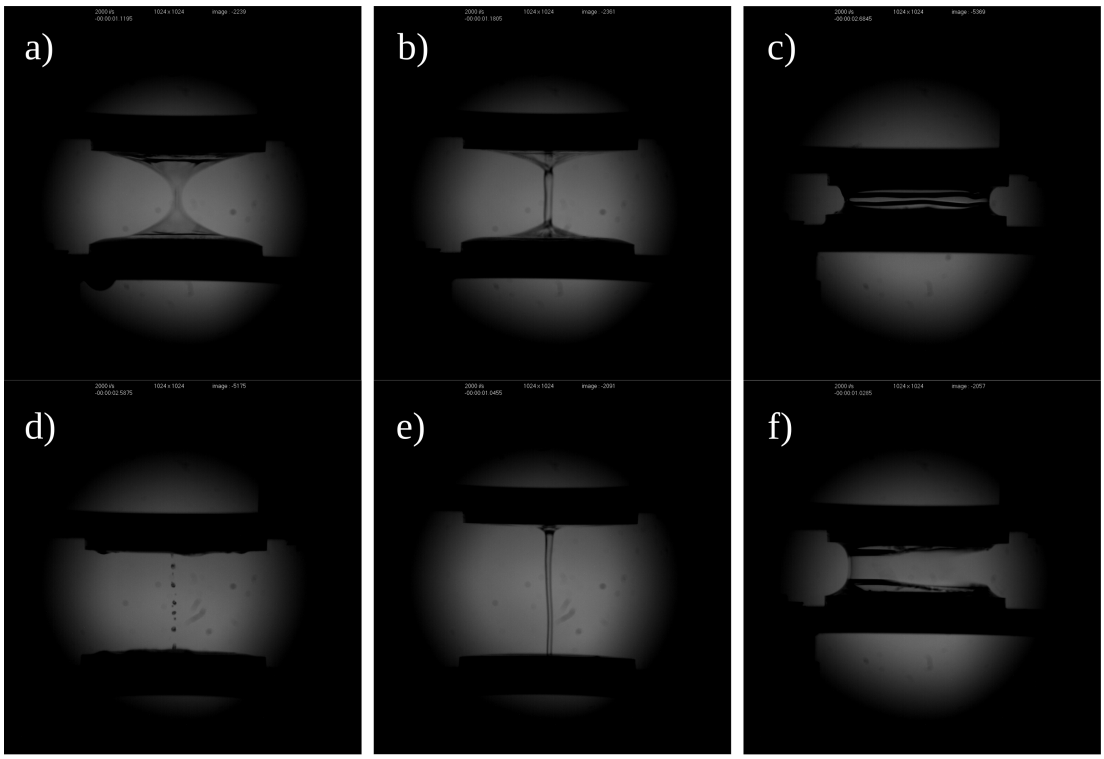

Figure 4.8 *Potential collapse scenarios of films made of 2NapFF,* ***a,d:*** *shrinkage: films prepared with magnesium sulfate* ***b,e:*** *thread: films prepared with sodium chloride and,* ***c,f:*** *rupture: films prepared with calcium chloride.*

4.4.2 Evolution of the radius at the mid-plane of hydrogel films a/R as a function of distance h/R

In this section, we investigate the dynamic response of hydrogel films by computing the radius a and plotting it as a function of distance. The data is first presented for more simple systems, such as bare films made of pure water and films made of the invidual dipeptide (2NapFF or ThNapFF) dispersed in a basic solution (dispersion) to aid interpretation of the graphs. The measurements of the hydrogel films will be presented and discussed next.

Milli-Q water and dispersion films were first stretched to (i) aid with the interpretation of the data and (ii) use them as a controls and compare them to hydrogel films. The radius a for the minimal surface found theoretically (solid and dashed black lines), is plotted together with all the films as a guideline. The evolution of the radius a/R as a function of distance h/R for bare and dispersion films, stretched at different stretching velocities, is shown in Figure 4.9.

The radius a, shows a fast decrease at short distances ($h/R < 0.5$), followed by a slow down at intermediate distances ($0.5 < h/R < 1.2$) for bare films (see Figure 4.9a). Films stretched at a low stretching velocity, collapsed at $h/R \approx 1.05$, where its absolute area is equal to the area of the end rings (see Figure 4.3). The film bursts to relax by spliting up into two films that occupy the area of the end rings. The radius of films stretched at medium and high stretching velocities, decreases faster again at long distances ($h/R > 1.2$), until the films reach $h/R \approx 1.4$, where the radius drops to zero. The radius a, differs slightly between films stretched at different velocities, with films stretched at high velocity having the larger radius, followed by films stretched at low and medium velocity; this discrepancy increases when films become unstable.

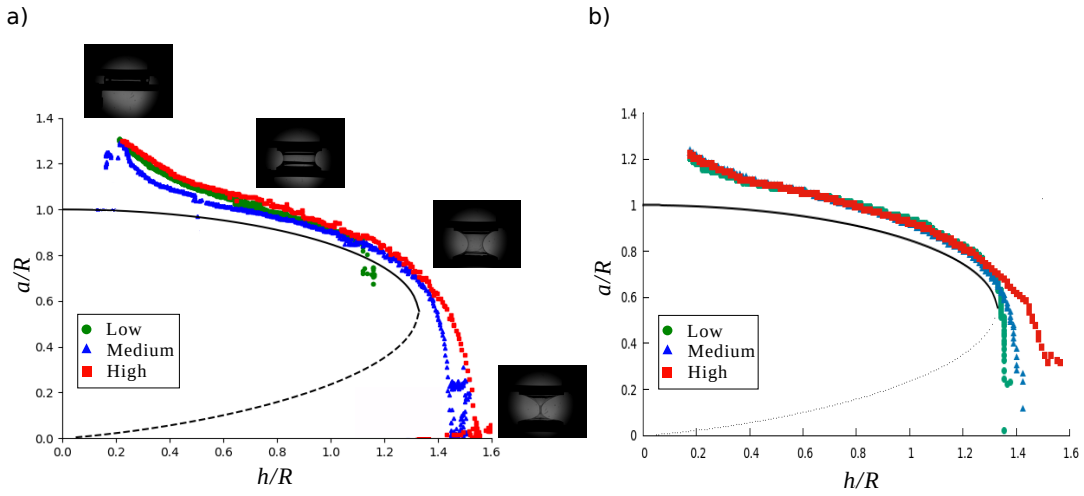

Figure 4.9 *Experimental evolution of the radius a/R as a function of distance h/R of* ***a:*** *bare and* ***b:*** *dispersion films, stretched at different stretching velocities. Photographs show a film being stretched at different points of the curve. The solid and dashed black lines are the radius of a stable and unstable catenoid film respectively. R is taken to be 9.25 mm.*

Similarly to bare films, the radius of films made of the dispersions show a fast decrease at short distances (see Figure 4.9b). The radius decreases more gently at intermediate distances ($0.5 < h/R < 1.20$), where the films are stable. Eventually, the radius of the films drops to zero when they become unstable at longer distances ($h/R > 1.3$). Contrary to bare films, the radius of these films decrease at the same rate when stretched at different velocities. However, these deviate when the films become unstable.

The inset images in Figure 4.9a show how the film looks like at that distance. At short distances ($h/R < 0.5$), the lower ring is set in motion and the water begins to stretch. The fast decrease in the radius observed in this region has been attributed to inertio-capillary oscillations of the fluid droplets attached to the end plates when stretching fluid filaments [149]. These ocillations are followed by a rapid development of a catenoid shaped stable film that shrinks quickly. In this region ($0.5 < h/R < 1.2$), gravitational effects can be neglected and therefore the shrinkage is most probably governed by a balance between inertia, surface tension and viscoelastic effects. At long distances ($\approx h/R > 1.2$), the area of the film has become higher than the area of the end rings and the film becomes unstable and shrinks extremely fast. The differences between radii, for different speeds, at long distances may be due to an increase on the limit of extensibility caused by the velocity at which the films are stretched. At low velocity, the viscous part of the material dominates and films collapse when they are not energetically favourable, whereas at higher velocities, the inertia results in the films becoming overstretched and they collapse at higher distances. In fact, when water was stretched at low velocity, the film collapsed at a distance of approximately 1.05, where its absolute area is equal to the area of the end rings (see Figure 4.3). This effect was not observed in dispersion films stretched at low velocity most probably because the surface tension of the films is significantly lower ($\approx$ 24 mN/m) than that of bare films (72 mN/m).

Hydrogel Films - 2NapFF

Salt concentration can significantly influence the rheological properties of hydrogels (see Chapter 3). Here, the evolution of the radius a/R of a series of hydrogel films prepared with different salts and concentrations, is plotted as a function of distance h/R to study their dynamic response (see Figures 4.10 and A.1).

Figure 4.10a shows the radius of three hydrogel films prepared at 1 mg/mL

magnesium sulfate, calcium chloride and sodium chloride, stretched at 5 mm/s. At short distances, the radius decreases faster for films prepared with sodium chloride, followed by films prepared with calcium chloride and magnesium sulfate. At intermediate distances, the radius decreases at the same rate for all hydrogel films; however, the radius of films prepared with sodium chloride decreases to a larger extent, which indicates a film with less resistance to deformation. Films prepared with calcium chloride collapsed at short distances when these were stretched at high velocities or prepared at higher salt concentrations than 1 mg/mL. This indicates that hydrogels made of 2NapFF prepared with calcium chloride, become elastic solid and rupture either when they are prepared at high salt concentrations or are deformed at high strain rates.

Increasing the concentration of calcium chloride, increases the number of calcium bridges formed between carboxylic acids (COOH), from the dipeptides and the ions. This, causes the film to become more brittle and collapse at a shorter distances. This has been shown before by Shi and co-workers [150], when they investigated the effects of calcium chloride on hydrogels elasticity. The authors found that by a small change in the concentration of calcium chloride, the elasticity of hydrogels increased over several orders of magnitude. The number of cross-links among interfibres increased along with the storage moduli of the peptide hydrogel with calcium chloride. [150].

The radius of curvature increases with salt concentration for films prepared with sodium chloride (see Figures 4.10a, 4.10c and 4.10e). Increasing the stretching velocity also alters the radius, but only when the films are unstable. The radius drops drastically for films stretched at low velocities, instead this decreses more slowly for films stretched at high velocities. These differences are most probably caused by an increase in the film's viscosity. Films prepared at 4 mg/mL sodium chloride, showed a thread that lasted for longer following cessation of the ring motion. In addition to this, when films become unstable, they shrink much more rapidly. This could result in a delay in the topological changes of films prepared with sodium chloride, especially those prepared at high salt concentration with higher particle density. A higher radius of curvature for the same distances is indicative of less deformed interfaces. This effect is more marked for interfaces prepared with sodium chloride and as a result of this, they become unstable at higher distances. However, we cannot say whether this effect is due to interfaces becoming stronger, more brittle or thicker.

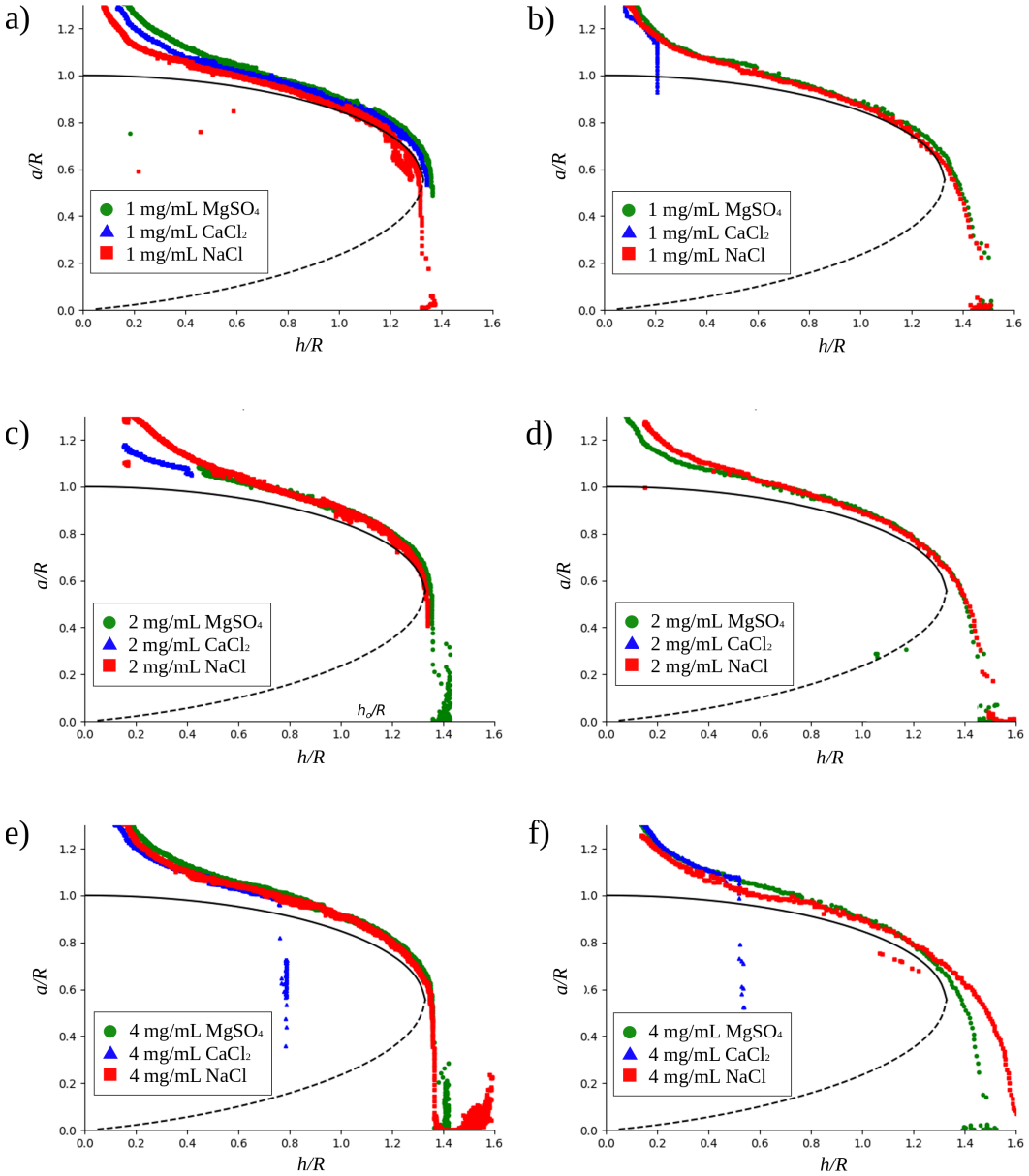

Figure 4.10 *Experimental evolution of the radius at the mid-plane of the film a/R as a function of distance h/R of dipeptide hydrogel films made of 2NapFF, prepared with different salts (magnesium sulfate, calcium and sodium chloride) concentrations (1, 2 and 4 mg/mL), stretched at* ***left column:*** *low and* ***right column:*** *high velocity. The solid and dashed black lines are the radius at the mid-plane of the film a of stable and unstable catenoid film respectively. R is taken to be 9.25 mm.*

Hydrogel Films - ThNapFF

ThNapFF dipeptides are similar to 2NapFF in that they are able to make stable hydrogels with similar mechanical properties ([151]). Hydrogels studied here, are

prepared by using our prefered salt, magnesium sulfate at 1, 2, 3 and 4 mg/mL and stretched at different stretching velocities.

Figure 4.11 shows the evolution of the radius a/R as a function of distance h/R. The radius of interfaces stretched at low velocity, decreases with increasing salt conentration, which may indicate that interfaces become weaker with increasing salt concentration. At higher velocities the radius increases for all interfaces, but the salt concentration effect vanishes, which may imply that the films become more elastic with increasing velocity. Interestingly, we do not observe the fast decrease of the radius at short distances as we observed in films made of 2NapFF. Althought it is difficult to draw a solid conclusion due to the lack of a cell to monitor the force exerted by the lower ring, it is tempting to conclude by saying that films with a greater resistance to compression will have a higher radius than films with lower resistance for the same distances. Certainly, what makes this

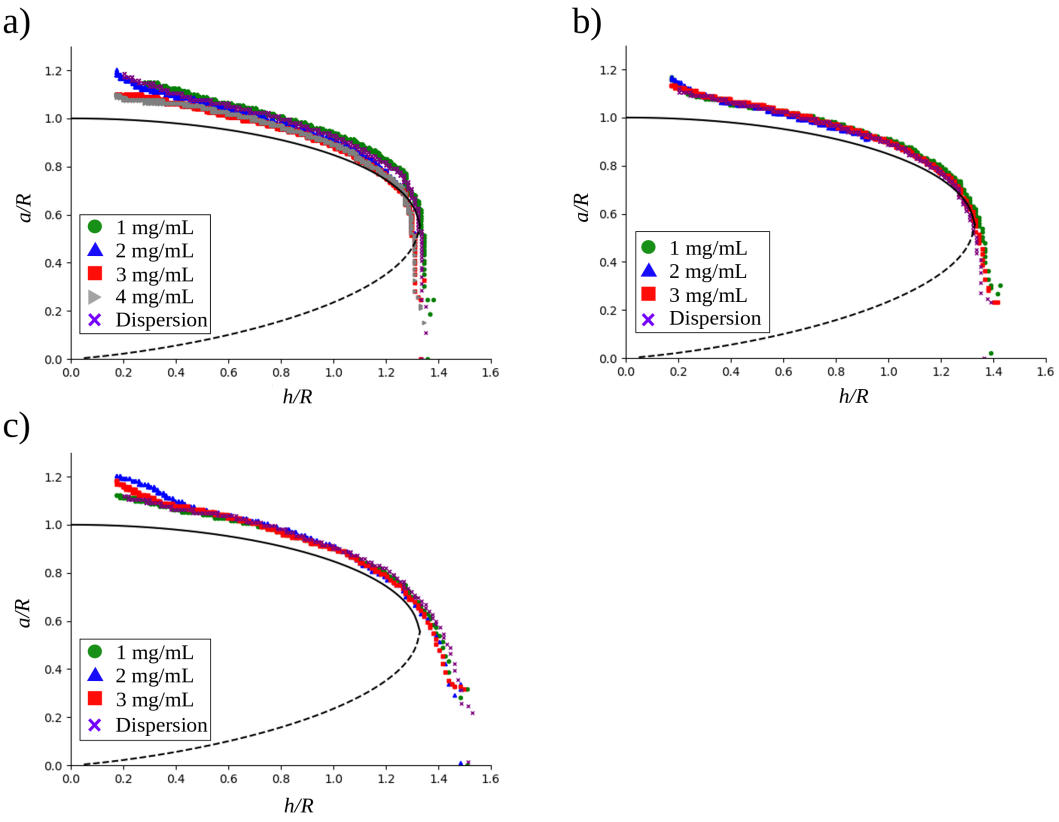

Figure 4.11 *Experimental evolution of the radius a/R as a function of distance h/R of hydrogel films made of ThNapFF prepared at 1, 2, 3 and 4 mg/mL magnesium sulfate, stretched at* ***a:*** *low,* ***b:*** *medium and* ***c:*** *high velocity. The solid and dashed black lines are the radius at the mid-plane of the film a of stable and unstable catenoid film respectively. R is taken to be 9.25 mm.*

resistance stronger or weaker, are the mechanical porperties of the films. Based on these figures and the colapse scenarios (see Section 4.4.1), we conclude saying that films made of 2NapFF prepared with sodium chloride become more viscous with increasing the concentration of salt. These films did not collapse, instead they formed a thread that broke under capillary action. On the other hand, films become more elastic and collapse at short distances when they are made of 2NapFF and prepared with calcium chloride. In between, films made of 2NapFF and THNapFF prepared with magnesium sulfate differ in that while the radius of films made of 2NapFF increases with increasing the concentration of salt, this decreases for interfaces prerpared with ThNapFF. Furthermore, the radius of interfces made of 2NapFF was affected by the concentration of salt, while for interfaces made of ThNapFF, the concentration of salt was not as important as the velocity at which the interfaces were stretched. However, interfaces elongated all the way until the neck of the film contacted with itself and collapsed in similar way for both dipeptide molecules.

In next section, we compute the surface area of the films and compare these against that of a minimal surface.

4.4.3 Evolution of image and equation based surface areas of hydrogel films S/R^2 as a function of distance h/R

In this section, the dynamic response of the films is investigated by computing the surface area in two ways; image-based surface areas were found by calculating the inner and outer area of the catenary curve and taking the average, while equation-based surface areas were found using the radius a of the catenary curves and the radius R of the rings instead and placing these in Equation 4.3. The data of bare and dispersion films is presented first, followed by the results of the hydrogel films that will be presented and discussed next.

Films - Water and Dispersions

Theoretically, a minimal surface is a surface that locally minimises its area. It is well established that, a film suspended between two coaxial circular rings of equal radius R, will form a surface of revolution with axial symmetry from which its radius a can be found by solving Equation 4.1 [147, 152]. There are two solutions

for $h/R < 1.33$, from which only one solution is stable (i.e. not the solution for $h/R > 1.33$, see Figure 4.3).

The evolution of image and equation based surface areas S/R^2 for bare and dispersion films stretched at different velocities is plotted as a function of distance h/R in Figure 4.12. The solid black line is the area of a film with a minimal surface calculated with Equation 4.3. The horizontal dashed black line corresponds to the area of the end rings. Vertical dashed black lines correspond to the point at which the surface area of the minimal surface equals the surface area of the end rings $h_o/R = 1.05$ and the critical distance h_c/R at which theoretically catenoid films cannot exist any more.

Equation based surface areas from bare films increasing at the same pace, are larger than the area of the minimal surface for all distances (see Figure 4.12a). This makes the area of bare films to reach the surface area of the end rings at shorter distances ($h/R \approx 1$) than the minimal surface. At this point, bare films stretched at a low velocity collapse when the area of the films is equal to the area of the end rings. However, the surface area of films stretched at medium and high velocities continue to increase like the theory results predict, until they reach the critical distance (h_c/R).

Surface areas found from the fitted equation for dispersion films (see Figure 4.12b), are identical to the areas of bare films. However, the area of films stretched at a low velocity keeps rising higher than the area of the end rings. As mentioned earlier, this is most probably due to the surface tension of these films being much lower than that of bare films. Interestingly, we observed large deviations at long distances, between image, and equation based surface areas. These discrepancies start at intermediate distances but are more marked when the area of the films approaches the area of the end rings. While equation based surface areas increase linearly until they reach a maximum at h_c/R, image based surface areas reach a maximum when they approach the area of the end rings.

At short distances ($h/R < 0.5$), image based surface areas and equation based areas of bare films are similar (see Figure 4.12a and 4.12c). At intermediate distances ($0.5 < h/R < 1$), image based surface areas increase more slowly than at short distances and intersect with the surface area of the minimal surface at $h/R \approx 0.9$. As the areas continue to increase more slowly than equation based surface areas, these reach the surface area of the end rings at a higher distances ($h/R \approx 1.15$). At this point, films stretched at a low velocity burst to relax occupying

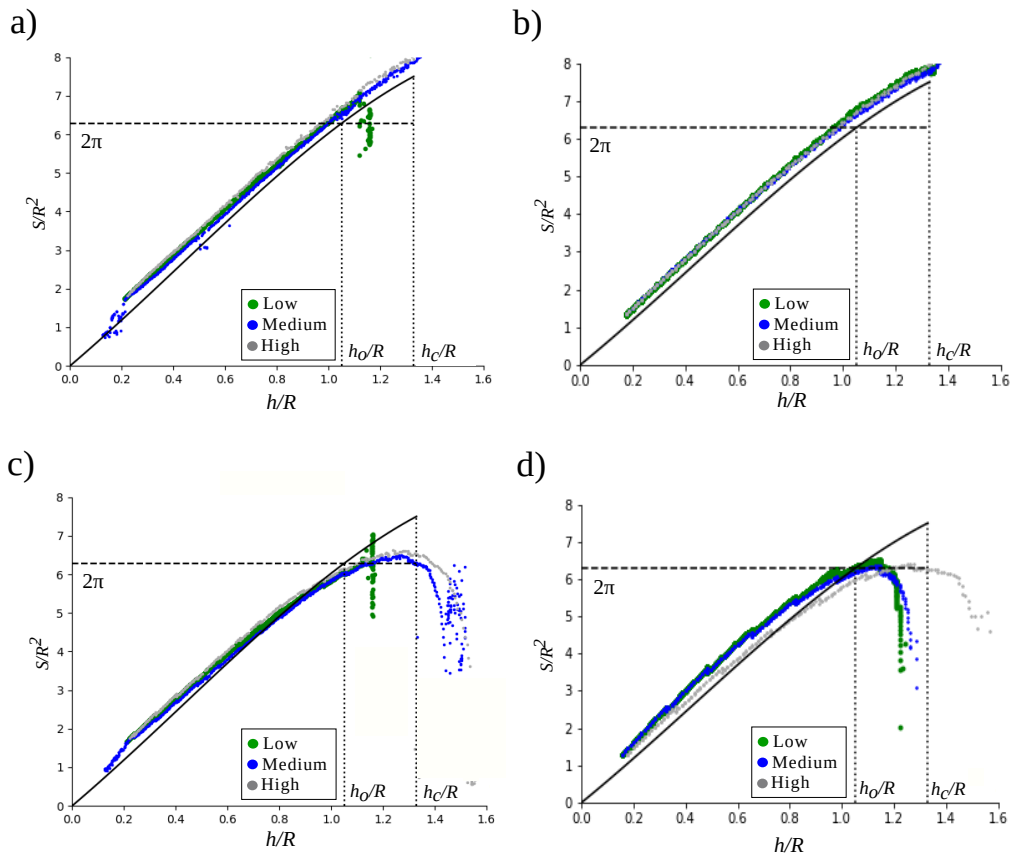

Figure 4.12 *Evolution of the surface area S/R^2 from* ***a,b:*** *equation based and* ***c,d:*** *image based as a function of distance h/R of* ***left column:*** *bare and* ***right column*** *dispersion films, stretched at low, medium and high velocity. The solid black line is the surface area of the minimal surface. The horizontal dashed line is the surface area of the end ring. The vertical dashed lines show phase divison, h_o/h is the distance at which the surface area of a film with minimal surface equals the surface area of the end rings and the critical distance h_c/h at which theoretically films cannot exist more. R is taken to be 9.25 mm.*

the area of the end rings, whereas the area of films stretched at medium and high velocities carry on increasing for longer distances before they reach a maximum at a distance ≈ 1.28, where eventually the area of the films drops.

Image based surface areas from dispersion films stretched at low and medium velocities (see Figure 4.12d) increase very much like to those found from the fitted equation at short and intermediate distances. However, contrary to equation based areas, they drop when they reach the area of the end rings at $h/R \approx 1.05$. The surface area of films stretched at high velocity is significantly lower than films stretched at low and medium velocities for all distances. This is interresting because we do not observe such differences between radii (see Figure 4.9b). The

film reaches the area of the end rings later, with a considerably large delay in the drop compared to films stretched at a lower velocities.

Hydrogel Films - 2NapFF

As mentioned above, films prepared with calcium chloride collapsed at very short distances. For this reason, the results presented next will be from films prepared with magnesium sulfate and sodium chloride.

Surface areas found from the fitted equation for hydrogel films are similar to those descrived above for bare and dispersion films. These areas increase linearly for all the films and stop when they approach the critical distance. No significant differences were observed between these areas when films are prepared with magnesium sulfate or sodium chloride at different concentrations or the films are stretched at different stretching velocities (see Figures 4.13, 4.14 and A.2b,d,f). Conversly, image based surface areas did not increase at the same rate and to the same extent for films stretched at different stretching velocities. The area of films stretched at low velocity (see Figure 4.13a,c,e) increased faster and to a larger extent than the area of films stretched at medium and high velocities (see Figures 4.14a,c,e and A.2a,c,e). The area of films stretched at medium and high velocity increases more slowly at intermediate and long distances and deviate from the area of the minimal surface at a shorter distance (≈ 0.65) than films stretched at low velocities. The area of hydrogel films prepared at 1 mg/mL sodium chloride, stretched at a low velocity, reaches its maximum far before this reaches the area of the end rings. Similarly, the areas of films stretched at medium and high velocities barely reach the area of the end rings before they rupture.

Similarly to bare and dispersion films from above, the rate at which image based surface areas increases, slows down with distance. This is more marked in films prepared with sodium chloride at low salt concentrations or with increasing the stretching velocity. Even more disconcerting are the differences between image and equation based surface areas. These results start to deviate at intermediate distances and grow with increasing distance. While equation based areas keep increasing lenearly when they overtake the area of the end rings, image based surface areas drop when they reach or are near this point.

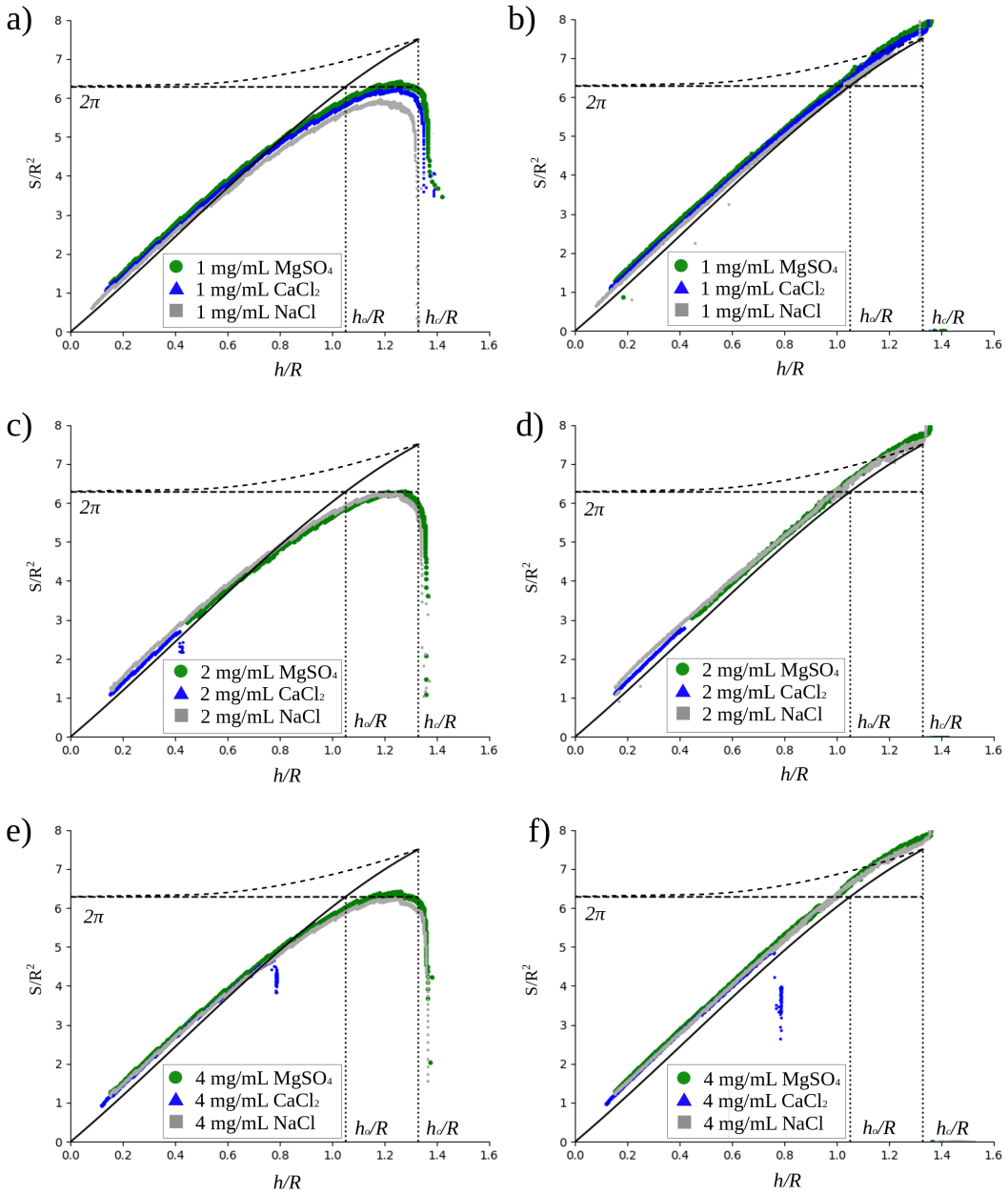

Figure 4.13 *Evolution of the surface area S/R^2 calculated* ***left column:*** *numerically and* ***right colum:*** *analytically as a function of distance h/R of dipeptide hydrogel films prepared with different salts (magnesium sulfate, calcium and sodium chloride) concentrations (1, 2 and 4 mg/mL), stretched at low velocity. The solid black curve is the surface area of the stable minimal surface. The dashed black curve is the surface area of the unstable minimal surface. The horizontal dashed line is the surface area of the end rings. The vertical dashed lines show from left to right: the division between the bulk and the film phases, the distance at which the surface area of a film with minimal surface equals the surface area of the end rings (h_o/h) and the critical distance at which theoretically films cannot exist more (h_c/h). R is taken to be 9.25 mm.*

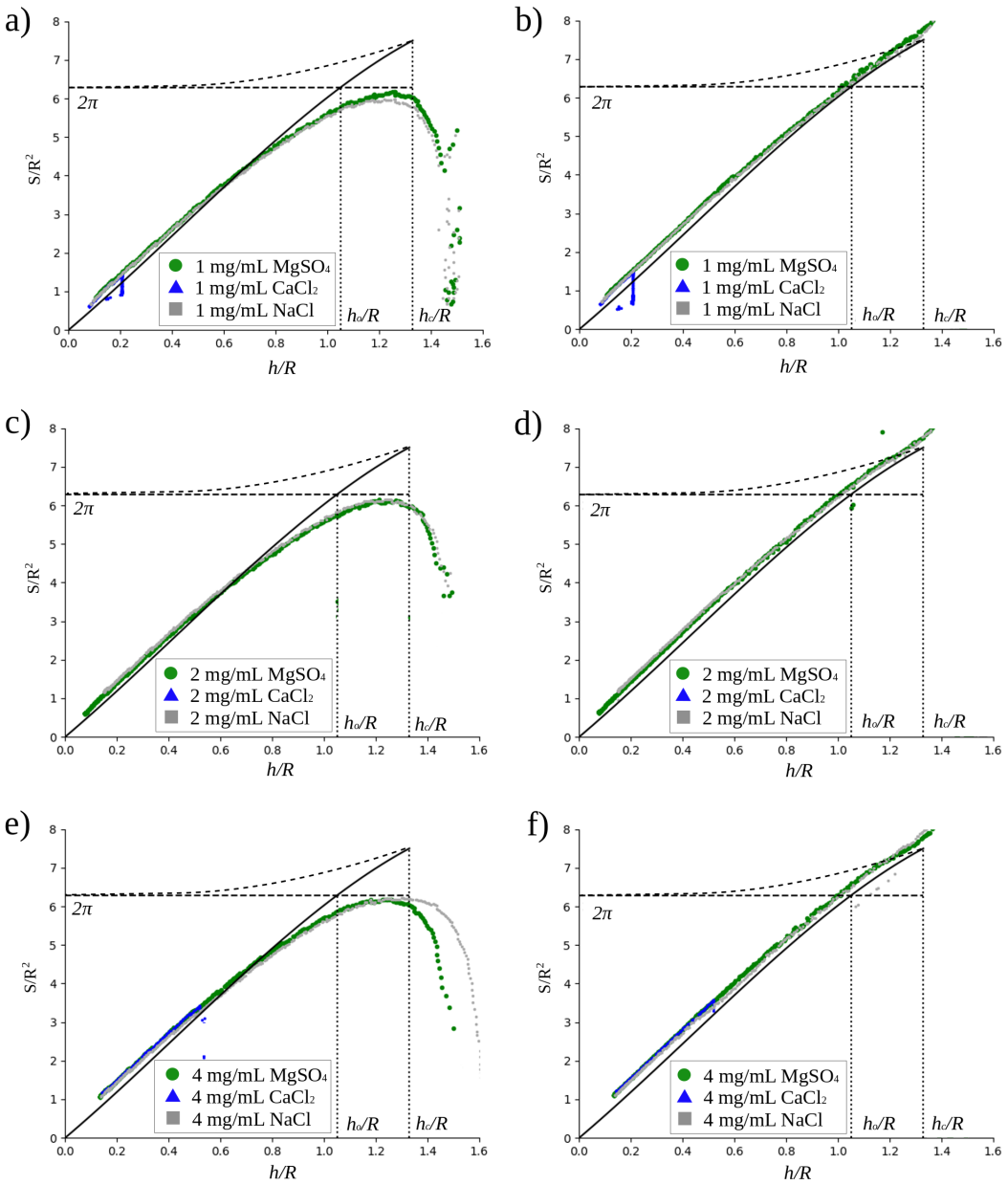

Figure 4.14 *Evolution of the surface area S/R^2 calculated* ***left column:*** *numerically and* ***right colum:*** *analytically as a function of distance h/R of dipeptide hydrogel films prepared with different salts (magnesium sulfate, calcium and sodium chloride) concentrations (1, 2 and 4 mg/mL), stretched at high velocity. The solid black curve is the surface area of the stable minimal surface. The dashed black curve is the surface area of the unstable minimal surface. The horizontal dashed line is the surface area of the end rings. The vertical dashed lines show from left to right: the division between the bulk and the film phases, the distance at which the surface area of a film with minimal surface equals the surface area of the end rings (h_o/h) and the critical distance at which theoretically films cannot exist more (h_c/h). R is taken to be 9.25 mm.*

Hydrogel Films - ThNapFF

Measurements for hydrogels made of ThNapFF, were carried out in the same manner as for hydrogels made of 2NapFF. Likewise, these were prepared with magnesium sulfate at different concentrations and stretching velocities. The surface area for hydrogel and dispersion films is shown in Figure 4.15 as a function of distance. Image based surface areas increase at a similar rate and to the same extent for films stretched at medium and high velocities (see Figure 4.15c,e). The area of these films reaches the area of the end rings at a distance of ≈ 1.25 before this drops. At low velocity, image based surface areas vary with salt concentration (see Figure 4.15a). While the area of films prepared at low salt concentration rose higher than the area of the end rings, the area of films prepared at higher salt concentrations dropped before they reached this point. These differences in areas of films stretched at low velocity are also observed in equation based surface areas, where the slope of the area from films prepared at low salt concentration is slightly steeper than the areas of hydrogel films prepared at higher salt concentrations (see Figure 4.15b). At higher stretching velocities, equation based areas clump together as we observed before in films made of 2NapFF.

These results indicate that dipeptides fibres as well as the type and concentration of salt or the velocity at which films are stretched, had an effect on the rheological properties of the films. Cross-linked dipeptide fibres in hydrogel films, do not have the same degree of freedom as water molecules in bare films or fibers in dispersion films. Certainly this has effects on the properties of hydrogel films, not allowing them to elongate as fast as bare or dispersion films do at intermediate and long distances, hence dalying the distance at which these reach the area of the end rings. This is even more marked for hydrogels stretched at higher velocities. Nonetheless, hydrogel films collapse at similar separations compared to bare films, but these have a lower surface area, most probably caused by a higher resistance to elongate. Lastly, as for films made of 2NapFF, we observe drastic discrepancies between image and equation based surface areas starting at intermediate distances and pregressively becoming worse at long distances.

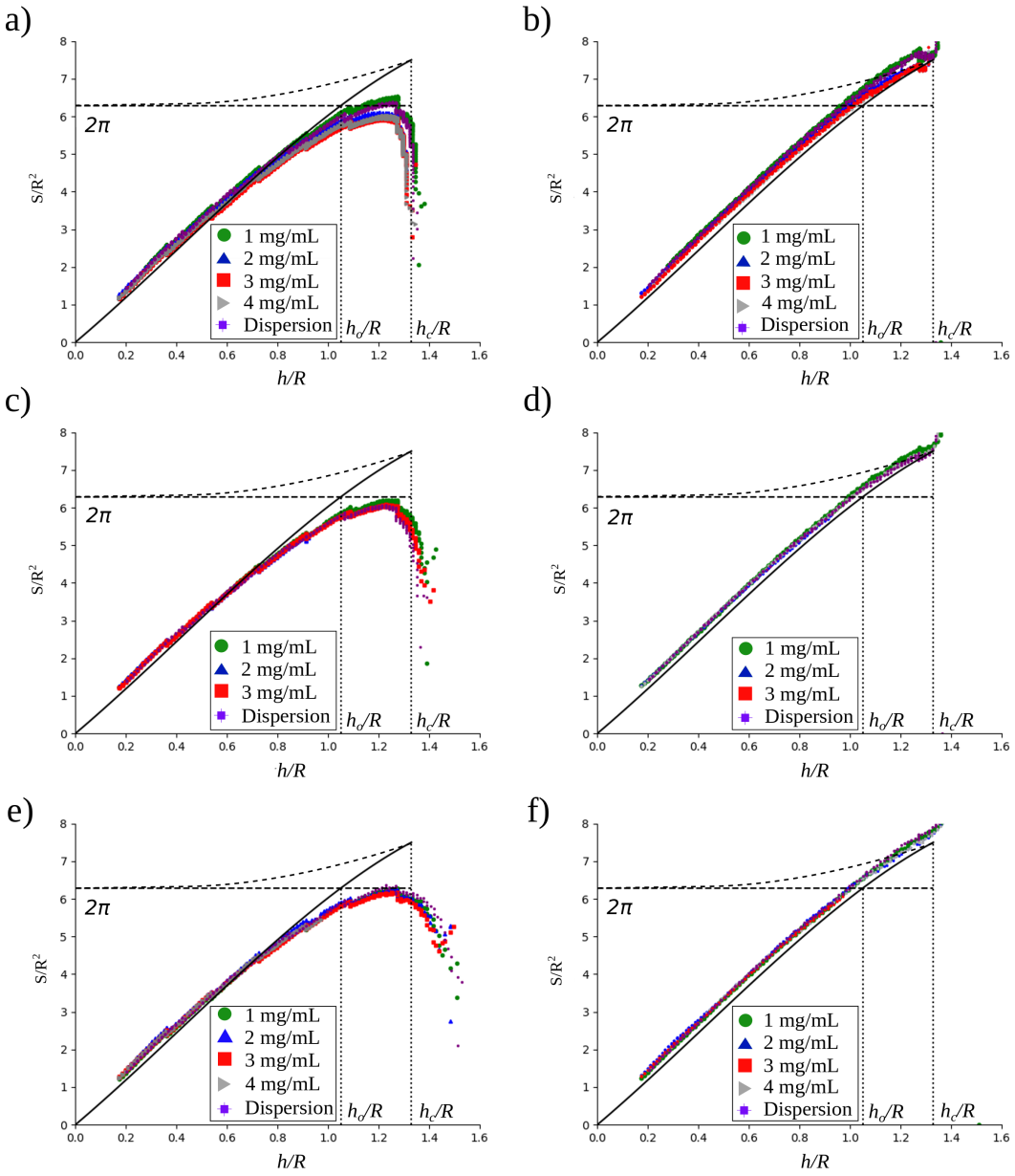

Figure 4.15 *Evolution of the surface area S/R^2 calculated* ***left column:*** *numerically and* ***right column:*** *analytically as a function of distance h/R of hydrogel films made of ThNapFF, prepared at 1, 2, 3 and 4 mg/mL magnesium sulfate, stretched at* ***a,b:*** *low,* ***c,d:*** *medium and* ***e,f:*** *high velocity. The solid black curve is the surface area of the stable minimal surface. The dashed black curve is the surface area of the unstable minimal surface. The horizontal dashed line is the surface area of the end rings and the vertical dashed lines are the the critical distance h_c/h at which films cannot exist any more and h_o/h is the distance at which the surface area of the films equals the surface area of the end rings. R is taken to be 9.25 mm.*

Discrepancies between image and equation based surface areas

We cannot ignore the differences between image and equation based surface areas. While areas found with the equation increase linearly until they reach the critical distance ($h/R = 1.33$), image based areas increase more slowly at intermediate and long distances, until they reach a maximum near the area of the end rings before they drop back to zero. In order to investigate this disagrement, we fit a best fit curve to the extracted film profile with the equation of a catenary expressed as

$$Y_i = Y_L + B(cosh((X_i - X_L)/B) - 1) \tag{4.4}$$

where X_i is the horizontal coordinate (*distance*), Y_i is the height of the point, Y_L is the height of the lowest point of the curve (radius at the mid-plane of the film) and B is a coefficient describing the shape of the curve.

The root mean square error (RMSE) from the regression line and the data points of a hydrogel film prepared at 1 mg/mL magnesium sulfate, stretched at low velocity is depicted in Figure 4.16 (for the rest of the hydrogel films see Appendix A). The RMSE grows exponentially but overall it is very low, showing a good

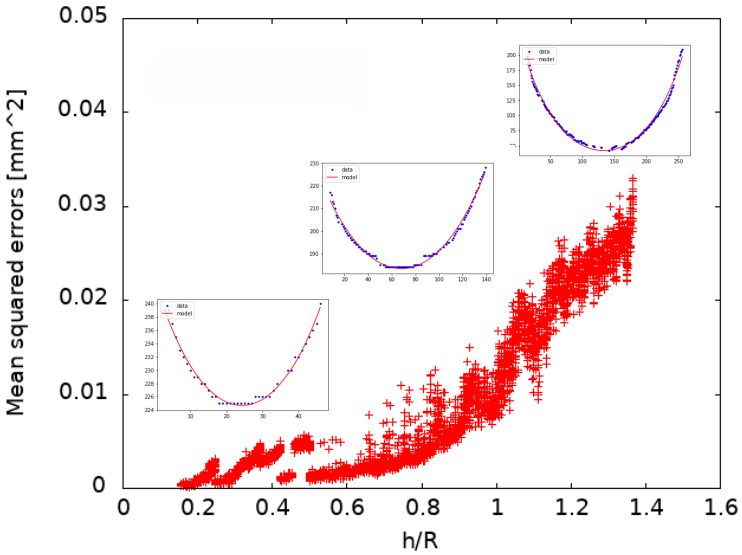

Figure 4.16 *Mean squared error from from the regression line and the data points of a hydrogel film prepared at 1 mg/mL magnesium sulfate stretched at low velocity. Insets show the data points with the fitted line of three random frames chosen at short, intermediate and long distances. R is taken to be 9.25 mm.*

fit for all distances. Likewise, the rest of the films show a good fit as well, which means that the discrepancies between equation and image based areas are not caused by the films becoming distorted at intermediate and long distances. Interestingly, we observe a pattern in some of the figures. While RMSE is close to zero at short distances, at intermediate distances this starts to take off and increases with distance. The distance at which RMSE starts to take off, turns out to be the same distance at which image based surface areas begin to increase more slowly and deviate from equation based areas. Although the overall fit is excellent, we think that the increase in RMSE at intermediate and long distances, may be caused by the film getting increasingly distorted near the end rings, where the film attaches to the apparatus.

These results are indicative of an urderlying discrepancy between the model and image based points, where Equation 4.3 does not capture the underlying trend of the data points at long distances. Image and equation based surface areas agree at short distances but these start to deviate at intermediate distances, until eventually they diverge as the film begins the transition to the end rings.

4.5 Evolution of the ratio of the axial radius profile to the radius at the mid-plane of the film R_z/a as a function of distance h/R

Minimal surfaces in soft materials originate from the competition between surface tension, that reduces the area of the interface at the expense of increasing its curvature and the elasticity of the film that resists deformation [153]. In this section, we further investigate the dynamic response of the films by measuring the ratio of the axial radius to the catenoid radius R_z/a as a function of distance. Figure 4.17 shows a visual representation of the evolution of the axial radius profile R_z and the radius at the mid-plane of the film a of a hydrogel film formed between end rings. At the starting position, the sides of the hydrogel are straight and the circumference at the air-fluid interface has not been formed yet (not shown). Eventually the lower ring is set in motion and the circumference forms while the radius a decreases slightly (see Figure 4.17a). As the distance between the end rings increases, the axial radius R_z grows faster than a decreases (see Figure 4.17b,c). Inmediately after, the films begin the transition to the end rings

and shrink more rapidly. This causes the radius a to decrease extremely fast and R_z to decrease slowly before the film collapses (see Figure 4.17d).

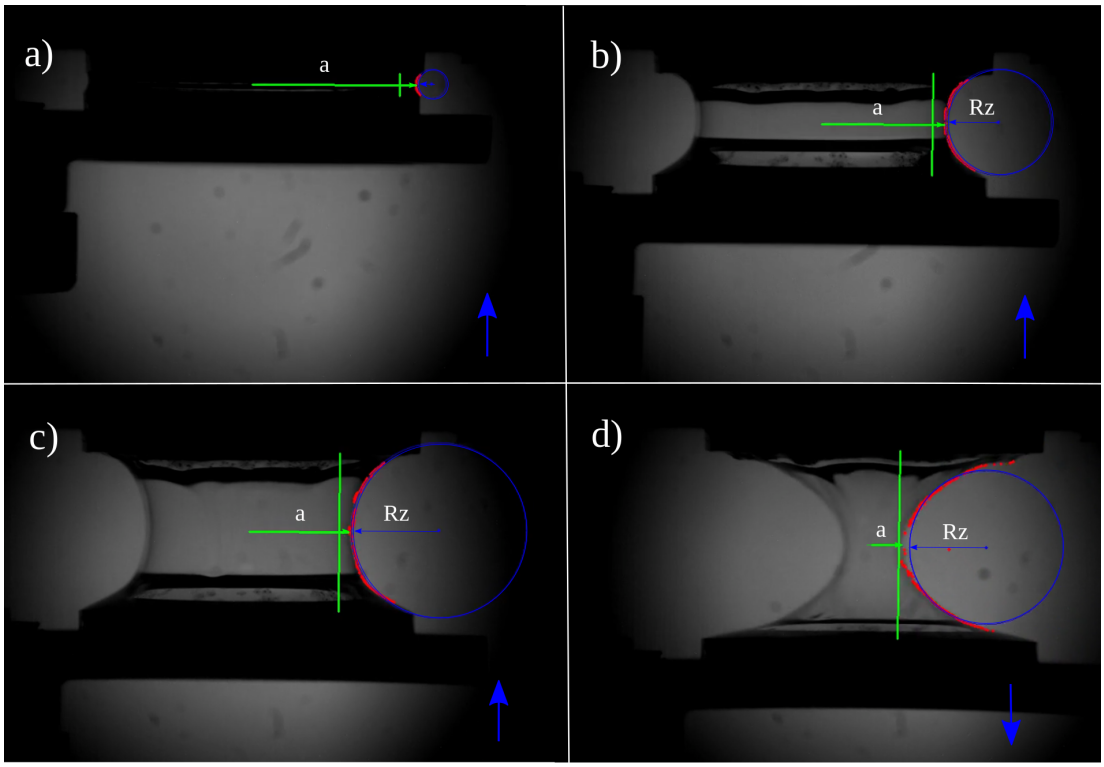

Figure 4.17 *Evolution of the axial radius profile R_z and the radius at the mid-plane of the film a of a hydrogel film formed between end rings. The blue arrow at the bottom right corner indicates if the axial radius Rz increases or decreases when the film is at that distance.*

Films - Water and Dispersions

The evolution of the ratio R_z/a measured as a function of distance for a series of bare and dispersion films stretched at different stretching velocities is shown in Figure 4.18. The ratio R_z/a for bare films increases evenly at short and intermediate distances (see Figure 4.18a). This increases slightly faster at h/R 1.1 due to the radius a decresing rapidly when the films become unstable. At a distance of approximately 1.5, R_z/a increases dramatically due to the radius a approching zero. The stretching velocity at which bare films were stretched did not have any influence on the ratio R_z/a.

Dispersion films showed a slightly different trend (see Figure 4.18b). While the ratio R_z/a increased evenly at short and intermediate distances for bare films,

for dispersion films it starts to rise faster at intermediate distances. At half way between intermediate and long distances ($h/R \approx 1$), R_z/a increases more slowly until it reaches a maximum distance were it rose sharply. The stretching velocity at which dispersion films were stretched did not have an effect on the ratio R_z/a until the very end where films are collapsing.

It is worth noting that, the ratio R_z/a is equal to 1 at a distance ≈ 1.4 in bare films. Interestingly, a ratio of 1 occurs at the same distance at which the radius of the films is 0.55, where films become experimentally unstable (see Figure 4.9a). It seems that this could be a good indicator to determine the point at which films become unstable; however, this seems not to be the case for dispersion films. In fact, when the ratio approaches 1 in dispersion films, these are at a distance of 1.2, which is far from the distance at which the films become experimentally unstable (see Figure 4.9b).

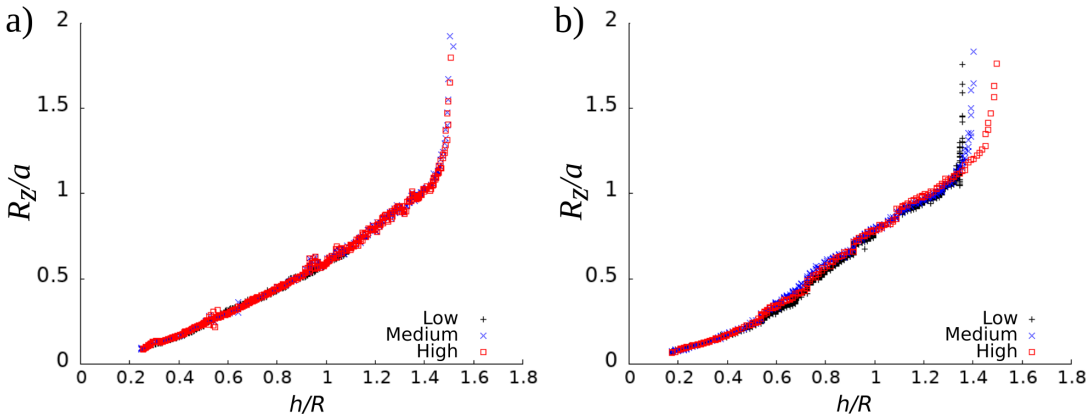

Figure 4.18 *Evolution of the ratio of the axial radius of the curvature to the radius of the catenoid R_z/a as a function of distance for* ***a:*** *bare films and* ***b:*** *dispersion films stretched at different stretching velocities. R is taken to be 9.25 mm.*

Hydrogel Films - 2NapFF

The ratio R_z/a for hydrogel films made of 2NapFF prepared with different salts and concentrations, stretched at different velocities is shown in Figure 4.19. Just as the ratio of disperson films, R_z/a increases faster at intermediate distances for all hydrogel films; this is more noticeable in some films than in others. In the case of films prepared with sodium chloride at low and high salt concentrations, the increase in R_z/a is more marked than for films prepared at intermediate salt concentrations. On the contrary, the bump in the ratio R_z/a is more marked in

films prepared with magnesium sulfate at intermediate salt concentrations and this vanished in films prepared at low and high salt concentrations. Similarly to dispersion films, hydrogel films become unstable at a ratio R_z/a higher than 1 and it is salt concentration and velocity dependent.

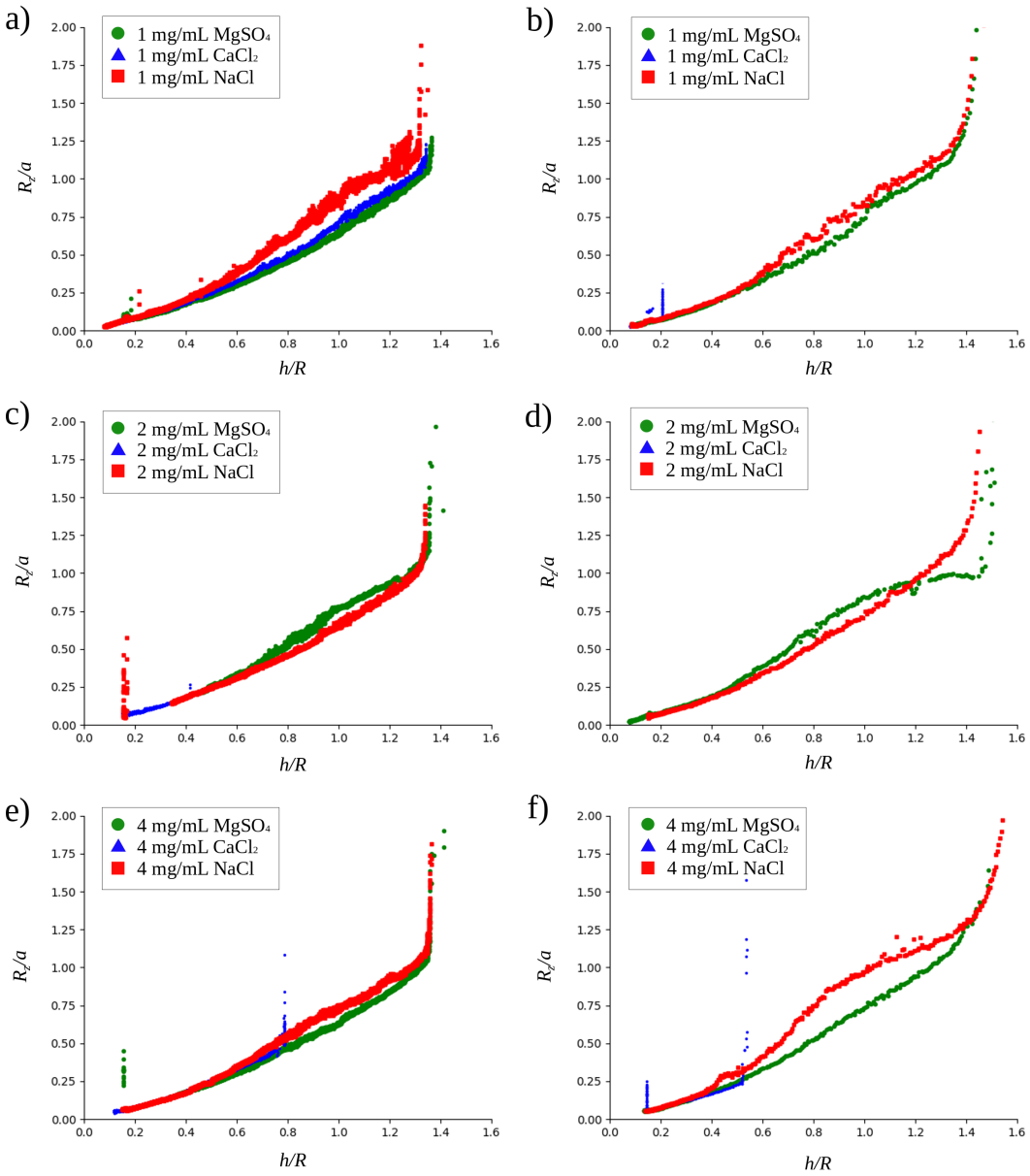

Figure 4.19 *Experimental evolution of the ratio of the axial radius profile to the radius at the mid-plane of the film R_z/a as a function of distance h/R of hydrogel films prepared with different salts (magnesium sulfate, calcium and sodium chloride) concentrations (1, 2 and 4 mg/mL), stretched at* ***left column:*** *low and* ***right column:*** *high velocity. R is taken to be 9.25 mm.*

Hydrogel Films - THnapFF

The ratio R_z/a for hydrogel films made of ThNapFF, prepared with magnesium sulfate at different salt concentrations and stretched at different velocities is depicted in Figure 4.20. R_z/a increases faster and to a larger extent with increasing the salt concentration and with velocity. At low an medium stretching velocities, R_z/a increases faster at intermediate distances for films prepared at 3 and 4 mg/mL; films prepared at 2 mg/mL showed the lowest ratio of all films and stretching velocities.

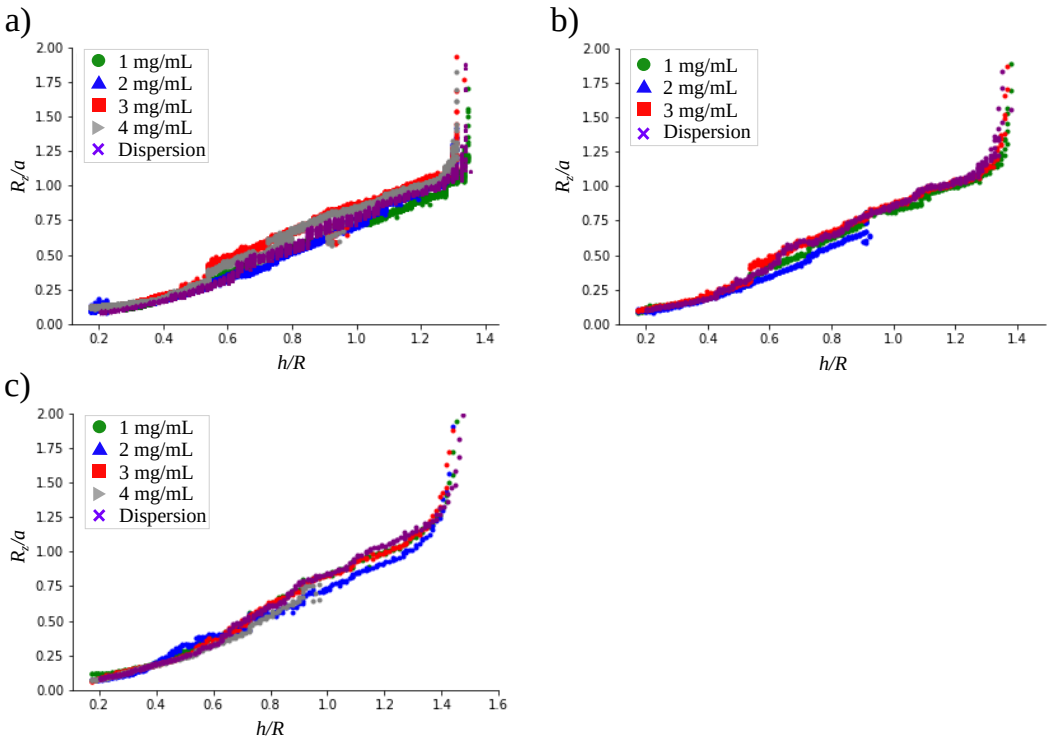

Figure 4.20 *Experimental evolution of the ratio of the axial radius profile to the radius at the mid-plane of the film R_z/a as a function of distance h/R of hydrogel films made of ThNapFF, prepared at 1, 2, 3 and 4 mg/mL magnesium sulfate, stretched at* ***a:*** *low,* ***b:*** *medium and* ***c:*** *high velocity. R is taken to be 9.25 mm.*

By looking at these figures, it is challenging to rationalize these results. First, we need to think that an elastic film (bare film), should have an homogeneous increasing R_z/a, so that the film is stable. This is because for an elastic film hanging between two coaxial planar disks of identical diameter, the film will form a symmetric catenoid. As the distance between the end rings increases, the film trying to minimize its energy will decrease its surface area from the weakest point, the mid-plane of the film. As the film does that, the radius will decrease linearly, with distance. As the catenoid grows with distance, the axial radius R_z, will also

increase linearly for stable films. Now, when the end rings reach the distance at which films become unstable (theory ≈ 1.05 and experimentally ≈ 1.3), the radius of the catenoid film starts to decrease at a faster speed and the axial radius stops growing and begin to decrease slowly.

In next section we investigate the images of the catenoid films in more detail and explain these results.

Analysis of the uneven R_z/a

To gain a better understanding of these curves, we studied carefully the images of a sample with a distinctive bump in the ratio R_z/a and explained these by dividing a curve in four regions (see Figure 4.21).

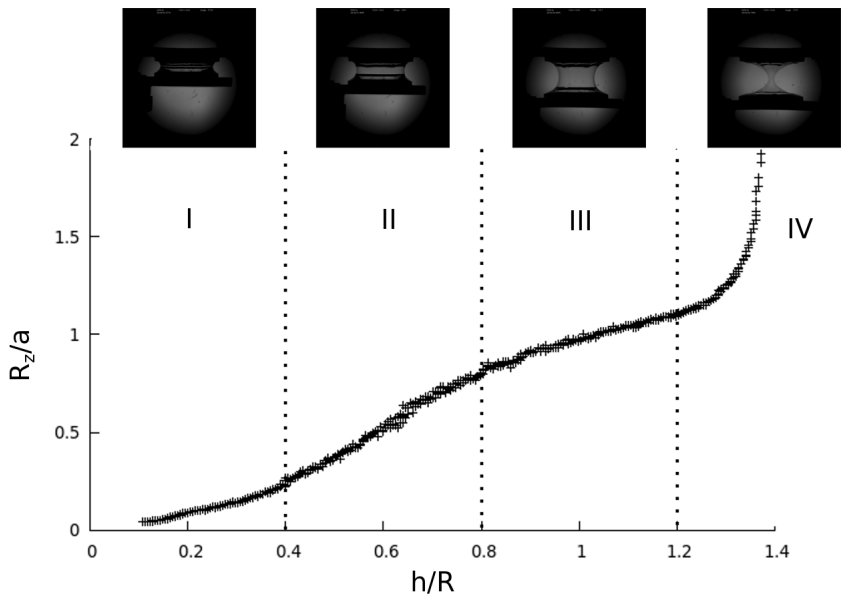

Figure 4.21 *Evolution of the ratio of the axial radius R_z/a with increasing distance of a hydrogel film prepared at 4 mg/mL sodium chloride, stretched at high velocity. In region I, the film has yet not been formed and the hydrogel that is being pulled down by the lower ring, gets compressed from the middle and the radius a decreases slightly. In region II, the new born film resists the compression force in the middle, hence does not deform yet. In region III, the film starts to deform from the middle because the distance between the rings increases and the film cannot extand the compression force further. In region IV the film reaches the critical distance ($h_c \approx 1.33$) and this becomes unstable and collapses. R is taken to be 9.25 mm.*

- Region I: the film has not formed yet in this region. As the distance between the rings increases, the stretched sample tries to minimise its surface area and this makes the sample to bend from the weaker point, the mid-plane of the film. This forms the curvature profile at the air-water interface with an axial radius R_z smaller than the radius a. The axial radius R_z increases in this region, whereas the ratio a decreases. As a consequence of this, the ratio R_z/a increases slowly in this region.

- Region II: in this region we observe the first alteration in the ratio R_z/a at a distance of 0.4. While bare films form symmetric catenoids right from the begining, dispersion and hydrogel films show a cylindrical shape at first instead, hence causing the radius a to decrease more slowly than in bare films. This is because, unlike water molecules with higher freedom to diffuse through the sample homogeneously as this stretches, cross-linked fibers cannot pass each other and therefore these filmsexhibit a less homogeneous increase in R_z/a. A second increase in R_z/a is observed at around 0.6 for some hydrogel films. Apparently, this second fluctuation is caused by a partial decohesion between the sample and the end rings (we will discuss this later). It is worth mentioning though, that the second alteration is caused by a faster increasing axial radius R_z in this region, while the radius a seems to decrease at the same speed as for films without the characteristic bump.

- Region III: as the distance between the end rings increases, is probably that the surface tension overtakes the film strength and these start to bend from the mid-plane again. This causes the radius a to decrease faster than in the second region, while the axial radius R_z keeps increasing at the same rate, hence the slower increase in the ratio R_z/a seen in this region. Morever, the axial radius R_z reaches its maximum in this region.

- Region IV: in this region films become unstable. Due to films shrinking rapidly the radius a drops drastically. Despite the axial radius R_z in this region also decreases, this decreases slow, hence the sharp increase in the ratio.

The second alteration observed in region II is investigated by studying the frames of two hydrogel films found in this region; one film with a linear response and

a second film with a nonlinear response. Figure 4.22 shows the hydrogel film from Figure 4.21, prepared at 4 mg/mL sodium chloride and stretched at high velocity with an uneven ratio R_z/a (Figure 4.22a,b) and a film prepared at 2 mg/mL sodium chloride stretched at low velocity with a more even ratio (Figure 4.22c,d), both at a similar distance between the end rings. Despite both hydrogels films having the same radius a at this distance, the one with the uneven ratio R_z/a (Figure 4.22a,b) shows a significant higher axial radius R_z than the film with a smooth R_z/a (Figure 4.22c,d). Data from more frames can be found in Table 4.1.

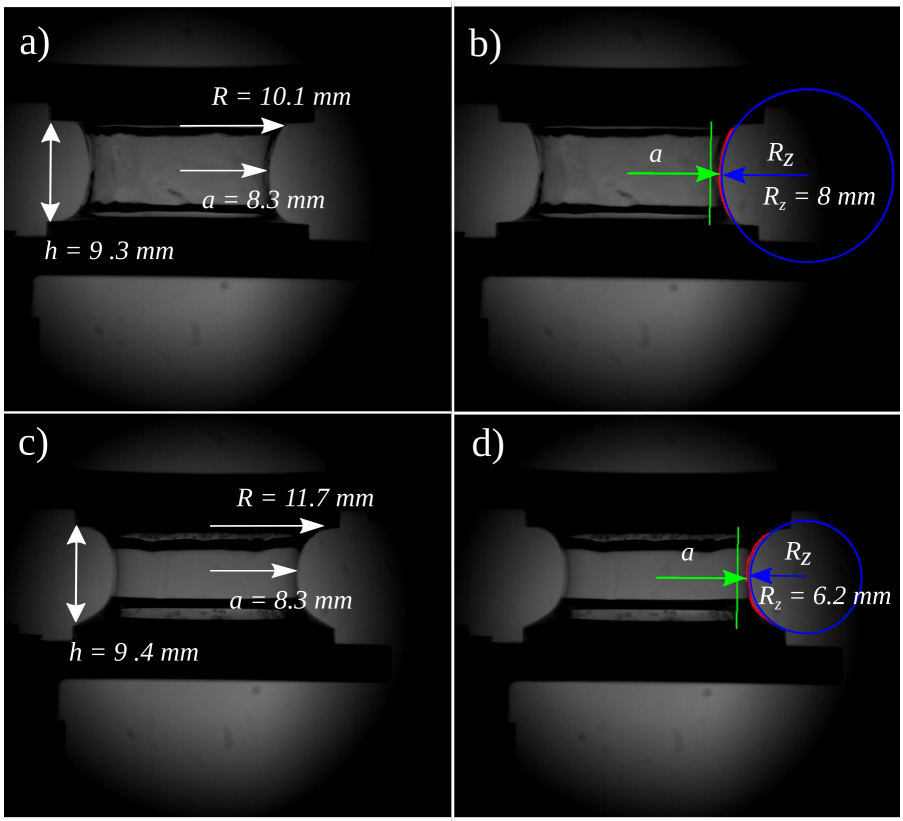

Figure 4.22 *Slip-stick effect for dipeptide hydrogel films prepared at* ***a,b:*** *4 mg/ml sodium chloride, stretched at high velocity and at* ***c,d:*** *2 mg/ml sodium chloride, stretched at low velocity.*

While studying these frames, we noticed an elastic instability near the end rings, where the film is attached to the apparatus, causing the radius of the end rings R to decrease (see Figure 4.22a,b). As shown by the series of different uneven ratios (see Figures 4.19, A.3 and 4.20), this instability is more marked for some hydrogel films than for others. A decrease in R, changes the curvature at the air-fluid interface where we fit the circumference. The smaller the radius

R, the bigger becomes the circumference that we fit and therefore its radius (R_z). Partial decohesion of fluid filaments from the end rings, has been observed before in viscoelastic polymer solutions in extensional flow ([154]). The authors observed that elastic instabilities only occured in tests conducted with the most elastic fluids and at high strain rates. These instabilities were attributed to an axisymmetry-breaking meniscus instability in the heterogeneous region of the highly deformed fluid, near the rigid endplate.

Looking at the ratio R_z of pure water films (Figure 4.18a) we observe that the ratio R_z/a does not change with velocity. However, this is not the case for dispersion films (Figure 4.18b), where dipeptide fibres go from being dispersed in the bulk phase to occupy a more constrained region such as the interfacial film. Evidently, dipeptides influence the properties of intefaces, that we try to characterise and understnad by plotting the ratio R_z/a as a function of distnace. Figure 4.18 show three distinctive regimes; the first regime could well be the critical point at which samples become films. The second regime, where films are stable, gives an indication of the film properties. A faster incrase in the ratio R_z/a means that the film deforms faster and hence is weaker. On the contrary, films with a lower ratio for the same distances, is due to films deforming less and hence being stronger, or more elastic. Finally, the last regime tell us the point at which films become unstable, which for dispersion films is velocity dependent.

In next section we find the radius of the end rings R for each film and link these to the results from R_z/a figures.

Table 4.1 *Values of R_z, a and h of hydrogel films prepared with 2 and 4 mg/mL sodium chloride, stretched at different stretching velocities shown in Figure 4.22. In blue are highlighted h and a from frames with similar values. In orange is highlighted the axial radius R_z of these frames to show the difference between both samples. In bold are the specific values of frames shown in Figure 4.22.*

	2 mg/mL			4 mg/mL		
Frame No.	*Rz* (mm)	*a* (mm)	*h* (mm)	*Rz* (mm)	*a* (mm)	*h* (mm)
50	0.7	11.8	1.4	1	10.9	2.1
75	0.7	11.8	1.5	1.3	10.5	2.6
100	0.8	11.6	1.5	1.8	10	3.5
125	0.8	11.3	1.8	2.8	9.7	4.3
150	1.1	10.9	2.3	3.5	9.4	5.5
175	1.4	10.5	2.9	5.2	9.2	6.6
200	1.8	10.2	3.6	7.1	8.9	7.8
225	2.4	10	4.5	**8**	**8.3**	**9.3**
250	3.2	9.6	5.5	8.2	7.4	11.1
275	4	9.2	6.6	7.7	6.3	12.6
300	5.2	8.8	7.8	7.1	4.7	13.8
325	**6.2**	**8.3**	**9.4**	6.4	1.1	14.7
350	6.8	7.5	10.8	-	-	-
375	7	6.3	12.1	-	-	-

Elastic instabilities

Extracting the coordinates of the films near the end rings can be challenging. An alternative approach to find the radius R at this point is by rearranging Equation 4.2.

$$R = acosh^{-1}\left(\frac{h}{2a}\right) \tag{4.5}$$

The mean radius R of dispersion and hydrogel films made of 2NapFF and ThNappFF prepared with different salts and concentrations, is shown in Figure 4.23. The mean radius R is larger in films stretched at high velocity and tends to decrease with velocity. In the case of hydrogel films made of 2NapFF and prepared with magnesium sulfate, R is slightly smaller for films prepared at 2

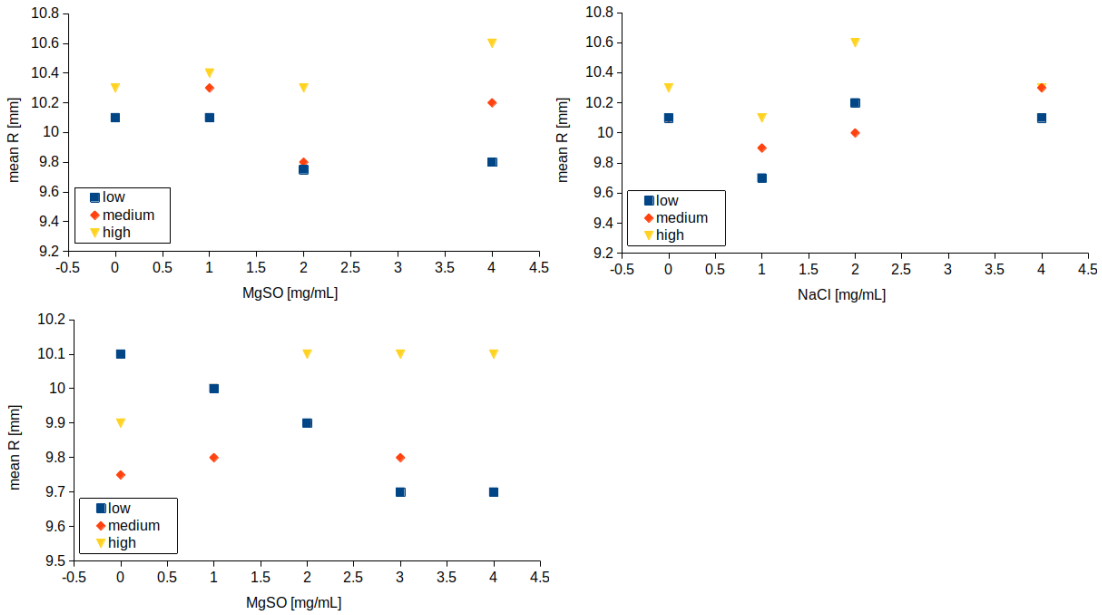

Figure 4.23 *Radius R found with Equation 4.5 for a set of hydrogel films made of 2NapFF prepared with* ***a:*** *magnesium sulfate,* ***b:*** *sodium chloride and films made of ThNapFF prepared with* ***c:*** *magnesium sulfate at 1, 2, 3 and 4 mg/mL, stretched at different stretching velocities. Where the points at 0 mg/mL are the dispersion films at different stretching velocities.*

mg/mL and increases for films prepared at 1 and 4 mg/mL (Fsee igure 4.23a), which is consistent with the ratio R_z/a from Figures 4.19 and A.3. On the other hand, the mean radius R increases for hydrogel films made of 2NapFF prepared at 2 mg/mL sodium chloride, whereas it decreases for films prepared at 1 and 4 mg/mL (see Figure 4.23b), which again is consistent with the data shown in Figures 4.19 and A.3. In the case of hydrogels films made of ThNapFF stretched at low velocity, the radius R decreases with increasing the concentration of salt until this plateaus at high salt concentrations; this peaks at a concentration of 2 mg/mL for films stretched at medium velocity, which again agree with the data of the ratio shown in Figure 4.20a,b.

Elastic instabilities were observed in some hydrogel films and were not observed in other hydrogel films, bare films and dispersion films. Partial decohesion is often larger in multi-component systems than in single-components [155]; however, this does not imply that slip did not occur in all samples, as the slip length may be just as small as few nanometers. In fact, slip may be inevitable on microscopic and molecular scale [156, 157]. Partial decohesion was observed to be higher in the upper ring than in the lower ring, which implies that gravitational force might be a contributing factor to the formation of a depletated region between the sample

and the end ring [158, 159]. A depleted layer could cause a drop in the viscosity in this region and hence slip enhancement. Instabilities (smaller radius R) were more pronounced in films stretched at low and medium velocity (see Figure 4.23). This is particularly true for shear-thinning fluids due to the fact that the slip at large deformations is reduced by a drop in the bulk viscoisty at these regimes [160, 161]. A factor that may initiate the onset of a slip effect, is the properties of the fluid. In the case of complex systems such as gels, instabilities may depend on the concentration, the particle size and shape, the molecular weight and the concentration of salt ([162–167]).

Films prepared with magnesium sulfate at 2 mg/mL and sodium chloride at 1 and 4 mg/mL showed a non-monotonic trend in the ratio R_z/a with distance, characteristic of a partial decohesion effect between the sample and the end rings. Shear flow near the end rings, where the film is attached to the end ring, makes the hydrogel contact point move towards the inner edge of the ring causing the radius R to decrease and hence revealing the distortions on the curves. It is well established that the elasticity of salt induced hydrogels can be tailored by a small change in the concentration of salt [150]. In fact, the storage modulus of hydrogels prepared with calcium chloride has been observed to reach a maximum at a ratio of calcium:carboxylic acid of 2:1 [2]. For this reason, the instability observed in hydrogel films prepared with magnesium sulfate at 2 mg/mL, may very well be caused by an increase in the film elasticity at such concentration. In a hypothetical scenario like this, where the concentration of salt is favourable, the diameter of the fibres as well as the number of cross-links could increase, thus making it more difficult for the fibres to stretch and eventually align. On the contrary, we observed instabilities at 1 and 4 mg/mL for films prepared with sodium chloride, whereas at 2 mg/mL these vanish. While we attribute this slip effect to the strength of the film in the case of films prepared with magnesium sulfate, we think that for films prepared with sodium chloride is for different reasons. The reason for this is that in the case of magnesium sulfate, the samples did gel, whereas for those prepared with sodium chloride did not. This could be due to a phenomenon such as the ‘tackiness’, but for a more solid explanation we believe that more experiments are needed to explain the lack of instabilities in films prepared at 2 mg/mL, specially after seeing these in films prepared at 1 mg/mL.

4.6 Conclusions

In this chapter we have investigated a series of hydrogel films with a new extensional device that provides a means of probing the dynamic response of viscoelastic films during transient uniaxial elongation. The results of these experiments should be considered to be preliminary because only a few experiments were undertaken. Having said that, the dynamic response of hydrogel films can be described. Hydrogels turned into elastic solid films that collapsed at short distances when prepared with calcium chloride. By contrast, hydrogels prepared with sodium chloride developed into extremely viscous films that did not burst; they instead, formed a thread that broke under capillarity. Somewhere in between, were the viscoelastic films made of hydrogels prepared with magnesium sulfate, with a non-monotonic trend dependence of the film strength on salt concentration. This effect was observed in hydrogel films prepared at intermediate concentrations by the increase in the ratio R_z/a first and a partial-decohesion between the hydrogel and the end rings later on. Although, this phenomenon was also oberved in films prepared with sodium chloride, we could not reach a solid conclusion of why the instabilities were observed in films prepared at low salt concentrations and not in films prepared at 2 mg/mL. Last, we observe a large disagreement between image and equation based surface areas at intermediate and long distances. While equation based surface areas keep increasing after these are overtaken the area of the end rings, image based surface areas drop to zero when these are equal or near the area of the rings.

With this technique we have shown that the type of salt and the concentration used affects the mechanical properties of the interfaces. The radius a varies between catenary interfaces stretched for the sames distances, which indicates that interfaces have different strengths. The surface area decreasing at long distances implies that interfaces become unstable and hence have reached their maximum extension distance. Furthermore, by measuring the force we would be able to calculate the stress and the extensional viscosity. By plotting the extensional viscosity as a function of time for different strain rates deformations, we can observe whether interfaces strain harden or strain soften, and determine the degree of viscoelasticity of each of them. In spite of a quite good understanding of fluid response to an impose extensional stretch, there is not much known about elongational flow behavior of emulsions. Due to their high surface area to volume ratio, interfaces in emulsions play a key role in determining the behaviour of the emulsions. Because of this, studying interfaces imposed to

extensional deformations and comparing the results to those from shear interfacial rheology, could bring new insights to the study of emulsions.

Chapter 5

Nonlinear dilatational rheology of liquid-liquid interfaces stabilized by dipeptide hydrogels

5.1 Abstract

We present the effects of salt concentration on the rheological properties of dipeptide hydrogel fibres at liquid-liquid interfaces. The interfaces were subjected to large amplitude oscillatory dilational (LAOD) deformations across a range of oscillation frequencies. Lissajous plots of pressure-strain were used for identifying apparent yield responses and for characterizing the properties of viscoelastic interfaces. We show that the rheological response of the interfaces vary significantly with salt concentration. At low and high salt concentrations, the interfaces were characterised by weak moduli; the interfaces yield first and then strain soften at low deformations. On the other hand, interfaces prepared at the highest salt concentration used showed stronger moduli but yield at low strains as well. However, the moduli for these interfaces continue to grow with increasing deformation. In between, at intermediate salt concentrations, interfaces displayed a more viscoelastic response. To fully capture the range of behaviour, we suggest a modification of the analysis to calculate the strain-stiffening ratio S used to quantify the degree of nonlinearities from Lissajous figures, so as to better reveal the presence of instant strain softening and hardening responses.

5.2 Introduction

Emulsions are multiphase systems consisting of at least two immiscible liquids: oil-in-water (O/W), water-in-oil (W/O), and oil-in-oil (O/O), with one of the phases dispersed in the form of small droplets throughout the other [169]. They are ubiquitous in many applications in science and technology. The positive increase in surface free energy gained by mixing the two immiscible liquids, makes emulsions thermodynamically unstable and hence phase separate [170]. To satisfactorily dispersed immiscible liquids, one needs a third constituent, commonly known as emulsifier. Similarly, stabilisers are incorporated to achieve "long-term" stable emulsions. These constituents will adsorbed or spread at interfaces, transforming them into more complex interfaces with properties that can have a significant effect on the overall dynamics of multiphase systems, such as emulsions and foams [171]. Such is the case that, an enormous number of papers are continuously being published each year on the dynamic properties of liquid-liquid and air-water interfaces stabilised by a wide range of constituents, including, low molecular weight (LMW) surfactants [172, 173], proteins [173, 174], lipids [175, 176], colloidal particles [24, 173, 177], mixtures of proteins and polysaccharides [178–180], asphaltenes [181] or gels [1, 182, 183].

Here, we use a dipeptide to stabilise liquid-liquid interfaces that have been introduced previously in Chapter 2. Under the right conditions, this dipeptide forms a hydrogel of fibres, from which the behaviour under fast deformations was studied in Chapter 4. In this Chapter, we use the hydrogel to prepare fibre-coated liquid-liquid interfaces and explore their properties using nonlinear surface dilatational rheology.

The study of the rheological properties of complex interfaces, involves the imposition of area (dilatational rheology) and shape (shear rheology) variations. The former involves changes in size of an interfacial area without changing its shape by sinusoidally compressing and expanding the interface [184]. The latter requires a change in shape, while the interfacial area remains the same, by either continuously or periodically shearing the interface [184]. In dilatational and shear rheology, frequency and strain sweep experiments are performed to study the behaviour of the interface. In frequency sweeps, the strain amplitude is kept constant, whereas for strain sweeps, the frequency is the one that is kept fixed. Amplitude sweeps are usually conducted as a first step to determine the critical strain value in viscoelastic materials. At small strains, the moduli component is independent of strain up to a critical strain, where the behaviour

of the interface becomes nonlinear. Once the critical strain of the interface has been defined by conducting strain sweeps, the properties of the interface can be further interrogated by applying frequency sweeps in the linear and/or nonlinear regime.

Besides frequency sweeps, in the nonlinear regime, strain sweeps are also performed to characterise interfaces with thixotropic response. Thixotropic materials are those that flow when stress is applied and become solid-like when the stress is removed. An example of thixotropic materials are ketchup, toothpaste, paints or personal care products such as creams. The network within these materials collapses when it is stressed and reforms when the stress stops. These materials are known to be time-dependent due to the time-scale being longer for the structure to build up compared to the structure breaking down. As a consequence of the time-scale difference between the two events, the surface pressure does not follow the same path when strain is applied to interfaces compared to when it is removed, thus making strain sweeps in the nonlinear regime interesting to study the behaviour of interfaces with thixotropic response. The dilatational properties of viscoelastic protein layers adsorbed to liquid-liquid interfaces were interrogated by subjecting these to step strain experiments in combination with frequency sweeps [185]. In this study, β-lactoglobulin dipeptides showed a linear regime, whereas β-lactoglobulin fibrils and monomers demonstrated linear and nonlinear response when oscillated at different strain amplitudes. However, the viscoelastic moduli of β-lactoglobulin dipeptides deviate from linear at high deformations when the interfaces were gelled by increasing the pH from 2 to 10. In this work, the authors found large differences between the interfacial tensions of interfaces during expansion and compression, and realized the need to develop a method to quantify the degree of nonlinearities between extension and compression runs.

The approach to quantify the degree of nonlinearities in Lissajous plots from large amplitude oscillatory dilatational (LAOD) experiments, was recently introduced and studied by van Kempen et al. [186]. A series of strain and frequency sweeps were performed at air-water interfaces stabilised by oligofructose and sucrose esters. The critical strain value was first defined by applying different strain amplitudes. Once the critical strain value had been defined, strain and frequency sweeps were carried out within the nonlinear regime for interfaces with different pressures. Interfaces stabilised by sucrose esters showed viscous Lissajous plots without asymmetries, while oligofructose ester stabilised interfaces exhibit elastic Lissajous. Lissajous plots where further characterised by quantifying the degree

of nonlinearities, using the approach described in [6] (see Section 5.3). Here, short (12 carbon) oligofructose esters coated interfaces exhibited an absence of nonlinearities (indicating an elastic response), up to a strain equal to 5%. At higher strain amplitudes, nonlinearities emerged during both, extension and compression. During extension, the *S–factor* (strain-stiffening ratio) increased with amplitude, implying aN interface with a constant increase strain hardening response. On the other hand, the *S–factor* became more negative with decreasing amplitude, indicating a strain-softening response during compression. Interfaces stabilised by long (18 carbon) oligofructose esters however, presented a higher elastic response with the absence of nonlinearities until a strain equal to 10%. At higher strains, the interface strain hardened during extension (positive *S–factor*) and compression (negative *S–factor*). Interestingly, after the strain hardening observed in extension, interfaces strained soften (*S–factor* became negative) at higher strains (20% and 30%).

The nonlinear rheological properties of cellulose nanocrystals at air-water interfaces were characterised using interfacial oscillatory dilatational rheology [187]. Lissajous plots revealed rhombus-like shapes for interfaces with lower concentration of hydroxyl groups (-OH) and leaf-like shapes for interfaces with higher concentration of -OH. Leaf-shape Lissajous plots imply interfaces with a gentle yield, where the rate at which the pressure is increasing, decreases slowly. Interfaces with a rhombus-like shape instead, flow after they yield, with a near zero slope change in pressure. Here, nonlinearities in Lissajous plots were only calculated for the extension run and not for compression. For interfaces with high and intermediate concentration of -OH, the *S–factor* was extremely similar; it increased fast at very low strains until it reached a plateau at an amplitude equal to 1%. Interfaces with the lowest concentration of -OH groups showed an overall lower *S–factor* which suggested aN interface with a higher elastic response. The authors concluded that LAOD experiments showed a better differentiation between similar samples than large amplitude oscillatory shear (LAOS).

The nonlinear response of three whey protein isolate (WPI) systems: native, aggregates and beads at air-water interfaces subjected to LAOD were investigated in [174]. Interfaces stabilised by WPI native and aggregates showed a viscoelastic solid behaviour, whereas interfaces stabilised by WPI beads exhibited weaker interfaces with flow-like response. In this work, the authors noticed that the *S–factor* approach used to quantify the degree of nonlinearities from Lissajous plots, failed in interfaces with strain softening/hardening paradox response. The strain softening/hardening paradox is observe in numerous materials, since at the

first these materials exhibit strain softening when they are deformed. However, if the deformation is increased, the system strain hardens when reaching the maximum strain. This effect can be observed with Lissajous plots, where single cycles are being analysed. A commercial rheometer would show an overall stain softening response instead, as it only uses the first-harmonic to calculate the moduli.

In this chapter the mechanical properties of interfaces stabilised by dipeptide fibres are investigated by imposing large amplitude oscillatory dilatation (LAOD) to interfaces with the help of a drop profile tensiometer. The drop profile tensiometer and the theory behind oscillatory rheology is introduced in Section 5.3. Dipeptide based interfacial interfaces are first left to equilibrate until the interfacial tension levels off. Next, we demonstrate that interfaces are viscoelastic by plotting the interfacial tension and the area as a function of time and their moduli become nonlinear at intermediate and high strain amplitudes. The behaviour of interfaces is interrogated by plotting Lissajous plots with pressure as a function of strain and measure the degree of nonlinearities by calculating the *S–factor*.
The main findings in this chapter are that interfaces prepared at high salt concentrations become extremely elastic. At low salt concentrations, interfaces are viscous and collapse at intermediate strains. In between, interfaces become more viscoelastic at intermediate salt concentrations, bearing larger strains without collapsing. At high salt concentrations, interfaces start to become more elastic, showing a softening/hardening paradox response during extension that, to the best of our knowledge, it has never been reported in large amplitude oscillatory dilatational experiments before. Last, we realise that the dimensionless *S–factor* index sometimes fails to quantify the degree of nonlinearities of Lissajous plots and propose a subtle modification in the analysis of the *S–factor* to measure nonlinearities at different strains. The aim of this chapter was to study the interfacial properties of dipeptide fibres prepared with our preferred salt ($MgSO_4$), adsorbed at a sinusoidally oscillated interface formed between our preferred oil (isopropyl myristate) and water.

5.3 Materials and methods

5.3.1 Materials

The 2NapFF dipeptides were synthesized as described elsewhere [42]. The solvents and chemicals were purchased from Sigma-Aldrich and used as received. Isopropyl myristate (Sigma-Aldrich $\geq$ 98% pure) was filtered three times through alumina (Honeywell, Aluminium Oxide, activated, basic, Brockmann I) placed in a Whatman filter to trace impurities in the oil phase. A solution of 100 mL (1 M) magnesium sulfate was dissolved in water by placing the vial in an ultrasonic bath for 5 minutes and used as aliquots. Millipore water (resistivity = 18.2 MΩ. cm) was used throughout. For pendant drop experiments water was degassed by heating and stirring under reduced pressure for one hour to avoid bubbles disrupting oscillations.

5.3.2 Methods

Sample preparation

Samples were prepared in 20 mL glass vials by adding 10 mM of NaOH to 10 mL of degassed water to achieve a pH 11 $\pm$ 0.5 measured with a Seven Easy pH probe (Mettler Toledo AG). 2NapFF dipeptides (0.01 wt%) were then added on top of the basic solution and dispersed by placing the vial sealed with parafilm sealing film in an ultrasonic bath for 0.5 hours until a translucent slightly viscous solution was formed. After this, the sample was then left to cool to room temperature (22 °C) before this was transferred to a 36 x 36 x 30 mm glass cuvette once the apparatus had been equilibrated.

Pendant drop tensiometer

The pendant drop tensiometer apparatus is remarkably simple and straightforward to use; however, the reproducibility and accuracy of the measurements can be challenging and time consuming, and thus hard to accomplish. These will be easier to achieve if the person using the instrument is familiar with the limitations of the device. The experimental set up consists of a diffused light, a camera (780 x 580 pixels) and a vertical J-shape needle (1.83 mm interior diameter), from which the oil droplet rises due to the density difference between the phases. The diffuse light is placed behind the drop to project its silhouette, which is being captured by the camera that magnifies and sends the image to the PC. Lastly,

the droplet can be studied either in static or in dynamic mode. In static mode, the drop volume is kept constant and is often used to study the interfacial tension as a function of time, where surfactants, particles or proteins, are used to modify the energetics of the interface. On the contrary, in dynamic mode the droplet is sinusoidally expanded and compressed by altering its volume (amplitude). The amplitude and the rate (frequency) at which a whole cycle occurs can be altered with the help of a pc-controlled piezoelectric pump that is, in the last instance, governed by the operator. A basic diagram of the instrument set up is shown in Figure 5.1.

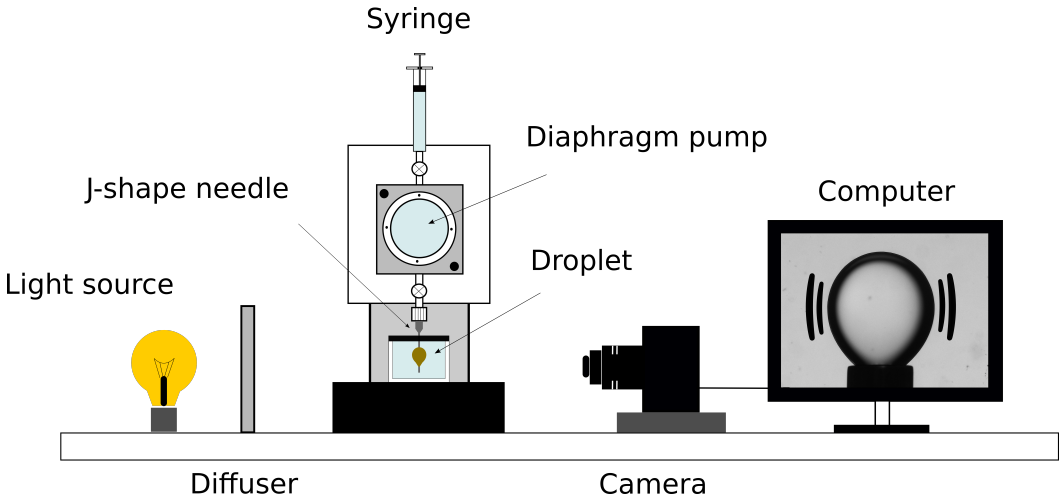

Figure 5.1 *Schematic representation of the drop profile tensiometer.*

Pendant drop method

The interfacial tension γ, the area A_d and the volume V_d of the oil droplet were determined using the pendant drop method of a drop shape analyser (Krüss DSA-100). The technique Axisymmetric Drop Shape Analysis (ADSA), uses the profile of the drop to fit it to the Young-Laplace equation, where discrepancies between the theoretical curve and the profile extracted are evaluated. These discrepancies are the sum of the squares of the normal distances between the calculated Laplacian curve and the measured points of the drop profile [188]. The Young-Laplace equation relates the pressure difference across the interface (Laplace pressure = ΔP), with the principal radii of curvature R_1 and R_2 (see Figure 5.2b) by

$$\gamma \left(\frac{1}{R_1} + \frac{1}{R_2} \right) = \Delta P \equiv \Delta P_0 - \Delta \rho g z \tag{5.1}$$

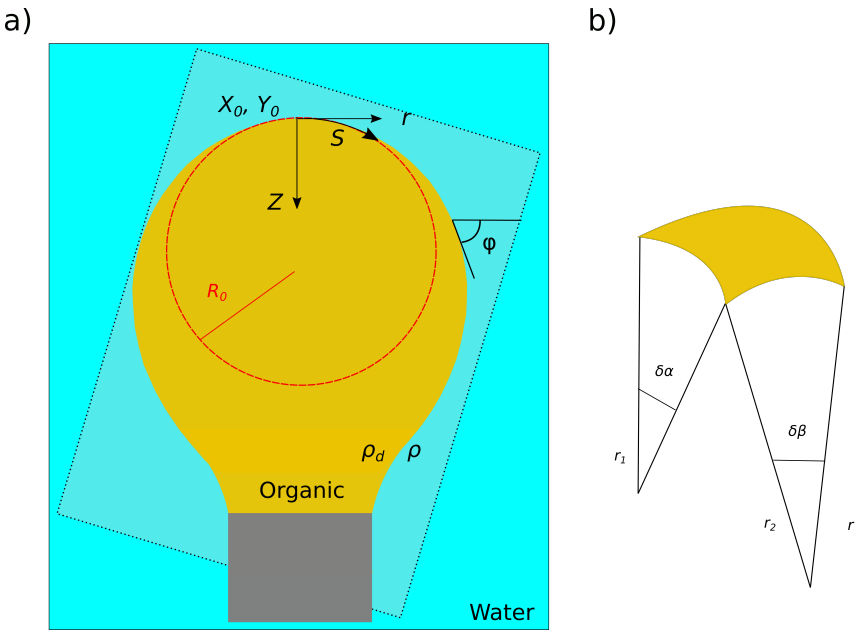

Figure 5.2 *Schematic representation of* ***a:*** *an oil drop rising from a vertical needle used by the software to calculate Bond number and* ***b:*** *a section of the oil droplet to show the principal radii of curvature* R_1 *and* R_2*.*

where ΔP_0 - $\Delta\rho gz$ is the hydrostatic pressure caused by the density difference between the liquids, ΔP_0 is the pressure difference at a reference plane, z is the vertical coordinate of the drop measured from the reference plane, $\Delta\rho = \rho_d$ - ρ is the density difference between the two liquids, ρ_d and ρ are the density of the droplet phase and the continuous phase respectively and g is the acceleration due to gravity. The axis symmetry of the drop makes possible that Equation 5.1 can be expressed as cylindrical coordinates; r, z and the tangent angle φ (see Figure 5.2). With the introduction of these parameters, the drop can be calculated numerically by a set of three-ordinary differential equations

$$\frac{d\varphi}{d\bar{s}} = 2 - Bo\bar{z} - \frac{\sin\varphi}{\bar{r}} \tag{5.2}$$

$$\frac{d\bar{r}}{d\bar{s}} = \cos\varphi \tag{5.3}$$

$$\frac{d\bar{z}}{d\bar{s}} = \sin\varphi \tag{5.4}$$

with boundary values

$$\bar{r} = 0,\ \bar{z} = 0,\ \varphi = 0 \ \ at \ \ \bar{s} = 0 \tag{5.5}$$

where the bar denotes normalisation by R_0 the radius of curvature at the drop apex (see Figure 5.2a) and Bo is the Bond number which quantifies the relative importance of gravity and interfacial tension, is given by

$$Bo = \frac{\Delta\rho g R_o^2}{\gamma} \tag{5.6}$$

from which γ can be calculated. In addition to the Bond number, the best fit Young-Laplace solution 5.1 returns the drop volume V_d and the drop surface area A_d.

Large amplitude oscillatory shear (LAOS) of complex bulk fluids

In this section the analysis for nonlinear dilatational rheology data is presented. For small sinusoidal strain amplitudes, the stress of viscoelastic materials is assumed to oscillate sinusoidally with amplitude, as well as to be fully captured by conventional test protocols [189]. However, when the applied strain amplitude is increased from small to large, a transition between linear and nonlinear regimes can emerge [4]. Figure 5.3 shows the typical output of an oscillatory strain-sweep experiment with fixed frequency. For small strain amplitudes, the storage *G'* and loss *G"* modulus are independent of strain and thus the oscillatory stress is sinusoidal. However, with increasing the strain amplitude, nonlinearities appear and *G'* and *G"* are not longer independent of strain and fail to capture the nonlinearities manifested in the raw data signal; the oscillatory stress in this regime is distorted [4]. For linear viscoelastic regimes, the stress response is computed using the first-harmonic coefficients G'_1 and G''_1, which is a measure of the average moduli in the material response. While this approach is robust to measure the viscoelastic response in the linear regime, for nonlinear regimes often fails because it does not give very useful information, as the stress cannot be modelled by a single sinusoidal.

For a more significant physical meaning, the interpretation can be made by the inspection of stationary closed curves, known as Lissajous plots, by plotting the stress as a function of strain (elastic modulus) or the strain rate (dynamic viscosity)(see Figure 5.4) [190]. For a perfect elastic solid, the Lissajous plot shows a straight line; for a pure viscous response exhibits a perfect circle and; for a viscoelastic fluid displays an ellipse. Viscoelastic fluids in the nonlinear regime, will deviate from ellipsoidal (see Section 5.3.2).

The storage and loss moduli of most materials under LAOS sweep experiments, falls into one of the four types (see Figure 5.5). Type I, strain thinning, G' and

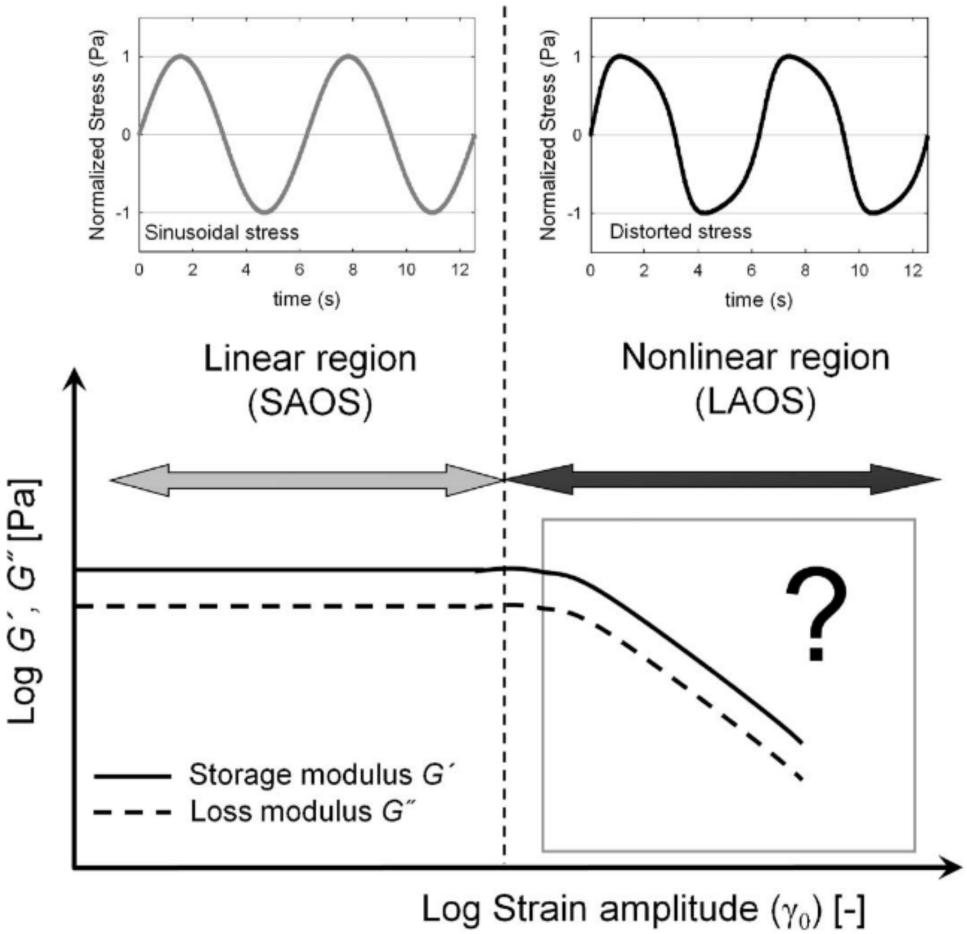

Figure 5.3 *Schematic representation of a strain amplitude sweep test at a fixed frequency. The storage G' and loss G" moduli in the linear regime are independent of strain amplitude; the resulting stress in this region oscillates sinusoidally. However, in the nonlinear regime, G' and G" become dependent of strain amplitude and hence the sinusoidal stress waveforms deform in this region. Experiments in the linear regime are commonly known as small amplitude oscillatory shear (SAOS) and for experiments in the nonlinear regime, these are known as large amplitude oscillatory shear (LAOS). Reproduced from [4] with permission.*

.

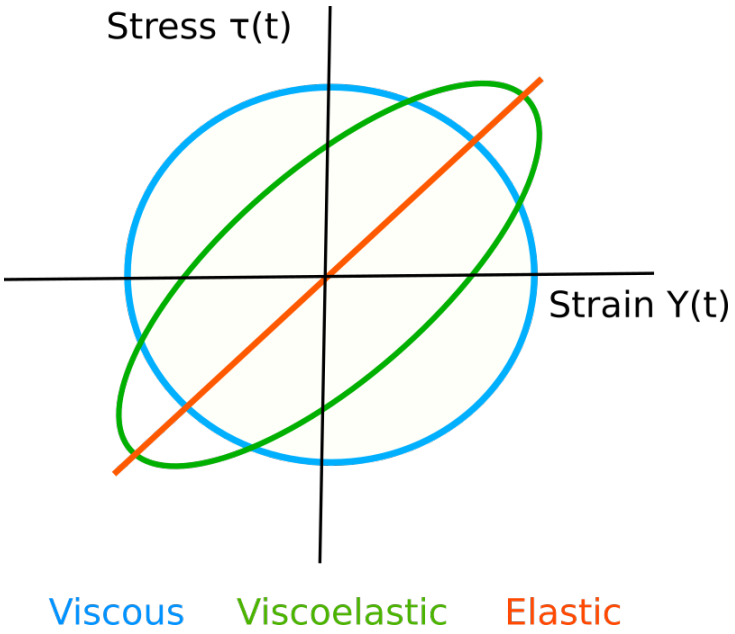

Figure 5.4 *Lissajous plots of elastic solid, Newtonian fluid and viscoelastic fluids under small oscillatory shear.*

G" decrease (see Figure 5.5a); type II, strain hardening, G' and G" increase (see Figure 5.5b); type III, weak strain overshoot, G' decreases and G" increases at first and then decreases (see Figure 5.5c) and; type IV, strong strain overshoot, G' and G" increase followed by a decrease (see Figure 5.5d) [5]. Most of the polymer solutions and melts fall in type I (strain thinning). Apparently, the origin of strain thinning is believed to be similar to that of shear thinning [5]. In shear thinning, macromolecules that were entangled and forming three-dimensional coils at rest, start to orient in the direction of the shear flow when stress is applied. In doing this, the molecules disentangle to some extent and lowers the flow resistance [191]. On the other hand, strain hardening is the opposite of strain thinning (type I), where the loss and storage moduli increases with strain amplitude. Strain hardening it is believed to be caused by the formation of complex microstructures. Alginate gels, which show strain hardening, are reported to form a complex of network chains and metal ions, which form large junctions zones that give more strength and rigidity to the system [192]. Weak strain overshoot, is the result of the resistance to structural collapse of the material, usually made of weak associations, like hydrogen bonds [193]. The distinctive feature in these materials is the pronounced local maximum in the loss moduli G" while G' decreases. This effect is observed in soft glassy materials such as, concentrated emulsions, suspensions, pastes, soft hydrogels, etc., and in polymer solutions like, Xantham gum solutions [4]. If the strain is large enough, the polymers chains align with

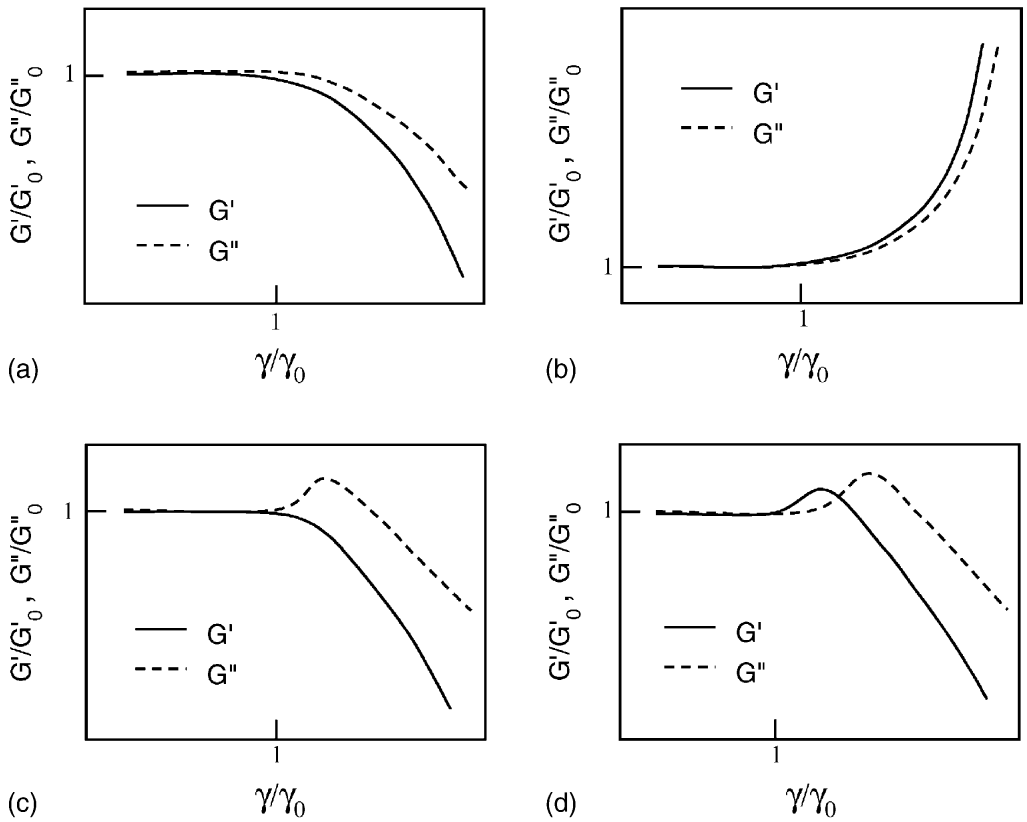

Figure 5.5 *Storage and loss moduli of most materials under LAOS:* ***a:*** *strain thinning,* ***b:*** *strain hardening,* ***c:*** *weak strain overshoot and* ***d:*** *strong strain overshoot Reproduced from [5] with permission.*

the flow making G" to decrease. The strong strain overshoot (type IV), has been observed before in polymers chains with a network that consist in both intra- and intermolecular associations of hydrophobic groups [194]. At large enough strains, both the G' and G" show a significant increase above its linear viscoelastic value. If the strain is increased beyond such point, the structure of the system collapses and makes G' and G" to decrease.

Viscoelastic moduli

Lissajous figures have been used for decades in LAOS experiments to study the rheological properties of viscoelastic materials in the nonlinear regime including, polymer solutions [195], creams [196] and clay-water systems [197, 198]. However, it has not been until recently that a set of elastic moduli has been introduced to quantify the elastic response of nonlinear viscoelastic materials at small and large strain amplitudes [6]. To capture the elastic response, Ewoldt and co-workers introduced the following expressions

$$G'_M \equiv \left.\frac{d\sigma}{d\gamma}\right|_{\gamma=0} = \sum_{n\ odd} nG'_n = e_1 - 3e_3 + \cdots \tag{5.7}$$

$$G'_L \equiv \left.\frac{\sigma}{\gamma}\right|_{\gamma=\pm\gamma 0} = \sum_{n\ odd} G'_n(-1)^{(n-1)/2} = e_1 + e_3 + \cdots \tag{5.8}$$

where γ is the strain, G'_M is the minimum strain modulus, measured by the slope of the stress of a non-deformed interface (γ=0) and G'_L is the large strain modulus ,which is the slope of the line formed between the origin and the stress when the interface is deformed at the largest strain. By including higher harmonics in equations 5.7 and 5.8, the authors were able to capture the local behaviour, otherwise impossible to observe by using only the first-harmonic. G'_M and G'_L can be visualised graphically in the Lissajous plots shown in Figure 5.6a for a linear regime and in Figure 5.6b for a nonlinear regime. G'_L sometimes can be misinterpreted by the slope of the semi-major axis of the ellipse, instead G'_L is the slope of the secant at maximum strain, which might happen to be the same as the semi-major axis. Similarly, the viscous response is represented by the expressions

$$\eta'_M \equiv \left.\frac{d\sigma}{d\dot{\gamma}}\right|_{\dot{\gamma}=0} = \sum_{n\ odd} nG''_n = e_1 - 3e_3 + \cdots \tag{5.9}$$

$$\eta'_L \equiv \left.\frac{\sigma}{\dot{\gamma}}\right|_{\dot{\gamma}=\pm\dot{\gamma}_0} = \sum_{n\ odd} G''_n(-1)^{(n-1)/2} = e_1 + e_3 + \cdots \tag{5.10}$$

where η'_M and η'_L is the minimum and large-rate dynamic viscosity and $\dot{\gamma}$ is the strain rate and are calculated in the same manner as G'_M and G'_L.

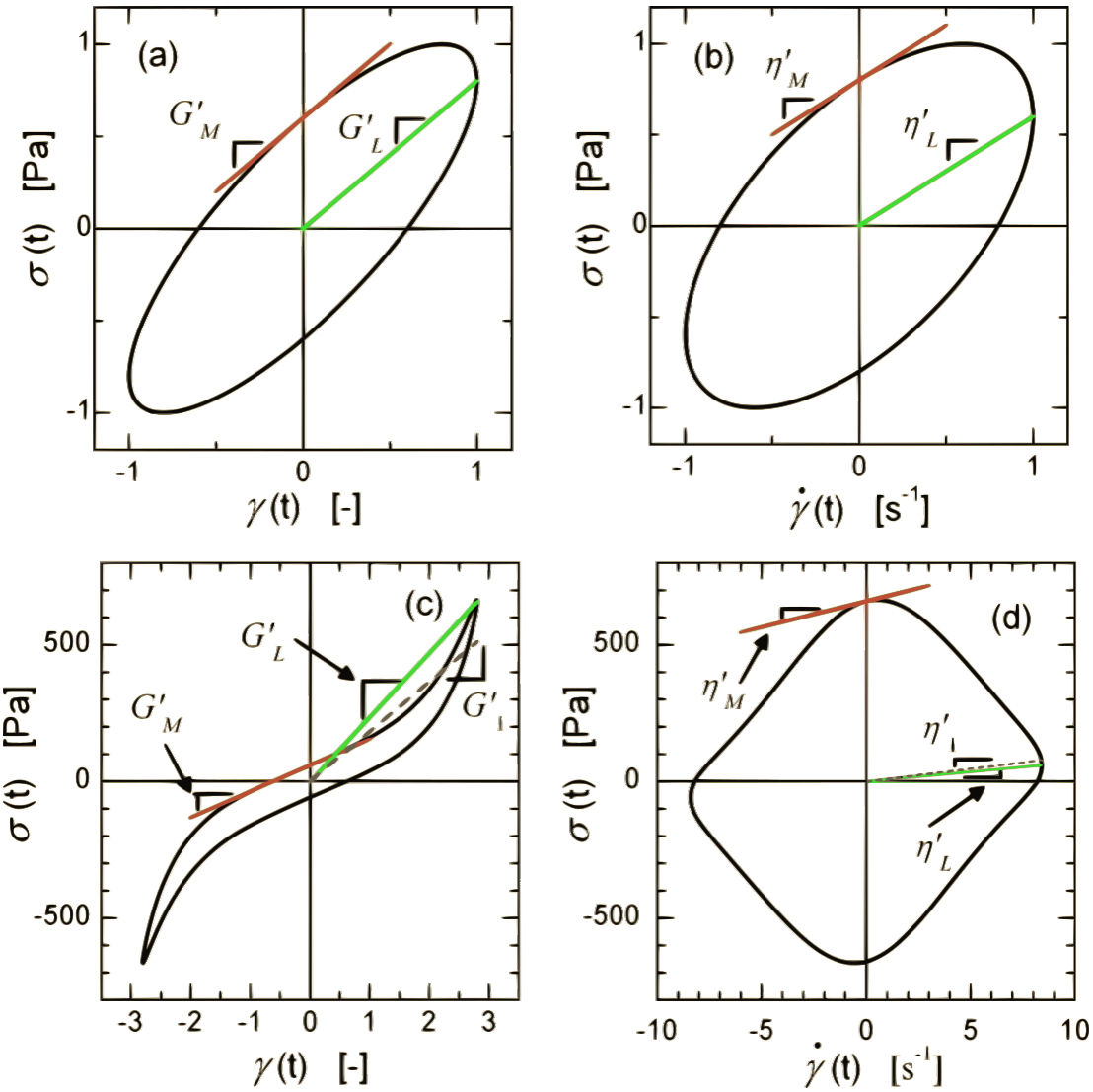

Figure 5.6 *New measurements for reporting:* ***a:*** *the elastic moduli,* ***b:*** *and dynamic viscosities of a linear viscoelastic response,* ***c:*** *the elastic moduli and* ***d:*** *dynamic viscosities of a nonlinear response. For the linear regimen* ***a,b:*** *all measures are equal to the viscoelastic moduli, while for the nonlinear regime* ***c,d:*** *these differ for each material measure. Here γ and $\dot{\gamma}$ are strain and strain rate respectively. Reproduced from [6] with permission.*

Dimensionless *S–factor*

To compare the nonlinearities distorting the ellipse, the authors defined the strain-stiffening ratio by

$$S \equiv \frac{G'_L - G'_M}{G'_L} = \frac{4e_3 + \cdots}{e_1 + e_3 + \cdots} \tag{5.11}$$

from which the strain thinning and strain thickening can be quantified by

$$S \begin{cases} > & 0 \text{ strain stiffening,} \\ = & 0 \text{ linear elastic,} \\ < & 0 \text{ strain softening} \end{cases}$$

Dimensionless *S–factor* for complex interfaces

Ewoldt's approach to calculate the *S–factor* (see Equation 5.11), was extended by van Kempen et al. [186] to characterise the rheological behaviour of air-water interfaces in large amplitude oscillatory dilatational (LAOD) experiments. The output of a conventional drop profile tensiometer was used to construct Lissajous plots of surface pressure–strain. Surface pressure here is defined as:

$$\Pi = \gamma - \gamma_0 \tag{5.12}$$

where γ is the instantaneous interfacial tension and γ_0 is the interfacial tension of a non-deformed interface. Strain is defined as:

$$\varepsilon = \delta A / A_0 \tag{5.13}$$

where A is the instantaneous surface area and A_0 is the surface area of a non-deformed interface. Due to the asymmetry in the Lissajous plots during a full cycle (extension and compression), the strain-stiffening ratio S is defined for both regimes, extension and compression by

$$S_{ext} \equiv \frac{E'_{L,E} - E'_{M,E}}{E'_{L,E}} \tag{5.14}$$

$$S_{com} \equiv \frac{E'_{L,C} - E'_{M,C}}{E'_{L,C}} \tag{5.15}$$

where $E'_{M,E}$ and $E'_{M,C}$ are the slope at the minimum strain elastic modulus in extension and compression respectively and $E'_{L,E}$ and $E'_{L,C}$ are the slope of the line between the origin and the large elastic strain modulus in extension and compression respectively. With these new definitions it is possible to distinguish nonlinearities between compression and the extension.

Apparatus validation

One of the main concerns during pendant drop experiments, is that the droplet will always tend to dissolve or evaporate to the other phase with time. In our system, the droplet phase is made up of oil and the bulk phase is 99.9% water plus 0.1% dipeptide. Apparently, this problem seems to be minimal for low solubility liquids [199], however, if dissolution happened, it would be a tiny amount of water dissolving into the oil and hence we neglect this problem. However, to avoid the bulk phase evaporating to the air, the cuvette was covered with a lid.

Another factor that may influence the accuracy of the pendant drop tensiometer, is the volume of the droplet. Drops with a shape close to spherical have been proved to yield inconsistent results [188]. To avoid this, we increased the volume of the droplet until the interfacial tension of the bare interface equalled the one reported in literature (29 ± 0.3 mN/m) [200]. The volume required to achieve the correct interfacial tension was 25 μL, but sometimes the volume had to be decreased to 23 μL to avoid the droplet detaching from the needle at large strain amplitudes and at high salt concentrations.

Another limitation is the accuracy or fit error. The method used by the software to evaluate the drop shape is a statistical method characterised by its ability against "outliers" [201]. After optimisation is done, the software shows the mean squared deviation of the profile from the fit and hence determines the quality of the fit. A high fit error, in the range of tens or hundreds of microns, is associated with solidifying interfaces, where wrinkles are observed in compressed interfacial films [202]. A high fit error was also observed at first, due to the bulk gelling, but this was solved by decreasing the concentration of the dipeptide from 0.1 wt% to 0.01 wt%. A bare organic/water interface gives a fit error < 1 μm and thus experiments with fit errors > 1 μm were rejected.

Next, we verify that the subphase contributions do not dominate over interfacial

stresses by calculating the Boussinesq number [203, 204] by

$$Bq = \frac{\nu_D}{\nu L} \tag{5.16}$$

where ν_D is the interfacial dilatational viscosity, ν the bulk viscosity and L is the length-scale of the system or radius of the drop. For our system, the interfacial dilatational elasticity E' dominates and hence interfacial stresses are considered to arise from this [205], therefore we define Bq by

$$Bq = \frac{E'}{\omega \nu L} \tag{5.17}$$

For the smallest $E' = 0.05$ mN/m and the highest frequency = 0.2 Hz, $L = 1$ mm and $\nu = 1.02$ mPa s at 20°C we find a $Bq > 10^2$. A $Bq > 1$, indicates that the interfacial dilatational elasticity dominates while for $Bq < 1$ the bulk viscosity dominates, therefore this proves that the interfacial stresses prevail over the bulk stresses.

Experiment setup

After a deep cleaning of the instrument parts with hexane, followed by methanol and rinsing with milliQ water, the instrument was equilibrated by placing milliQ water in the cuvette and forming an air bubble with a J-shaped needle to achieve an interfacial tension of 72 ± 0.5 mN/m at 22 °C. Next, the air is removed from the needle and filled with isopropyl myristate to form a drop of 25 μL with comparable interfacial tension γ (29 ± 0.5 mN/m at 22 °C) to that reported in literature (29.7 ± 0.3 mN/m) [200]. Once the instrument had been equilibrated, the water in the cuvette was replaced by the basic solution with the dipeptides dispersed in it. To equilibrate the solution, we form again the oil droplet and left it to equilibrate one more time (≈ 5 minutes). Due to the tiny size of the fibre micelles, γ drops rapidly (< 1 second) from ≈ 29 mN/m to ≈ 25 mN/m. Once the solution is in equilibrium, aliquots of different salt concentrations (0.1 to 0.4 mg/mL) were added on top of the sample to induce film gelation. Finally, the cuvette was covered with a lid to avoid evaporation.
The surface tension of interfaces from a static droplet was measured before, during and after the addition of salt and left until the sample reached equilibrium (≈ 5 hours). With the sample in equilibrium, the surface tension was followed by amplitude and frequency sweep experiments to study the nonlinear response

of complex interfaces. During the sweep tests, sinusoidal oscillations with a strain amplitude and frequency that increased from 1.5% to 25% and 0.02 Hz to 0.2 Hz respectively were performed. The experiments consisted of 20 cycles of oscillations with 5 minutes rest between experiments. The initial and final cycles were removed from the analysis to eliminate the influence of potential outliers that could affect the mean. Outliers were removed from the raw data in both axis (x, y) and smoothing was carried out by interpolating the resulting data to achieve more robust results.

5.4 Results and discussion

In this chapter, we investigate the dilatational rheological properties of liquid-liquid interfaces in the nonlinear regime by imposing large amplitude oscillatory dilatation (LAOD) strains to interfaces stabilised by hydrogel fibres.
Using a concentration of 0.1 wt% 2NapFF (as in previous chapters), makes the bulk gel after a timescale of several hours and hence the droplet shape can no longer be described by the Young-Laplace equation 5.1. To solve this problem and achieve a fit error lower than 1 μm, such as the one we get for bare isopropyl myristate/water interfaces, the concentration of dipeptide had to be decreased. Linking micellar structures made of 2NapFF to hydrogelation formation using calcium chloride, Cardoso et al., [206] showed that the minimum concentration of 2NapFF needed to form a gel was 0.02 wt%. At this concentration the sample partially passed the inversion vial test. The inversion vial test is a common test where the vial containing the sample is turned upside-down and then the observer waits to see whether the sample flows under its own weight or not [207]. For this reason, to avoid hydrogelation of the bulk phase, we decided to lower the concentration of 2NapFF to 0.01 wt%. Likewise, we accordingly decreased the concentration of the salt used to trigger gelation. Dilatational rheology involves the deformation of an interface and subsequent analysis of the interface response over the experiment time-scale. It is therefore important to ensure that no significant interfacial tension changes take place over the oscillation time-scale. Based on this fact, we described a route (see Section 5.3.2), to achieve interfaces in equilibrium at the start of the experiment.
The interfacial tension measured during adsorption of 2NapFF fibres prepared with magnesium sulfate to an isopropyl myristate/water interface as a function of time is shown in Figure 5.7a. The interfacial tension of bare interfaces is around

$\gamma = 29 \pm 0.5$ mN/m at a temperature $t = 22$ °C (data not shown). However, the interfacial tension decreases to ≈ 25 mN/m when dipeptide molecules are dispersed in the solution. Following the addition of salt (shown by a black arrow in Figure 5.7), γ drops even further to approximately 16.5 mN/m and 13.5 mN/m for interfaces prepared at 0.2 and 0.3 mg/mL magnesium sulfate respectively. After 4 h, the interfaces have reached equilibrium and are ready to start the experiments.

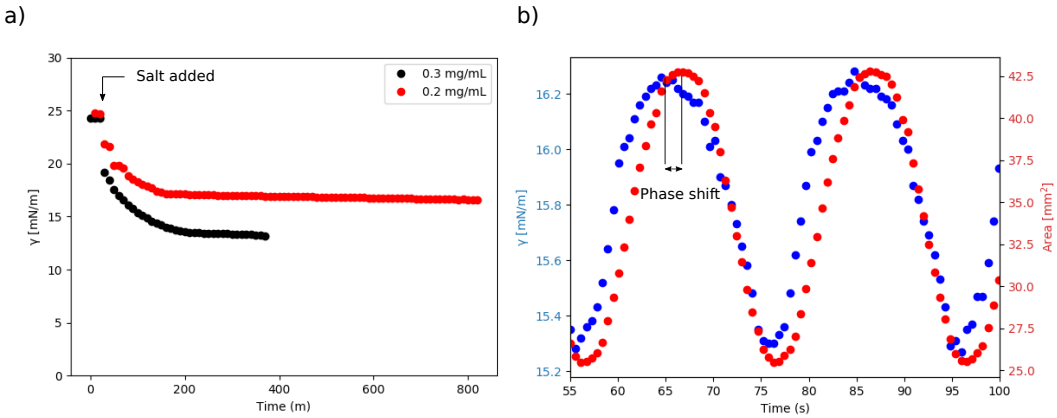

Figure 5.7 ***a:*** *interfacial tension γ of interfaces made of 0.01 wt% 2NapFF prepared at 0.2 and 0.3 mg/mL magnesium sulfate. Static oil droplets are left until the interfacial tension plateaus, which denotes that the interface has reached equilibrium.* ***b:*** *γ and surface area A of a sinusoidally oscillated isopropyl myristate-water stable interface made of 0.01 wt% 2NapFF at 0.2 mg/mL magnesium sulfate. The oil droplet was oscillated for 20 cycles at at 25% strain amplitude and 0.05 Hz.*

Amplitude and frequency sweep experiments were conducted after 5 h of adding the salt to ensure that the interfaces have reached equilibrium. The raw data from a stable interface oscillated at 25% strain amplitude and 0.05 Hz is shown in Figure 5.7b. The resulting periodic γ waveform shows a phase shift with respect to the surface area A with sinusoidal waveform, which indicates that the interface is viscoelastic and hence time-dependent strain. The interfacial tension also gets distorted at high strain amplitudes, losing its sinusoidal shape and hence implying strong non-linearities. Using the data generated by the DSA to calculate the viscoelastic response of the interfaces, gives unrealistic results and therefore we use Lissajous plots instead.

5.4.1 Dilatational viscoelastic properties

The surface pressure (Equation 5.12) of interfaces made of 0.01 wt% 2NapFF prepared at different salt concentrations (0.1 to 0.4 mg/mL magnesium sulfate) is shown in Figures 5.8 to 5.11 and Figures B.1 and B.2 from Appendix B. Interfaces were oscillated for 20 cycles at different strain amplitudes (1.5%, 8%, 16.5% and 25%) and frequencies (0.02 Hz, 0.05 Hz, 0.1 Hz and 0.2 Hz). The initial and last cycles of each experiment were removed from the analysis to eliminate the influence of potential outliers that could affect the mean.

The pressure of stable interfaces prepared at 0.1 mg/mL magnesium sulfate and oscillated at 1.5% strain amplitude (see Figure B.1 left panel in Appendix B), was barely captured by the drop profile tensiometer. The instrument reaches its detection limit before it detects the low torque stress values generated by the change on the surface area of the interface. As a result, the analysed data shows scattered curves with no physical meaning. Nonetheless, at small strain amplitudes ($\approx 10^{-2}$), the viscoelastic moduli of dispersed systems is supposed to remain in the linear regime for small amplitude oscillatory shear tests [4]. Therefore, based on these results, we decide to increase the strain amplitude.

Strain amplitude and frequency sweep experiments for stable interfaces prepared at 0.1 mg/mL magnesium sulfate are shown in Figure 5.8. All interfaces show a viscoelastic response indicated by the shape of the Lissajous plots. The pressure increases with frequency for interfaces oscillated at 8% strain amplitude (see Figures 5.8a,c,e,g). Similarly, the viscoelastic moduli increase with frequency as well, as demonstrated by the Lissajous plots becoming steeper (increased elasticity) and wider (increased viscosity). Nonetheless, the viscoelastic properties of these interfaces still, like those oscillated at 1.5%, in the linear regime, confirmed by the lack of a yielding effect of the network. The interfaces exhibit superimposed oscillations during extension and compression. Superimposed oscillations during compression, have been previously observed in thixotropic systems and attributed to the entangled network reforming again and tilting or sliding over or both, because the interface starts to buckle [208]. We hypothesize that during extension, superimposed oscillations may be caused by the network collapsing. At such a low salt concentration, interfaces may be too weak to support strains of 8%. Indeed, oscillations increase with increasing frequency, suggesting a network collapsing to a greater extent (see Figure 5.8e,g). However, when the interface reaches the maximum strain, the network gradually reforms as shown by the pressure drop.

The viscoelastic moduli becomes nonlinear when interfaces prepared at 0.1

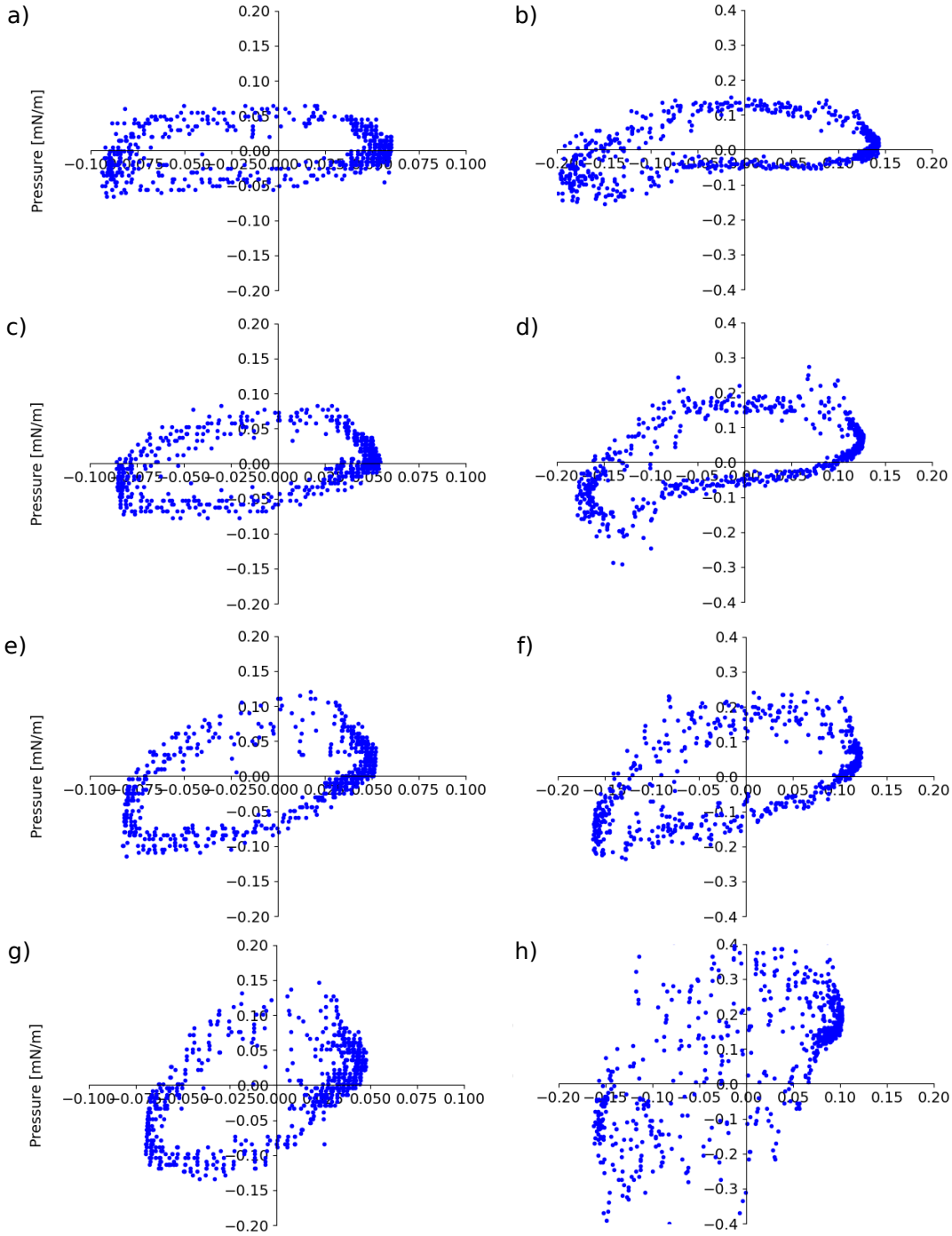

Figure 5.8 *Pressure response from strain amplitude and frequency sweep experiments performed on interfaces made of 0.01 wt% 2NapFF and prepared at 0.1 mg/ml magnesium sulfate. Interfaces were oscillated at a strain amplitude of* ***left panel:*** *8% and* ***right panel:*** *16.5% and a frequency of* ***a,b:*** *0.02 Hz,* ***c,d:*** *0.05 Hz,* ***e,f:*** *0.1 Hz and* ***g,h:*** *0.2 Hz.*

mg/mL magnesium sulfate are oscillated at 16.5% amplitude (see Figure 5.8 right panel). Lissajous plots transform from a simple ellipse shape representing the linear response to a complex deformed ellipse shape. After the initial linear region, the interface yields, followed by a flowing effect represented by the pressure barely changing with strain. During compression, the interface continues to flow implying that the network do not have enough time to reform while the interface reaches the maximum strain in extension. With further decreasing of the strain, the interface strain hardens at a strain approximately to -0.085 has been accumulated, suggesting a network gradually reforming.

Interfaces prepared at 0.2 mg/mL magnesium sulfate show a viscoelastic linear response when oscillated at 8% strain amplitude (see Figure 5.9a,c,e,g). Similar to interfaces prepared at 0.01 mg/mL magnesium sulfate, the viscoelastic response increases as well when interfaces are oscillated at higher frequencies. However, these interfaces seem to be stronger as we do not observe superimposed oscillations until they are oscillated at higher frequencies. Superimposed oscillations start to show up in interfaces oscillated at 0.2 Hz, supporting the idea of the interface breaking apart during extension mentioned above. A frequency of 0.2 Hz may be too fast for the fibres to align and hence the network begins to collapse. The pressure in these interfaces is slightly lower than that of interfaces prepared at 0.1 mg/mL magnesium sulfate, oscillated for the same strain amplitudes and frequencies. This may be caused by an increase in the elastic moduli component when interfaces are prepared at 0.2 mg/mL magnesium sulfate.

Figure 5.9 (right panel) shows the pressure of interfaces prepared at 0.2 mg/mL magnesium sulfate oscillated at 16.5% strain amplitude. The ellipse shape observed in interfaces oscillated at 8%, vanishes when they are oscillated at 16.5%, similar to interfaces prepared at 0.1 mg/mL magnesium sulfate. However, these interfaces differ from those prepared at 0.1 mg/mL in that they do not show secondary oscillations in the linear response, both in extension and in compression and in that they do not yield. Instead, interfaces prepared at 0.2 mg/mL start to strain softening when reaching a strain around zero, where the strain rate is at its highest value. After this point, the pressure keeps increasing at a lower rate before this starts to decrease, implying thixotropic response when the strain rate decreases. In interfaces oscillated at 0.02 Hz, we observe a strain hardening effect that vanishes with increasing frequency.

Interfaces prepared at 0.2 mg/mL magnesium sulfate were further oscillated at 25% strain amplitude (see Figure B.1 right panel). At this amplitude, superimposed oscillations start to materialise. After these oscillations, the

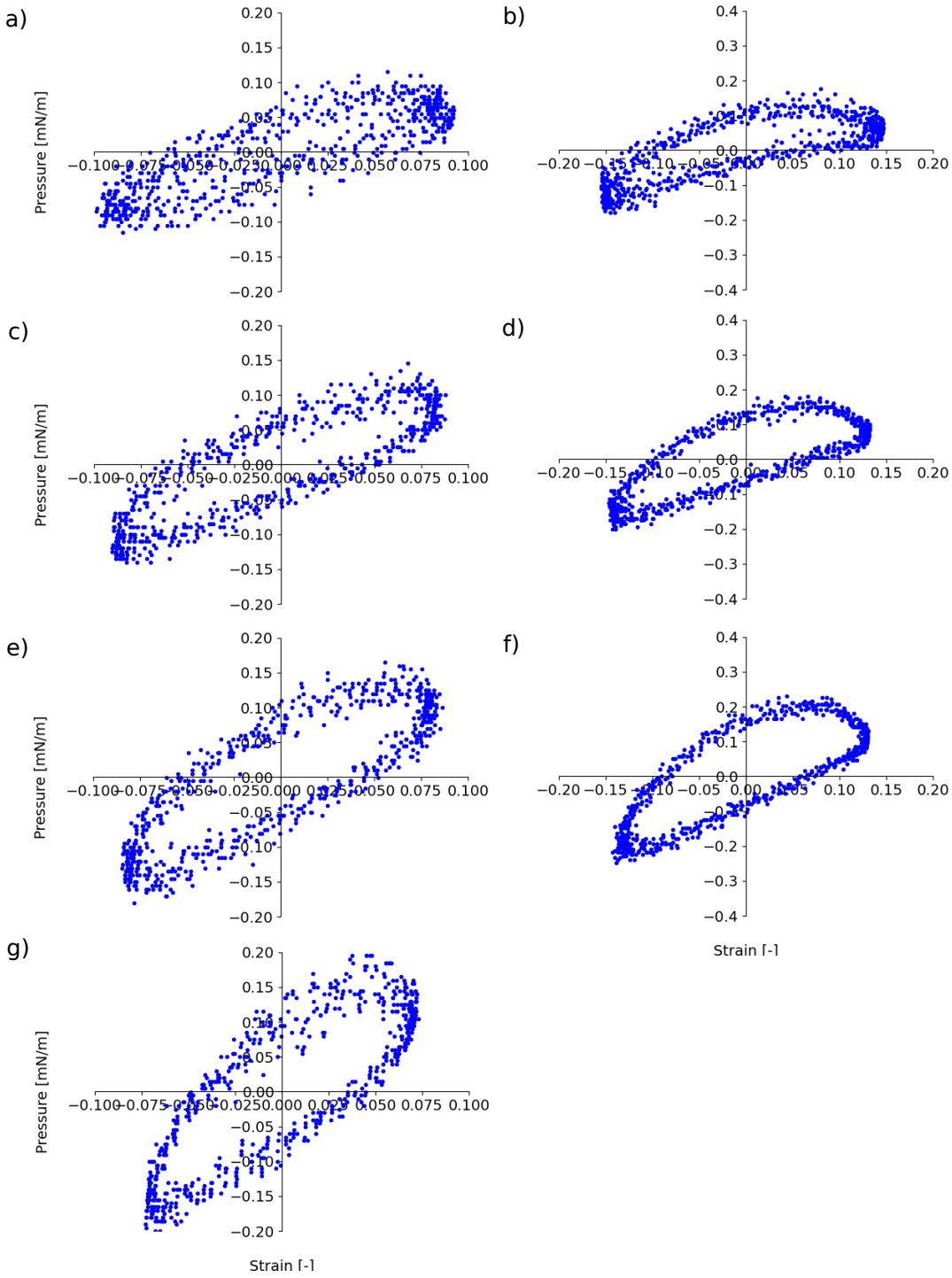

Figure 5.9 *Pressure response from strain amplitude and frequency sweep experiments performed on interfaces made of 0.01 wt% 2NapFF and prepared at 0.2 mg/ml magnesium sulfate. Interfaces were oscillated at a strain amplitude of* ***left panel:*** *8% and* ***right panel:*** *16.5% and a frequency of* ***a,b:*** *0.02 Hz,* ***c,d:*** *0.05 Hz,* ***e,f:*** *0.1 Hz and* ***g,h:*** *0.2 Hz.*

pressure keeps increasing as opposed to interfaces prepared at 0.1 mg/mL oscillated at 16.5%. These results indicate that interfaces prepared at 0.2 mg/mL don't entirely collapse like interfaces prepared at 0.1 mg/mL magnesium sulfate and hence they are stronger.

The pressure for interfaces prepared at 0.3 mg/mL magnesium sulfate, oscillated at 8% strain amplitude and low frequencies (0.02 Hz and 0.05 Hz) is extremely noisy (see Figure 5.10a,b). Increasing the frequency to 0.1 Hz, made the noise vanish and the Lissajous plots adopt an almost perfect ellipse shape, similar to the observe in interfaces prepared at 0.2 mg/mL magnesium sulfate. Likewise, superimposed oscillations appeared on interfaces oscillated at 0.2 Hz (see Figure 5.10g).

At 16.5% strain amplitudes, the moduli component becomes nonlinear as shown by the asymmetry in the Lissajous plots (see Figure 5.10 right panel). The elastic response of these interfaces lies somewhere in between interfaces prepared at 0.1 mg/mL and 0.2 mg/mL magnesium sulfate. The pressure increases until the interfaces reach approximately a zero strain as opposed to interfaces prepared at 0.1 mg/mL, where the pressure plateaus at negative strains. On the other hand, the pressure in interfaces prepared at 0.2 mg/mL keeps increasing until the end of the half cycle (extension), where the strain rate starts to decrease and the interface starts to reform. In addition to this, the decrease observed in pressure at intermediate to high strains, reveals a strain hardening response at the maximum strain, which is not observed in interfaces prepared at lower salt concentrations. To our knowledge, this response has been observed before in LAOS experiments for bulk [209] and interfaces [174, 210], however not in LAOD experiments for interfaces. The hardening response increases with increasing frequency, observed by the increase in surface pressure by the end of extension. The time of structure recovery in interfaces prepared at 0.3 mg/mL may be shorter than in interfaces prepared at lower salt concentrations and hence the interface is perhaps sliding or tilting off the interface as observed in compression. This would explain the increase in pressure materialising the strain hardening response observed at high strains during extension. To observe a strain hardening response after an interface has strain softened, may seem unusual but it has been reported before in polysaccharides and in gels, and it is known as the softening/hardening paradox [211]. This response is observed because the data exhibited in Lissajous plots is from intra-cycle measurements, showing local behaviour. We hypothesized that the strain hardening response could be caused by the combination of two factors: (i) the interface reaching the maximum strain, where the strain rate is

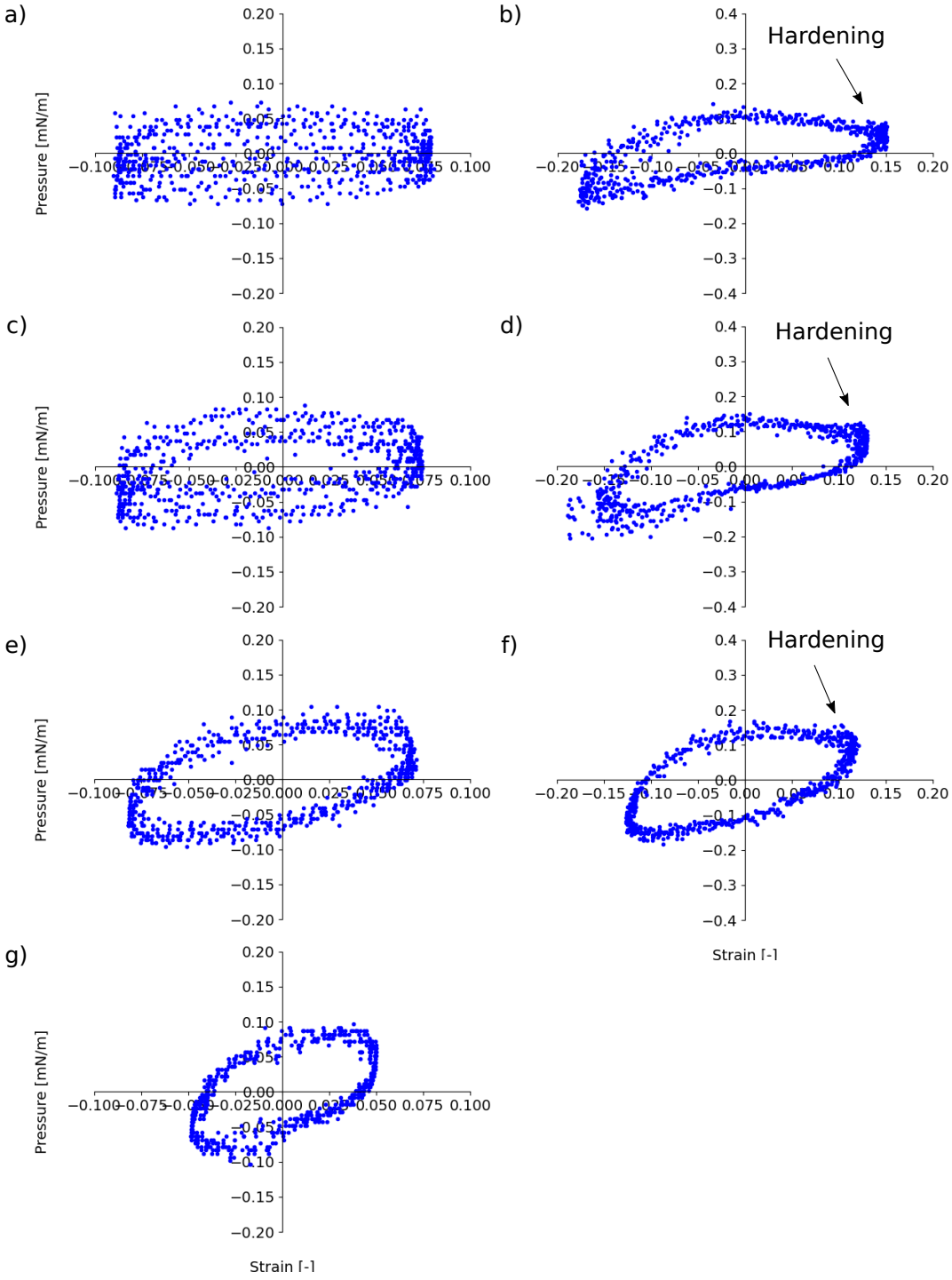

Figure 5.10 *Pressure response from strain amplitude and frequency sweep experiments performed on interfaces made of 0.01 wt% 2NapFF and prepared at 0.3 mg/ml magnesium sulfate. Interfaces were oscillated at a strain amplitude of* ***left panel:*** *8% and* ***right panel:*** *16.5% and a frequency of* ***a,b:*** *0.02 Hz,* ***c,d:*** *0.05 Hz,* ***e,f:*** *0.1 Hz and* ***g,h:*** *0.2 Hz.*

zero and (ii) the decrease in interfacial area caused by the compression (half) cycle starting. The network starts to reform at zero strain rate, however, the process is accelerated by the decrease of the interfacial area when compression starts.

Interfaces prepared at 0.3 mg/mL oscillated at 25% strain amplitude (see Figure B.2 left panel) show Lissajous plots with larger asymmetries than interfaces oscillated at 16.5%. The strain hardening response is significantly higher, especially during compression where the pressure 5.12 drops to -0.6 mN/m in interfaces oscillated at higher frequencies. In these interfaces secondary oscillations appear for the first time at high strains during compression. This phenomenon could be caused by the tilted interface rearranging back on the interface after extension, as these vanish at around zero strain before they come back again at minimum strains.

Interfaces prepared at 0.4 mg/mL magnesium sulfate, show a linear viscoelastic response when oscillated at 8% strain amplitude as most of the other interfaces prepared at lower salt concentrations (see Figure 5.11 left panel). Interfaces oscillated at 16.5%, exhibited a pressure similar to interfaces prepared at 0.2 mg/mL, in that this keeps increasing after strain softening (see Figures 5.11 right panel). A strain hardening response is observed at high strains during extension similar to interfaces prepared at 0.3 mg/mL, but more marked. This indicates that interfaces may become more elastic with increasing salt concentration. Likewise, superimposed oscillations show up at high strains in compression as for interfaces prepared at 0.3 mg/mL oscillated at 25%. Interestingly, these interfaces show a yield response when oscillated at 25% (see Figure B.2 right panel). However, the pressure keeps increasing as opposed to interfaces prepared at 0.1 mg/mL. In addition to this, the yielding occurs when the pressure 5.12 reaches zero, while for all the other interfaces, the strain softening response occurs at a zero strain instead. The strain hardening response observed in interfaces oscillated at 16.5% seems to vanish at 25% in extension, however, this is more marked during compression.

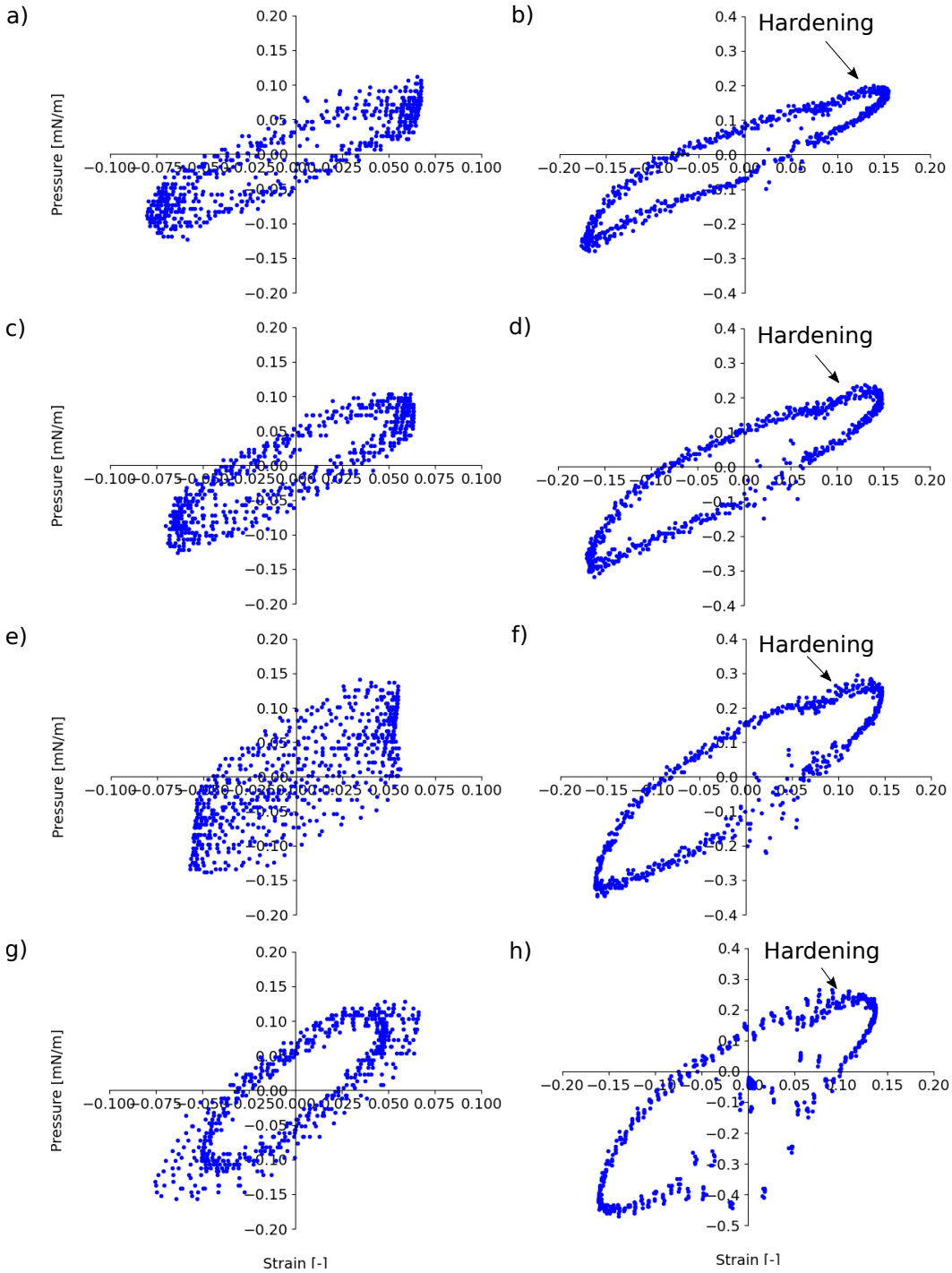

Figure 5.11 *Pressure response from strain amplitude and frequency sweep experiments performed on interfaces made of 0.01 wt% 2NapFF and prepared at 0.4 mg/ml magnesium sulfate. Interfaces were oscillated at a strain amplitude of* ***left panel:*** *8% and* ***right panel:*** *16.5% and a frequency of* ***a,b:*** *0.02 Hz,* ***c,d:*** *0.05 Hz,* ***e,f:*** *0.1 Hz and* ***g,h:*** *0.2 Hz.*

Figure 5.12 shows the Lissajous plots described above individually, plotted together as for different salt concentrations. The rows represent the strain amplitudes and the columns represent the frequencies at which interfaces were oscillated. Despite the pressure being mostly noise, interfaces oscillated at 8% (bottom row), show Lissajous plots with an overall ellipse shape, which indicates that G' and G" moduli are still in the linear regime. The slope of the ellipses vary between salt concentrations. For example, interfaces prepared at 0.2 mg/mL and 0.4 mg/mL oscillated at 8% show a steeper slope than interfaces prepared at 0.1 mg/mL and 0.3 mg/mL, which indicates that the former are more elastic than the latter. Likewise, interfaces prepared at 0.2 mg/mL oscillated at 8% stretch to higher strains values than the other interfaces, suggesting interfaces with lower resistance to deformation (red curves in bottom row). However, this effect shifts to interfaces prepared at 0.4 mg/mL when they are oscillated at intermediate strain amplitudes. Nonlinearities are more marked at low frequencies, where the elastic response is stronger and become more subtle with increasing frequency most probably because of the increase in viscosity. Both, the pressure and nonlinearities increase further for interfacial interfaces oscillated at 25% strain amplitude. A strain hardening effect in both, extension and compression, is observed in interfaces prepared at 0.3 mg/mL and 0.4 mg/mL magnesium sulfate. During extension, the response is more marked in V oscillated at 16.5% strain amplitude, while during compression this is stronger in interfaces oscillated at 25% strain amplitude. Finally, the strain hardening response becomes stronger with increasing salt concentration and/or frequency; the viscosity increases with increasing frequency and nonlinearities increase with increasing strain amplitude and/or decreasing frequency.

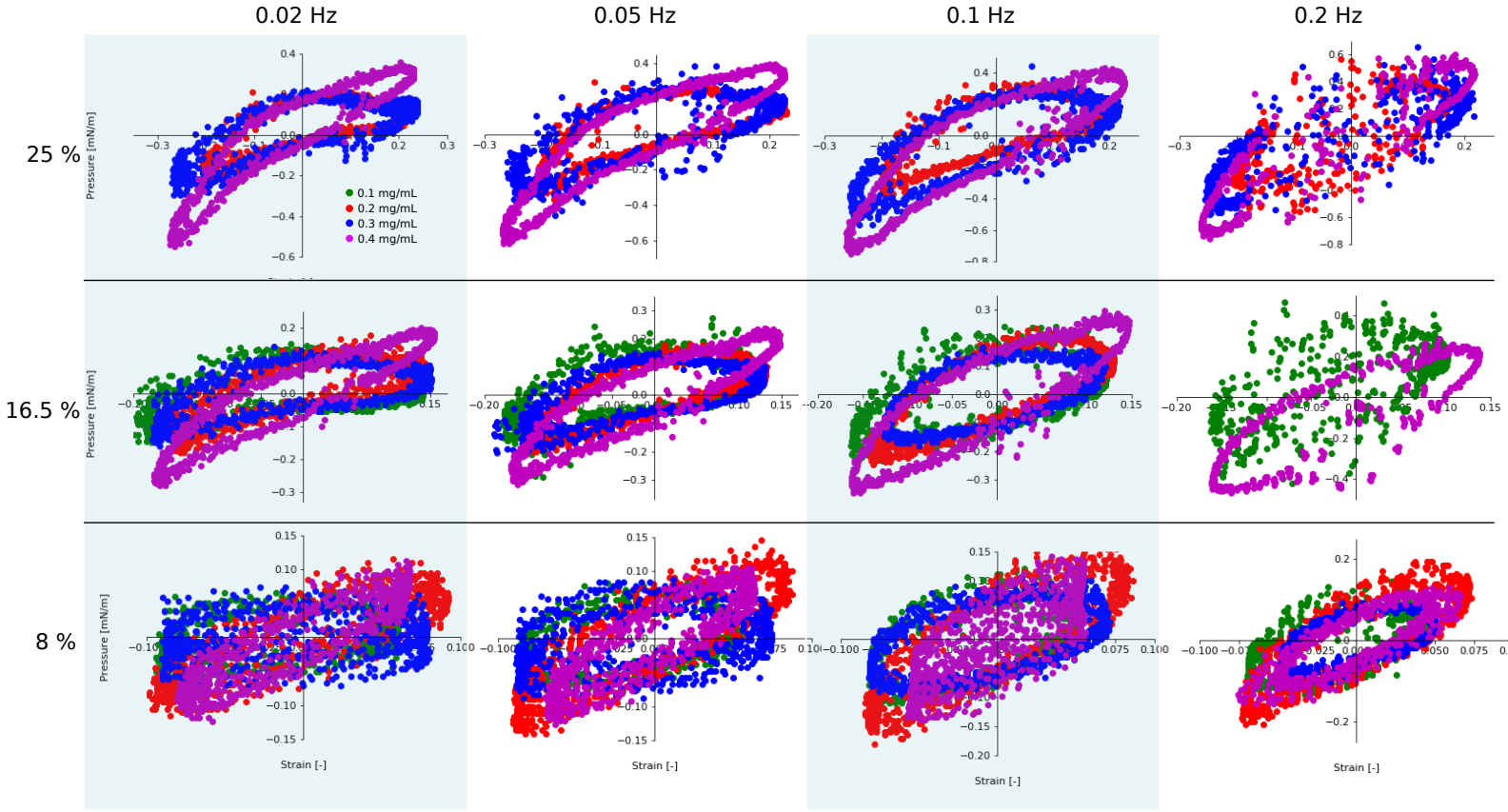

Figure 5.12 *Lissajous plots made of interfaces made of 0.01 wt% 2NapFF prepared at 0.1 mg/mL, 0.2 mg/mL, 0.3 mg/mL and 0.4 mg/mL magnesium, sulfate. Interfaces were oscillated at* ***1st row:*** *8%,* ***2nd row:*** *16.5% and* ***3rd row:*** *25% and at* ***1st column:*** *0.02 Hz,* ***2nd column:*** *0.05 Hz,* ***3rd column:*** *0.1 Hz and* ***4th column:*** *0.2 Hz.*

5.4.2 Degree of nonlinearities quantification

The degree of nonlinearities in Lissajous plots can be quantified by calculating the strain-stiffening ratio S (see Equations 5.14 and 5.15). An *S–factor* with a value close to zero indicates an elastic response, whereas a negative and positive value corresponds to an intracycle strain softening and hardening response respectively. For comparison, the *S–factor* was only calculated for interfaces oscillated at 16.5% strain amplitude and 0.02 Hz, 0.05 Hz and 0.1 Hz. The *S–factor* of interfaces oscillated at 8% strain amplitude was not computed because most of the interfaces show an ellipse shape, which indicates that the rheological components E' and E" still in the linear regime. Similarly, the *S–factor* was not calculated for interfaces oscillated at 25% strain amplitude or at 0.2 Hz because of the noise observed in these Lissajous plots would make these difficult to quantify. Interfaces prepared at 0.1 mg/mL and 0.3 mg/mL show a clear strain hardening response (*S–factor* 5.11 > 0) for both, extension and compression (see Figures 5.13a,c). This, however, decreases with increasing frequency, which indicates that the interfaces become softer and more elastic. In contrast, interfaces prepared at 0.2 mg/mL and 0.4 mg/mL show an overall more elastic response (*S–factor* 5.11 ≈ 0) (see Figures 5.13b,d). Similarly to interfaces prepared at 0.1 mg/mL, the strain hardening response decreases with frequency for both interfaces during compression and for interfaces prepared at 0.4 mg/mL during extension. While interfaces prepared at 0.2 mg/mL and oscillated at the lowest frequency show a pure elastic response during extension, these show a strong strain softening response when oscillated at 0.05 Hz, that decreases when interfaces are further oscillated at 0.1 Hz (see Figures 5.13b). When plotting the *S–factor* as a function of frequency, we soon realised that the method fails to quantify the degree of nonlinearities shown in some Lissajous plots. For example, for interfaces prepared at 0.3 mg/mL, where the strain hardening response increases for the extension part of the cycle with increasing frequency (see Figure 5.10)c,d,f), while in Figure 5.13c we observe a lower *S–factor* at a frequency of 0.1 Hz than at 0.05 Hz.

The *S–factor* has been extensively used before satisfactorily by other authors to measure the magnitude of nonlinearities in Lissajous plots, both in complex interfaces [212] and complex bulk fluids [6] systems. Van der Berg and others, investigating the rod-like particles at interfaces, were probably the first reporting a positive *S–factor* in interfaces with squared-like Lissajous plots, which indicates a clear yield-like behaviour. The authors did not comment on the discrepancies observed between the results from the *S–factor* and the Lissajous plots [187]. Soon after, Yang and others, studying the role of different colloid systems structures

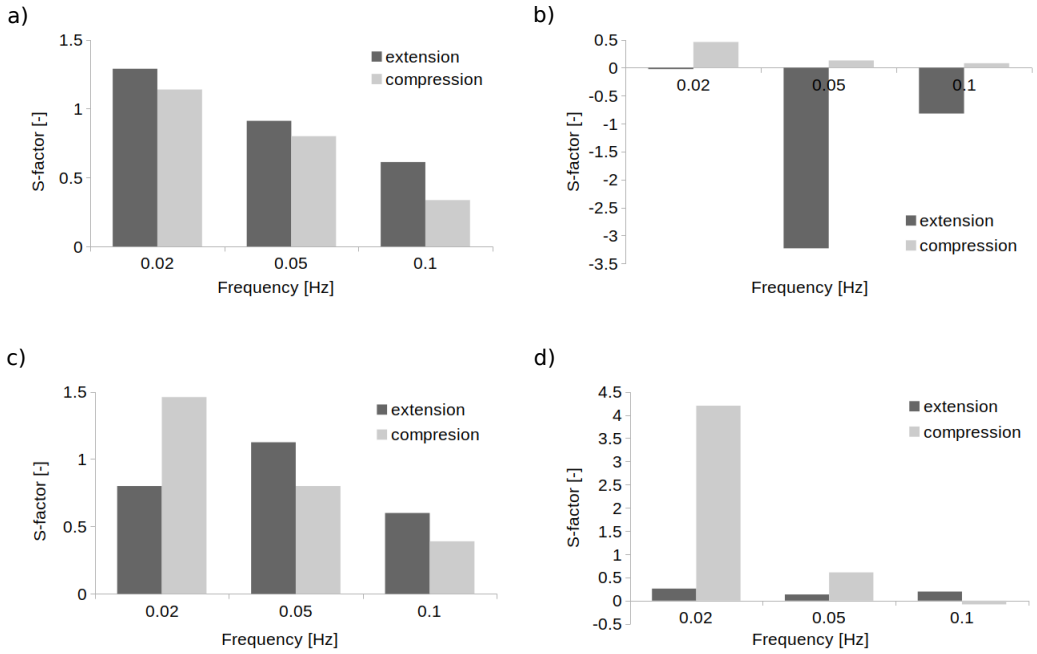

Figure 5.13 *Strain stiffening ratio S as a function of frequency, calculated from the Lissajous plots of interfaces made of 0.01 wt% NapFF prepared at* ***a:*** *0.1 mg/mL,* ***b:*** *0.2 mg/mL,* ***c:*** *0.3 mg/mL and* ***d:*** *0.4 mg/mL magnesium sulfate, oscillated at 16.5%. An S-factor with a value close to zero indicates an elastic response, a negative value corresponds to an intracycle strain softening, whereas a positive value refers to an intracycle strain hardening.*

at interfaces, came across with the same problem and attributed this error to the softening/hardening paradox reported before by Mermet-Guyennet and others [174].

Here, we report that the *S–factor* not only fails to quantify nonlinearities when the Lissajous plots show a clear softening/hardening paradox effect, as commented by Yang and others [174], but also fails for interfaces with a strain softening response. Figure 5.14 shows a Lissajous plot of a stable interface prepared at 0.2 mg/mL oscillated at 16.5% strain amplitude and 0.05 Hz, yielding at a strain ≈ -0.05 and hence exhibiting a strain softening response. Measuring E_{ME} in interfaces yielding at negative strain, may cause THIS to be smaller than E_{LE}, resulting in a positive *S–factor*, or strain hardening response.

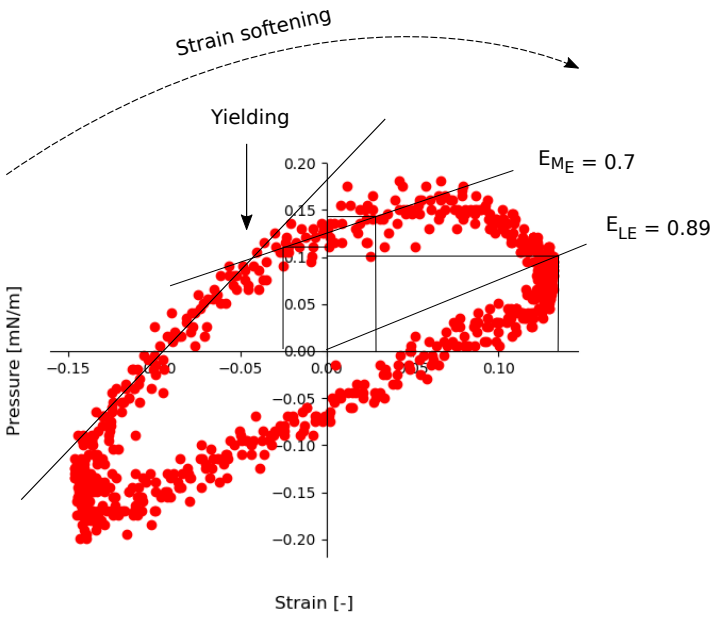

Figure 5.14 *Lissajous plot of an interface made of 0.01 wt% 2NapFF prepared at 0.2 mg/mL magnesium sulfate and oscillated at 16.5% and 0.05 Hz. The interfaces shows a clear strain softening response at a strain ≈ -0.05 that continues along the whole strain range. Interfaces yielding at negative strain, cause E_{ME} to be smaller than E_{LE} when they are measured at zero strain, resulting in a positive S–factor, characteristic of interfaces strain hardening.*

5.4.3 New approach to quantify nonlinearities

In this section, we report a more robust approach of reporting the *S–factor*, which is able to embrace nonlinearities at different strains. Rather than using the minimum-elastic modulus E_M or tangent modulus at zero strain to calculate the *S–factor*, we use the elastic modulus E (slope of the strain at that instant) to calculate the *S–factor*. The new *S–factor* is then:

$$S_{ext} \equiv \frac{E - E_{L,E}}{E_{L,E}} \tag{5.18}$$

$$S_{com} \equiv \frac{E - E_{L,C}}{E_{L,C}} \tag{5.19}$$

where S_{ext} and S_{com} are the new *S–factor* in extension and compression respectively. With these changes we can analise nonlinearities in a more robust way than the traditional *S–factor* presented in 5.3.2.

Figure 5.15 shows the new *S–factor* for extension and compression as a function of strain of an interface prepared at 0.2 mg/mL magnesium sulfate, oscillated at

16.5% and 0.05 Hz. The interface shows a positive *S–factor*, implying an elastic response at very low strains during extension. As the strain increases, the *S–factor* decreases and becomes negative at large strains, where the interface shows a strong strain softening, depicted by the Lissajous plot in the inset. The *S–factor* during compression shows an overall elastic response along the whole cycle.

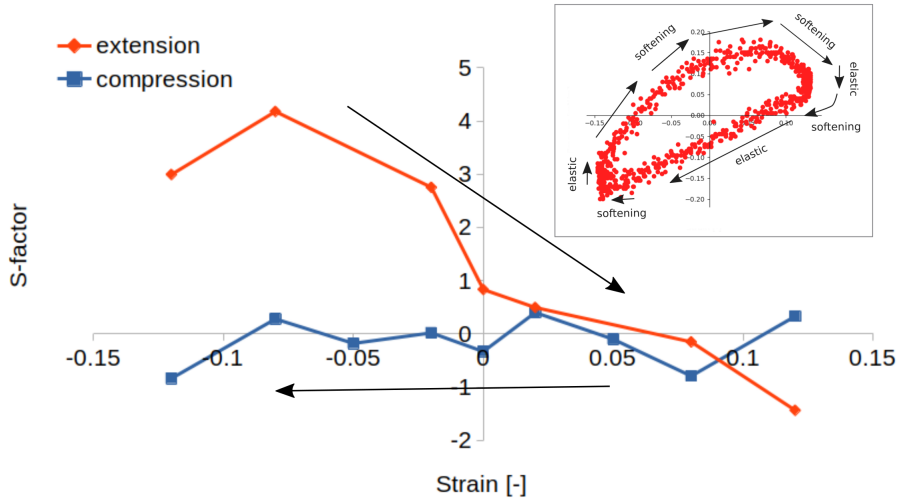

Figure 5.15 *S–factor as a function of strain calculated from the Lissajous plot of an interfaces made of 0.01 wt% 2NapFF prepared at 0.2 mg/mL magnesium sulfate and oscillated at 16.5% and 0.05 Hz. Black arrows indicate the direction of the cycle (expansion and compression). The inset shows the Lissajous plot from the interface the S–factor is being characterised. The black arrows are to aid with the interfaces response and indicates also the direction of the cycle. The S-factor calculated using the conventional approach in Section 5.4.2 is ≈ -3.2 for extension and ≈ 0.1 for compression.*

Similarly, the *S–factor* is positive in extension at low strains for interfaces prepared at 0.3 mg/mL magnesium sulfate, oscillated at 16.5% and 0.05 Hz (see Figure 5.16). The *S–factor* decreases with increasing the strain and becomes negative at a strain near zero, indicative of a weaker interface than interfaces prepared at 0.2 mg/mL. As the strain continues to increase, the *S–factor* keeps decreasing until reaches a strain equal to 0.08, where increases back from ≈ -1 to ≈ 0.2, hence indicating a hardening response by the end of the extension part of the cycle. This response is highlighted by the curved black arrow pointing upwards at large strains (Lissajous plot inset).

Interfaces prepared at 0.4 mg/mL magnesium sulfate oscillated at 16.5% and 0.05 Hz show a lower initial *S–factor* in extension than interfaces prepared at lower salt concentration (see Figure 5.17). The *S–factor* decreases with increasing the strain and reaches a negative value at a strain close to zero. The *S–factor* keeps

decreasing as the interface deforms further, until it reaches a minimum at 0.08 strain. At this point, the interface hardens, showed by the increase in the *S–factor* from ≈ -1.3 to ≈ 0.2. During compression, the *S–factor* decreases and increases along the whole strain range, with an overall elastic response, similar to that of the other interfaces prepared at lower salt concentration.

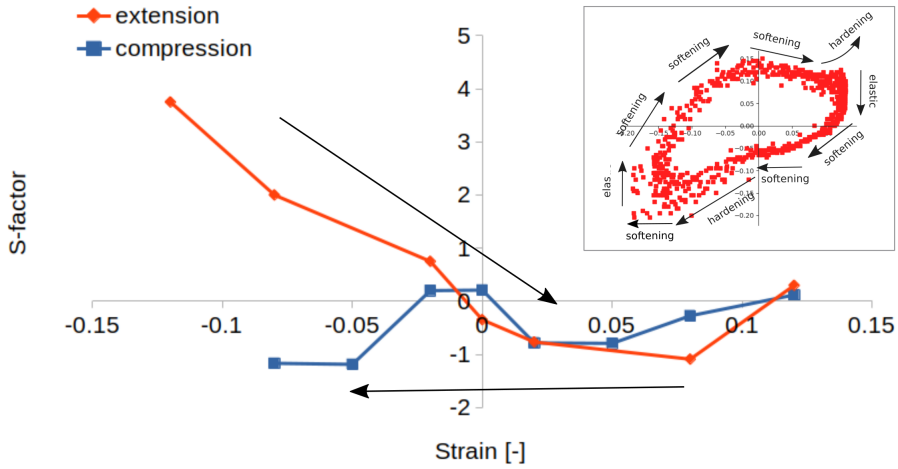

Figure 5.16 *S–factor as a function of strain calculated from the Lissajous plot of an interface made of 0.01 wt% 2NapFF prepared at 0.3 mg/mL magnesium sulfate and oscillated at 16.5% and 0.05 Hz. Black arrows indicate the direction of the cycle (expansion and compression). The inset shows the Lissajous plot from the interface the S–factor is being characterised. The black arrows are to aid with the interface response and indicates also the direction of the cycle. The S-factor calculated using the conventional approach in Section 5.4.2 is ≈ 1.1 for extension and ≈ 0.8 for compression.*

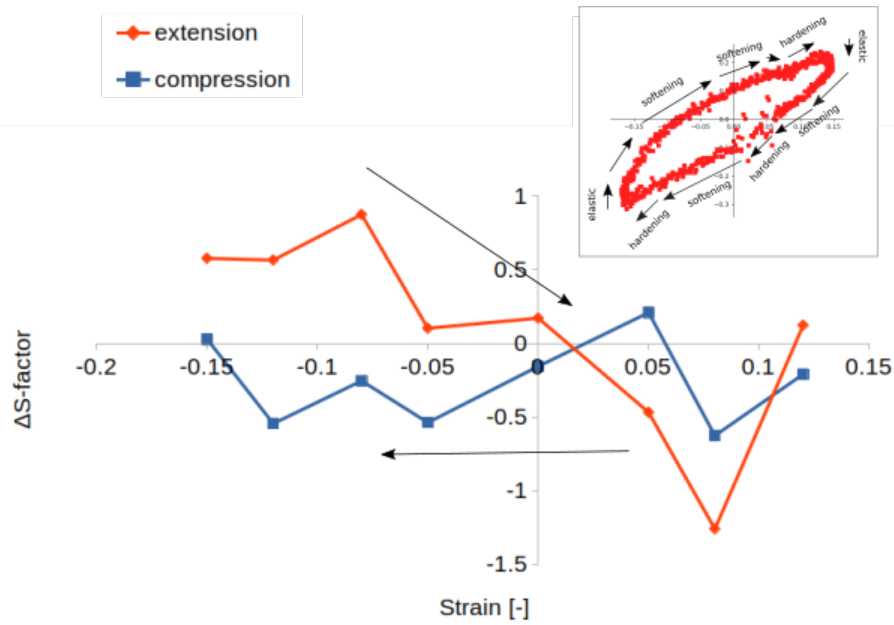

Figure 5.17 *S–factor as a function of strain calculated from the Lissajous plot of an interface made of 0.01 wt% 2NapFF prepared at 0.4 mg/mL magnesium sulfate and oscillated at 25% and 0.05 Hz. Black arrows indicate the direction of the cycle (expansion and compression). The inset shows the Lissajous plot from the interface the S–factor is being characterised. The black arrow are to aid with the interface response and indicates also the direction of the cycle. The S-factor calculated using the conventional approach in Section 5.4.2 is ≈ 0.1 for extension and ≈ 0.6 for compression.*

5.5 Conclusions

In this chapter we have further examined the rheological properties of interfaces made of dipeptide fibres prepared at different salt concentrations by performing strain and frequency sweeps via a drop profile tensiometer. Interfaces oscillated at 8%, exhibit Lissajous plots with an ellipse shape, which tell us that the viscoelastic properties of the interfaces are still in the linear regime. Nonlinearities start to appear at 16.5% and become more marked at 25%. Interfaces prepared at 0.4 mg/mL magnesium sulfate show the highest elastic response of all interfaces, with a pressure increasing after yielding. At the other end, interfaces prepared at 0.1 mg/mL and 0.3 mg/mL present weaker interfaces with the pressure decreasing once the interfaces reach zero strain. In between, interfaces prepared at 0.2 mg/mL magnesium sulfate, show a more viscoelastic response, with interfaces strain softening as they are being enlarged. The surface pressure only decreases when interfaces have reached the maximum strain where the strain rate is zero. A strain hardening effect is observed in interfaces prepared at 0.3 mg/mL and

0.4 mg/mL at large strains in extension that to our knowledge, has never been reported in oscillatory dilatational rheology before. Finally, we realised that the *S–factor* used to quantify nonlinearities in Lissajous plots fails when these are from interfaces with softening/hardening paradox response and with a clear strain softening response yielding at negative strains. Therefore, we propose a different approach capable of taking into account nonlinearities that span over the whole range of strains. Finally, this approach could be extended to quantify the nonlinear material properties of complex bulk fluids subjected to large amplitude oscillatory shear as well.

Chapter 6

Effect of salt triggered hydrogel emulsions on the lipid digestion; an *in vitro* study

6.1 Abstract

The mechanical properties of hydrogel emulsions made of 2NapFF prepared at different salt ($MgSO_4$ and $CaCl_2$) concentrations (1–4 mg/mL) were investigated to determine the impact of salt on lipid digestion. The rate of hydrolysis was calculated using an *in-vitro* intestinal digestion model for two hours. The microscopic characteristics of fresh and digested emulsions were analised using confocal laser scanning microscopy (CLSM) and laser light scattering. The rate and extent of lipid bioaccessibility was higher for emulsions prepared with calcium chloride and increased with salt concentration. In addition to this, we observe that the rate and extent of lipid digestion does not increases monotonically for emulsions prepared with magnesium sulfate, which could be due to the non-monotonic effect shown in Chapter 4. We surmised that the faster lipolysis observed in emulsions prepared with calcium chloride may be due to the rigid network, which could become extremely fragile under stress. These results indicate that the mechanical properties of emulsions play an important role on lipid digestion and hence these must be taken into account when designing novel emulsion-based foods.

6.2 Introduction

Immiscible liquids are brought together in many natural and technological circumstances. When mixed, by mechanical or chemical energy, these immiscible liquids transform into emulsions, which have already been introduced in Chapter 1. Emulsions have been exploited by academic and industrial researchers for many years because they add something new. For example, placing active constituents inside coated oil droplets, has lead to the construction of delivery systems for protection, transport and release [213]. It is increasingly clear, that a well designed matrix for such systems is crucial, not just because it protects functional ingredients from enzymatic reactions and mechanical forces, but because influences the rate and extent in the gastro-intestinal tract [214, 215]. This has been nicely demonstrated by Dias and others, by showing the effect of food structure on lipid digestion through *in vitro* oral, gastric and intestinal digestion. Experiments were also carried out *in vivo* with healthy young adults consuming the same test foods as for in vitro experiments. Three samples, made with the same ingredients and calorie content were prepared in different ways. Liquid and semi-solid samples were prepared by mixing the ingredients with water in a blender; the latter was placed in a water bath and baked at 180 °C for 30 minutes after mixing. For solid samples, a higher concentration of oil was used to prepare a dough, which was later baked at 120 °C for 18 minutes. Solid foods differed from the alternatives in that had a lower pH, bigger droplet size and smaller amount of fat collected at the end of the gastric digestion, hence affecting the digestion kinetics during intestinal digestion addition. In addition, the solid food delivered higher fullness and satisfaction among participants and resulted being more healthy, with a lower increase in serum triglycerides than the liquid food. [216]. Similarly, the effect of different dairy systems on lipid and protein bioaccessibility in an in vitro digestion model was studied by Mulet-Cabero et al. [217]. Both samples had the same caloric content; the first was a mixture of cheese and yogurt with a semi-solid matrix and the second an oil-in-water emulsion with a liquid bulk. The samples presented structural changes during the gastric phase; the semi-solid sample sedimented and the lipid sample creamed. These changes affected nutrients adsorption in the small intestine, with the semi-solid sample showing a slower release than the lipid sample.

Sometimes, like in the case of cheese and yogurt mentioned above, enzymes are used that cause reactions so that the pH of the food is altered and consequently its structure, with the aim of achieving more stable products, among many other

things, i.e., achieve the desired flavour and texture or increase shelf life. On other occasions, salts that form bonds with proteins (known as salt bridges) are used sometimes for similar reasons. It is more and more apparent, that salts play an important role on the kinetics and degree of lipid digestion. For instance, the presence of calcium chloride has been observed to be essential for the activity of pancreatic lipase [218–220]. Similarly, in one study the authors found that the rate of total free fatty acids (FFAs) released from the interface increased with calcium chloride concentration for emulsions stabilised by different surfactants [221]. Another study showed that after an initial increase in the rate of lipolysis influenced by the concentration of bile salts during the first 5 minutes, the rate of lipolysis became directly related to calcium chloride concentration [222].
Since scientists realised of the potential link between health and nutritional attributes to the properties of foods, there is a special interest in controlling the digestibility of lipids within the gastrointestinal tract [223–226]. Many of these studies have been conducted via *in vitro* models, proving to be a powerful tool to study a number of aspects, including structural changes, digestibility and release of food constituents within the upper gastrointestinal (GI) tract [227]. The GI tract consisting of mouth, stomach and small intestine, providing insights in the physicochemical processes occurring during digestion. Static *In vitro* methods can then be correlated with those obtained using *in vivo* studies to predict possible effects of food on human health [228, 229]. In static *in vitro* models, the main digestion conditions of pH, enzyme activity, temperature are fixed in each step. This methodology is simple to use, more accessible and reproducible. However, it cannot simulate some complex processes that occur in the GI tract such as the mechanical contractions of the stomach, the gastric emptying or the progressive delivery of the digestive fluids, which is better simulated in semi-dynamic and dynamic digestion models. Recently, a standardised static in vitro static digestion protocol has been developed by the INFOGEST COST Action, which allows obtaining data that can be compared [230]. To mimic the small intestinal conditions, the pH stat method is among the most chosen methods used to investigate the digestion kinetics of macronutrients (i.e., proteins, lipids and carbohydrates)[220, 229]. A schematic representation of the pH stat *in vitro* digestion model used to determine lipid digestibility is shown in Figure 6.1. The emulsion, placed in a vessel with the simulated intestinal fluid (SIF), is kept to a constant pH by adding a volume of NaOH to neutralise the FFAs released from TAGs during a 2 hours digestion.

Lipid digestibility involves hydrolysis of triglycerides (TAG) by enzymes,

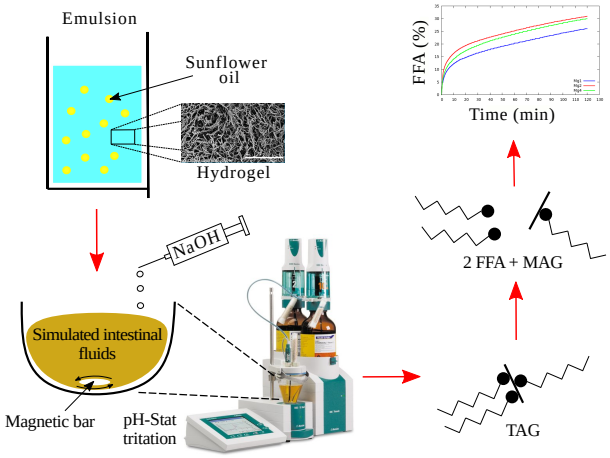

Figure 6.1 *Schematic of a static in vitro digestion model used to determine lipid digestibility. See Methods section for lipid digestion protocol.*

with 5-40% [231] occurring in the stomach by gastric lipase and generating diacylglycerols (DAGs), free fatty acids (FFAs) and some 2-monoacylglycerols (2-MAG)[232]. Hydrolysis continues in the small intestine, where pancreatic lipase and estereases together with colipase and bile salts [233] break TAGs and DAGs further down into FFAs and 2-MAG [232]. When fully digested, two FFAs are released from each TAG, hence the percentage of FFAs can be calculated by knowing, (i) the amount of total TAGs present in the vessel and (ii) the number of total FFAs released after a certain digestion time [234]. Li and McClements, developed a mathematical model that characterises FFAs as a function of time resulting from the pH stat method. To calculate the FFAs released, the authors divide the number of moles of alkali (NaOH) needed to neutralise the FFAs by the number of moles of FFAs release from a TAG after a full digestion (assumed to be 2 FFAs per TAG after a full digestion) [234]:

$$\%FFAs = 100 \times \left(\frac{V_{NaOH} \times m_{NaOH} \times M_{lipid}}{W_{lipid} \times 2} \right)$$

where V_{NaOH} is the volume of sodium hydroxide needed to neutralised the FFAs released, m_{NaOH} is the concentration of the sodium hydroxide used (in M), W_{lipid} is the total mass of the triacylglycerol oil initially present in the vessel (in g) and M_{lipid} is the molecular weight of the TAG (in g/mol[1]) [234].

In this chapter, we investigate the effect of salt triggered hydrogel emulsions with different mechanical properties on the lipid digestion using a static *in vitro* model. The main goal of this chapter, was to verify whether the mechanical properties of

the emulsions have any impact on the rate and extent of lipid digestion. The results show that the rate and extent of lipolysis increases, at short and at long periods for emulsions prepared with calcium chloride. We surmise that this effect is mainly due to the structure of the emulsions becoming too brittle, hence disrupting faster under mechanical forces. Under this scenario, oil droplets are released faster from strong but brittle matrices, than from weaker but flexible ones i.e., with more viscoelastic properties. For emulsions prepared with magnesium, we observe a non-monotonic effect dependence of digestion on salt concentration; at an intermediate salt concentration, emulsions showed higher rate and extent lipolysis than emulsions prepared at the lowest and highest salt concentrations. These are preliminary results and therefore a greater number of experiments need to be performed to investigate further the effect of stiffness on digestibility.

6.3 Materials and methods

6.3.1 Materials

2NapFF was synthesised as described previously [42]. Sunflower seed oil from Helianthus annuus was purchased from Sigma-Aldrich and treated with Florisil® (Sigma, Poole, UK) to remove polar, surface-acive compounds from the oil. The enzyme activities and bile salt concentrations in the bile extracts were measured according to the assays detailed in [230]. The solvents hexane and ethanol, were purchased from Fisher Scientific UK. All other chemicals used were of analytical grade and were obtained from Sigma-Aldrich unless specified.

6.3.2 Methods

Hydrogel preparation

Hydrogels and emulsions used in this study were prepared using the procedures described in [1]. Before 2NapFF molecules are dispersed, a high pH environment needs first to be created. To do so, 0.3 mL NaOH (0.1 M aq) aliquots were added to millipore water (resistivity = 18.8 MΩ. cm). Then, 0.5 wt% 2NapFF were added to the basic solution, which was then placed in an ultrasonic bath for 1 hour and stirred with a magnetic bar until a clear solution was achieved. Gelation was triggered by adding calcium chloride or magnesium sulfate already dissolved on top of the clear solution by pipetting 1, 2 or 4 mg/mL (1M aq) and left to stand for 12 hours at room temperature to equilibrate.

Table 6.1 shows the salts and concentrations used during the experiments to (i) trigger gelation and (ii) perform the digestions, such as that recommended in simulated intestinal fluids (SIF) from the INFOGEST protocol. The maximum salt concentration used to trigger gelation was 36.7 mM for calcium chloride and 16.5 mM for magnesium sulfate, whereas in the vessel was 5.7 mM and 2.3 mM respectively.

Table 6.1 *Salt concentration used in each sample to form the gels and the total salt concentration used for the digestions (including the recommended concentration in Simulated Intestinal Fluid (SIF) from INFOGEST protocol).*

Salt	Total salt in sample (mg/sample - mmol L^{-1})	Total salt in SIF (mmol L^{-1})	Total salt in vessel (mmol L^{-1})
$CaCl_2$	5 - 9	0.6	1.86
	10 - 18	0.6	3.12
	20 - 36.74	0.6	5.74
$MgSO_4$	5 - 4.05	-	0.56
	10 - 8.11	-	1.13
	20 - 16.5	-	2.31

Emulsion preparation

Emulsions were prepared by adding 5% sunflower oil to the gels, which were then mixed using an ultra-turrax (IKA Eurostar 40), operating at 10,000 rpm (shear rate $\approx$ 17,135 s^{-1}) and 8 mm head for 50 seconds.

Small intestinal in vitro digestion of emulsions

The small intestinal digestion was simulated using the pH stat method and the INFOGEST static digestion conditions as described in [235]. The simulated intestinal fluid (SIF) was made in the same manner than that in INFOGEST static digestion but sodium bicarbonate ($NaHCO_3$) was replaced by sodium chloride (NaCl) to avoid pH changes due to the formation of CO_2. 5 grams of emulsion sample was placed in a reaction vessel jacketed at 37 °C. The final composition in the reaction system was 0.006 wt% lipid, 10mM bile salts and 500 μ/mL pancreatin (based on lipase activity). The pH was maintained at 7.0 by constant titration of 0.1 M NaOH into the digestion mixture, using an automatic potentiometric titrator (AT-700, KEM, Japan) for 120 minutes, and constant stirring (500 rpm). The percentage of FFAs released was then calculated from

the volume of NaOH solution used to neutralise the FFAs using Equation 6.2. The digestion of each salt concentration was performed in triplicate.

Droplet size distribution of emulsions

The droplet size distribution of emulsions was measured immediately after emulsion preparation and after *in vitro* intestinal digestions by using a laser diffraction particle size analyser (Beckman Coulter, LSI3320, Fullerton, CA, USA). A minimum volume of initial and digested emulsions was used to reach 8% laser obscuration when possible. The relative refractive index parameters used during measurements were 1.473 for the dispersed phase (sunflower oil) and 1.333 for the bulk. The absorbance value for the droplets was 0.001.

Confocal laser scanning microscopy (CLSM)

Measurements were carried out using confocal laser scanning microscopy (Model Leica TCS SP5). 0.1 % Nile red in polyethylene glycol and 0.1 % fast green in water were used to label the dipeptides and the lipid respectively. 50 μL of the mixed dyes was then added on top of 500 μL of the initial/digested emulsion sample and gently stirred until mixed. Nile red and fast green dyes were excited using an argon laser at 488 nm and HeNe laser at 633 nm respectively. Enzymatic activity was stopped immediately after emulsions were prepared and digestions had finished. Aliquots of a previously prepared mixture made of 100 mg of 4-bromophenylboronic acid dissolved in 0.5 mL of methanol were added to 0.5 mL emulsion samples by pipetting 2.5 μL aliquots of this mixture plus 50 μL of Bowman-Birk inhibitor (BBI) on top of these. Finally, to stop oil droplets undergoing flocculation and/or coalescence, formalin was added on top of these solutions, such that the final ratio of formalin to the initial emulsion sample (0.5 mL) was 1:10. Samples then were left in the fridge until confocal microscopy was conducted (24-48 hours). Dipeptides and lipids were labelled by using nile red and fast green FCF respectively at a ratio of 1:1. Then, 500 μL of the emulsion (either initial, digested or control), was gently mixed with 50 μL of mixed dye. Finally, a droplet of the final mixture was placed on a microscope slide, excited with a semiconductor laser at 633 nm and 488 nm and measured with a 63× oil immersion objective.

6.4 Results and Discussion

In an effort to determine whether the hydrogel reforms between oil droplets after emulsification, emulsions prepared with calcium chloride and magnesium sulfate were inverted to perform an inverted vial test. This test is used for phase behaviour determination; vials containing the sample are turned upside-down to observe whether the sample supports its own weight [207]. Hydrogels and emulsions prepared in the same way as for those used in digestions were left upside-down for 12 hours. After 12 hours hydrogels prepared with calcium chloride and magnesium sulfate passed the test satisfactory. However, after the hydrogel has being disrupted by the ultra-turrax to form the emulsion, only those prepared with calcium chloride reformed again between oil droplets. Emulsions prepared with magnesium sulfate resulted in primarily viscous properties, with samples flowing slowly when the vial was inverted. In the case of emulsions prepared with calcium chloride, the emulsions are solid and become stiffer when the salt concentration is increased (observed when manipulating the sample with a spatula).

Figure 6.2 shows the microscopic characteristics of initial emulsions (left hand side column), digested emulsions after 2 hours of digestion by pancreatin (middle column) and control emulsions after 2 hours of digestion with no pancreatin added (right hand side column). Initial emulsions prepared with calcium chloride shows a network made of stiff fibres with distorted oil droplets entrapped in it (see Figure 6.2 left hand side column). Light being scattered increases with salt concentration, suggesting that a higher number of cross-links among interfibres of supramolecular nanofibres within the hydrogel increases along with the storage moduli [150]. The strength of hydrogels made of 2NapFF and triggered with calcium chloride have been found to increase with salt concentration before. At a ratio of 1:1 calcium chloride ions to COOH from 2NapFF the hydrogel strength reaches its maximum, which if this is surpassed, the strength decreases to values of lower calcium chloride concentration [2, 150] (in this study we never reached such a threshold). By contrast, emulsions prepared with magnesium sulfate, led to emulsions with a more homogeneous matrix made of small fibres and spherical oil droplets are bigger than those observed in emulsions prepared with calcium chloride. After 2 hours of digestion with pancreatic enzymes, lipids and dipeptides have vanished, which suggests that have been digested (see Figure 6.2 middle column).

Control emulsions were prepared to verify that dipeptides and lipids had been

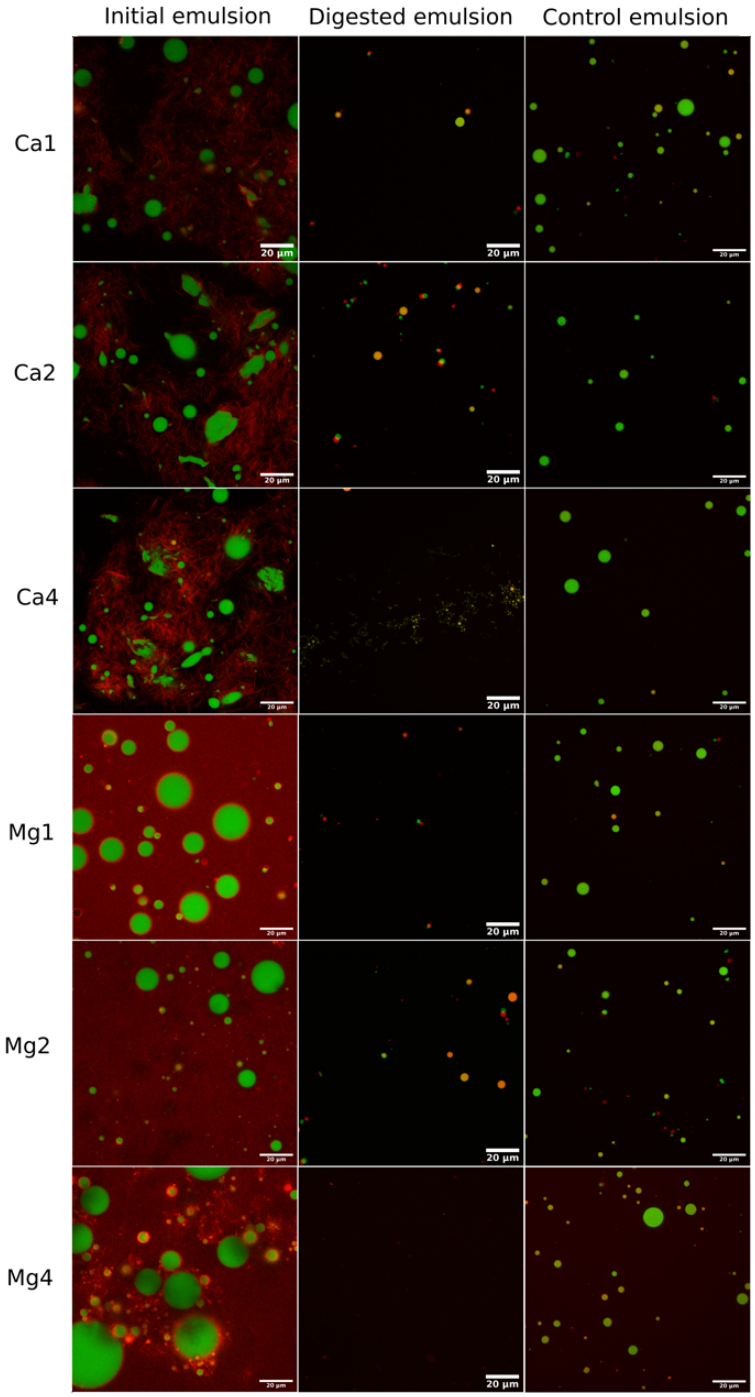

Figure 6.2 *Microscopic characteristics of 0.5 wt% 2NapFF and 5 % sunflower oil emulsions, prepared at 1, 2 and 4mg/mL calcium chloride and magnesium sulfate. Images were taken for initial (left hand side column), digested (middle column) and control (right hand side column) emulsions. Dipeptides fibres and lipid droplets were labelled with Nile Red and Fast Green FCF respectively. Scale bar is 20 µm.*

digested by pancreatic enzymes and these did not vanish because of agitation. Controls were performed in the same manner than the digestions but without the inclusion of pancreatin (see Figure 6.2 right hand side column). After 2 hours of simulated digestion, dipeptide fibres surrounding the oil droplets have vanished (note that in the case of emulsions prepared with calcium chloride the oil droplets have been pulled back into a spherical shape). We believe that the structure of emulsions get destroyed by placing the emulsions together with the SIF in the reaction vessel and by agitation. However, oil droplets, although lower in number and size than in initial emulsions, remain in the sample. It is possible, that agitation may not be so fast as to prevent larger oil droplets from rising to the surface. Based on these results, it is clear that mechanical agitation aids lipid hydrolysis by disrupting the hydrogel network in the continuous phase in such a way that it is less difficult for enzymes to reach the interface of oil droplets.

Figure 6.3 shows the droplet size distribution curves, as determined by laser light scattering of initial, digested and control emulsions. Overall, a broad size distribution is observed in all emulsions, characteristic of emulsions with a wide spectrum of oil droplet sizes. The size distribution was remarkably similar between salt concentrations for initial emulsions prepared with calcium chloride, with 80% of the volume being between 24 and 213 $\pm$ 0.15 μm in diameter. On the contrary, the droplet size distribution for initial emulsions prepared with magnesium sulfate is diverse, with shoulders at low (2 mg/mL) and large (4 mg/mL) droplet size and increases with salt concentration, with a 90% volume percentile (Dv90) of 123, 178 and 282.6 μm for 1, 2 and 4 mg/mL respectively. We observed a similar behaviour before in Chapter 3, where foams made of hydrogels triggered with magnesium sulfate resulted in higher-quality foams with small average bubble size when prepared at lower salt concentrations. After 2 hours of digestion, the volume of large oil droplets decreases, while the volume for small oil droplets with sizes between 0.1 and 1 μm increases. Droplet size distributions in the controls are similar to those observed in initial emulsions, albeit with a slightly smaller average oil droplet size, most probably caused by agitation.

When we compare the methods used to measure the droplet size distribution of the emulsions, we notice a large disagreement between them. While confocal images show an average droplet size of approximately 11 and 13 μm for calcium chloride and magnesium sulfate respectively for initial emulsions (see Figure 6.4), this increases almost an order of magnitude (91 and 112 μm) when measured with laser light scattering (see Figure 6.3a,b). These discrepancies may be because of the samples used in the confocal were diluted and left in the fridge for 24–48

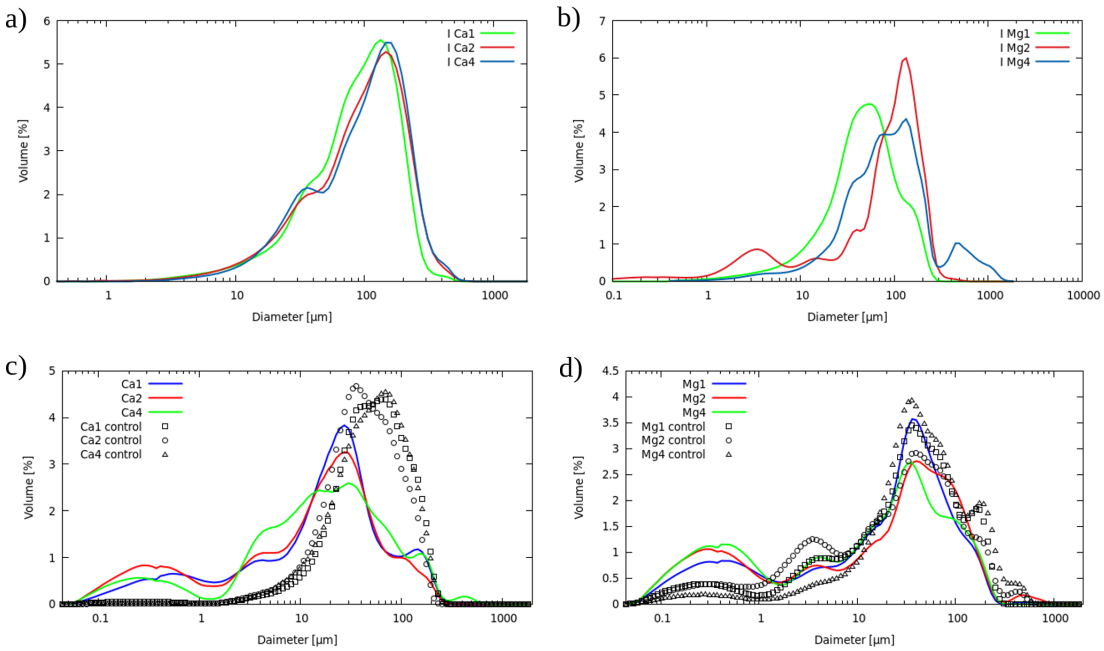

Figure 6.3 *Droplet size distribution curves as determined by laser light scattering of 0.5 wt% 2NapFF and 5% sunflower oil emulsions. Initial emulsions prepared with* ***a:*** *calcium chloride and* ***b:*** *magnesium sulfate. Emulsions after 2 hours of digestion by pancreatin (solid lines) and with no pancreatin added (empty symbols) prepared with* ***c:*** *calcium chloride and* ***d:*** *magnesium sulfate (mean = 3).*

h. The gel network between oil droplets is disrupted when diluting the samples and it is possible that bigger droplets without this structure, cream, coalescence and ultimately phase separate. Under this scenario, tiny droplets will remain for longer than bigger ones. In fact, the microscopic characteristics of emulsions prepared in a similar manner to the emulsions used in the digestions, (albeit with different oils), had a droplet size of approximately 100 μm (Chapter 3), which are in line with measurements taken with the laser light scattering approach (see Figure 6.3).

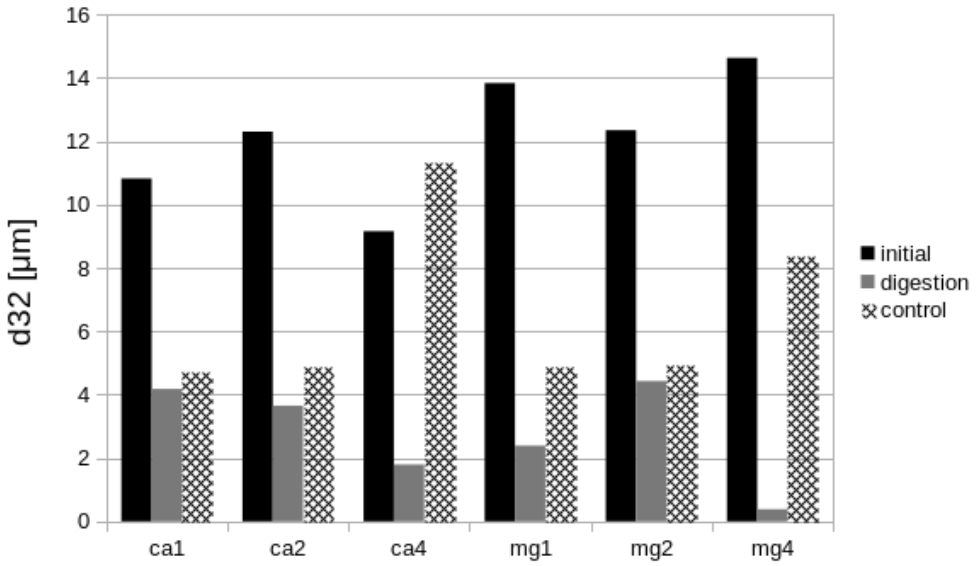

Figure 6.4 *Mean surface diameter ($D_{3,2}$) measurements of 2NapFF 0.5 wt% and 5% sunflower oil emulsions calculated from confocal images from Figure 6.2.*

Figure 6.5 shows the total amount of FFAs released from emulsions in the presence of different calcium chloride and magnesium sulfate concentrations during a static *in vitro* intestinal digestion as a function of time. Lipids in emulsions prepared with calcium chloride were digested rapidly within the first minute with approximately 6% of total FFAs released, followed by a progressive increase to 32 , 35 and 41 % hydrolysis for 1, 2 and 4 mg/mL calcium chloride respectively after 2 hours. Similarly, the amount of total FFAs released from emulsions prepared with magnesium sulfate increased fast during the first minute, proceeded by a rather slower increase hydrolysis compared to emulsions prepared with calcium chloride. Interestingly, unlike emulsions prepared with calcium chloride, the total FFAs released did not increase monotonically for these emulsions. Emulsions prepared with magnesium sulfate at 1 and 4 mg/mL shown a total FFAs released of about 5%, whereas for emulsions prepared at 2 mg/mL, the total FFAs increased roughly to 9% within the first minute. At longer periods, lipids in emulsions prepared at 2 mg/mL were again digested faster than lipids in emulsions prepared at low and high salt concentrations, with the former reaching a total lipolysis of approximately 34% and the later 26 and 30% after 2 hours of digestion.
The rate of lipolysis increases rapidly for the first minute but suddenly decreases and grows more slowly for all emulsions; first this decreases after one minute and subsequently levels off again at about after 10 minutes. These changes have been observed to be caused for different reasons. In bulks liquids, the change can be

caused by oil droplets flocculating and/or coalescing. On the contrary, for dense samples like solid gels, these changes can be induced by a lower concentration of enzymes at lipid interfaces. For example, before lipase and co-lipase enzymes can reach the interfaces, they first have to diffuse through the hydrogel matrix. Soon after, FFAs and monoacylglycerols (MAG) will have to diffuse back out of the matrix to avoid building up at the interface, thereby delaying lipolysis [236, 237].

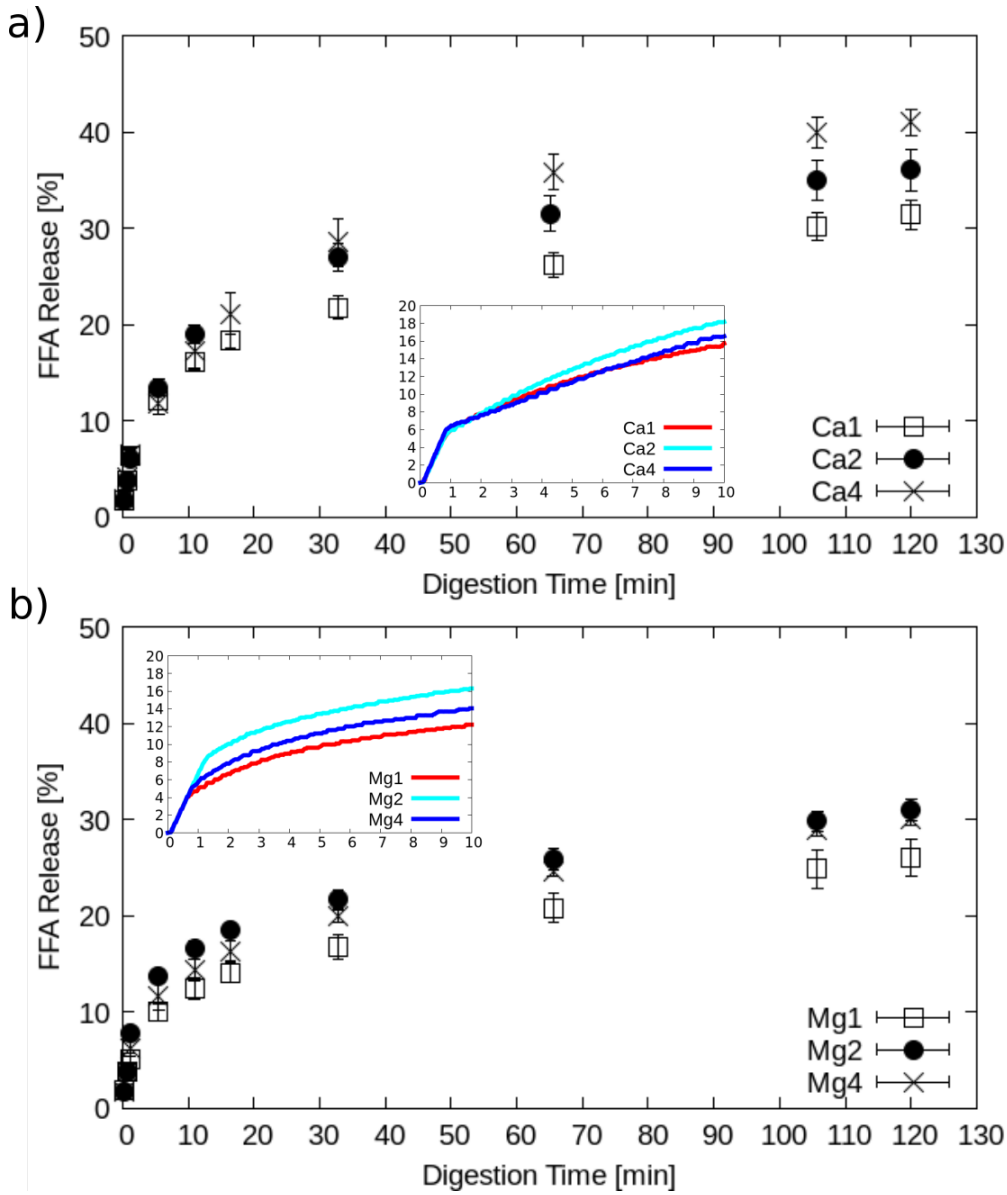

Figure 6.5 *Influence of* ***a:*** *calcium chloride and* ***b:*** *magnesium sulfate in the pH-stat reaction vessel on the rate and extent of lipid digestion determined by monitoring the FFAs released over time. Insets show the first 10 minutes of digestion (mean ± standard deviation, n = 3).*

Soluble salts have been observed to release FFAs at a faster rate than insoluble

ones [238]. This would have explain the faster lipolysis observe in emulsions prepared with calcium chloride, hence this is twice as soluble (740 mg/ml) as magnesium sulfate (350 mg/ml). However, the concentrations of magnesium sulfate and calcium chloride used in this chapter were far way below the saturation concentration and hence we believe this did not have a direct effect on the higher rate and extent of lipolysis observed in calcium. More recently, Torcello-Goméz et al. found that the presence of calcium chloride promotes the kinetics of lipolysis due to the complexation between the ions and the fatty acids [239]. Furthermore, long chain fatty acids were found to precipitate in the presence of calcium chloride, thereby accelerating lipid digestion [222]. However, in some cases the use of calcium chloride has been found to slow down hydrolysis [240]. This may be related to the fact that calcium chloride is sometimes used to trigger gelation during gel formation, hence this has been found to increase the moduli of the gels orders of magnitude higher than other salts [2]. More specifically, the moduli of the hydrogels made of 2NapFF have been found to increase with calcium chloride concentration until it reaches a maximum before starts to decrease again (we never reached such threshold) [2]. Certainly, the strength and structure of the gel has been observed to affect the rate of digestion, where weak gels break down and release oil droplets more rapidly than stronger ones [240–242]. In spite of emulsions prepared with calcium chloride having a higher moduli than emulsions prepared with magnesium sulfate, lipids in the former are digested faster and to a higher extent than in the latter.

Droplet size have been found to influence the rate and extent of lipid digestion [243]. Given that the surface area is inversely related to the size of the droplets [244] and lipid digestion is an interfacial process [243], it is fair to think that the rate of lipid digestion should increase for emulsions with smaller droplets. However, the digestion rate and extent for emulsions prepared at 1 mg/mL $MgSO_4$, with the smallest droplet size of all emulsions studied here (see Table 6.2), were found to be the ones with slowest rate and extent of all digestions. What is more, emulsions prepared with calcium chloride, with an overall bigger droplet size, shown a faster rate with higher extent lipolysis compared to emulsions with lower droplet size.

Table 6.2 *Volume percentiles calculated from the droplet size distribution curves from Figure 6.3.*

Salt	Concentration (mg/mL - mmol L^{-1})	Initial	Digested	Initial	Digested
		Dv10 (μm)	Dv10 (μm)	Dv90 (μm)	Dv90 (μm)
$CaCl_2 \bullet 2H_2O$	1 - 1.5	24.95	0.63	185.57	88
	2 - 3.0	23.84	0.34	213.21	69.61
	4 - 6.1	24.95	0.55	213.21	92.10
$MgSO_4 \bullet 7H_2O$	1 - 0.6	12.40	0.34	123	92.10
	2 - 1.3	3.52	0.25	178	111
	4 - 2.5	21.72	0.25	282.56	101.01

6.5 Conclusions

Lipid digestion in the small intestine was simulated using the pH stat method in order to study the impact of the mechanical properties on the lipid digestion. Emulsions were stabilised by dipeptide hydrogels with salt tunable matrices. These results should be considered preliminary given that experiments were undertaken during a visit to a collaborating laboratory and the time was limited. The strength of the matrix holding the droplets in place is higher for emulsions prepared with calcium chloride than for emulsions prepared with magnesium sulfate. In the case of emulsions prepared with calcium chloride, the gel reforms between oil droplets after this has been disrupted during emulsification. Furthermore, the stiffness of the gel increases with salt concentration. In contrast, emulsions prepared with magnesium sulfate flow slowly after emulsion formation and it is not clear whether the strength of the structure increases with salt concentration. The rate and extent of lipid digestibility was observed to be higher for emulsions prepared with calcium chloride than with magnesium sulfate. Despite emulsions prepared with calcium chloride having very similar droplet size, the speed and total FFAs released increases with salt concentration, theoretically due to the number of calcium soaps rising with the amount of salt and being removed from the interface afterwards. Emulsions prepared with magnesium sulfate, shown a non-monotonic dependence of digestion on salt. At intermediate salt concentrations, emulsions prepared with magnesium sulfate exhibited the highest lipolysis rate and extent of its counterparts (1 and 4 mg/mL). The volume of tiny droplets is also higher for intermediate salt concentration emulsions,

which could make us believe that the digestion rate could have been affected by this, rather than because of salt concentration. However, droplets in emulsions prepared at 4 mg/mL, were significantly bigger compared to emulsions prepared at 1 mg/mL and we did not observe a lower rate or extent for these emulsions. Based on these results, we surmise that strong emulsions with a rigid matrix can be significantly fragile. Under stress, brittle emulsions reach their maximum strain values before emulsions with higher viscoelastic properties, hence breaking at shorter elastic deformations. In such scenario, oil droplets within strong highly elastic networks - such as those observed in emulsions prepared with calcium chloride - would be released faster under a mechanical force than droplets immersed in weaker, yet more deformable matrices. Certainly, more experiments need to be performed to turn this initial sketch into a complete picture. Nonetheless, based on our results, we believe that it is worthwhile to investigate the effect of hydrogel-emulsions with different mechanical properties on the lipid digestion.

Chapter 7

Conclusions and Outlook

7.1 Emulsions stabilised using dipeptide hydrogel fibres

In this thesis, we have investigated the behaviour of dipeptide molecules (2NapFF and ThNapFF), that are able to form hydrogels that we use to impart stabilisation to emulsions. Dipeptides molecules behave as an emulsifier, as a stabiliser and as a gelling agent. When dispersed in a basic solution ($\approx$ 11 pH), dipeptides self-assemble to form nanofibres that adsorb to liquid-liquid interfaces. At high enough concentration, the nanofibres start to entangle in response to the addition of metal ions, holding large amounts of water and subsequently solidifying the continuous phase.

We have investigated the behaviour of 2NapFF at low concentration (0.1 wt%) in Chapter 3. To do this, we first have presented a route to achieve repeatable hydrogels. Here, various methods and temperatures have been studied to improve dipeptide dispersion. Following this, we tried different routes to trigger gelation, until stable hydrogels, with no signs of phase separation were achieved. We then use the hydrogels to form foams and emulsions using different oils. Foams became less stable than foams prepared at higher 2NapFF concentrations studied in [56]. However, emulsions remained stable for more than one year. While dipeptide fibres are found to adsorb to air-water interfaces, the gel structure is now too weak to keep the bubbles immobile. Evidently, this is not the case for emulsions, where drops, with higher similarity in density to water than bubbles, seem not to be affected by the lack of gel network at such dipeptide concentration.

Next, during emulsification, droplets and thin films deform under shear flow. To mimic this behaviour, we have investigated the dynamic behaviour of interfacial

films under uniaxial stretching using a custom made interfacial extensional tensiometer (see Figure 4.4) in Chapter 4. Hydrogels made of 2NapFF and ThNapFF prepared with different salts and salt concentrations were placed between two open circular rings of equal diameter (see Figure 4.5) and stretched at different velocities. As the lower ring is set in motion, the hydrogel stretches until eventually becomes a film. The main results of this chapter are that film's collapse is salt dependent. Hydrogels prepared with $CaCl_2$ turned into elastic solid films that collapse immediately after the film has formed. By contrast, hydrogels prepared with sodium chloride developed into extremely viscous films that flow when the ring reaches its maximum aperture. In between, hydrogels prepared with magnesium sulfate turned into viscoelastic films that collapse when the film makes contact with itself in the middle region. In addition to this, films prepared with magnesium sulfate showed a non-monotonic trend dependence of film strength at intermediate salt concentration, observed by a subtle increase in the ratio R_z/a, followed by partial-decohesion between the hydrogel and the end rings. Last, a large disagreement was found between image and equation based surface areas at intermediate and long distances; while equation based surface areas kept increasing for all distances, image based surface areas dropped when they equalled the surface area of the two rings.

In Chapter 5 we have examined the behaviour of interfaces with different mechanical properties by performing strain amplitude and frequency sweeps via a drop profile tensiometer. Interfaces were made of 2NapFF and prepared at different concentrations of magnesium sulfate. Interfaces oscillated at the lowest strain, exhibited symmetric Lissajous plots, which indicates that the mechanical properties of the interfaces, are still in the linear regime. Nonlinearities started to appear at intermediate strains and become more marked at higher strains. Interfaces prepared at high salt concentration, showed the highest elastic response of all films, with surface pressure even increasing after yielding. At the other end, films prepared at the lowest salt concentration, were the weakest of all interfaces, showing a surface pressure yielding at lower strains and then decreases . Similar to films studied in Chapter 4, interfaces prepared at intermediate salt concentration, showed a more viscoelastic response, with a surface pressure yielding at higher strains than the rest of interfaces. Finally, we realised that the strain-stiffening ratio S used to quantify nonlinearities from Lissajous plots can display confusing results to quantify nonlinearities from interfaces with softening/hardening paradox response and interfaces yielding at negative strains. Therefore, we suggest a small modification in the analysis of Lissajous plots to

include all interfaces.

For the last experimental chapter, we wanted to link our work to a good or application. Emulsion lipid digestion is influenced by physiological parameters and emulsion properties [245]. For this reason in Chapter 6, we have studied the effect of the mechanical properties of emulsions on lipid digestion. The hydrogels used to form the emulsions were prepared in the same manner and concentration as in Chapter 4. The rate and extent of FFAs released during the digestions, was higher for emulsions prepared with calcium chloride than for magnesium sulfate. Initial emulsions prepared with calcium chloride showed a network made of stiff fibres with distorted oil droplets entrapped in it, whereas emulsions prepared with magnesium sulfate, led to emulsions with a more homogeneous matrix made of small fibres and spherical oil droplets. Based in results from Chapter 4, we hypothesise that this could be due to emulsions prepared with calcium chloride having a more brittle gel network. Under this scenario, these emulsions would be stronger than those prepared with magnesium sulfate, however, a brittle network can be significantly more fragile under stress. On the contrary, a hydrogel emulsion with a weaker but more viscoelastic network, could support better the stress and hence delayed the released of FFAs.

In conclusion, the work in this thesis has investigated the behaviour of dipeptide fibres in the bulk phase and adsorbed to interfaces. It has been observed that the properties of the continuous phase and of interfaces can be affected by the presence of dipeptide molecules and that these are altered by the type and concentration of salt used to trigger gelation. For example, calcium chloride increased the elasticity of the interfaces. On the contrary, interfaces prepared with sodium chloride became more viscous and somewhere in between were interfaces prepared with magnesium sulfate. The mechanical properties of the interfaces appears to become more marked with increasing salt concentration. However, for interfaces prepared with magnesium sulfate, seems to show a peak at intermediate salt concentration, where the elastic response may be higher. Lastly, the effect of salt on the mechanical properties of emulsions play an important role as observed in lipid digestions. The work done in this thesis adds to the research community and learning how to control the mechanical properties of systems such as foams and emulsions is key to develop new products and improve existing ones.

7.2 Future research

This thesis was initially motivated by the need to improve the understanding of the behaviour of dipeptides at interfaces. Therefore, we propose a number of research suggestions that could be interesting to follow and easy to implement in future research experiments. The first and probably the most interesting experiment to investigate would be the phase separation observed with octanol in the first experimental chapter. The ratio octanol:water could be varied to observe whether this can be reversed to a oil-in-water emulsion and if the concentration of salt has any effect on this. In Chapter 4, developing further the custom-made film tensiometer could be stimulating, as it could bring new insights into the field of interfacial rheology. For instance to add a force sensor to measure the stress at different velocities or study the evolution of the film thickness profile using interference reflection macroscopic. Other changes that are cheaper and easier to implement are, roughing the rings to avoid wall slip or changing the piezoelectric motor unit to have a better control of the velocity at which the lower ring moves; with a wider range of velocities and an option to choose between increasing this linearly or exponentially, as this could influence the results. Finally, the code to extract the profile of the film such that this is extracted in a more robust manner, especially near the end rings where the film attaches to the instrument and seems to fail in doing that sometimes. Likewise, visual data should be implemented in the code at different points of the process, as sometimes it is difficult to understand what this is doing at different steps. Finally, it could be interesting to use interfacial dilational rheology to study interfaces prepared with calcium chloride and magnesium sulfate, salts used in Chapter 4 as well, different oils, such those used in Chapter 3 or food grade oils.

Appendix A

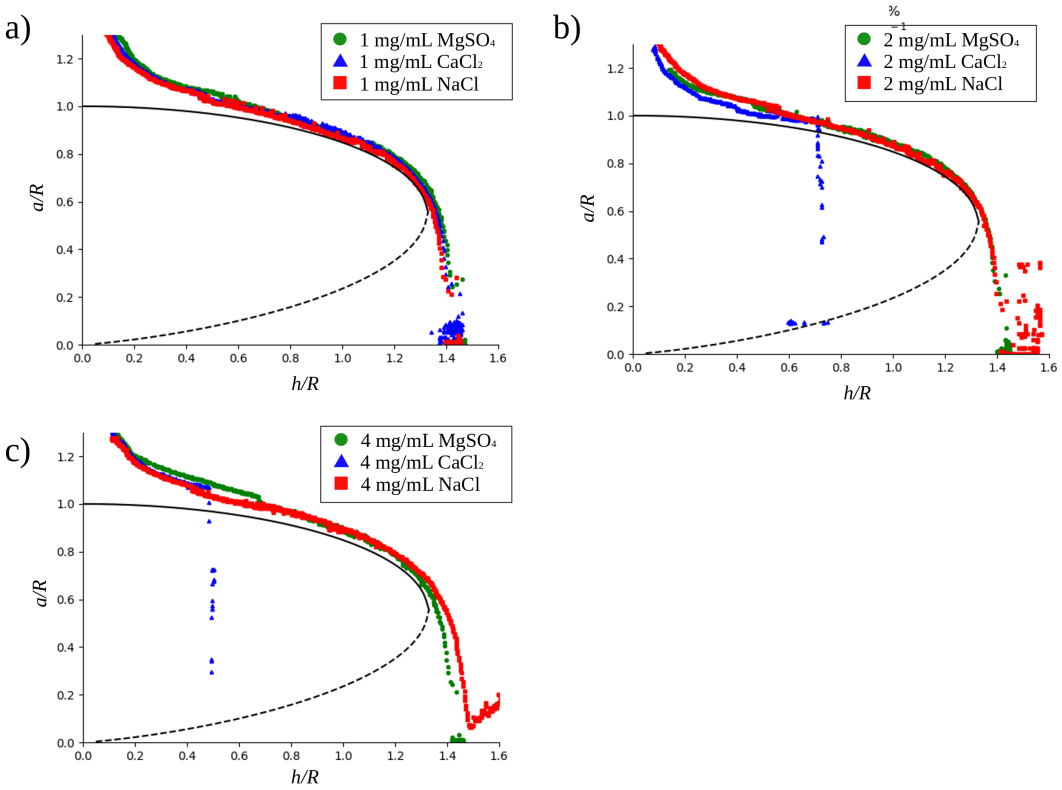

Figure A.1 *Experimental evolution of the radius a/R as a function of distance h/R of hydrogelled films made of 2NapFF, prepared with different salts (magnesium sulfate, calcium and sodium chloride) concentrations (1, 2 and 4 mg/mL), stretched at medium speed. The solid and dashed black lines are the radius at the midplane of the film a of stable and unstable catenoid film respectively. Where R is taken to be 9.25 mm.*

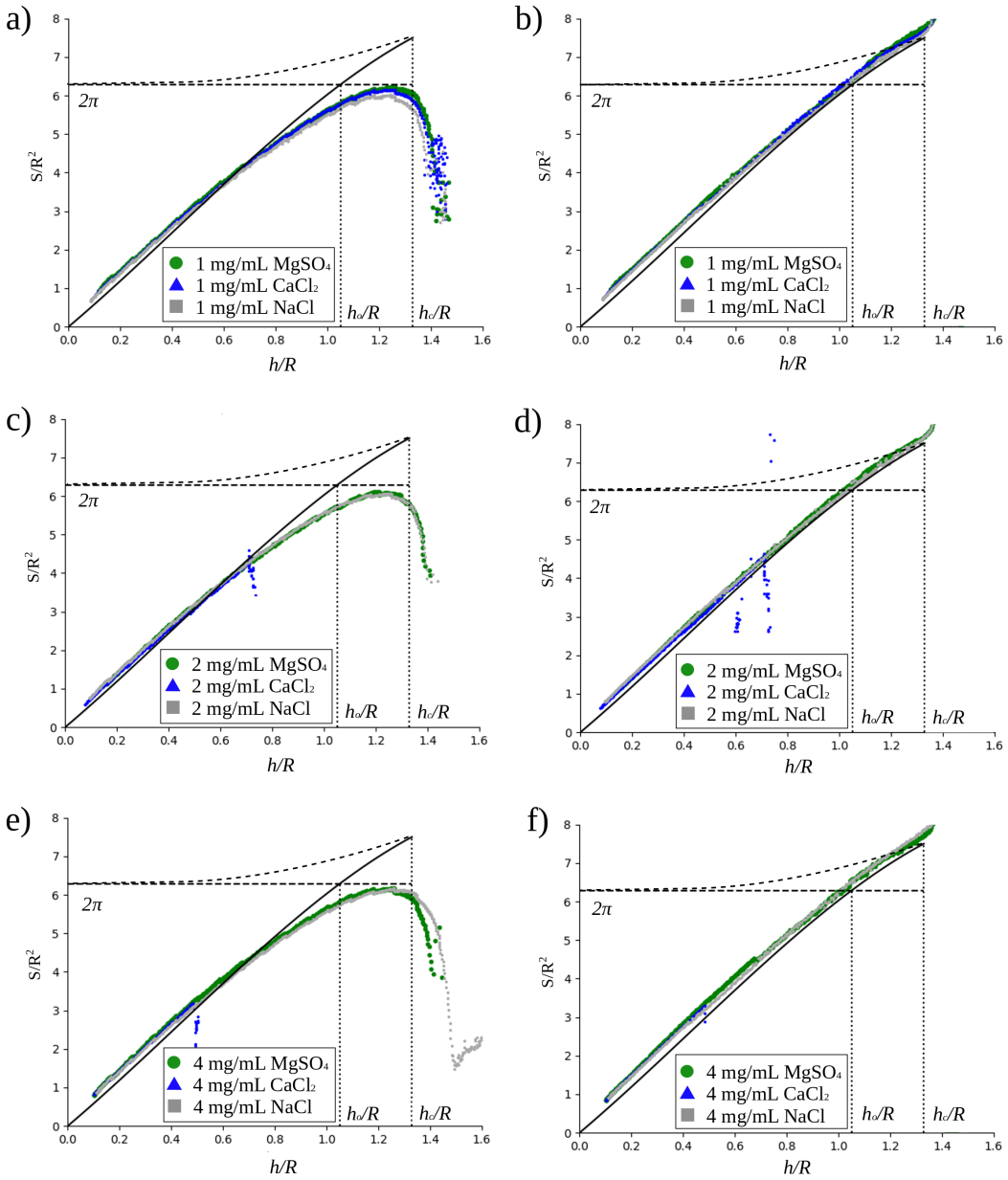

Figure A.2 *Evolution of the surface area S/R^2 calculated* ***left column:*** *numerically and* ***right column:*** *analytically as a function of distance h/R of hydrogelled films made of 2NapFF, prepared with different salts (magnesium sulfate, calcium and sodium chloride) concentrations (1, 2 and 4 mg/mL), stretched at medium speed. The solid black curve is the surface area of the stable minimal surface. The dashed black curve is the surface area of the unstable minimal surface. The horizontal dashed line is the surface area of the two rings and the vertical dashed lines are the the critical distance h_c/h at which films cannot exist any more and h_o/h is the distance at which the surface area of the films equals the surface area of the two rings. Where R is taken to be 9.25 mm.*

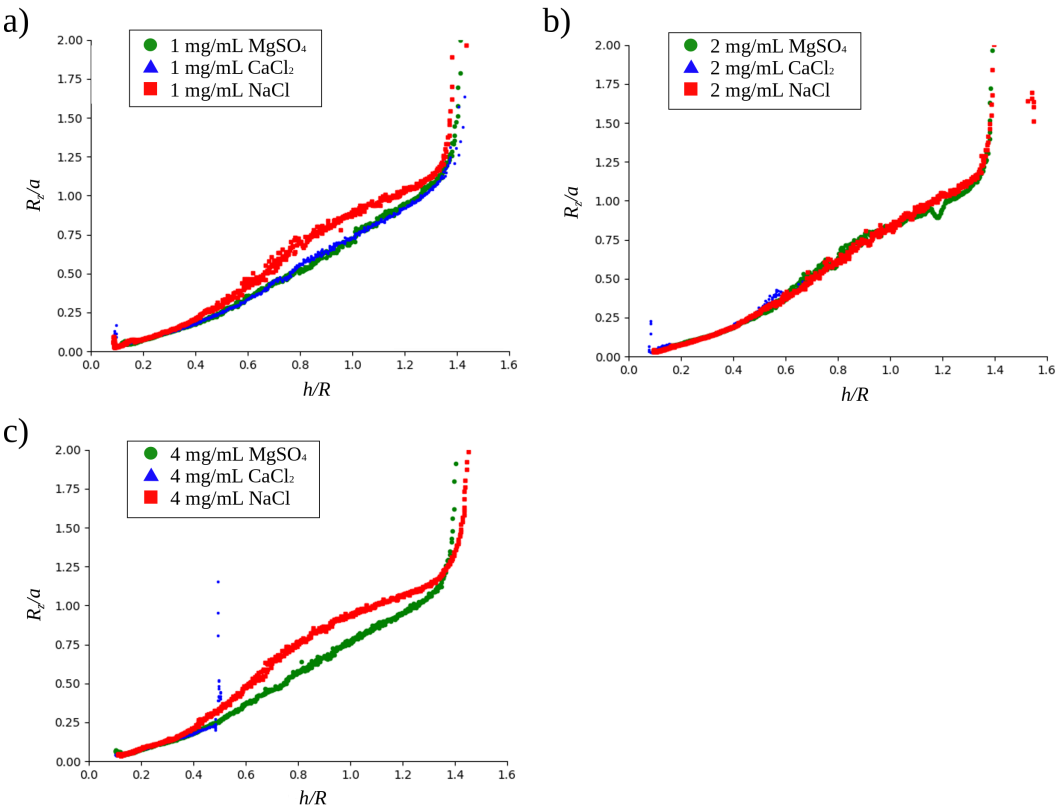

Figure A.3 *Experimental evolution of the ratio axial radius profile to the radius at the midplane of the film R_z/a as a function of distance h/R of hydrogelled films made of 2NapFF, prepared with different salts (magnesium sulfate, calcium and sodium chloride) concentrations (1, 2 and 4 mg/mL), stretched at medium speed. Where R is taken to be 9.25 mm.*

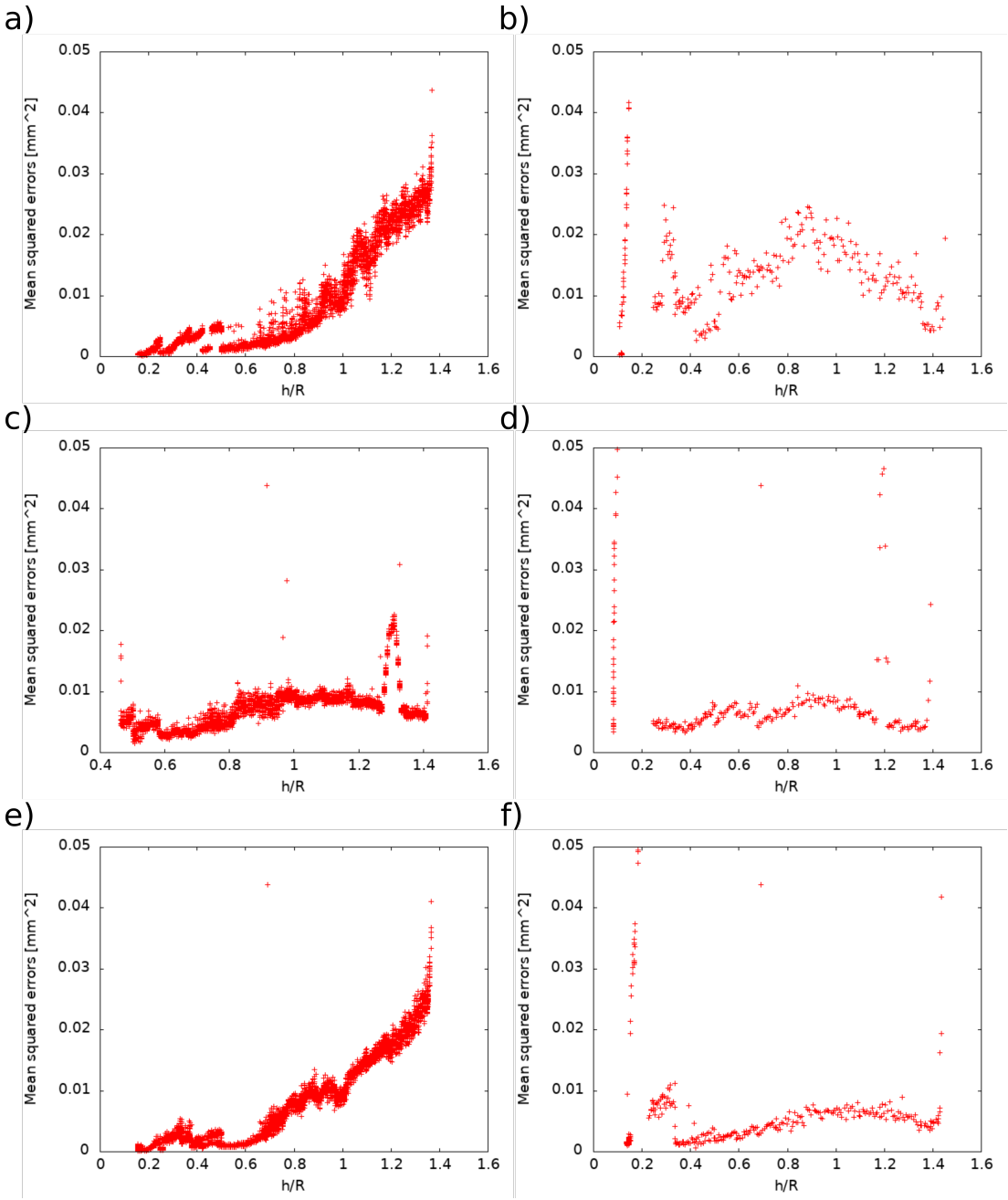

Figure A.4 *Root mean square error from from the regression line and the data points of hydrogelled films made of 2NapFF, prepared at* ***a,b:*** *1,* ***c,d:*** *2 and* ***e,f:*** *4 mg/mL magnesium sulfate, stretched at* ***left column:*** *low and* ***right column:*** *high speed.*

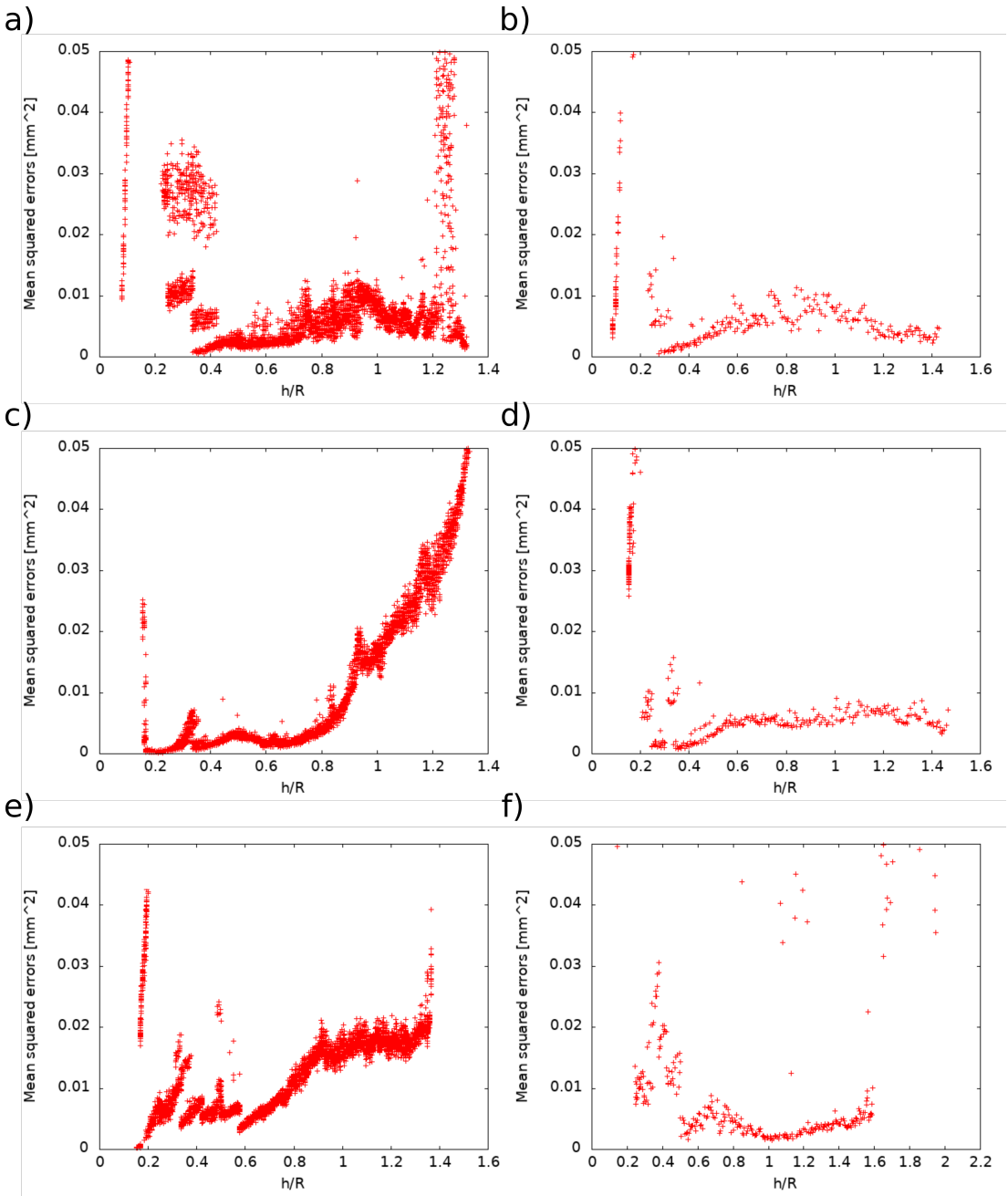

Figure A.5 *Root mean square error from from the regression line and the data points of hydrogelled films made of 2NapFF, prepared at* ***a,b:*** *1,* ***c,d:*** *2 and* ***e,f:*** *4 mg/mL sodium chloride, stretched at* ***left column:*** *low and* ***right column:*** *high speed.*

Table A.1 *Shows the collapse scenario for hydrogel films made of 2NapFF, prepared with different salts and concentrations and stretched at different velocities.*

Salt Type	Conc. (mg/mL)	Speed (mm/s)	Rupture Scenario	Shrinkage Scenario	Thread Scenario
$MgSO_4$	1	low		✓	
		medium		✓	
		high		✓	
	2	low		✓	
		medium		✓	
		high		✓	
	4	low		✓	
		medium		✓	
		high		✓	
$CaCl_2$	1	low		✓	
		medium	✓		
		high	✓		
	2	low	✓		
		medium	✓		
		high	✓		
	4	low	✓		
		medium	✓		
		high	✓		
NaCl	1	low			✓
		medium			✓
		high			✓
	2	low			✓
		medium			✓
		high			✓
	4	low			✓
		medium			✓
		high			✓

Table A.2 *Shows the life time for a set of hydrogel films, made of 2NapFF, prepared with different salts and concentrations and stretched at different velocities.*

Salt Type	Conc. (mg/mL)	Speed (mm/s)	Start time (ms)	End time (ms)	Life time (ms)
$MgSO_4$	1	low	3219	785	2434
		medium	1249	972	277
		high	1165	997	168
	2	low	-	1271	-
		medium	2333	2087	246
		high	2772	2590	182
	4	low	5300	1120	4180
		medium	1374	1085	289
		high	1374	1235	139
$CaCl_2$	1	low	3433	2391	1042
		medium	1386	1115	271
		high	-	-	-
	2	low	2822	2310	512
		medium	3004	2867	137
		high	2770	2656	114
	4	low	2335	1031	1304
		medium	1180	1074	106
		high	1056	970	86
NaCl	1	low	3412	970	2442
		medium	1122	824	298
		high	942	768	174
	2	low	3327	970	2357
		medium	1170	897	273
		high	1046	887	159
	4	low	3627	1185	2442
		medium	1631	1298	333
		high	1287	1121	166

Appendix B

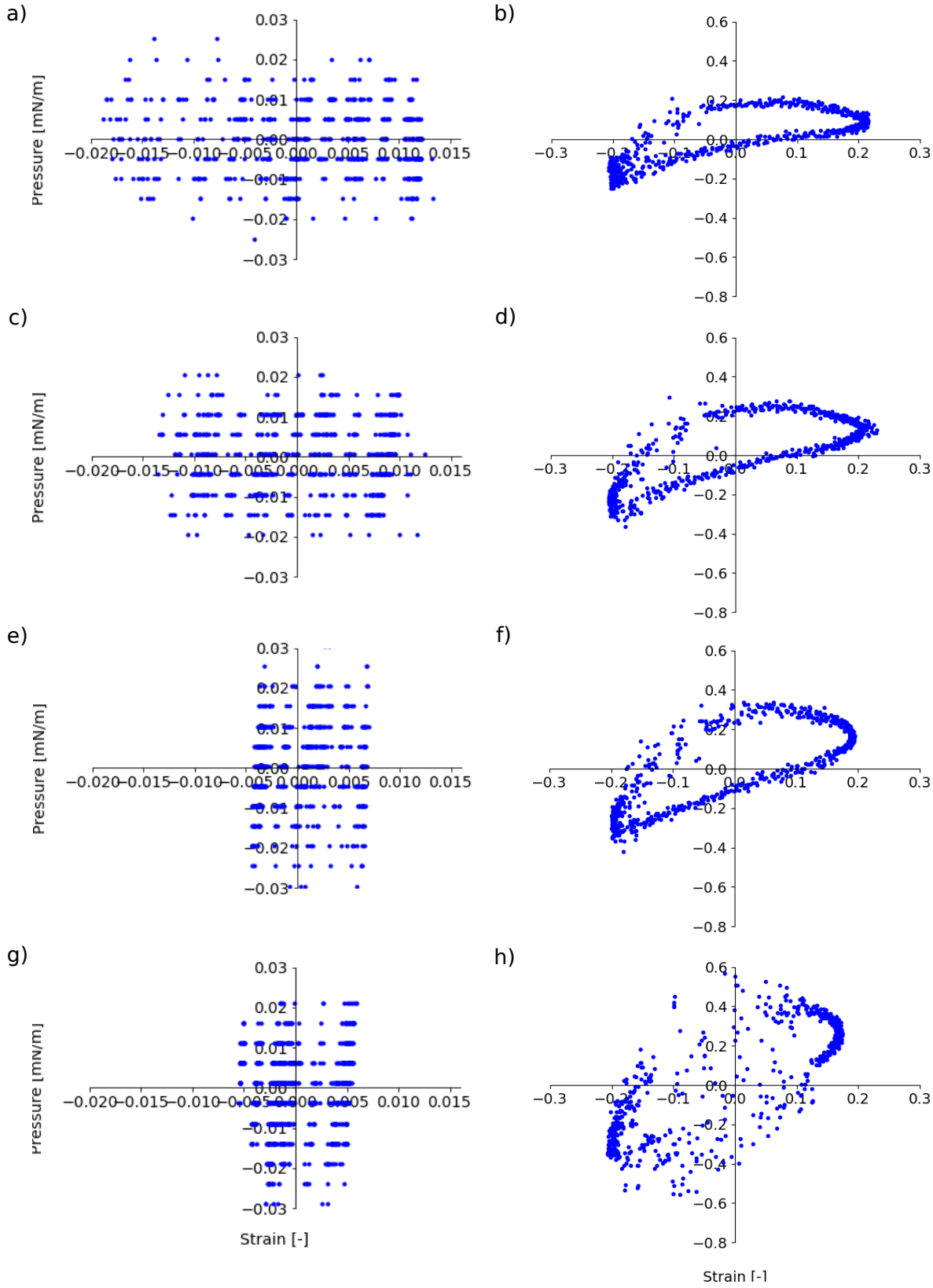

Figure B.1 *Surface pressure response from strain amplitude and frequency sweeps experiments performed on stable films made of 0.01 wt% 2NapFF prepared at* ***left panel:*** *0.1 mg/mL and* ***right panel:*** *0.2 mg/mL magnesium sulfate. Films were oscillated at a strain amplitude of* ***left panel:*** *1.5% and* ***right panel:*** *25% with frequencies* ***a,b:*** *0.02 Hz,* ***c,d:*** *0.05 Hz,* ***e,f:*** *0.1 Hz and* ***g,h:*** *0.2 Hz.*

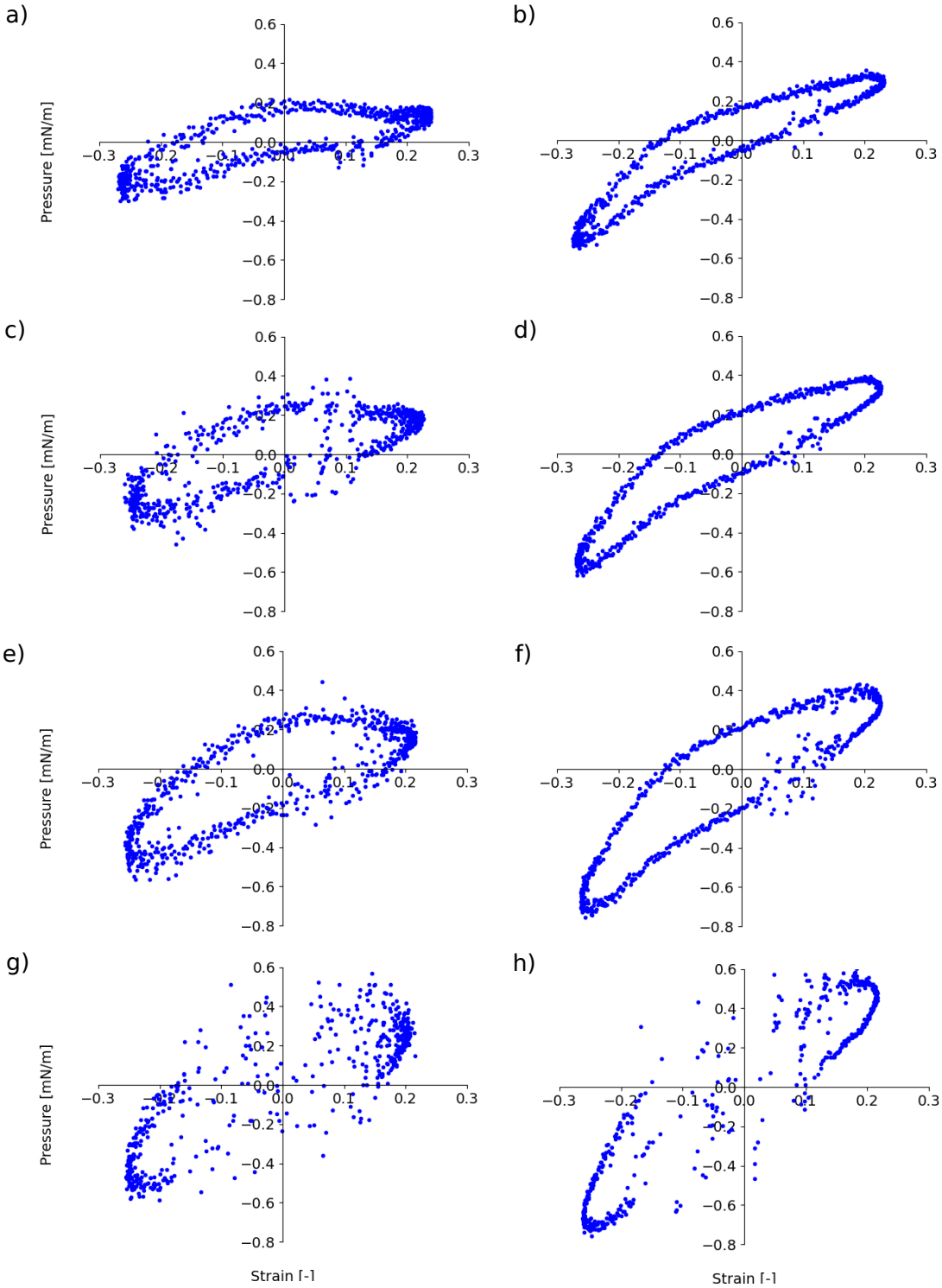

Figure B.2 *Surface pressure response from strain amplitude and frequency sweeps experiments performed on stable films made of 0.01 wt% 2NapFF prepared at* ***left panel:*** *0.3 mg/mL and* ***right panel:*** *0.4 mg/mL magnesium sulfate. Films were oscillated at a strain amplitude of 25% with frequencies* ***a,b:*** *0.02 Hz,* ***c,d:*** *0.05 Hz,* ***e,f:*** *0.1 Hz and* ***g,h:*** *0.2 Hz.*

Bibliography

[1] Fernando Aviño, Andrew B Matheson, Dave J Adams, and Paul S Clegg. Stabilizing bubble and droplet interfaces using dipeptide hydrogels. *Organic & biomolecular chemistry*, 15(30):6342–6348, 2017.

[2] Lin Chen, Guillaume Pont, Kyle Morris, Gudrun Lotze, Adam Squires, Louise C Serpell, and Dave J Adams. Salt-induced hydrogelation of functionalised-dipeptides at high ph. *Chemical communications*, 47(44):12071–12073, 2011.

[3] Emily R Draper and Dave J Adams. Low-molecular-weight gels: the state of the art. *Chem*, 3(3):390–410, 2017.

[4] Kyu Hyun, Manfred Wilhelm, Christopher O Klein, Kwang Soo Cho, Jung Gun Nam, Kyung Hyun Ahn, Seung Jong Lee, Randy H Ewoldt, and Gareth H McKinley. A review of nonlinear oscillatory shear tests: Analysis and application of large amplitude oscillatory shear (laos). *Progress in Polymer Science*, 36(12):1697–1753, 2011.

[5] Kyu Hyun, Sook Heun Kim, Kyung Hyun Ahn, and Seung Jong Lee. Large amplitude oscillatory shear as a way to classify the complex fluids. *Journal of Non-Newtonian Fluid Mechanics*, 107(1-3):51–65, 2002.

[6] Randy H Ewoldt, AE Hosoi, and Gareth H McKinley. New measures for characterizing nonlinear viscoelasticity in large amplitude oscillatory shear. *Journal of Rheology*, 52(6):1427–1458, 2008.

[7] Drew Myers et al. *Surfaces, interfaces, and colloids*, volume 415. Wiley New York, 1999.

[8] SR Derkach, J Krägel, and R Miller. Methods of measuring rheological properties of interfacial layers (experimental methods of 2d rheology). *Colloid journal*, 71(1):1–17, 2009.

[9] M.J. Boussinesq.). *Ann. Chim. Phys*, 29:349, 1913.

[10] David Julian McClements. *Food emulsions: principles, practices, and techniques*. CRC press, 2015.

[11] Jordi Esquena. Water-in-water (w/w) emulsions. *Current Opinion in Colloid & Interface Science*, 25:109–119, 2016.

[12] V Jaitely, T Sakthivel, G Magee, and AT Florence. Formulation of oil in oil emulsions: potential drug reservoirs for slow release. *Journal of Drug Delivery Science and Technology*, 14(2):113–117, 2004.

[13] Kai Seng Koh and Voon Loong Wong. Nanoemulsions-properties, fabrications and applications. 2019.

[14] Christopher Hill and Julian Eastoe. Foams: From nature to industry. *Advances in colloid and interface science*, 247:496–513, 2017.

[15] Ashley J Wilson. *Foams: physics, chemistry and structure*. Springer Science & Business Media, 2013.

[16] Eric Dickinson. *Introduction to food colloids*. Oxford university press, 1992.

[17] Stig Friberg, Kare Larsson, and Johan Sjoblom. *Food emulsions*. CRC Press, 2003.

[18] Raffaele Mezzenga and Peter Fischer. The self-assembly, aggregation and phase transitions of food protein systems in one, two and three dimensions. *Reports on Progress in Physics*, 76(4):046601, 2013.

[19] DE Graham and MC Phillips. Proteins at liquid interfaces. *Journal of colloid and interface science*, 70(3):403–414, 1979.

[20] Eric Dickinson. Adsorbed protein layers at fluid interfaces: interactions, structure and surface rheology. *Colloids and surfaces B: Biointerfaces*, 15(2):161–176, 1999.

[21] Srinivasan Damodaran. Protein stabilization of emulsions and foams. *Journal of Food Science*, 70(3):R54–R66, 2005.

[22] EH Lucassen-Reynders and J Benjamins. Food emulsions and foams: Interfaces, interactions and stability., 1999.

[23] Samuel Levine, Bruce D Bowen, and Susan J Partridge. Stabilization of emulsions by fine particles i. partitioning of particles between continuous phase and oil/water interface. *Colloids and surfaces*, 38(2):325–343, 1989.

[24] Bernard P Binks. Colloidal particles at a range of fluid–fluid interfaces. *Langmuir*, 33(28):6947–6963, 2017.

[25] Philip Finkle, Hal D Draper, and Joel H Hildebrand. The theory of emulsification1. *Journal of the American Chemical Society*, 45(12):2780–2788, 1923.

[26] Yuehua Yuan and T Randall Lee. Contact angle and wetting properties. In *Surface science techniques*, pages 3–34. Springer, 2013.

[27] Robert Aveyard, Bernard P Binks, and John H Clint. Emulsions stabilised solely by colloidal particles. *Advances in Colloid and Interface Science*, 100:503–546, 2003.

[28] Gerard L Hasenhuettl, Richard W Hartel, et al. *Food emulsifiers and their applications*, volume 40. Springer, 2008.

[29] David Julian Mcclements. Critical review of techniques and methodologies for characterization of emulsion stability. *Critical reviews in food science and nutrition*, 47(7):611–649, 2007.

[30] Nicholas A Peppas. *Biomedical applications of hydrogels handbook*. Springer Science & Business Media, 2010.

[31] Ruijiao Dong, Yan Pang, Yue Su, and Xinyuan Zhu. Supramolecular hydrogels: synthesis, properties and their biomedical applications. *Biomaterials science*, 3(7):937–954, 2015.

[32] Rui Li, Conor C Horgan, Benjamin Long, Alexandra L Rodriguez, Lauren Mather, Colin J Barrow, David R Nisbet, and Richard J Williams. Tuning the mechanical and morphological properties of self-assembled peptide hydrogels via control over the gelation mechanism through regulation of ionic strength and the rate of ph change. *RSC advances*, 5(1):301–307, 2015.

[33] Jaclyn Raeburn, Andre Zamith Cardoso, and Dave J Adams. The importance of the self-assembly process to control mechanical properties of low molecular weight hydrogels. *Chemical Society Reviews*, 42(12):5143–5156, 2013.

[34] Kai Liu, Ruirui Xing, Chengjun Chen, Guizhi Shen, Linyin Yan, Qianli Zou, Guanghui Ma, Helmuth Möhwald, and Xuehai Yan. Peptide-induced hierarchical long-range order and photocatalytic activity of porphyrin assemblies. *Angewandte Chemie International Edition*, 54(2):500–505, 2015.

[35] Chunyu Xu and Jindřich Kopeček. Genetically engineered block copolymers: influence of the length and structure of the coiled-coil blocks on hydrogel self-assembly. *Pharmaceutical research*, 25(3):674–682, 2008.

[36] Shuming Zhang, Megan A Greenfield, Alvaro Mata, Liam C Palmer, Ronit Bitton, Jason R Mantei, Conrado Aparicio, Monica Olvera De La Cruz, and Samuel I Stupp. A self-assembly pathway to aligned monodomain gels. *Nature materials*, 9(7):594–601, 2010.

[37] Frank Versluis, Hana Robson Marsden, and Alexander Kros. Power struggles in peptide-amphiphile nanostructures. *Chemical Society Reviews*, 39(9):3434–3444, 2010.

[38] Natalia Sánchez De Groot, Teodor Parella, Francesc X Aviles, Josep Vendrell, and Salvador Ventura. Ile-phe dipeptide self-assembly: clues to amyloid formation. *Biophysical journal*, 92(5):1732–1741, 2007.

[39] Xuewen Du, Jie Zhou, Junfeng Shi, and Bing Xu. Supramolecular hydrogelators and hydrogels: from soft matter to molecular biomaterials. *Chemical reviews*, 115(24):13165–13307, 2015.

[40] Pierre Terech and Richard G Weiss. Low molecular mass gelators of organic liquids and the properties of their gels. *Chemical reviews*, 97(8):3133–3160, 1997.

[41] AJ Zamith Cardoso. *Linking micellar phases to peptide supramolecular hydrogels*. PhD thesis, University of Liverpool, 2017.

[42] Lin Chen, Steven Revel, Kyle Morris, Louise C. Serpell, and Dave J Adams. Effect of molecular structure on the properties of naphthalene- dipeptide hydrogelators. *Langmuir*, 26(16):13466–13471, 2010.

[43] Lara A Estroff and Andrew D Hamilton. Water gelation by small organic molecules. *Chemical reviews*, 104(3):1201–1218, 2004.

[44] Ivana M Geremias-Andrade, Nayla PBG Souki, Izabel CF Moraes, and Samantha C Pinho. Rheology of emulsion-filled gels applied to the development of food materials. *Gels*, 2(3):22, 2016.

[45] Yasuki Matsumura, Il-Jun Kang, Hiroko Sakamoto, Masao Motoki, and Tomohiko Mori. Filler effects of oil droplets on the viscoelastic properties of emulsion gels. *Food Hydrocolloids*, 7(3):227–240, 1993.

[46] Eric Dickinson. Emulsion gels: The structuring of soft solids with protein-stabilized oil droplets. *Food hydrocolloids*, 28(1):224–241, 2012.

[47] A Panwar, N Upadhyay, M Bairagi, S Gujar, G Darwhekar, and D Jain. Emulgel: a review. *Asian J Pharm Life Sci*, 2231:4423, 2011.

[48] Hui-Peng Lim, Kiang-Wei Ho, Charanjit Kaur Surjit Singh, Chien-Wei Ooi, Beng-Ti Tey, and Eng-Seng Chan. Pickering emulsion hydrogel as a promising food delivery system: Synergistic effects of chitosan pickering emulsifier and alginate matrix on hydrogel stability and emulsion delivery. *Food Hydrocolloids*, 103:105659, 2020.

[49] Ophelie Torres, Brent Murray, and Anwesha Sarkar. Emulsion microgel particles: Novel encapsulation strategy for lipophilic molecules. *Trends in Food Science & Technology*, 55:98–108, 2016.

[50] Toktam Farjami and Ashkan Madadlou. Aview on preparation of emulsion-filled gels and emulsion particulate gels. *Trends in Food Science & Technology*, 86:85–94, 2019.

[51] J Chen and E Dickinson. Interfacial ageing effect on the rheology of a heat-set protein emulsion gel. *Food Hydrocolloids*, 13(5):363–369, 1999.

[52] Laura Oliver, Lieke Berndsen, George A van Aken, and Elke Scholten. Influence of droplet clustering on the rheological properties of emulsion-filled gels. *Food Hydrocolloids*, 50:74–83, 2015.

[53] T Van Vliet. Rheological properties of filled gels. influence of filler matrix interaction. *Colloid and Polymer Science*, 266(6):518–524, 1988.

[54] Guido Sala. *Food gels filled with emulsion droplets: linking large deformation properties to sensory perception*. 2007.

[55] Tao Li, Michail Kalloudis, Andre Zamith Cardoso, Dave J Adams, and Paul S Clegg. Drop-casting hydrogels at a liquid interface: The case of hydrophobic dipeptides. *Langmuir*, 30(46):13854–13860, 2014.

[56] Tao Li, Fabio Nudelman, Joe W Tavacoli, Hugh Vass, Dave J Adams, Alex Lips, and Paul S Clegg. Long-lived foams stabilized by a hydrophobic dipeptide hydrogel. *Advanced Materials Interfaces*, 3(3):1500601, 2016.

[57] Tao Li, Michail Kalloudis, Andre Zamith Cardoso, Dave J Adams, and Paul S Clegg. Drop-casting hydrogels at a liquid interface: the case of hydrophobic dipeptides. *Langmuir*, 30(46):13854–13860, 2014.

[58] Ashkan Dehsorkhi, Valeria Castelletto, and Ian W Hamley. Self-assembling amphiphilic peptides. *Journal of Peptide Science*, 20(7):453–467, 2014.

[59] IW Hamley. Self-assembly of amphiphilic peptides. *Soft Matter*, 7(9):4122–4138, 2011.

[60] Abba Kastin. *Handbook of biologically active peptides*. Academic press, 2013.

[61] Galit Fichman and Ehud Gazit. Self-assembly of short peptides to form hydrogels: Design of building blocks, physical properties and technological applications. *Acta biomaterialia*, 10(4):1671–1682, 2014.

[62] Scott Fleming and Rein V Ulijn. Design of nanostructures based on aromatic peptide amphiphiles. *Chemical Society Reviews*, 43(23):8150–8177, 2014.

[63] Jindřich Kopeček and Jiyuan Yang. Smart self-assembled hybrid hydrogel biomaterials. *Angewandte Chemie International Edition*, 51(30):7396–7417, 2012.

[64] Ayala Lampel. Biology-inspired supramolecular peptide systems. *Chem*, 2020.

[65] Karen JL Burg, Scott Porter, and James F Kellam. Biomaterial developments for bone tissue engineering. *Biomaterials*, 21(23):2347–2359, 2000.

[66] Caroline Bonnans, Jonathan Chou, and Zena Werb. Remodelling the extracellular matrix in development and disease. *Nature reviews Molecular cell biology*, 15(12):786–801, 2014.

[67] WT Tsai, JM Yang, CW Lai, YH Cheng, CC Lin, and CW Yeh. Characterization and adsorption properties of eggshells and eggshell membrane. *Bioresource technology*, 97(3):488–493, 2006.

[68] Derek M Ryan and Bradley L Nilsson. Self-assembled amino acids and dipeptides as noncovalent hydrogels for tissue engineering. *Polymer Chemistry*, 3(1):18–33, 2012.

[69] Biji Balakrishnan and R Banerjee. Biopolymer-based hydrogels for cartilage tissue engineering. *Chemical reviews*, 111(8):4453–4474, 2011.

[70] Tobin E Brown and Kristi S Anseth. Spatiotemporal hydrogel biomaterials for regenerative medicine. *Chemical Society Reviews*, 46(21):6532–6552, 2017.

[71] Jianyu Li and David J Mooney. Designing hydrogels for controlled drug delivery. *Nature Reviews Materials*, 1(12):1–17, 2016.

[72] Yong Qiu and Kinam Park. Environment-sensitive hydrogels for drug delivery. *Advanced drug delivery reviews*, 53(3):321–339, 2001.

[73] Robert Wieduwild, Swati Krishnan, Karolina Chwalek, Annett Boden, Mirko Nowak, David Drechsel, Carsten Werner, and Yixin Zhang. Noncovalent hydrogel beads as microcarriers for cell culture. *Angewandte Chemie*, 127(13):4034–4038, 2015.

[74] Myunghwan Choi, Jin Woo Choi, Seonghoon Kim, Sedat Nizamoglu, Sei Kwang Hahn, and Seok Hyun Yun. Light-guiding hydrogels for cell-based sensing and optogenetic synthesis in vivo. *Nature photonics*, 7(12):987–994, 2013.

[75] Vineetha Jayawarna, Murtza Ali, Thomas A Jowitt, Aline F Miller, Alberto Saiani, Julie E Gough, and Rein V Ulijn. Nanostructured hydrogels for three-dimensional cell culture through self-assembly of fluorenylmethoxycarbonyl–dipeptides. *Advanced materials*, 18(5):611–614, 2006.

[76] Dave J Adams, Michael F Butler, William J Frith, Mark Kirkland, Leanne Mullen, and Paul Sanderson. A new method for maintaining homogeneity during liquid–hydrogel transitions using low molecular weight hydrogelators. *Soft Matter*, 5(9):1856–1862, 2009.

[77] Rolands Vegners, Irina Shestakova, Ivars Kalvinsh, Robert M Ezzell, and Paul A Janmey. Use of a gel-forming dipeptide derivative as a carrier for antigen presentation. *Journal of peptide science: an official publication of the European Peptide Society*, 1(6):371–378, 1995.

[78] Koji Nagahama, Tatsuro Ouchi, and Yuichi Ohya. Temperature-induced hydrogels through self-assembly of cholesterol-substituted star peg-b-plla copolymers: an injectable scaffold for tissue engineering. *Advanced Functional Materials*, 18(8):1220–1231, 2008.

[79] Thomas Liebmann, Susanna Rydholm, Victor Akpe, and Hjalmar Brismar. Self-assembling fmoc dipeptide hydrogel for in situ 3d cell culturing. *BMC biotechnology*, 7(1):1–11, 2007.

[80] Sibaprasad Maity, Pankaj Kumar, and Debasish Haldar. Sonication-induced instant amyloid-like fibril formation and organogelation by a tripeptide. *Soft Matter*, 7(11):5239–5245, 2011.

[81] Michal E Roth-Konforti, Michela Comune, Michal Halperin-Sternfeld, Irena Grigoriants, Doron Shabat, and Lihi Adler-Abramovich. Uv light–responsive peptide-based supramolecular hydrogel for controlled drug delivery. *Macromolecular Rapid Communications*, 39(24):1800588, 2018.

[82] Jeffrey D Hartgerink, Elia Beniash, and Samuel I Stupp. Peptide-amphiphile nanofibers: a versatile scaffold for the preparation of self-assembling materials. *Proceedings of the National Academy of Sciences*, 99(8):5133–5138, 2002.

[83] Anika M Jonker, Dennis WPM Löwik, and Jan CM van Hest. Peptide-and protein-based hydrogels. *Chemistry of Materials*, 24(5):759–773, 2012.

[84] Lihi Adler-Abramovich and Ehud Gazit. The physical properties of supramolecular peptide assemblies: from building block association to technological applications. *Chemical Society Reviews*, 43(20):6881–6893, 2014.

[85] Yan Zhang, Hongwei Gu, Zhimou Yang, and Bing Xu. Supramolecular hydrogels respond to ligand- receptor interaction. *Journal of the American Chemical Society*, 125(45):13680–13681, 2003.

[86] Jaclyn Raeburn, Guillaume Pont, Lin Chen, Yann Cesbron, Raphaël Lévy, and Dave J Adams. Fmoc-diphenylalanine hydrogels: understanding the variability in reported mechanical properties. *Soft Matter*, 8(4):1168–1174, 2012.

[87] Wilda Helen, Piero de Leonardis, Rein V Ulijn, Julie Gough, and Nicola Tirelli. Mechanosensitive peptide gelation: mode of agitation controls mechanical properties and nano-scale morphology. *Soft Matter*, 7(5):1732–1740, 2011.

[88] Lin Chen, Kyle Morris, Andrea Laybourn, David Elias, Matthew R Hicks, Alison Rodger, Louise Serpell, and Dave J Adams. Self-assembly mechanism for a naphthalene- dipeptide leading to hydrogelation. *Langmuir*, 26(7):5232–5242, 2010.

[89] Stephan J Zuend, Matthew P Coughlin, Mathieu P Lalonde, and Eric N Jacobsen. Scaleable catalytic asymmetric strecker syntheses of unnatural α-amino acids. *Nature*, 461(7266):968–970, 2009.

[90] Roberto J Brea, M Pilar López-Deber, Luis Castedo, and Juan R Granja. Synthesis of ω-(hetero) arylalkynylated α-amino acid by sonogashira-type reactions in aqueous media. *The Journal of organic chemistry*, 71(20):7870–7873, 2006.

[91] Lin Chen, Guillaume Pont, Kyle Morris, Gudrun Lotze, Adam Squires, Louise C Serpell, and Dave J Adams. Salt-induced hydrogelation of functionalised-dipeptides at high ph. *Chemical Communications*, 47(44):12071–12073, 2011.

[92] Andre Zamith Cardoso, Laura LE Mears, Beatrice N Cattoz, Peter C Griffiths, Ralf Schweins, and Dave J Adams. Linking micellar structures to hydrogelation for salt-triggered dipeptide gelators. *Soft matter*, 12(15):3612–3621, 2016.

[93] Catherine Colquhoun, Emily R Draper, Ralf Schweins, Marco Marcello, Devkee Vadukul, Louise C Serpell, and Dave J Adams. Controlling the network type in self-assembled dipeptide hydrogels. *Soft matter*, 13(9):1914–1919, 2017.

[94] Junfeng Shi, Yuan Gao, Ye Zhang, Yue Pan, and Bing Xu. Calcium ions to cross-link supramolecular nanofibers to tune the elasticity of hydrogels over orders of magnitude. *Langmuir*, 27(23):14425–14431, 2011.

[95] WF DeGrado and JD Lear. Induction of peptide conformation at apolar water interfaces. 1. a study with model peptides of defined hydrophobic periodicity. *Journal of the American Chemical Society*, 107(25):7684–7689, 1985.

[96] Ying-Ching Yu, Peter Berndt, Matthew Tirrell, and Gregg B Fields. Self-assembling amphiphiles for construction of protein molecular architecture. *Journal of the American Chemical Society*, 118(50):12515–12520, 1996.

[97] Peter Berndt, Gregg B Fields, and Matthew Tirrell. Synthetic lipidation of peptides and amino acids: monolayer structure and properties. *Journal of the American Chemical Society*, 117(37):9515–9522, 1995.

[98] Anton PJ Middelberg, Clay J Radke, and Harvey W Blanch. Peptide interfacial adsorption is kinetically limited by the thermodynamic stability of self association. *Proceedings of the National Academy of Sciences*, 97(10):5054–5059, 2000.

[99] Hanna Rapaport, Kristian Kjaer, Torben R Jensen, Leslie Leiserowitz, and David A Tirrell. Two-dimensional order in β-sheet peptide monolayers. *Journal of the American Chemical Society*, 122(50):12523–12529, 2000.

[100] Qun Huo, Guodong Sui, Yujun Zheng, Peter Kele, Roger M Leblanc, Takeshi Hasegawa, Jujiro Nishijo, and Junzo Umemura. Metal complexation with langmuir monolayers of histidyl peptide lipids. *Chemistry–A European Journal*, 7(22):4796–4804, 2001.

[101] Yooseong Hong, Lue Shunn Lau, Raymond L Legge, and P Chen. Critical self-assembly concentration of an ionic-complementary peptide eak16-i. *The Journal of Adhesion*, 80(10-11):913–931, 2004.

[102] Changqing Li, Jhony Orbulescu, Guodong Sui, and Roger M Leblanc. Amyloid-like formation by self-assembly of peptidolipids in two dimensions. *Langmuir*, 20(20):8641–8645, 2004.

[103] Annette F Dexter, Andrew S Malcolm, and Anton PJ Middelberg. Reversible active switching of the mechanical properties of a peptide film at a fluid–fluid interface. *Nature Materials*, 5(6):502–506, 2006.

[104] Annette F Dexter and Anton PJ Middelberg. Switchable peptide surfactants with designed metal binding capacity. *The Journal of Physical Chemistry C*, 111(28):10484–10492, 2007.

[105] Tao Li, Fabio Nudelman, Joe W Tavacoli, Hugh Vass, Dave J Adams, Alex Lips, and Paul S Clegg. Long-lived foams stabilized by a hydrophobic dipeptide hydrogel. *Advanced Materials Interfaces*, 3(3), 2016.

[106] Gary G Scott, Paul J McKnight, Tell Tuttle, and Rein V Ulijn. Emulsifiers: Tripeptide emulsifiers (adv. mater. 7/2016). *Advanced Materials*, 28(7):1329–1329, 2016.

[107] Shuo Bai, Charalampos Pappas, Sisir Debnath, Pim WJM Frederix, Joy Leckie, Scott Fleming, and Rein V Ulijn. Stable emulsions formed by self-assembly of interfacial networks of dipeptide derivatives. *ACS nano*, 8(7):7005–7013, 2014.

[108] Inês P Moreira, Ivan Ramos Sasselli, Daniel A Cannon, Meghan Hughes, Dimitrios A Lamprou, Tell Tuttle, and Rein V Ulijn. Enzymatically activated emulsions stabilised by interfacial nanofibre networks. *Soft matter*, 12(9):2623–2631, 2016.

[109] Sudipta Mondal, Maxim Varenik, Daniel Nir Bloch, Yoav Atsmon-Raz, Guy Jacoby, Lihi Adler-Abramovich, Linda JW Shimon, Roy Beck, Yifat Miller, Oren Regev, et al. A minimal length rigid helical peptide motif allows rational design of modular surfactants. *Nature communications*, 8:14018, 2017.

[110] Yuki Nishida, Akiko Tanaka, Shota Yamamoto, Yudai Tominaga, Nobuaki Kunikata, Minoru Mizuhata, and Tatsuo Maruyama. In situ synthesis of a supramolecular hydrogelator at an oil/water interface for stabilization and stimuli-induced fusion of microdroplets. *Angewandte Chemie*, 129(32):9538–9542, 2017.

[111] Srinivasan Damodaran. Protein stabilization of emulsions and foams. *Journal of Food Science*, 70(3), 2005.

[112] Annette F Dexter, Andrew S Malcolm, and Anton PJ Middelberg. Reversible active switching of the mechanical properties of a peptide film at a fluid–fluid interface. *Nature materials*, 5(6):502–506, 2006.

[113] Annette F Dexter and Anton PJ Middelberg. Switchable peptide surfactants with designed metal binding capacity. *The Journal of Physical Chemistry C*, 111(28):10484–10492, 2007.

[114] Justin T Russell, Yao Lin, Alexander Böker, Long Su, Philippe Carl, Heiko Zettl, Jinbo He, Kevin Sill, Ravisubhash Tangirala, Todd Emrick, et al. Self-assembly and cross-linking of bionanoparticles at liquid–liquid interfaces. *Angewandte Chemie International Edition*, 44(16):2420–2426, 2005.

[115] Lucio Isa, Jin-Mi Jung, and Raffaele Mezzenga. Unravelling adsorption and alignment of amyloid fibrils at interfaces by probe particle tracking. *Soft Matter*, 7(18):8127–8134, 2011.

[116] Aiqian Ye, Xangqian Zhu, and Harjinder Singh. Oil-in-water emulsion system stabilized by protein-coated nanoemulsion droplets. *Langmuir*, 29(47):14403–14410, 2013.

[117] Mridul Sarker, Nikodem Tomczak, and Sierin Lim. Protein nanocage as a ph-switchable pickering emulsifier. *ACS Applied Materials & Interfaces*, 9(12):11193–11201, 2017.

[118] Zhiming Gao, Junjun Zhao, Ying Huang, Xiaolin Yao, Ke Zhang, Yapeng Fang, Katsuyoshi Nishinari, Glyn O Phillips, Fatang Jiang, and Hao Yang. Edible pickering emulsion stabilized by protein fibrils. part 1: Effects of ph and fibrils concentration. *LWT-Food Science and Technology*, 76:1–8, 2017.

[119] Rein V Ulijn and Andrew M Smith. Designing peptide based nanomaterials. *Chemical Society Reviews*, 37(4):664–675, 2008.

[120] Enas M Ahmed. Hydrogel: Preparation, characterization, and applications: A review. *Journal of advanced research*, 6(2):105–121, 2015.

[121] Shuo Bai, Charalampos Pappas, Sisir Debnath, Pim WJM Frederix, Joy Leckie, Scott Fleming, and Rein V Ulijn. Stable emulsions formed by self-assembly of interfacial networks of dipeptide derivatives. *ACS nano*, 8(7):7005–7013, 2014.

[122] Wenhui Lv, Tan Hu, Ahmed Taha, Zhongkun Wang, Xiaoyun Xu, Siyi Pan, and Hao Hu. Lipo-dipeptide as an emulsifier: Performance and possible mechanism. *Journal of agricultural and food chemistry*, 67(22):6377–6386, 2019.

[123] Jacek K Wychowaniec, Ronak Patel, James Leach, Rachel Mathomes, Vikesh Chhabria, Yogita Patil-Sen, Araida Hidalgo-Bastida, Robert T Forbes, Joseph M Hayes, and Mohamed A Elsawy. Aromatic stacking facilitated self-assembly of ultra-short ionic complementary peptide sequence: β-sheet nanofibres with remarkable gelation and interfacial properties. *Biomacromolecules*, 2020.

[124] Bum Jun Park, To Ngai, Hanying Zhao, Stefan AF Bon, Paul Clegg, Chaoyang Wang, Yoshimune Nonomura, Simon Biggs, Ian Norton, Zhenghe Xu, et al. *Particle-stabilized emulsions and colloids: formation and applications*. Royal Society of Chemistry, 2014.

[125] Bum Jun Park, Daeyeon Lee, and Eric M Furst. Interactions and conformations of particles at fluid-fluid interfaces. In *Particle-Stabilized Emulsions and Colloids*, pages 8–44. 2014.

[126] Meina Xiao, Anli Xu, Tongtong Zhang, and Liangzhi Hong. Tailoring the wettability of colloidal particles for pickering emulsions via surface modification and roughness. *Frontiers in chemistry*, 6:225, 2018.

[127] Zifu Li and To Ngai. Emulsions stabilized by soft microgel particles. In *Particle-Stabilized Emulsions and Colloids*, pages 93–128. 2014.

[128] Kentaro Matsumiya and Brent S Murray. Soybean protein isolate gel particles as foaming and emulsifying agents. *Food Hydrocolloids*, 60:206–215, 2016.

[129] Chuan-He Tang. Emulsifying properties of soy proteins: A critical review with emphasis on the role of conformational flexibility. *Critical Reviews in Food Science and Nutrition*, 57(12):2636–2679, 2017.

[130] Bo Jiao, Aimin Shi, Qiang Wang, and Bernard P Binks. High-internal-phase pickering emulsions stabilized solely by peanut-protein-isolate microgel particles with multiple potential applications. *Angewandte Chemie*, 130(30):9418–9422, 2018.

[131] Ya Zhu, Xiaogang Luo, Xia Wu, Wei Li, Bin Li, Ang Lu, and Shilin Liu. Cellulose gel dispersions: fascinating green particles for the stabilization of oil/water pickering emulsion. *Cellulose*, 24(1):207–217, 2017.

[132] Brent S Murray. Pickering emulsions for food and drinks. *Current Opinion in Food Science*, 27:57–63, 2019.

[133] Anwesha Sarkar, Valerie Ademuyiwa, Samuel Stubley, Nur Hanesa Esa, Francisco M Goycoolea, Xiaofei Qin, Fernando Gonzalez, and Clarita Olvera. Pickering emulsions co-stabilized by composite protein/polysaccharide particle-particle interfaces: Impact on in vitro gastric stability. *Food Hydrocolloids*, 84:282–291, 2018.

[134] Lin Chen, Tom O McDonald, and Dave J Adams. Salt-induced hydrogels from functionalised-dipeptides. *RSC Advances*, 3(23):8714–8720, 2013.

[135] Dave J Adams. Dipeptide and tripeptide conjugates as low-molecular-weight hydrogelators. *Macromolecular bioscience*, 11(2):160–173, 2011.

[136] Rossitza G Alargova, Devdutta S Warhadpande, Vesselin N Paunov, and Orlin D Velev. Foam superstabilization by polymer microrods. *Langmuir*, 20(24):10371–10374, 2004.

[137] Bernard P Binks. Particles as surfactants—similarities and differences. *Current opinion in colloid & interface science*, 7(1):21–41, 2002.

[138] Nikolaos A Peppas. *Hydrogels in medicine and pharmacy: fundamentals*, volume 1. CRC press, 2019.

[139] Saehun Mun, Yong-Ro Kim, Malshick Shin, and David Julian McClements. Control of lipid digestion and nutraceutical bioaccessibility using starch-based filled hydrogels: Influence of starch and surfactant type. *Food Hydrocolloids*, 44:380–389, 2015.

[140] Sruthi Srinivasan, Heinz Otchere, Mili Yu, Jeffery Yang, Doerte Luensmann, and Lyndon Jones. Impact of cosmetics on the surface properties of silicone hydrogel contact lenses. *Eye & contact lens*, 41(4):228–235, 2015.

[141] Kuen Yong Lee and David J Mooney. Hydrogels for tissue engineering. *Chemical reviews*, 101(7):1869–1880, 2001.

[142] Morteza Bahram, Naimeh Mohseni, and Mehdi Moghtader. An introduction to hydrogels and some recent applications. In *Emerging concepts in analysis and applications of hydrogels*. IntechOpen, 2016.

[143] AJ Zamith Cardoso. *Linking micellar phases to peptide supramolecular hydrogels*. PhD thesis, University of Liverpool, 2017.

[144] Naziha Chirani, Lukas Gritsch, Federico Leonardo Motta, Silvia Fare, et al. History and applications of hydrogels. *Journal of biomedical sciences*, 4(2), 2015.

[145] Jonathan P Rothstein and Gareth H McKinley. Inhomogeneous transient uniaxial extensional rheometry. *Journal of Rheology*, 46(6):1419–1443, 2002.

[146] Cyril Isenberg. *The science of soap films and soap bubbles*. Tieto Cleveton, UK, 1978.

[147] Louis Salkin, Alexandre Schmit, Pascal Panizza, and Laurent Courbin. Influence of boundary conditions on the existence and stability of minimal surfaces of revolution made of soap films. *American Journal of Physics*, 82(9):839–847, 2014.

[148] Rémi Deleurence, Tamar Saison, François Lequeux, and Cécile Monteux. Foaming of transient polymer hydrogels. *ACS Omega*, 3(2):1864–1870, 2018.

[149] Mónica SN Oliveira, Roger Yeh, and Gareth H McKinley. Iterated stretching, extensional rheology and formation of beads-on-a-string structures in polymer solutions. *Journal of non-Newtonian fluid mechanics*, 137(1-3):137–148, 2006.

[150] Junfeng Shi, Yuan Gao, Ye Zhang, Yue Pan, and Bing Xu. Calcium ions to cross-link supramolecular nanofibers to tune the elasticity of hydrogels over orders of magnitude. *Langmuir*, 27(23):14425–14431, 2011.

[151] Riaz Akhtar, Emily R Draper, Dave J Adams, and Jennifer Hay. Oscillatory nanoindentation of highly compliant hydrogels: A critical comparative analysis with rheometry. *Journal of Materials Research*, 33(8):873–883, 2018.

[152] Loyal Durand. Stability and oscillations of a soap film: An analytic treatment. *American Journal of Physics*, 49(4):334–343, 1981.

[153] Luca Giomi. Hyperbolic interfaces. *Physical review letters*, 109(13):136101, 2012.

[154] Stephen H Spiegelberg and Gareth H McKinley. Stress relaxation and elastic decohesion of viscoelastic polymer solutions in extensional flow. *Journal of Non-Newtonian Fluid Mechanics*, 67:49–76, 1996.

[155] Gerald Henry Meeten. Squeeze flow of soft solids between rough surfaces. *Rheologica acta*, 43(1):6–16, 2004.

[156] Elmar Bonaccurso, Michael Kappl, and Hans-Jürgen Butt. Hydrodynamic force measurements: boundary slip of water on hydrophilic surfaces and electrokinetic effects. *Physical Review Letters*, 88(7):076103, 2002.

[157] Christophe Cheikh and Ger Koper. Stick-slip transition at the nanometer scale. *Physical review letters*, 91(15):156102, 2003.

[158] Y Cohen and AB Metzner. An analysis of apparent slip flow of polymer solutions. *Rheologica acta*, 25(1):28–35, 1986.

[159] Howard A Barnes. A review of the slip (wall depletion) of polymer solutions, emulsions and particle suspensions in viscometers: its cause, character, and cure. *Journal of Non-Newtonian Fluid Mechanics*, 56(3):221–251, 1995.

[160] William B Russel and Mae Chen Grant. Distinguishing between dynamic yielding and wall slip in a weakly flocculated colloidal dispersion. *Colloids and Surfaces A: Physicochemical and Engineering Aspects*, 161(2):271–282, 2000.

[161] Güneri Akovali. *The interfacial interactions in polymeric composites*, volume 230. Springer Science & Business Media, 2012.

[162] A Maciel, V Salas, JFA Soltero, J Guzmán, and O Manero. On the wall slip of polymer blends. *Journal of Polymer Science Part B: Polymer Physics*, 40(4):303–316, 2002.

[163] Tatiana Schmatko, Hubert Hervet, and Liliane Leger. Friction and slip at simple fluid-solid interfaces: the roles of the molecular shape and the solid-liquid interaction. *Physical review letters*, 94(24):244501, 2005.

[164] MC Sánchez, C Valencia, JM Franco, and C Gallegos. Wall slip phenomena in oil-in-water emulsions: effect of some structural parameters. *Journal of colloid and interface science*, 241(1):226–232, 2001.

[165] Krittalak Chakrabandhu and Rakesh K Singh. Wall slip determination for coarse food suspensions in tube flow at high temperatures. *Journal of food engineering*, 70(1):73–81, 2005.

[166] QD Nguyen and DV Boger. Measuring the flow properties of yield stress fluids. *Annual Review of Fluid Mechanics*, 24(1):47–88, 1992.

[167] JM Franco, C Gallegos, and HA Barnes. On slip effects in steady-state flow measurements of oil-in-water food emulsions. *Journal of Food Engineering*, 36(1):89–102, 1998.

[168] Howard A Barnes. *A handbook of elementary rheology*, volume 1. University of Wales, Institute of Non-Newtonian Fluid Mechanics Aberystwyth, 2000.

[169] emulsion emulsion definition. https://pharmlabs.unc.edu/labs/emulsions/intro.htm.

[170] Tharwat F Tadros. Emulsion formation, stability, and rheology. *Emulsion formation and stability*, 1:1–75, 2013.

[171] Leonard MC Sagis. Dynamic properties of interfaces in soft matter: Experiments and theory. *Reviews of Modern Physics*, 83(4):1367, 2011.

[172] Bob Aveyard. *Surfactants: in solution, at interfaces and in colloidal dispersions*. Oxford University Press, USA, 2019.

[173] Morfo Zembyla, Brent S Murray, and Anwesha Sarkar. Water-in-oil emulsions stabilized by surfactants, biopolymers and/or particles: A review. *Trends in Food Science & Technology*, 2020.

[174] Jack Yang, Ilonka Thielen, Claire C Berton-Carabin, Erik van der Linden, and Leonard MC Sagis. Nonlinear interfacial rheology and atomic force microscopy of air-water interfaces stabilized by whey protein beads and their constituents. *Food Hydrocolloids*, 101:105466, 2020.

[175] Ioanna Zafeiri, Paul Smith, Ian T Norton, and Fotis Spyropoulos. O/w emulsions stabilised by solid lipid particles: Understanding how the particles' pickering functionality can be retained post their dehydration and subsequent rehydration. *Colloids and Surfaces A: Physicochemical and Engineering Aspects*, page 124916, 2020.

[176] Gabriel Brossard, Christian Clasen, and Jan Vermant. Interfacial rheology of triglyceride lipid emulsion. In *Joint Symposium of the Belgian Group of Rheology, German Rheological Society, ProcessNet-Subject Division „Rheology ", Date: 2018/03/19-2018/03/20, Location: Luxembourg, Luxembourg*, 2018.

[177] Paul S Clegg. *Bijels: Bicontinuous Particle-stabilized Emulsions*, volume 10. Royal Society of Chemistry, 2020.

[178] Thomas Moschakis, Nikos Chantzos, Costas G Biliaderis, and Eric Dickinson. Microrheology and microstructure of water-in-water emulsions containing sodium caseinate and locust bean gum. *Food & function*, 9(5):2840–2852, 2018.

[179] Luis J Pérez-Córdoba, Ian T Norton, Hannah K Batchelor, Konstantinos Gkatzionis, Fotios Spyropoulos, and Paulo JA Sobral. Physico-chemical, antimicrobial and antioxidant properties of gelatin-chitosan based films loaded with nanoemulsions encapsulating active compounds. *Food Hydrocolloids*, 79:544–559, 2018.

[180] Pascal Bertsch, Alexandra Thoma, Jotam Bergfreund, Thomas Geue, and Peter Fischer. Transient measurement and structure analysis of protein–polysaccharide multilayers at fluid interfaces. *Soft matter*, 15(31):6362–6368, 2019.

[181] Simone Bochner de Araujo, Maria Merola, Dimitris Vlassopoulos, and Gerald G Fuller. Droplet coalescence and spontaneous emulsification in the presence of asphaltene adsorption. *Langmuir*, 33(40):10501–10510, 2017.

[182] Yan Yang, Julia Maldonado-Valderrama, and Alberto Martín-Molina. Temperature and electrostatics effects on charged poly (n-isopropylacrylamide) microgels at the interface. *Journal of Molecular Liquids*, 303:112678, 2020.

[183] Brent S Murray. Microgels at fluid-fluid interfaces for food and drinks. *Advances in colloid and interface science*, 271:101990, 2019.

[184] Reinhard Miller, Rainer Wüstneck, Jürgen Krägel, and Günter Kretzschmar. Dilational and shear rheology of adsorption layers at liquid interfaces. *Colloids and Surfaces A: Physicochemical and Engineering Aspects*, 111(1-2):75–118, 1996.

[185] Patrick A Rühs, Christine Affolter, Erich J Windhab, and Peter Fischer. Shear and dilatational linear and nonlinear subphase controlled interfacial

rheology of β-lactoglobulin fibrils and their derivatives. *Journal of Rheology*, 57(3):1003–1022, 2013.

[186] Silvia EHJ van Kempen, Henk A Schols, Erik van der Linden, and Leonard MC Sagis. Non-linear surface dilatational rheology as a tool for understanding microstructures of air/water interfaces stabilized by oligofructose fatty acid esters. *Soft Matter*, 9(40):9579–9592, 2013.

[187] Merel EH Van Den Berg, Simon Kuster, Erich J Windhab, Leonard MC Sagis, and Peter Fischer. Nonlinear shear and dilatational rheology of viscoelastic interfacial layers of cellulose nanocrystals. *Physics of Fluids*, 30(7):072103, 2018.

[188] M Hoorfar and AW Neumann. Recent progress in axisymmetric drop shape analysis (adsa). *Advances in colloid and interface science*, 121(1-3):25–49, 2006.

[189] John M Dealy and Kurt F Wissbrun. *Melt rheology and its role in plastics processing: theory and applications*. Springer Science & Business Media, 2012.

[190] JM Dealy, TT Tee, and JF Petersen. A concentric-cylinder rheometer for polymer melts. In *Rheological Theories · Measuring Techniques in Rheology Test Methods in Rheology · Fractures Rheological Properties of Materials · Rheo-Optics · Biorheology*, pages 466–474. Springer, 1975.

[191] Thomas G Mezger. *The rheology handbook: for users of rotational and oscillatory rheometers*. Vincentz Network GmbH & Co KG, 2006.

[192] Junhua Zhang, Christopher R Daubert, and E Allen Foegeding. A proposed strain-hardening mechanism for alginate gels. *Journal of Food Engineering*, 80(1):157–165, 2007.

[193] May Sui Mei Wee. *Physico-chemical characterisation and functionality of the polysaccharide extracted from the New Zealand black tree fern, Cyathea medullaris (Mamaku): a thesis presented in partial fulfilment of the requirements for the degree of Doctor of Philosophy in Food Technology at Massey University, Palmerston North, New Zealand*. PhD thesis, Massey University, 2015.

[194] V Tirtaatmadja, KC Tam, and RD Jenkins. Superposition of oscillations on steady shear flow as a technique for investigating the structure of associative polymers. *Macromolecules*, 30(5):1426–1433, 1997.

[195] W Philippoff. Vibrational measurements with large amplitudes. *Transactions of the Society of Rheology*, 10(1):317–334, 1966.

[196] Stanley S Davis. Viscoelastic properties of pharmaceutical semisolids iv: Destructive oscillatory testing. *Journal of pharmaceutical sciences*, 60(9):1356–1360, 1971.

[197] AR Payne and RE Whittaker. Low strain dynamic properties of filled rubbers. *Rubber chemistry and technology*, 44(2):440–478, 1971.

[198] Raymond J Krizek. Rheologic behavior of clay soils subjected to dynamic loads. *Transactions of the Society of Rheology*, 15(3):433–489, 1971.

[199] Joseph D Berry, Michael J Neeson, Raymond R Dagastine, Derek YC Chan, and Rico F Tabor. Measurement of surface and interfacial tension using pendant drop tensiometry. *Journal of colloid and interface science*, 454:226–237, 2015.

[200] Isopropyl myristate interfacial tension. http://www.chemspider.com/Chemical-Structure.7751.html.

[201] krussmanual. *Software for Drop Shape Analysis Installation Manual*.

[202] Jonas Hegemann, Sebastian Knoche, Simon Egger, Maureen Kott, Sarah Demand, Anja Unverfehrt, Heinz Rehage, and Jan Kierfeld. Pendant capsule elastometry. *Journal of colloid and interface science*, 513:549–565, 2018.

[203] Kendra A Erk, Jeffrey D Martin, Jonathan T Schwalbe, Frederick R Phelan Jr, and Steven D Hudson. Shear and dilational interfacial rheology of surfactant-stabilized droplets. *Journal of colloid and interface science*, 377(1):442–449, 2012.

[204] Howard Brenner. *Interfacial transport processes and rheology*. Elsevier, 2013.

[205] Rudi Mears. Structure and mechanical properties of model colloids at liquid interfaces. 2020.

[206] Andre Zamith Cardoso, Laura LE Mears, Beatrice N Cattoz, Peter C Griffiths, Ralf Schweins, and Dave J Adams. Linking micellar structures to hydrogelation for salt-triggered dipeptide gelators. *Soft Matter*, 12(15):3612–3621, 2016.

[207] Srinivasa R Raghavan and Bani H Cipriano. Gel formation: phase diagrams using tabletop rheology and calorimetry. In *Molecular gels*, pages 241–252. Springer, 2006.

[208] LMC Sagis, KNP Humblet-Hua, and SEHJ Van Kempen. Nonlinear stress deformation behavior of interfaces stabilized by food-based ingredients. *Journal of Physics: Condensed Matter*, 26(46):464105, 2014.

[209] Fabian C Birbaum, Sanna Haavisto, Antti Koponen, Erich J Windhab, and Peter Fischer. Shear localisation in interfacial particle layers and its influence on lissajous-plots. *Rheologica Acta*, 55(4):267–278, 2016.

[210] Juntae Kim, Dimitri Merger, Manfred Wilhelm, and Matthew E Helgeson. Microstructure and nonlinear signatures of yielding in a heterogeneous colloidal gel under large amplitude oscillatory shear. *Journal of Rheology*, 58(5):1359–1390, 2014.

[211] MRB Mermet-Guyennet, J Gianfelice de Castro, M Habibi, N Martzel, MM Denn, and D Bonn. Laos: The strain softening/strain hardening paradox. *Journal of Rheology*, 59(1):21–32, 2015.

[212] Gerard Giménez-Ribes, Mehdi Habibi, and Leonard MC Sagis. Interfacial rheology and relaxation behavior of adsorption layers of the triterpenoid saponin escin. *Journal of Colloid and Interface Science*, 563:281–290, 2020.

[213] DJ McClements, EA Decker, and J Weiss. Emulsion-based delivery systems for lipophilic bioactive components. *Journal of food science*, 72(8):R109–R124, 2007.

[214] J Parada and JM Aguilera. Food microstructure affects the bioavailability of several nutrients. *Journal of food science*, 72(2):R21–R32, 2007.

[215] Ourania Gouseti, Gail M Bornhorst, Serafim Bakalis, and Alan Mackie. *Interdisciplinary Approaches to Food Digestion*. Springer, 2019.

[216] Cintia B Dias, Xiangqian Zhu, Abby K Thompson, Harjinder Singh, and Manohar L Garg. Effect of the food form and structure on lipid digestion and postprandial lipaemic response. *Food & function*, 10(1):112–124, 2019.

[217] Ana-Isabel Mulet-Cabero, Neil M Rigby, André Brodkorb, and Alan R Mackie. Dairy food structures influence the rates of nutrient digestion through different in vitro gastric behaviour. *Food Hydrocolloids*, 67:63–73, 2017.

[218] Thomas F Whayne Jr and James M Felts. Activation of lipoprotein lipase: evaluation of calcium, magnesium, and ammonium as cofactors. *Circulation research*, 28(6):649–654, 1971.

[219] Hiroshi Kimura, Yoshitaka Futami, Sei-ichiro TARUI, and Takaaki SHINOMIYA. Activation of human pancreatic lipase activity by calcium and bile salts. *The Journal of Biochemistry*, 92(1):243–251, 1982.

[220] Martine Armand, Patrick Borel, Pascale Ythier, Guy Dutot, Christian Melin, Michèle Senft, Huguette Lafont, and Denis Lairon. Effects of droplet size, triacylglycerol composition, and calcium on the hydrolysis of complex emulsions by pancreatic lipase: an in vitro study. *The Journal of Nutritional Biochemistry*, 3(7):333–341, 1992.

[221] Min Hu, Yan Li, Eric Andrew Decker, and David Julian McClements. Role of calcium and calcium-binding agents on the lipase digestibility of emulsified lipids using an in vitro digestion model. *Food Hydrocolloids*, 24(8):719–725, 2010.

[222] Niels Hønberg Zangenberg, Anette Müllertz, Henning Gjelstrup Kristensen, and Lars Hovgaard. A dynamic in vitro lipolysis model: I. controlling the rate of lipolysis by continuous addition of calcium. *European Journal of Pharmaceutical Sciences*, 14(2):115–122, 2001.

[223] Uri Lesmes and David Julian McClements. Controlling lipid digestibility: Response of lipid droplets coated by β-lactoglobulin-dextran maillard conjugates to simulated gastrointestinal conditions. *Food Hydrocolloids*, 26(1):221–230, 2012.

[224] Meinou N Corstens, Claire C Berton-Carabin, Renko de Vries, Freddy J Troost, Ad AM Masclee, and Karin Schroën. Food-grade micro-encapsulation systems that may induce satiety via delayed lipolysis: a review. *Critical reviews in food science and nutrition*, 57(10):2218–2244, 2017.

[225] Yan Li, Jonggun Kim, Yeonhwa Park, and David Julian McClements. Modulation of lipid digestibility using structured emulsion-based delivery systems: comparison of in vivo and in vitro measurements. *Food & function*, 3(5):528–536, 2012.

[226] Krassimir P Velikov and Eddie Pelan. Colloidal delivery systems for micronutrients and nutraceuticals. *Soft matter*, 4(10):1964–1980, 2008.

[227] Sun Jin Hur, Beong Ou Lim, Eric A Decker, and D Julian McClements. In vitro human digestion models for food applications. *Food Chemistry*, 125(1):1–12, 2011.

[228] Christopher JH Porter, Ann Marie Kaukonen, Agnes Taillardat-Bertschinger, Ben J Boyd, Jacquelyn M O'Connor, Glenn A Edwards, and William N Charman. Use of in vitro lipid digestion data to explain the in vivo performance of triglyceride-based oral lipid formulations of poorly water-soluble drugs: studies with halofantrine. *Journal of pharmaceutical sciences*, 93(5):1110–1121, 2004.

[229] Torsten Bohn, F Carriere, L Day, Amélie Deglaire, L Egger, Daniela Freitas, M Golding, Steven Le Feunteun, Adam Macierzanka, Olivia Menard, et al. Correlation between in vitro and in vivo data on food digestion. what can we predict with static in vitro digestion models? *Critical reviews in food science and nutrition*, 58(13):2239–2261, 2018.

[230] M Minekus, Marie Alminger, Paula Alvito, S Ballance, TORSTEN Bohn, C Bourlieu, F Carriere, Rachel Boutrou, M Corredig, Didier Dupont, et al. A standardised static in vitro digestion method suitable for food–an international consensus. *Food & function*, 5(6):1113–1124, 2014.

[231] Martine Armand. Lipases and lipolysis in the human digestive tract: where do we stand? *Current Opinion in Clinical Nutrition & Metabolic Care*, 10(2):156–164, 2007.

[232] Huiling Mu and Carl-Erik Høy. The digestion of dietary triacylglycerols. *Progress in lipid research*, 43(2):105–133, 2004.

[233] Ana Mulet Cabero. *Effect of Dairy Structures on Gastric Behaviour and Nutrient Digestion Kinetics using a Semi-Dynamic Model*. PhD thesis, University of Easy Anglia, 2018.

[234] Yan Li and David Julian McClements. New mathematical model for interpreting ph-stat digestion profiles: Impact of lipid droplet characteristics on in vitro digestibility. *Journal of agricultural and food chemistry*, 58(13):8085–8092, 2010.

[235] Damien JL Mat, Steven Le Feunteun, Camille Michon, and Isabelle Souchon. In vitro digestion of foods using ph-stat and the infogest protocol: Impact of matrix structure on digestion kinetics of macronutrients, proteins and lipids. *Food Research International*, 88:226–233, 2016.

[236] G Fave, TC Coste, and M Armand. Physicochemical properties of lipids: new strategies to manage fatty acid bioavailability. *Cellular and molecular biology*, 50(7):815–832, 2004.

[237] E Bauer, S Jakob, and R Mosenthin. Principles of physiology of lipid digestion. *Asian-Australasian Journal of Animal Sciences*, 18(2):282–295, 2005.

[238] Aiqian Ye, Jian Cui, Xiangqian Zhu, and Harjinder Singh. Effect of calcium on the kinetics of free fatty acid release during in vitro lipid digestion in model emulsions. *Food chemistry*, 139(1-4):681–688, 2013.

[239] Amelia Torcello-Gómez, Chloé Boudard, and Alan R Mackie. Calcium alters the interfacial organization of hydrolyzed lipids during intestinal digestion. *Langmuir*, 34(25):7536–7544, 2018.

[240] Qing Guo, Nick Bellissimo, and Dérick Rousseau. Role of gel structure in controlling in vitro intestinal lipid digestion in whey protein emulsion gels. *Food hydrocolloids*, 69:264–272, 2017.

[241] Qing Guo, Aiqian Ye, Mita Lad, Douglas Dalgleish, and Harjinder Singh. Effect of gel structure on the gastric digestion of whey protein emulsion gels. *Soft matter*, 10(8):1214–1223, 2014.

[242] Kéra Nyemb, Catherine Guérin-Dubiard, Stéphane Pézennec, Julien Jardin, Valérie Briard-Bion, Chantal Cauty, Shane M Rutherfurd, Didier Dupont, and Françoise Nau. The structural properties of egg white gels impact the extent of in vitro protein digestion and the nature of peptides generated. *Food Hydrocolloids*, 54:315–327, 2016.

[243] L Salvia-Trujillo, C Qian, O Martín-Belloso, and DJ McClements. Influence of particle size on lipid digestion and β-carotene bioaccessibility in emulsions and nanoemulsions. *Food chemistry*, 141(2):1472–1480, 2013.

[244] Karl-Erich Jaeger, Stéphane Ransac, Bauke W Dijkstra, Charles Colson, Margreet van Heuvel, and Onno Misset. Bacterial lipases. *FEMS microbiology reviews*, 15(1):29–63, 1994.

[245] Thuy Minh Giang, Sebastien Gaucel, Pierre Brestaz, Marc Anton, Anne Meynier, Ioan-Cristian Trelea, and Steven Le Feunteun. Dynamic modeling of in vitro lipid digestion: individual fatty acid release and bioaccessibility kinetics. *Food Chemistry*, 194:1180–1188, 2016.

[246] SA Chime, FC Kenechukwu, and AA Attama. *Nanoemulsions—advances in formulation, characterization and applications in drug delivery*, volume 3. chapter, 2014.

[247] _S Benita and MY Levy. Submicron emulsions as colloidal drug carriers for intravenous administration: comprehensive physicochemical characterization. *Journal of Pharmaceutical Sciences*, 82(11):1069–1079, 1993.

[248] M Chappat. Some applications of emulsions. *Colloids and Surfaces A: Physicochemical and Engineering Aspects*, 91:57–77, 1994.

[249] M Kónya, M Sorrenti, F Ferrari, S Rossi, I Csóka, C Caramella, G Bettinetti, and I Erős. Study of the microstructure of o/w creams with thermal and rheological methods. *Journal of thermal analysis and calorimetry*, 73(2):623–632, 2003.

[250] Eric Dickinson and Soon-Taek Hong. Influence of water-soluble nonionic emulsifier on the rheology of heat-set protein-stabilized emulsion gels. *Journal of Agricultural and Food Chemistry*, 43(10):2560–2566, 1995.

[251] Francesca R Lupi, Domenico Gabriele, Lucia Seta, Noemi Baldino, Bruno de Cindio, and Rosamaria Marino. Rheological investigation of pectin-based emulsion gels for pharmaceutical and cosmetic uses. *Rheologica Acta*, 54(1):41–52, 2015.

[252] Laura Oliver, Elke Scholten, and George A van Aken. Effect of fat hardness on large deformation rheology of emulsion-filled gels. *Food Hydrocolloids*, 43:299–310, 2015.

[253] Chantal Boutin, Hélène J Giroux, Paul Paquin, and Michel Britten. Characterization and acid-induced gelation of butter oil emulsions produced from heated whey protein dispersions. *International Dairy Journal*, 17(6):696–703, 2007.

[254] Paula Rosa, Guido Sala, TON Van Vliet, and Fred Van De Velde. Cold gelation of whey protein emulsions. *Journal of Texture Studies*, 37(5):516–537, 2006.

[255] K-H Kim, JMS Renkema, and T Van Vliet. Rheological properties of soybean protein isolate gels containing emulsion droplets. *Food hydrocolloids*, 15(3):295–302, 2001.

[256] Mangang Wu, Youling L Xiong, and Jie Chen. Rheology and microstructure of myofibrillar protein–plant lipid composite gels: Effect of emulsion droplet size and membrane type. *Journal of food engineering*, 106(4):318–324, 2011.

[257] V.V Krotov. Basics of interfacial rheology). (1):1–37, 2008.

[258] Konstantinos Koumpouras and J Andreas Larsson. Distinguishing between chemical bonding and physical binding using electron localization function (elf). *Journal of Physics: Condensed Matter*, 32(31):315502, 2020.

[259] Ibrahim M Banat, Ravinder S Makkar, and Swaranjit Singh Cameotra. Potential commercial applications of microbial surfactants. *Applied microbiology and biotechnology*, 53(5):495–508, 2000.

[260] Joachim J Hug and Rolf Müller. Host development for heterologous expression and biosynthetic studies of myxobacterial natural products. 2020.

[261] Lin Yu and Jiandong Ding. Injectable hydrogels as unique biomedical materials. *Chemical Society Reviews*, 37(8):1473–1481, 2008.

[262] Huiyuan Wang and Sarah C Heilshorn. Adaptable hydrogel networks with reversible linkages for tissue engineering. *Advanced Materials*, 27(25):3717–3736, 2015.

[263] Catherine Colquhoun, Emily R Draper, Ralf Schweins, Marco Marcello, Devkee Vadukul, Louise C Serpell, and Dave J Adams. Controlling the network type in self-assembled dipeptide hydrogels. *Soft Matter*, 13(9):1914–1919, 2017.

[264] Laurier L Schramm, Elaine N Stasiuk, and D Gerrard Marangoni. 2 surfactants and their applications. *Annual Reports Section" C"(Physical Chemistry)*, 99:3–48, 2003.

[265] Lin Chen, Kyle Morris, Andrea Laybourn, David Elias, Matthew R Hicks, Alison Rodger, Louise Serpell, and Dave J Adams. Self-assembly mechanism for a naphthalene- dipeptide leading to hydrogelation. *Langmuir*, 26(7):5232–5242, 2009.

[266] Lin Chen, Steven Revel, Kyle Morris, Louise C. Serpell, and Dave J Adams. Effect of molecular structure on the properties of naphthalene- dipeptide hydrogelators. *Langmuir*, 26(16):13466–13471, 2010.

[267] Julius WJ de Folter, Marjolein WM van Ruijven, and Krassimir P Velikov. Oil-in-water pickering emulsions stabilized by colloidal particles from the water-insoluble protein zein. *Soft Matter*, 8(25):6807–6815, 2012.

[268] R Pichot, L Duffus, I Zafeiri, F Spyropoulos, and IT Norton. Particle-stabilized food emulsions. In *Particle-Stabilized Emulsions and Colloids*, pages 247–282. 2014.

[269] Bernard P Binks. Particles as surfactants—similarities and differences. *Current opinion in colloid & interface science*, 7(1-2):21–41, 2002.

[270] L Andrew Lyon and Alberto Fernandez-Nieves. The polymer/colloid duality of microgel suspensions. *Annual review of physical chemistry*, 63:25–43, 2012.

[271] Richard G Weiss. The past, present, and future of molecular gels. what is the status of the field, and where is it going? *Journal of the American Chemical Society*, 136(21):7519–7530, 2014.

[272] Vineetha Jayawarna, Stephen M Richardson, Andrew R Hirst, Nigel W Hodson, Alberto Saiani, Julie E Gough, and Rein V Ulijn. Introducing chemical functionality in fmoc-peptide gels for cell culture. *Acta biomaterialia*, 5(3):934–943, 2009.

[273] Jayanta Nanda and Arindam Banerjee. β-amino acid containing proteolitically stable dipeptide based hydrogels: encapsulation and sustained release of some important biomolecules at physiological ph and temperature. *Soft Matter*, 8(12):3380–3386, 2012.

[274] Georgia Kaklamani, Diana Kazaryan, James Bowen, Fabrice Iacovella, Spiros H Anastasiadis, and George Deligeorgis. On the electrical conductivity of alginate hydrogels. *Regenerative biomaterials*, 5(5):293–301, 2018.

[275] Gary G Scott, Paul J McKnight, Tell Tuttle, and Rein V Ulijn. Tripeptide emulsifiers. *Advanced Materials*, 28(7):1381–1386, 2016.

[276] Sudipta Mondal, Maxim Varenik, Daniel Nir Bloch, Yoav Atsmon-Raz, Guy Jacoby, Lihi Adler-Abramovich, Linda JW Shimon, Roy Beck, Yifat Miller, Oren Regev, et al. A minimal length rigid helical peptide motif allows rational design of modular surfactants. *Nature communications*, 8:14018, 2017.

[277] Inês P Moreira, Ivan Ramos Sasselli, Daniel A Cannon, Meghan Hughes, Dimitrios A Lamprou, Tell Tuttle, and Rein V Ulijn. Enzymatically activated emulsions stabilised by interfacial nanofibre networks. *Soft matter*, 12(9):2623–2631, 2016.

[278] F Müller and R Stannarius. Collapse of catenoid-shaped smectic films. *EPL (Europhysics Letters)*, 76(6):1102, 2006.

[279] Ge Cheng, V Castelletto, CM Moulton, GE Newby, and IW Hamley. Hydrogelation and self-assembly of fmoc-tripeptides: unexpected influence of sequence on self-assembled fibril structure, and hydrogel modulus and anisotropy. *Langmuir*, 26(7):4990–4998, 2010.

[280] Huiyuan Wang, Alexandra Paul, Duong Nguyen, Annika Enejder, and Sarah C Heilshorn. Tunable control of hydrogel microstructure by kinetic

competition between self-assembly and crosslinking of elastin-like proteins. *ACS applied materials & interfaces*, 10(26):21808–21815, 2018.

[281] Bulent Ozbas, Juliana Kretsinger, Karthikan Rajagopal, Joel P Schneider, and Darrin J Pochan. Salt-triggered peptide folding and consequent self-assembly into hydrogels with tunable modulus. *Macromolecules*, 37(19):7331–7337, 2004.

[282] A Chiralt. Food emulsions. *Food engineering*, 2:150–175, 2009.

[283] Yuh-Fun Maa and Chung Hsu. Liquid-liquid emulsification by rotor/stator homogenization. *Journal of Controlled Release*, 38(2-3):219–228, 1996.

[284] Eric Dickinson and Martin E Leser, editors. *Food Colloids*. Special Publications. The Royal Society of Chemistry, 2007.

[285] E Desmond Goddard and James V Gruber. *Principles of polymer science and technology in cosmetics and personal care*. CRC Press, 1999.

[286] Martin Rieger. *Surfactants in cosmetics*. Routledge, 2017.

[287] Mitali Kakran and Maria N Antipina. Emulsion-based techniques for encapsulation in biomedicine, food and personal care. *Current opinion in pharmacology*, 18:47–55, 2014.

[288] Jonathan R Lindner. Microbubbles in medical imaging: current applications and future directions. *Nature reviews Drug discovery*, 3(6):527, 2004.

[289] Robert Antonie Debruijn. Deformation and breakup of drops in simple shear flows. 1991.

[290] M Döring. Ink-jet printing. *Philips Tech. Rev*, 40(7):192–198, 1982.

[291] Howard A Stone and L Gary Leal. The effects of surfactants on drop deformation and breakup. *Journal of Fluid Mechanics*, 220:161–186, 1990.

[292] SP Sutera and MH Mehrjardi. Deformation and fragmentation of human red blood cells in turbulent shear flow. *Biophysical journal*, 15(1):1–10, 1975.

[293] AK Gupta and S Basu. Deformation of an oil droplet on a solid substrate in simple shear flow. *Chemical engineering science*, 63(22):5496–5502, 2008.

[294] Lin Changzhi and GUO Liejin. Experimental study of drop deformation and breakup in simple shear flows. *Chinese Journal of Chemical Engineering*, 15(1):1–5, 2007.

[295] Cambridge Polymer Group. The capillary breakup extensional rheometer. Available at http://web.mit.edu/rsi/www/pdfs/bibtex-format.pdf (2019/07/11).

[296] Howard A Stone and L Gary Leal. Relaxation and breakup of an initially extended drop in an otherwise quiescent fluid. *Journal of Fluid Mechanics*, 198:399–427, 1989.

[297] DC Vadillo, TR Tuladhar, AC Mulji, S Jung, SD Hoath, and MR Mackley. Evaluation of the inkjet fluid's performance using the "cambridge trimaster" filament stretch and break-up device. *Journal of Rheology*, 54(2):261–282, 2010.

[298] Valentin Goussard, François Duprat, Vincent Gerbaud, Jean-Luc Ploix, Gérard Dreyfus, Véronique Nardello-Rataj, and Jean-Marie Aubry. Predicting the surface tension of liquids: Comparison of four modeling approaches and application to cosmetic oils. *Journal of chemical information and modeling*, 57(12):2986–2995, 2017.

[299] NB Vargaftik, BN Volkov, and LD Voljak. International tables of the surface tension of water. *Journal of Physical and Chemical Reference Data*, 12(3):817–820, 1983.

[300] P Cheng, D Li, L Boruvka, Y Rotenberg, and AW Neumann. Automation of axisymmetric drop shape analysis for measurements of interfacial tensions and contact angles. *Colloids and Surfaces*, 43(2):151–167, 1990.

[301] Shahab Lahooti, I del Rio, P Cheng, and AW Neumann. Axisymmetric drop shape analysis (adsa). In *Applied Surface Thermodynamics*, pages 459–526. CRC Press, 1996.

[302] Surendra N Ganeriwala and Christopher A Rotz. Fourier transform mechanical analysis for determining the nonlinear viscoelastic properties of polymers. *Polymer Engineering & Science*, 27(2):165–178, 1987.

[303] Kyu Hyun, Jung Gun Nam, Manfred Wilhelm, Kyung Hyun Ahn, and Seung Jong Lee. Nonlinear response of complex fluids under laos (large amplitude oscillatory shear) flow. *Korea-Australia Rheology Journal*, 15(2):97–105, 2003.

[304] Claire C Berton-Carabin, Anja Schröder, Ana Rovalino-Cordova, Karin Schroën, and Leonard Sagis. Protein and lipid oxidation affect the viscoelasticity of whey protein layers at the oil–water interface. *European Journal of Lipid Science and Technology*, 118(11):1630–1643, 2016.

[305] Enrica Caló and Vitaliy V Khutoryanskiy. Biomedical applications of hydrogels: A review of patents and commercial products. *European Polymer Journal*, 65:252–267, 2015.

[306] Ye Zhang, Yi Kuang, Yuan Gao, and Bing Xu. Versatile small-molecule motifs for self-assembly in water and the formation of biofunctional supramolecular hydrogels. *Langmuir*, 27(2):529–537, 2011.

[307] thixotropic thixotropic effect. https://wiki.anton-paar.com/uk-en/basics-of-thixotropy.

[308] Eric Dickinson. Colloids in food: ingredients, structure, and stability. *Annual review of food science and technology*, 6:211–233, 2015.

[309] Artur J Martins, António A Vicente, Rosiane L Cunha, and Miguel A Cerqueira. Edible oleogels: an opportunity for fat replacement in foods. *Food & function*, 9(2):758–773, 2018.

[310] Hernan Brice Kenmogne-Domguia, Anne Meynier, Michèle Viau, Geneviève Llamas, and Claude Genot. Gastric conditions control both the evolution of the organization of protein-stabilized emulsions and the kinetic of lipolysis during in vitro digestion. *Food & function*, 3(12):1302–1309, 2012.

[311] Jahangir Iqbal and M Mahmood Hussain. Intestinal lipid absorption. *American Journal of Physiology-Endocrinology and Metabolism*, 296(6):E1183–E1194, 2009.

[312] R Wüstneck, J Krägel, R Miller, VB Fainerman, Peter J Wilde, DK Sarker, and David C Clark. Dynamic surface tension and adsorption properties of β-casein and β-lactoglobulin. *Food Hydrocolloids*, 10(4):395–405, 1996.

[313] David Julian McClements and Yan Li. Review of in vitro digestion models for rapid screening of emulsion-based systems. *Food & function*, 1(1):32–59, 2010.

[314] Theo BJ Blijdenstein, Cecile Veerman, and Erik van der Linden. Depletion-flocculation in oil-in-water emulsions using fibrillar protein assemblies. *Langmuir*, 20(12):4881–4884, 2004.

[315] Kitty Verhoeckx, Paul Cotter, Iván López-Expósito, Charlotte Kleiveland, Tor Lea, Alan Mackie, Teresa Requena, Dominika Swiatecka, and Harry Wichers. *The impact of food bioactives on health: in vitro and ex vivo models*. Springer, 2015.

[316] Agnes G Oomen, Alfons Hack, Mans Minekus, Evelijn Zeijdner, Christa Cornelis, Greet Schoeters, Willy Verstraete, Tom Van de Wiele, Joanna Wragg, Cathy JM Rompelberg, et al. Comparison of five in vitro digestion models to study the bioaccessibility of soil contaminants. *Environmental science & technology*, 36(15):3326–3334, 2002.